forests

Wood Properties and Processing

Edited by

Miha Humar

Printed Edition of the Special Issue Published in *Forests*

www.mdpi.com/journal/forests

MDPI

Wood Properties and Processing

Wood Properties and Processing

Special Issue Editor

Miha Humar

MDPI • Basel • Beijing • Wuhan • Barcelona • Belgrade • Manchester • Tokyo • Cluj • Tianjin

Special Issue Editor
Miha Humar
University of Ljubljana
Slovenia

Editorial Office
MDPI
St. Alban-Anlage 66
4052 Basel, Switzerland

This is a reprint of articles from the Special Issue published online in the open access journal *Forests* (ISSN 1999-4907) (available at: https://www.mdpi.com/journal/forests/special_issues/Wood_properties).

For citation purposes, cite each article independently as indicated on the article page online and as indicated below:

LastName, A.A.; LastName, B.B.; LastName, C.C. Article Title. *Journal Name* **Year**, *Article Number*, Page Range.

ISBN 978-3-03928-821-2 (Hbk)
ISBN 978-3-03928-822-9 (PDF)

Cover image courtesy of Miha Humar.

© 2020 by the authors. Articles in this book are Open Access and distributed under the Creative Commons Attribution (CC BY) license, which allows users to download, copy and build upon published articles, as long as the author and publisher are properly credited, which ensures maximum dissemination and a wider impact of our publications.
The book as a whole is distributed by MDPI under the terms and conditions of the Creative Commons license CC BY-NC-ND.

Contents

About the Special Issue Editor

Miha Humar, Profesor of Wood Science and Technology at University of Ljubljana.

Preface to "Wood Properties and Processing"

Wood is one of the most important building materials, and its importance has been increasing in recent decades. This trend is also likely to continue in the future. This book addresses relevant problems in wood science and technology. These problems are not limited to a certain country or territory but are generally experienced all over the world. In the first part, contributions addressing the question of how to assess wood quality in forests. Novel non-destructive techniques offer cost- and time-effective solutions. In the second part, contributions are dedicated to primary wood processing, wood drying, machining, and the development and performance of advanced wood-based composites. The third section is dedicated to the performance of wood in outdoor applications. Special emphasis is given to esthetic performance. The fourth section is devoted to the development of final products (furniture) and market analysis. The last section examines the use of bamboo-based materials in the harsh conditions of cooling towers. Thus, this book brings good insight into the recent developments within wood science and technology.

Miha Humar
Special Issue Editor

forests

MDPI

Article

Effect of Rotation Age and Thinning Regime on Visual and Structural Lumber Grades of Douglas-Fir Logs

Eini C. Lowell [1,*], Eric C. Turnblom [2], Jeff M. Comnick [2] and CL Huang [3]

[1] USDA Forest Service Pacific Northwest Research Station, 620 SW Main Street Suite 502, Portland, OR 97205, USA
[2] School of Environmental and Forest Sciences, College of the Environment, University of Washington, Seattle, WA 98195, USA; ect@uw.edu (E.C.T.); jcomnick@u.washington.edu (J.M.C.)
[3] School of Environmental and Forest Sciences, College of the Environment, Formerly (While Contributing to This Project) University of Washington, Seattle, WA 98195, USA; clhuang@uw.edu
* Correspondence: elowell@fs.fed.us; Tel.: +1-503-808-2072

Received: 24 July 2018; Accepted: 8 September 2018; Published: 18 September 2018

Abstract: Douglas-fir, the most important timber species in the Pacific Northwest, US (PNW), has high stiffness and strength. Growing it in plantations on short rotations since the 1980s has led to concerns about the impact of juvenile/mature wood proportion on wood properties. Lumber recovered from four sites in a thinning trial in the PNW was analyzed for relationships between thinning regime and lumber grade yield. Linear mixed-effects models were developed for understanding how rotation age and thinning affect the lumber grade yield. Log small-end diameter was overall the most important for describing the presence of an appearance grade, generally exhibiting an indirect relationship with the lower quality grades. Stand Quadratic Mean Diameter (QMD) was found to be the next most uniformly important predictor, its influence (positive or negative) depending on the lumber grade. For quantity within a grade, as log small-end diameter increased, the quantity of the highest grade increased, while decreasing the quantity of the lower grades differentially. Other tree and stand attributes were of varying importance among grades, including stand density, tree height, and stand slope, but logically depicted the tradeoffs or rebalancing among the grades as the tree and stand characteristics change. Structural lumber grade presence was described best by acoustic wave flight time, log position (decreasing presence in upper logs), and an increasing presence with rotation age. A smaller set of variables proved useful for describing quantity within a structural grade. Forest managers can use these results in planning to best capture value in harvesting, allowing them to direct raw materials (logs) to appropriate manufacturing facilities given market demand.

Keywords: Douglas-fir; lumber; non-destructive testing; modulus of elasticity (MOE); stiffness; thinning; silviculture

1. Introduction

Douglas-fir (*Pseudotsuga menziesii* (Mirb.) Franco), the most important commercial timber species in the Pacific Northwest (PNW), is predominantly recognized for its stiffness and strength [1]. About 70% of the harvested Douglas-fir is for lumber products, which includes less than 5% machine graded lumber (machine-stress-rated (MSR) and machine-evaluated-lumber (MEL)). Due to its value, intensively managed stands in the PNW are primarily Douglas-fir [2]. Intensive management and an improved genetic stock have increased the growth and yield amounts and tree size in young Douglas-fir plantations. Geneticists are also studying the heritability of the stiffness trait [3,4]. What has not been addressed fully are the effects of this management choice on wood quality. In the 1980s, an emphasis on

volume production and short rotations in plantations led to concerns about the proportion of juvenile wood to mature wood [5,6] and its impact on stiffness and strength. Properties of juvenile wood, such as a lower wood density and a higher microfibril angle [7], can make it unsuitable for higher value, structural products. Megraw [8] reported that there was a broader juvenile wood zone than that found in other species. Increasing the complexity of determining the impact of juvenile wood on wood quality are the findings of Abdel-Gadir and Krahmer [9] who wrote that variation in the age of wood density maturation for Douglas-fir ranged from 15–38 years old. Aubry [10] found that wood density significantly influenced economic value using MSR grading rules. A symposium held in 1985, "Douglas-fir Stand Management for the Future", spoke to these concerns as did a report prepared by Forintek Canada Corp. for the British Columbia (BC) Ministry of Forests Douglas-fir Task Force [11].

Faster grown trees have a higher proportion of juvenile wood in the core. Barrett and Kellogg [12,13] found a decline in strength and stiffness properties of second-growth Douglas-fir 5.1 × 10.2 cm (2 × 4 in) lumber relative to established standards for young-growth Douglas-fir and related it to the proportion of juvenile wood. They examined changes in the Modulus of Elasticity (MOE, or stiffness) and Modulus of Rupture (MOR, or strength) based on visual grade, log position, and percent of juvenile wood and found that MOE and MOR decreased with increasing height in the tree and with an increased overall percentage of juvenile wood.

In examining the product potential of Douglas-fir from young-growth, managed stands, Fahey [14] conducted a lumber recovery study in western Oregon, USA (OR) and Washington, USA (WA). They found that knot size and the amount of juvenile wood had a significant impact on the yields of visually and machine-stress-rated lumber and visually graded veneer. This study demonstrated that there can be a wide range of wood quality within the young-growth resource as a result of the management strategies employed and confirmed the results from other studies [11,13,15] that examined the structural properties of lumber manufactured from juvenile wood.

Knots are another wood quality concern, as noted in several research studies [14,16]. Silvicultural regimes that promote fast grown trees, such as wide initial spacing, also impact crown length, rate of crown recession [17], and branch longevity thus attainable branch size [18]. Weiskettel [19] found the maximum branch size to be very responsive to silvicultural treatment and Brix [20] saw thinning effects predominately in the bottom half of the crown. Predicting branch size has been the focus of several studies including those by Maguire [21,22] and Briggs [23]. The timing of thinning is also influential. Pre-commercial thinning in younger stands will have more of an impact on branch size in the lower bole [24] than a thinning conducted later (e.g., 40 years or more) [25].

Branches translate to knots in products and are considered defects that impact both the visual grades and structural properties. Visual lumber grading rules [26] have criteria for knot size, location (center or edge), number, and condition (sound or unsound) for a given width board in assigning a grade. In a study by Middleton and Munro [27], knots prevented lumber from being assigned to the highest grade Select Structural about 30% of the time. Grain deviation around knots has a strength- and stiffness-reducing effect [5].

Barratt and Kellogg [13] found that it was hard to recognize lumber from second-growth trees with high stiffness and strength by visual grades. A continued reliance on visual grades for Douglas-fir lumber grading may be due, in part, to its intrinsic microfibril angle (MFA) patterns. When compared to other species, the volume of low MFA or low shrinkage wood in a Douglas-fir log is large, which renders a stable lumber product [14]. Therefore, the lumber value of a Douglas-fir tree is mainly driven by the size (volume) of the log. The volume of logs in a tree is principally affected by tree diameter, height, and taper/form, all of which can be impacted by silviculture. These findings have led to additional research on the ability to predict lumber quality from a standing tree or bucked log attributes. Briggs [28] found that measuring the largest branch in the breast height region or calculating the branch index (the average of the largest four branches in each quadrant) could be used to predict product (lumber or veneer) quality in the first 4.9 m (16 ft) log (butt log) and was easy to measure. The use of non-destructive testing (NDT) tools (acoustic velocity) for predicting the potential

of a log or a tree to produce stress-rated lumber is also becoming more common [23,29–35]. Branches can influence acoustic readings as Amishev and Murphy [36] found a negative correlation between branches size and acoustic velocity. They also noted that branches accounted for some of the variation noted in the acoustic measurements.

The impacts of the increased mix of juvenile wood and branch size on the performance of lumber products are of concern to the wood products industry. A diverse structural-grade yield among different plantation stands is not uncommon. The range of MOEs found among logs of the same morphology or grade is very large and with the increasing amount of juvenile wood in the log market, it is becoming more challenging to find high stiffness logs for mills producing structural and engineered wood products (EWP) in the PNW [6].

The effects of rotation age and cultural treatments on lumber grade recovery and the effects of MOE on different lumber products is presented first, followed by findings from exploratory modeling efforts to further understand and explain more rigorously how rotation age and other factors (site, silviculture, tree characteristics) act together to determine the presence and amount of lumber in particular grade classes. These results will assist land managers (a) in assessing if stands and stand treatments are within desired specifications and (b) in making improved marketing decisions. The acoustic data related to first-log lumber MOE results were previously summarized [37]. Here we quantify the distribution of lumber grades by silviculture and rotation age for all logs produced.

2. Materials and Methods

2.1. Study Sites

The Stand Management Cooperative (SMC), based at the University of Washington, established long-term research installations designed to address the effects of forest management regimes and silvicultural treatments on stand and tree growth and development. The SMC Type II installations were designed to provide data representative of plantations reaching a commercial thinning stage of development at the time of study establishment [38]. In 2006, these installations had reached the end of their designed measurement cycle and land owners were free to harvest them. Four of these installations (numbered 803, 805, 807, and 808) representing a wide geographic range and two rotation age levels (third and fifth decades) were selected for this study (Figure 1) in order to assess the relationship between lumber quality and stand/tree/log variables and to assess the effects of thinning on lumber stiffness at rotation (final harvest).

Each installation contained five plots (0.4 ha) representing different thinning regimes (Table 1) all harvested in the same calendar year (2006) to provide the material for this study. Thinnings were triggered (implemented) when the stand attained a particular value of Curtis' [39] stand relative density (RD). Curtis' relative density measures the extent that trees have captured available growing space. In the case of Douglas-fir, stands that have a measured RD lower than ~15 are essentially open-grown.

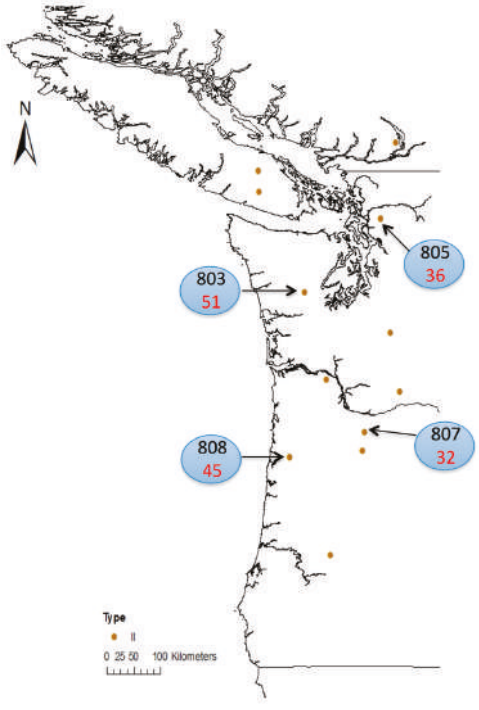

Figure 1. Locations of the Stand Management Cooperative (SMC) installations selected for this study. The numbers in red are the rotation ages of the stands when harvested.

Table 1. Thinning regime, Relative Density triggers, and thinning dates (with corresponding stand ages) with the last row containing the rotation ages (final harvest ages in years since planting) for each installation. Study trees came from the final harvest.

Treatment Code	Thinning Regime	RD [a] Trigger Sequence	Installation Thinning Dates (Age at Thinning)			
			803	805	807	808
A	No thinning (Control)		none	none	none	none
B	Thin heavy once	RD55-RD30; no further thinning	1987 (33)	1990 (21)	1989 (15)	1991 (31)
C	Delayed thinning	RD65-RD35; no further thinning	none	none	1993 (19)	1993 (33)
D	Repeated, heavy thinning	RD55-RD30; subsequent thinnings RD50-RD30	1987 (33)	1990 (21) 2004 (34)	1989 (15) 2001 (30)	1993 (33)
E	Repeated, light thinning	RD55-RD35; RD55-RD40; subsequent thinnings RD60-RD40	1987(33)	1996(27)	1989(15)	1991(31)
	Rotation age	(Final harvest age)	51	36	45	32

[a] RD = relative density [39].

Stands in which the RD is between ~15 to 30 are growing large individual trees rapidly, but generally at the expense of per hectare production. Stands that have a measured RD between 30 and 55 may have slower individual tree growth rates but are still increasing the per hectare production with increases in RD. Whereas stands beyond an RD of 55 are beginning to lose stems due to competition-induced mortality though the individual tree size continues to increase as does the per hectare yield. Generally speaking, for the objective of producing wood volume, one strategy is to commercially thin either once or several times to earn income during a rotation, which serves at the same time to maintain or enhance tree and stand growth rates after thinning. If multiple thinnings are contemplated, a general strategy is to thin less frequently and more lightly as the stand ages. For example, the thinning regime behind treatment code D allows a stand to just reach the imminent competition-induced mortality boundary and thins back nearly to a condition where the per hectare production may be sacrificed; subsequent thinnings maintain an overall lower density stand condition by keeping the RD no higher than 50.

Site, stand, and average tree characteristics by treated plot at the age when harvested appear in Table 2. The delayed thinning plot (C) of installation 808 was lost due to a windstorm, so no data were available for this treatment from that site.

Table 2. Selected site, stand and tree characteristics for the four installations by plot.

Inst. (elev, m)	Plot	SI [a]	Density	BA [b]	QMD [c]	Ht	Avg Stem Taper	LCR [d]	LLAD Butt Log [e]
(slope, %)		m@50y	trees/ha	m^2/ha	cm	m	cm/m	%	cm
803	A	36	791	56	30.0	36.6	1.05	30	2.54
(585)	B	37	306	45	43.4	39.0	1.12	37	2.54
(1)	C	35	899	52	26.9	35.1	0.97	29	1.78
	D	35	336	45	41.4	35.4	1.17	33	3.30
	E	34	459	47	36.1	33.8	1.05	30	1.78
805	A	38	860	52	27.7	30.8	0.94	36	4.57
(168)	B	40	454	40	33.5	31.4	1.03	37	3.05
(15)	C	39	366	33	34.0	32.3	1.00	41	4.32
	D	41	420	42	35.6	32.0	1.24	39	2.79
	E	39	405	36	33.8	32.3	1.12	39	5.33
807	A	33	1398	49	21.1	24.1	1.13	27	1.27
(152)	B	33	741	39	25.9	24.7	1.12	34	2.03
(1)	C	30	825	36	23.4	23.2	1.12	37	2.54
	D	35	395	27	29.2	25.9	1.17	43	3.05
	E	37	929	40	23.4	27.1	1.05	33	0.76
808	A	34	731	62	32.8	31.1	1.28	37	2.03
(762)	B	33	296	44	43.4	30.9	1.42	47	2.79
(5)	C	-	-	-	-	-	-	-	-
	D	31	247	42	46.7	28.7	1.57	51	2.29
	E	33	351	50	42.4	30.8	1.46	39	3.05

[a] SI = site index; [b] BA = basal area; [c] QMD = quadratic mean diameter; [d] LCR = live crown ratio; [e] LLAD = largest limb average diameter in first 4.9 m (16 ft).

2.2. Tree, Log, and Lumber Measurements

As there is a relationship among the NDT values of trees, logs, and lumber [34], TreeSonic velocity (TSV) was measured on the standing tree at breast-height as time-of-flight (nanoseconds) of an acoustic wave over a 1 m distance using the Fakopp TreeSonic instrument on 50 plot-centered trees on each of the plots. Mill trial trees were selected based on the distribution of the TSV. Twelve trees were selected from each plot. Two, four, four, and two trees from each plot were randomly selected from the following four TSV categories: The lowest 10%, medium-low 11–50%, medium-high 51–90%, and the top 10%, respectively for processing into lumber and veneer. Six trees were randomly chosen using the above TSV distribution and allocated to the lumber recovery study. The lumber recovery trees were bucked into 10 m (33 ft) logs in the woods, delivered to the South Union Sawmill in Elma, WA, and cut into 4.9 m (16 ft) logs in the log yard. From each tree, the resonant acoustic velocity of

the merchantable bole and the 10 m (33 ft) length logs was measured in the woods, and the 4.9 m (16 ft) logs were measured at the sawmill using the Director HM200 [34]. Logs were processed into predominantly 5.1 × 10.2 cm (2 × 4 in) and 5.1 × 15.2 cm (2 × 6 in) lumber. Most of the MSR and MEL lumber produced were of these sizes. In addition, the location and size of the largest knot in each quadrant of the 4.9 m (16 ft) log segments were measured to calculate the large limb average diameter (LLAD) also known as branch index (BIX). The location and size of any ramicorn branches were also recorded.

Logs were sawn using a Mighty Mite circular saw (7.1 mm or 0.28 in saw kerf) with horizontal edger blades. Each piece of lumber was labeled to identify the tree and log it came from as well as the log position within the tree. The lumber was kiln-dried and surfaced. Finished lumber was visually graded by a certified lumber grader from the Western Wood Products Association and grade-limiting defects were recorded for each piece. All lumber was shipped to the USDA Forest Products Laboratory (FPL), Madison, WI for MOE determination using the MetriGuard e-computer. All data were collected from fall 2006 through spring 2007.

The MOE was adjusted to 15% moisture content [40] to calculate the volume-weighted log MOE. The percentage of lumber that met the MSR/MEL grade requirements was calculated based on the moisture content adjusted MOE.

2.3. Data Analysis

First, the branch index, grade-limiting defect, and lumber stiffness were summarized by the stand and silviculture regime. Next, the lumber grade distributions among the silviculture regimes and MOE distributions by lumber grade were examined more rigorously through an explanatory modeling effort. One set of equations was developed to assess the effects of site, stand, tree and log attributes on the proportion of log volume by visual lumber grade and another set of equations generated to assess how the same attributes affect the proportion of lumber volume that meets the structural design specifications for each grade. Each set of equations was developed using a two-step process.

The proportion of log volume in a visual grade was modeled first. In the first step, a model was developed to predict the presence of a grade within a log. The presence was indicated with a one (1), absence with a zero (0). In the second step, the abundance of the grade was estimated given that the grade was present. Although on the surface our data contained what appeared to be a very large number of observed zeroes, which indicate the absence of a grade within a log, methods to account for such a condition [41] showed no improvement to the fit when the model was recast as a fractional regression. Therefore, a generalized linear mixed-effects model was chosen to describe the presence of a grade, linked to a logistic error distribution, which maximized the likelihood of the parameters when the response is Bernoulli. The model appears in Equation (1).

$$p = \frac{1}{\left(1 + e^{-(\beta_0 + b_{0i} + \beta_1 X_1 + \beta_2 X_2 + \ldots)}\right)} + \delta_i \quad (1)$$

where p denotes presence ($p = 1$) or absence ($p = 0$) of a grade within a log, e denotes the base of the natural logarithm, Xs denote the set of predictor variables examined, βs are the fixed model coefficients, b_{0i} are random deviations due to the plot from the fixed component of the model coefficient, β_0, and δ_i are random error terms describing the residual variation unexplained by the predictor variables and random plot effects.

In the second step, an abundance model to predict the proportion of log volume in a particular visual grade given its presence was developed using a linear mixed-effects regression model. Since the proportion of a particular grade within a log is, by definition, any number between zero (0) and one (1), the log odds-ratio transformation (logit) was applied to the observed response values to normalize their distribution. The model form appears in Equation (2).

$$logit(\theta) = \beta_0 + b_{0i} + \beta_1 X_1 + \beta_2 X_2 + \ldots e_i \quad (2)$$

where θ denotes the proportion of log volume in one of the grades, logit(θ) denotes the natural logarithm of the ratio of the proportion in the grade to the proportion that is not, or "log odds-ratio", X_is denote the set of predictor variables examined, β_is are fixed model coefficients, b_{0i} is the random deviation due to the plot from the fixed component of the model coefficient, β_0, and e_i are the random error terms describing the residual variation unexplained by the predictor variables and random plot effects.

The design values were assigned [42] to meet the engineering requirements of the intended end use of the lumber (structural capability). They differ not only by end use but also by species and are influenced by such features as knots and slope of grain. The size of lumber was also a consideration in assigning design value. Structural lumber (including dimension lumber) can be visually and/or mechanically (MSR) graded for its strength and physical working properties. The set of models, derived to estimate the proportion of lumber volume meeting the structural design values for Douglas-fir, were derived similarly to the visual grade models.

In the first step, a model was derived to predict the presence of lumber meeting the structural value within a grade using the same model as Equation (1), while the second step model estimated the proportion of volume meeting the structural design value given that it was present using the same model as Equation (2). A two-step modeling process, such as used here, has previously been used quite successfully in other contexts where the conceptual framework is analogous (see for example Reference [43]).

Installation, or geographic location, effects were accounted for as fixed effects in the models in the form of site attributes, such as slope, aspect, elevation, among others. The effects of the plot were considered random in all fitted models, to assess and characterize the magnitude of uncontrollable noise, i.e., variation that is unaccounted for by the treatments applied. The only exceptions to this were the Economy visual grade and No. 3 structural grade abundance models, each of which lacked a sufficiently large sample size to assess the plot variation adequately. Thinning methods were expected to express their influences in the form of differing stand density, basal area, and average stand diameter that were attained over the course of time through stand dynamics processes as moderated by silvicultural thinning. Tree variables (Diameter at Breast Height [DBH] total height, taper, height-diameter ratio) were considered to be fixed, measurable effects. Each model set was developed using a forward selection of variables, with a chosen significance level of 0.1 for all models. Given the high level of variation observed among plots and trees, this less conservative significance level was chosen in order to capture all important variables influencing the presence and abundance of the grades. Twenty candidate predictor variables were evaluated for each model including treatment (silviculture regime and harvest age), site (latitude, longitude, slope, aspect, and elevation), plot (Trees Per Hectare [TPH], Quadratic Mean Diameter [QMD], basal area, relative density, site index), tree (DBH, height, height-DBH ratio, taper, and acoustic velocity), and log (small-end diameter, position along the stem, and LLAD) attributes. Only main effects were considered. The lme4 R package was used for fitting the models [44].

For binary presence/absence models, methods to assess the fit in a meaningful way are not well defined, which also holds true for logit models, or models where proportions represent the response. We chose the following method for evaluating the overall combined fit for the two-model sets. After fitting the models, the mean predicted abundance for each grade was determined using a Monte Carlo simulation. In this process, a random number between zero and one was generated 500 times per grade for each log in the dataset and compared to the modeled probability of presence. The abundance was then tallied as either the predicted abundance when the random number did not exceed the modeled presence probability or zero otherwise. The results were averaged to calculate the mean response per grade for each log. Finally, the predicted abundance for all grades within a log was scaled proportionally to sum to one. The set of equations were evaluated as a system by comparing these predictions to the observed values by calculating the following set of fit statistics: The adjusted R-squared, root mean squared error, mean absolute deviation, mean bias, and mean percent error.

3. Results

3.1. Initial Data Summary

A total of 1758 pieces of lumber were sawn from 317 logs out of 97 trees. The reduced number of trees from the 112 trees originally selected was primarily due to weather conditions on installation 807 (13 trees were not transported to the mill) and the inability to saw the remaining four trees due to defects (sweep) and size (log small-end scaling diameter). About 25% of the lumber produced was 5.1 × 10.2 cm (2 × 4 in) and the remaining 75% was 5.1 × 15.2 cm (2 × 6 in). A very small amount of 2.5 cm (1 in) lumber was sawn. Restricting the lumber sizes allowed for a better assessment of the impact of knots on the lumber grade. The yield of No. 2 and better (a grade grouping often found in marketing Douglas-fir) lumber ranged from 91 to 95%. Table 3 shows the lumber data and grade yield from the study.

Table 3. Sample data and percent volume yield by lumber grade of the sampled installations.

Inst.	Age	Tree	DBH	Height	Logs Processed	Lumber Pieces	Lumber Grade				
	yr	n	cm	m	n	n	pct				
							Sel Str [a]	No. 1	No. 2	No. 3	Econ [b]
803	51	29	39.11	35.97	119	718	29	40	26	4	1
805	36	27	35.05	31.70	77	368	23	44	29	3	2
807	32	17	28.70	24.69	33	119	7	35	49	6	3
808	45	24	43.43	30.18	88	553	23	37	31	7	2
Total		97			317	1758					

[a] Sel Str = select structural lumber grade; [b] Econ = economy lumber grade.

3.1.1. Branch Index

Another of the main factors directly affecting the lumber grade is the size of knots, which start as branches on the tree. The branch index (LLAD) on the bottom 4.9 m (16 ft) log ranged from a low of 1.8 cm (0.7 in) to a high of 5.3 cm (2.1 in). Douglas-fir is not prone to self-pruning dead branches below the live crown [22]. Thus, thinning that impacts the crown structure can impact knot type and size. The butt log typically contains the highest value lumber.

3.1.2. Grade-Limiting Defect

Wane (85%) and knots (6%) were the dominant reasons for trimming lumber (about 190 pieces or 11%) to increase the grade (Figure 2a). These were also the two factors that were the grade-limiting defects, causing the lumber to be downgraded (Figure 2b). Intensive management can increase taper in a tree, especially in the upper stem, that leads to the presence of wane in lumber. Forty-two percent of the lumber was downgraded for wane. Face knots (the primary grade-limiting knot type) accounted for 37% of the downgrade. Spike and edge knots accounted for an additional 16% of the downgrade.

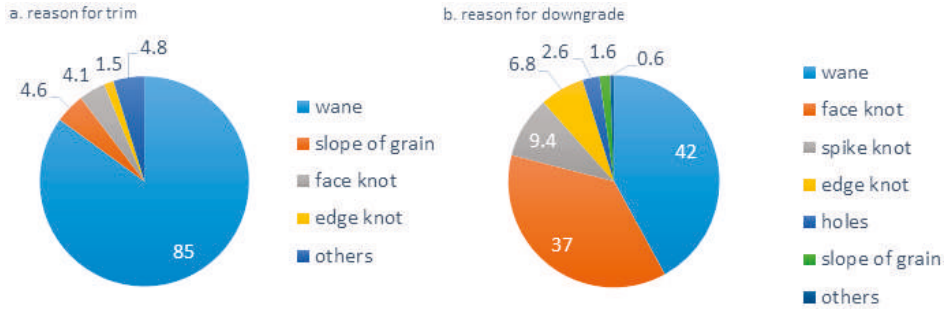

Figure 2. Percent of end-trim of lumber (**a**) and visual grade downgrade factors (**b**) for all lumber combined.

3.1.3. Lumber Stiffness

The volume-weighted MOE by log position of the tested installations is shown in Figure 3. The MOE exhibits gradients from the tree base to the tree top, being more variable in the younger stands (805 and 808). The log lumber MOE is related to other variables besides log diameter and log position, including juvenile wood proportion and wood density. Upper segments near the top of the tree (e.g., segment 4) generally have a higher proportion of juvenile wood and a lower wood density.

The percentage of Douglas-fir visual grade lumber that meets the design value is related to the amount of juvenile wood [13]. In this study, about 50% of the visually graded lumber met or exceeded the design value [26] (Figure 4). Of note is the small sample size of No. 3 grade lumber and the number of 5.1 × 10.2 cm (2 × 4 in) lumber that met the Select Structural grade.

Except for installation 803, the higher grades of the tested plantation lumber had average MOE values that fell below the published MOE design values (Table 4).

Table 4. Average density (weighted by lumber volume) and lumber MOE by site and visual grade (number in parentheses is MOE design value of the grade).

Site	Density	MOE	Sel Str (13,100)	No. 1 (11,721)	No. 2 (11,032)	No. 3 (9653)	Econ
	(kg/m^3)			MPa			
803	569	13,334	14,162 ^	12,473 *	12,638 *	12,555 **	12,052
805	551	11,625	12,114	11,438	11,052 ^	10,587 **	11,101
807	521	10,004	11,749	9694	9894	11,018 *	10,949
808	580	11,521	13,017	11,321	10,839	9218	10,018

^ MOE average meets the specification but its distribution does not; * MOE average meets MEL; ** MSR meets MOE specifications (the amount of below-grade MOE pieces is more lenient for MEL grading rules).

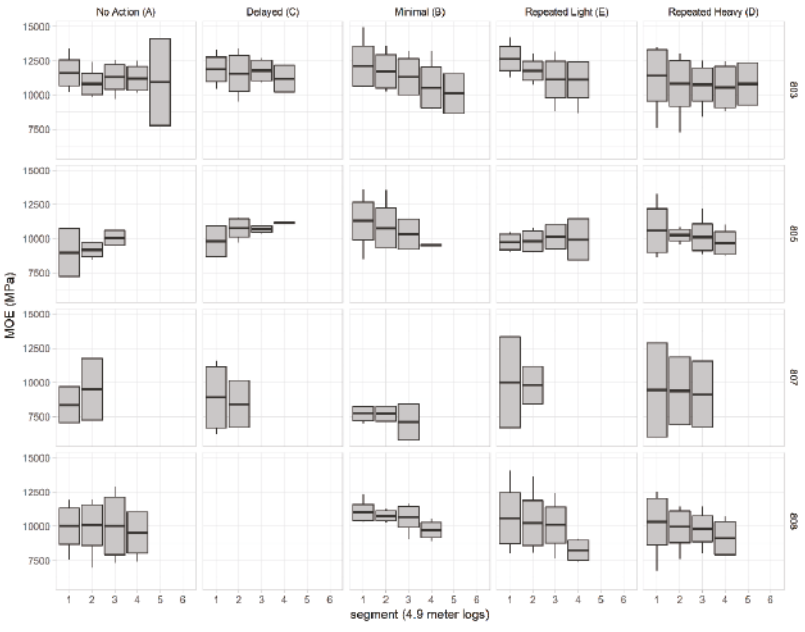

Figure 3. Log lumber MOE by segment (log position within the tree with the butt log being segment 1) and thinning type by installation. Note: Segments are 4.9 m logs (16 ft logs).

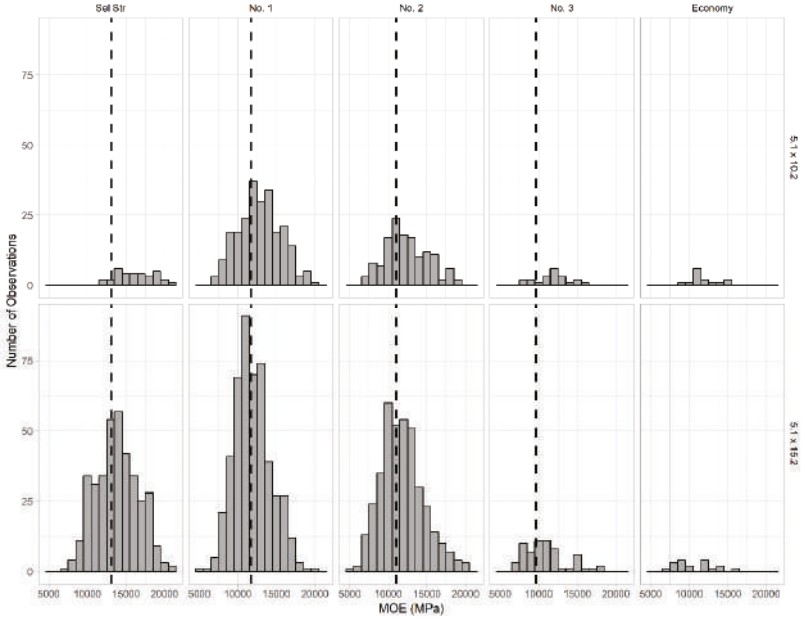

Figure 4. Distribution of lumber MOE by lumber size and visual grades. The dotted vertical line is the published MOE value for the specific grade. Economy lumber does not have a structural design value assigned to it.

The calculations used to derive the proportions meeting the design values relied only on the MOE limit, so if additional design limits were incorporated in those calculations, the amounts of below-grade lumber will probably be larger. One interesting observation of the test results is that when compared to pine species, the MOE of the lower visual grade Douglas-fir lumber was relatively high, which may be explained by the intrinsic stiffness property of Douglas-fir. There were many high MOE pieces within the visual grade plantation-grown lumber that keep the average MOE of the grade on par, but the amount of low MOE lumber in the distribution can fail the grading rules. The cause of the additional low MOE pieces could most likely be due to the increased proportion of juvenile wood within the log.

3.2. Modeling Summary

3.2.1. Lumber Grade Distribution

In the first step, the presence/absence of each grade within a log was modeled. This resulted in the selected predictor variables listed in Table 5 showing the coefficient estimates and significance. Intercepts were kept in all models, even if not significant, so that models remain unbiased and would at minimum be capable of predicting a mean presence value, in cases where there may be no significant tree or stand variables.

Table 5. Selected parameters and level of significance for lumber visual grade presence/absence models.

Variable	Sel Str	No. 1	No. 2	No. 3	Econ
Intercept	−3.4227 **	0.1283	1.4725	−4.6907 ***	−5.9568 ***
Plot QMD	0.0926 *		−0.0539 *		
Tree DBH				0.0943 ***	
Tree height			−0.1158 **		
Tree taper	−4.3120 ***				
Log SED	0.2006 ***	0.0707 *	0.1554 ***		0.1007 **
Log LLAD			0.1194 **		
Log position				−1.6142 *	
$\sigma^2_{b_0}$	0.4847	0.0789	0.0097	0.0958	0.9674

Significance level symbols ***, **, and * indicate p-value ranges of $p < 0.001$, $0.001 < p < 0.01$, and $0.01 < p < 0.05$, respectively. Intercept terms were always included regardless of significance to maintain unbiasedness.

In the second step, the abundance of each grade within a log, given that it was present, was modeled. This resulted in the selected predictor variables listed in Table 6, showing the coefficient estimates and level of significance. Here as well, intercepts were kept in all models, even if not significant, so that models remain unbiased and will at minimum be capable of predicting a mean abundance value, in cases where there may be no significant tree or stand variables.

Table 6. Selected parameters and level of significance for the lumber visual grade abundance models.

Variable	Sel Str	No. 1	No. 2	No. 3	Econ
Intercept	5.7471 **	1.9021	−1.1781 $^{+}$	−0.1635	1.620
Installation slope		0.0985 $^{+}$			
Plot TPA			0.0009 *		
Plot QMD	0.0491 $^{+}$				
Plot site index	−0.1135 *	−0.1440 **			
Tree DBH	−0.0481 *				
Tree height		0.0994 ***			
Tree taper	−1.6227 $^{+}$		1.3858 **		
Tree velocity		7.7888 *			
Log SED		−0.1264 ***	−0.0593 ***	−0.0384 *	−0.2373 $^{+}$
Log LLAD			0.0773 *		
$\sigma^2_{b_0}$	0.0661	0.0097	0.0132	0.0058	NA
σ^2_e	1.4872	1.6036	1.3930	0.4116	1.8578

Significance level symbols ***, **, *, and $^{+}$ indicate p-value ranges of $p < 0.001$, $0.001 < p < 0.01$, $0.01 < p < 0.05$, and $0.05 < p < 0.1$, respectively. Intercept terms were always included regardless of significance to maintain unbiasedness.

As stated in the methods section, each set of equations was evaluated as a system by comparing the Monte Carlo predicted values to the observed values. Summary statistics were calculated based on 1575 data points (315 logs × 5 lumber grades) and 34 parameters (Table 7).

Table 7. Summary of the fit statistics for the final lumber visual grade model system.

Statistic	Value
Adjusted R-squared	0.4279
Root Mean Squared Error	0.2015
Mean Absolute Deviation	0.1409
Mean Bias	2.4939×10^{-18}
Mean Percent Error	0.7045

The behaviors of the visual grade models as a system were explored by comparing the effects of log small-end diameter (SED), harvest age, and treatment regime on the predicted grade proportions. To accomplish this, linear regression models were first developed to predict model input parameters, including TPH, QMD, tree height, and LLAD, from harvest age and treatment regime. Harvest ages were chosen to range from 30 to 55 years by 5-year steps. The log SED values were chosen to range from 10.2 to 45.7 cm (6 to 18 in) by 7.6 cm (3 in) steps. The log position parameter was chosen to be 0.25, representing the butt log of the tree. The remaining parameters were set to median values for the data set. The results are illustrated in Figure 5.

Log SED and harvest age have the largest effects on the model. As the small-end diameter of a log increases, the proportion of the Select Structural grade increases at the expense of the No. 1 grade, while No. 2 and the remaining grades stay relatively flat. For a given harvest age, grade No. 2 has a positive relationship with the log SED at its low end but turns negative for larger SEDs. Increasing the harvest age results in proportionally larger amounts of Select Structural in the lower SED range, but proportionally smaller amounts in the larger SEDs. Proportionally more No. 1 grade was produced over all SEDs as the harvest age increased. The No. 2 grade decreases proportionally over the range of the SED with harvest age, while No. 3 and Economy (E) were predicted in very small proportions in all scenarios.

The thinning regime appears to have a much smaller effect on the distribution of grade, for reasons stated previously. Grades Select Structural and No. 1 occurred in slightly larger proportions in a smaller diameter, denser stands for a given harvest age and small end diameter. These results may differ for absolute abundance, as logs with larger small-end diameters would be expected to occur

more frequently in stands with a lower density (fewer trees per hectare that are larger in diameter for a given harvest age). This system of models provides a methodology to better understand the influences of silvicultural thinning on the tree and stand attributes that can be used directly to predict the proportion of lumber grades to expect under the different regimes. This will lead to greater accuracy and precision when appraising/valuing the resultant products produced.

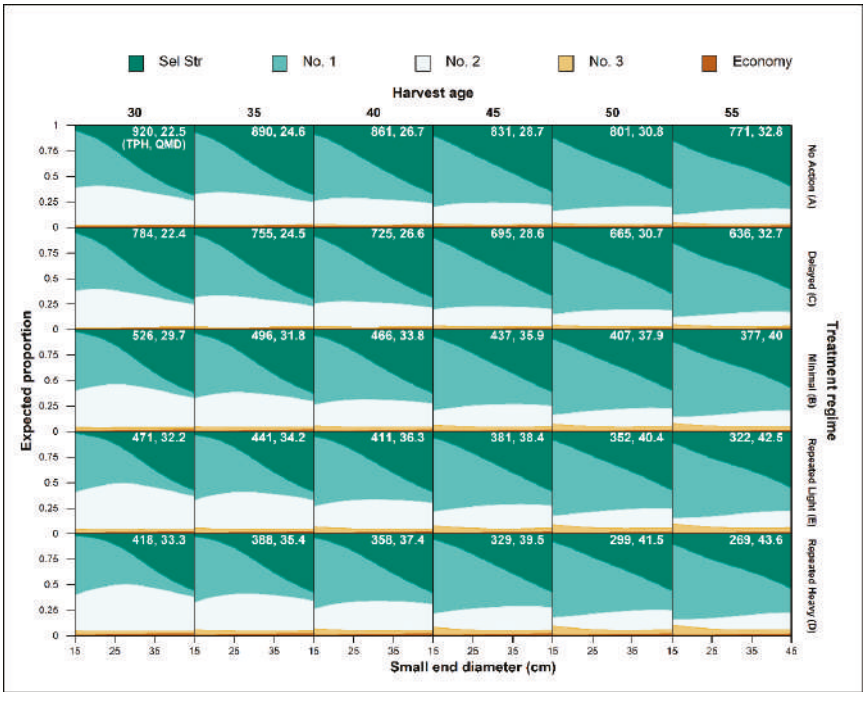

Figure 5. Expected proportion of log volume by lumber visual grade by harvest age, treatment regime, and log small end diameter. Trees per hectare (TPH) and quadratic mean diameter (QMD) for each rotation age by treatment panel are shown in the upper right corner.

3.2.2. Lumber Structural Grade

The proportion of lumber volume for a visual grade that met the MOE standard was calculated for each log. For presence/absence modeling purposes, presence was defined as any proportion greater than zero that met the MOE standard for a particular grade. Economy grade does not have a structural design standard. The selected variables and estimates of the coefficients are reported in Tables 8 and 9 for the presence/absence and abundance models, respectively.

Table 8. Selected parameters and level of significance for lumber structural grade presence/absence models.

Variable	Sel Str	No. 1	No. 2	No. 3
Intercept	−10.2863 **	−3.5808 ***	−4.1380 **	−29.5200 *
Harvest age	0.0997 **	0.0642 **		
Tree height			0.2028 ***	
Tree velocity	21.5060 *			83.0200 *
Log position	−3.0699 **		−2.1948 **	
Log SED		0.0642 **		
$\sigma^2_{b_0}$	0.0629	0.0770	0.1012	3.5360

Significance level symbols ***, **, *, and $^+$ indicate p-value ranges of $p < 0.001$, $0.001 < p < 0.01$, $0.01 < p < 0.05$, and $0.05 < p < 0.1$, respectively. Intercept terms were always included regardless of significance to maintain unbiasedness.

Table 9. Selected parameters and level of significance for lumber structural grade abundance models.

Variable	Sel Str	No. 1	No. 2	No. 3
Intercept	−6.4760 $^+$	−4.9053 $^+$	7.7580 ***	9.495 ***
Tree velocity	22.7280 **	16.6633 *		
Tree taper			−3.6568 ***	−4.2934 ***
Log LLAD			−0.1663 *	
$\sigma^2_{b_0}$	0.2970	9.142×10^{-16}	4.113×10^{-16}	NA
σ^2_e	4.4090	4.7690	4.3180	1.9061

Significance level symbols ***, **, *, and $^+$ indicate p-value ranges of $p < 0.001$, $0.001 < p < 0.01$, $0.01 < p < 0.05$, and $0.05 < p < 0.1$, respectively. Intercept terms were always included regardless of significance to maintain unbiasedness.

Overall, the structural grade models explained a very low amount of variation in the response variables. Summary statistics are reported in Table 10.

Table 10. Summary of the fit statistics for the two-equation structural grade model sets by visual grade.

Statistic	Sel Str	No. 1	No. 2	No. 3
Adjusted R-squared	0.1533	0.0407	0.1405	0.3649
Root Mean Squared Error	0.3714	0.3804	0.3821	0.3092
Mean Absolute Deviation	0.3269	0.3320	0.3403	0.2153
Mean Bias	-1.601×10^{-17}	2.0497×10^{-17}	-5.7301×10^{-19}	-4.8720×10^{-18}
Mean Percent Error	0.4631	0.5559	0.4952	0.2539

4. Discussion

The data themselves are highly variable, leading to somewhat low R-squared values in all models, but the main objective, again, was assessing the significance of factor effects to explain the responses, not necessarily creating a model with a high precision for predictive use; though that remains an outcome to be desired and eventually achieved. It should be noted that although treatment regime variables were actually tested throughout in all the models, they were always supplanted by the actual stand and tree attributes at final harvest. This does not mean that treatments were ineffective in producing differences in log and lumber grades, only that treatment affects themselves appear indirectly through their accumulated impact over the rotation on the responses by way of their influence on stand dynamics processes [19,45].

Considering first the lumber visual grade presence model (Table 5), it is seen that the greatest single impact on a single grade is tree taper. Logically, as taper increases, the presence of the Sel Str grade is less likely. The single predictor that had influence over most of the grades was the small-end diameter of the log (log SED) variable. This is completely expected since this is the main driving variable in the visual log grading system that is used in the Pacific Northwest [46]. Log small-end

diameter was most influential in the select structural lumber grade (largest coefficient), but it will be seen that a large diameter log benefits the presence of all grades (positive signs). The average diameter of the stand (plot QMD) positively influenced the presence of the Select Structural grade, as expected, further enhancing the positive effect of the log SED. For the Select Structural grade, a greater degree of taper negatively influenced its presence, likely due to less solid central wood in the log that is capable of producing higher grade lumber, i.e., a larger proportion of wood in jacket boards (lumber sawn from the outer portion of a log), slabs and edgings. The presence of the No. 2 grade was negatively impacted by stands with an overall larger plot QMD, and especially so if the tree was among the taller component. Though a large Tree DBH will help the probability that the No. 3 grade is present, it will be less likely in the upper logs. The Economy grade presence seems insensitive to all other stand and tree attributes, perhaps because it captures all the lumber not in the other grades.

When considering the abundance of visual grades, given their presence, we see again that log small-end diameter was the most important variable overall (Table 6), because it remained significant in four of the five grade models, which no other predictor variable did. Though the coefficients were all negative, we can interpret the magnitudes of the coefficients as indicating tradeoffs in lumber volume between grades. For example, a log with a large SED may produce all grades of lumber, but will produce the most Select Structural lumber (coefficient is zero, i.e., no negative impact from the SED), followed by No. 3 (smallest magnitude negative coefficient), then, No. 2 (next larger magnitude coefficient), No. 1 (even larger negative coefficient), and finally Economy (largest negative coefficient), respectively. The next overall most important variable might be considered to be either the plot site index or tree taper. A higher site index decreases the Select Structural and No. 1 grades, likely due to fewer rings per inch in the logs produced since the site index has been shown to be reflected visibly in rings per inch, the two variables being essentially interchangeable [47]. A greater tree taper negatively impacts the Select Structural grade, which seems to be offset by more No. 2 grade, another tradeoff. The slope of the ground at the site (installation slope) positively impacted the abundance of No. 1 grade lumber. This result was somewhat unexpected, and while further exploration of why this might be important is beyond the scope of this study, it is interesting to speculate how this and other environmental attributes or climatic variables may influence tree growth, wood production and subsequent lumber grade turnout; currently under investigation elsewhere [48]. Overall, stands with a larger average diameter produced relatively more Select Structural lumber, though it was tempered by individual tree DBH; its abundance was decreased to a greater degree if the tree had a DBH larger than QMD. As expected, grade No. 2 tolerates larger knots (LLAD) [26]. The net effect of high-density stands is to produce trees with less taper and seems to positively influence the abundance of No. 2 grade lumber. The magnitude of between-plot variation for the visual grade abundance models was quite small compared to residual error.

For the structural grade models (Tables 8 and 9), log position (inversely related to log diameter) or log SED were chosen for the Select Structural, No. 1, and No. 2 grades. Log diameter has been correlated to lumber grade recovery and thus value [27]. Harvest age and TSV (Tree Velocity) were each selected for multiple models. The presence of the Select Structural and No. 1 grades showed positive relationships with harvest age. This might be expected since as trees age, annual ring widths tend to become narrower, even if the growth rate doesn't slow because the annual wood layer would be laid down on an ever increasing diameter. This, in turn, would lead to an increased density in the outer rings (higher proportion of LW), leading to a greater stiffness. The tree velocity (TSV) showed a positive relationship with the response variables, also as expected, because the speed of an acoustic wave through wood is directly and positively correlated with wood stiffness; an important structural attribute [34]. The Select Structural and No. 1 grades of lumber were more likely to be present in larger diameter logs (occurring lower in the tree) harvested from older stands, as expected. The presence of No. 2 grade was more likely in logs from taller trees located lower in the bole. No. 3 grade presence was predicted by only the Tree velocity. The Economy grade is known not to yield any structural lumber, so there is no design value assigned to it.

The structural abundance models (Table 9), largely exhibited variables with signs that were easily interpreted. As expected, the greater the TSV, the greater the abundance of the Select Structural and No. 1 grades, given that they were present. Given the presence of the No. 2 and 3 grades, a greater tree taper reduced abundance. The abundance of the No. 2 grade was further negatively impacted when the LLAD was large, likely due to grain distortion around the knots. Fahey [14] also found that the LLAD influenced lumber grade recovery in Douglas-fir. The magnitude of plot-to-plot variation for the structural grade abundance models was relatively small compared to residual error.

Both sets of models for both the visual grade presence and abundance and presence and abundance of structural lumber within a grade clearly demonstrated that visual lumber grade alone is insufficient for predicting the actual quantity of lumber produced that meets the structural design values for each grade. The incorporation of other tree and stand variables, resulting from stand treatment, into the models helped the prediction of visual lumber grades more so than for structural lumber, as judged by the fit statistics evaluated (Tables 7 and 10).

5. Conclusions

Decision support tools need to be integrated at every step in the value chain, from stand management to log marketing. For a lumber mill, the amount of high MOE material is enough to satisfy the current small MSR/MEL market and the visual grade lumber is the main product. Therefore, the effects of low MOE wood on Douglas-fir lumber mills are relatively small as long as the majority of the lumber meets the visual specifications. On the other hand, the MOE is directly related to the value of engineered wood products (EWP), so for manufacturers producing EWP, the additional low MOE materials directly reduce mill profit. Not only does having surplus low MOE material cause waste in an EWP facility, but additional high MOE materials need to be purchased on the open market to fill customer orders. Unlike visually graded lumber, the internal strength and stiffness are the key value factors of EWP. Balancing the MOE in a log mix for EWP mills is getting more complicated with the increasing amount of low MOE juvenile wood in the wood basket.

The use of non-destructive, in-woods testing equipment to measure acoustic velocity was found to be the most important variable for predicting the presence of structural grades in the lumber produced.

The MOE is but one factor among other considerations in making various types of timberland investment and forest management decisions. Plantation forests are a long-term investment and knowledge gained from operational research, such as a mill trial, enables tree growers to tailor their prescriptions to meet customer needs and allocate logs for maximum profit. A clear understanding of the internal quality of standing timber provides flexibility for landowners to capture established and emerging markets and for manufacturers to meet product specifications, adapt to changing grading rules, and develop new products. Such knowledge is necessary to gain a market share and price advantage. Internal wood quality sorting technologies are necessary for log suppliers to deliver the right log to the right mill; however, the vendors may not have a sufficient understanding in operation constraints for developing cost-effective tools for the timberlands and the mills. Logs account for 50–70% of the operational cost of a mill, and a consistent and reliable supply of log mix is a necessity for mill managers. For some reason, communication barriers are frequently found between mills and log suppliers. The disappearance of vertically integrated forest companies makes the information sharing even more difficult.

Author Contributions: E.C.L. and E.C.T. conceived, designed, and performed the experiments. J.M.C. and E.C.T. conducted the analysis. E.C.L, E.C.T., C.H., and J.M.C. all contributed to the writing of the manuscript.

Funding: This project was funded through the Sustainable Forestry component of Agenda 2020, a joint effort of the USDA Forest Service Research & Development and the American Forest & Paper Association.

Acknowledgments: Research partners include the Stand Management and Precision Forestry Cooperatives and Rural Technology Initiative Program at the University of Washington, the School of Environmental and Forest Sciences, USDA Forest Service Pacific Northwest Research Station, CHH FibreGen, and the USDA Forest Service Forest Products Laboratory. The authors also wish to acknowledge the anonymous journal reviewers who provided input and insight thus improving this manuscript.

Conflicts of Interest: The authors declare no conflicts of interest.

References

1. Barbour, R.J.; Kellogg, R.M. Forest management and end-product quality: A Canadian perspective. *Can. J. For. Res.* **1990**, *20*, 405–414. [CrossRef]
2. Vance, E.D.; Maguire, D.A.; Zalesney, R.S., Jr. Research Strategies for Increasing Productivity of Intensively Managed Forest Plantations. *J. For.* **2010**, *108*, 183–192.
3. Cherry, M.; Vikas, V.; Briggs, D.; Cress, D.W.; Howe, G.T. Genetic variation in direct and indirect measures of wood stiffness in coastal Douglas-fir. *Can. J. For. Res.* **2008**, *38*, 2476–2486. [CrossRef]
4. Vikram, V.; Cherry, M.L.; Briggs, D.; Cress, D.W.; Evans, R.; Howe, G.T. Stiffness of Douglas-fir lumber: Effects of wood properties and genetics. *Can. J. For. Res.* **2011**, *41*, 1160–1173. [CrossRef]
5. Jozsa, L.A.; Middleton, G.R. *A Discussion of Wood Quality Attributes and Their Practical Implications, SP-34*; Forintek Canada Corp.: Vancouver, BC, Canada, 1994.
6. Kennedy, R.W. Coniferous wood quality in the future: Concerns and strategies. *Wood Sci. Technol.* **1995**, *29*, 321–338. [CrossRef]
7. Gartner, B.L. Assessing wood characteristics and wood quality in intensively managed plantations. *J. For.* **2005**, *103*, 75–77.
8. Megraw, R. Douglas-fir Wood Properties. In *Douglas-Fir: Stand Management for the Future*; Oliver, C.D., Hanley, D.P., Johnson, J.A., Eds.; College of Forest Resources, University of Washington: Seattle, WA, USA, 1986; pp. 81–96.
9. Abdel-Gadir, A.Y.; Krahmer, R.L. Estimating the age of demarcation of juvenile and mature wood in Douglas-fir. *Wood Fiber Sci.* **2007**, *25*, 242–249.
10. Aubry, C.A.; Adams, W.T.; Fahey, T.D. Determination of relative economic weights for multitrait selection in coastal Douglas-fir. *Can. J. For. Res.* **1998**, *28*, 1164–1170. [CrossRef]
11. Kellogg, R.M. *Second Growth Douglas-Fir: Its Management and Conversion for Value, SP-32*; Forintek Canada Corp.: Vancouver, BC, Canada, 1989.
12. Barratt, J.D.; Kellogg, R.M. Lumber Quality from second growth managed forests. In *A Technical Workshop: Juvenile Wood–What Does It Mean to Forest Management and Forest Products?* Forest Products Research Society: Madison, WI, USA, 1986; pp. 57–71.
13. Barrett, J.D.; Kellogg, R.M. Strength and Stiffness of Dimension Lumber. In *Second Growth Douglas-Fir; Its Management and Conversion for Value, Special Publ. SP-32*; Kellogg, R.M., Ed.; Forintek Canada Corp.: Vancouver, BC, Canada, 1989; pp. 50–58.
14. Fahey, T.D.; Cahill, J.M.; Snellgrove, T.A.; Heath, L.S. *Lumber and Veneer Recovery from Intensively Managed Young-Growth Douglas-Fir*; US Department of Agriculture, Forest Service: Portland, OR, USA, 1991.
15. Bendtsen, B.A.; Plantinga, P.L.; Snellgrove, T.A. The influence of juvenile wood on the mechanical properties of 2 by 4's cut from Douglas-fir plantations. In Proceedings of the International Conference on Timber Engineering, Pullman, WA, USA, 19–22 September 1988; Washington State Univ.: Pullman, WA, USA, 1988; pp. 226–240.
16. Lowell, E.C.; Maguire, D.A.; Briggs, D.G.; Turnblom, E.C.; Jayawickrama, K.J.; Bryce, J. Effects of silviculture and genetics on branch/knot attributes of coastal Pacific Northwest Douglas-fir and implications for wood quality—A Synthesis. *Forests* **2014**, *5*, 1717–1736. [CrossRef]
17. Curtis, R.O.; Reukema, D.L. Crown development and site estimates in a Douglas-fir plantation spacing test. *For. Sci.* **1970**, *16*, 287–301.
18. Grah, R.F. Relationship between tree spacing, knot size, and log quality in young Douglas-fir stands. *J. For.* **1961**, *59*, 270–272.
19. Weiskittel, A.R.; Maguire, D.A.; Monserud, R.A.; Rose, R.; Turnblom, E.C. Intensive management influence on Douglas fir stem form, branch characteristics, and simulated product recovery. *N. Z. J. For. Sci.* **2006**, *36*, 293–312.
20. Brix, H. Effects of thinning and nitrogen fertilization on branch and foliage production in Douglas-fir. *Can. J. For. Res.* **1981**, *11*, 502–511. [CrossRef]
21. Maguire, D.A.; Kershaw, J.A., Jr.; Hann, D.W. Predicting the effects of silvicultural regime on branch size and crown wood core in Douglas-fir. *For. Sci.* **1991**, *37*, 1409–1428.

22. Maguire, D.A.; Johnston, S.R.; Cahill, J. Predicting branch diameters on second-growth Douglas-fir from tree-level descriptors. *Can. J. For. Res.* **1999**, *29*, 1829–1840. [CrossRef]
23. Briggs, D.G.; Kantavichai, R.; Turnblom, E.C. Predicting the diameter of the largest breast-height region branch of Douglas-fir trees in thinned and fertilized plantations. *For. Prod. J.* **2010**, *60*, 322–330. [CrossRef]
24. Reukema, D.L. Crown expansion and stem radial growth of Douglas-fir as influenced by release. *For. Sci.* **1964**, *10*, 192–199.
25. Barbour, R.J.; Parry, D.L. *Log and Lumber Grades as Indicators of Wood Quality in 20- to 100-Year Old Douglas-Fir Trees from Thinned and Unthinned Stands*; US Department of Agriculture, Forest Service: Portland, OR, USA, 2001.
26. Western Wood Products Association (WWPA). *Western Lumber Grading Rules*; Western Wood Products Association: Portland, OR, USA, 2017.
27. Middleton, G.R.; Munro, B.D. Log and Lumber Yields. In *Second Growth Douglas-Fir: Its Management and Conversion for Value*; Kellogg, R.M., Ed.; Forintek Canada Corp.: Vancouver, BC, Canada, 1989; Chapter 7; pp. 66–74.
28. Briggs, D.G.; Ingaramo, L.; Turnblom, E.C. Number and Diameter of Breast-height Region Branches in a Douglas-fir Spacing Trial and Linkage to Log Quality. *For. Prod. J.* **2007**, *57*, 28–34.
29. Ross, R.J.; McDonald, K.A.; Green, D.W.; Schad, K. Relationship between log and lumber modulus of elasticity. *For. Prod. J.* **1997**, *47*, 89–92.
30. Ross, R.J.; Willits, S.A.; VonSegen, W.; Black, T.; Brashaw, B.K.; Pellerin, R.F. A stress wave based approach to NDE of logs for assessing potential veneer quality. Part I. Small diameter ponderosa pine. *For. Prod. J.* **1999**, *49*, 60–62.
31. Ridoutt, B.G.; Wealleans, K.R.; Booker, R.E.; McConchie, D.L.; Ball, R.D. Comparison of log segregation methods for structural lumber yield improvement. *For. Prod. J.* **1999**, *49*, 63–66.
32. Carter, P.; Briggs, D.; Ross, R.J.; Wang, X. Acoustic testing to enhance western forest values and meet customer wood quality needs. In *Productivity of Western Forests: A Forest Products Focus*; Harrington, C.A., Schoenholz, S.H., Eds.; US Department of Agriculture Forest Service: Portland, OR, USA, 2005; pp. 121–129.
33. Wang, X.; Ross, R.J.; McClellan, M.; Barbour, R.J.; Erickson, J.R.; Forsman, J.W.; McGinnis, G.D. Nondestructive evaluation of standing trees with a stress wave method. *Wood Fiber Sci.* **2001**, *33*, 522–533.
34. Wang, X.; Carter, P.; Ross, R.J.; Brashaw, B.K. Acoustic assessment of wood quality of raw forest materials—A path to increased profitability. *For. Prod. J.* **2007**, *57*, 6–14.
35. Wang, X.; Ross, R.J.; Carter, P. Acoustic evaluation of wood in standing trees. Part I. Acoustic wave behavior. *Wood Fiber Sci.* **2007**, *39*, 28–38.
36. Amishev, D.; Murphy, G.E. In-forest assessment of veneer grade Douglas-fir logs based on acoustic measurement of wood stiffness. *For. Prod. J.* **2008**, *58*, 42–47.
37. Briggs, D.G.; Thienel, G.; Turnblom, E.C.; Lowell, E.; Dykstra, D.; Ross, R.J.; Wang, X.; Carter, P. Influence of thinning on acoustic velocity of Douglas-fir trees in western Washington and western Oregon. In Proceedings of the 15th International Symposium on Nondestructive Testing of Wood, Duluth, MN, USA, 10–12 September 2007; pp. 113–123.
38. Maguire, D.A.; Bennett, W.S.; Kershaw, J.A., Jr.; Gonyea, R.; Chappell, H.N. *Establishment Report Stand Management Cooperative Project Field Installations, Institute of Forest Resources Contrib. 72*; College of Forest Resources, University of Washington: Seattle, WA, USA, 1991.
39. Curtis, R.O. A simple index of stand density for Douglas-fir. *For. Sci.* **1982**, *28*, 92–94.
40. Evans, J.W.; Kretschmann, D.E.; Herian, V.L.; Green, D.W. *Procedures for Developing Allowable Properties for a Single Species Under ASTM1900 and Computer Programs Useful for the Calculation*; US Department of Agriculture, Forest Service: Madison, WI, USA, 2001.
41. Ramalho, E.A.; Ramalho, J.J.; Murteira, J.M. Alternative estimating and testing empirical strategies for fractional regression models. *J. Econ. Surv.* **2011**, *25*, 19–68. [CrossRef]
42. American Forest and Paper Association/American Wood Council (AF & PA/AWC). *Wood Structural Design Data*; American Forest and Paper Association: Washington, DC, USA, 2004.
43. Zhao, D.; Borders, B.; Wang, M. Survival model for fusiform rust infected loblolly pine plantations with and without mid-rotation understory vegetation control. *For. Ecol. Manag.* **2006**, *235*, 232–239. [CrossRef]
44. Bates, D.; Maechler, M.; Bolker, B.; Walker, S.; Christensen, R.H.B.; Singmann, H.; Dai, B.; Scheipl, F.; Grothendieck, G.; Green, P. Linear Mixed-Effects Models Using 'Eigen' and S4: Package 'lme4'. 2018. Available online: https://cran.r-project.org/web/packages/lme4/lme4.pdf (accessed on 19 February 2018).

45. Oliver, C.D.; Larson, B.C. *Forest Stand Dynamics*; Update Edition; Wiley: New York, NY, USA, 1996; 520p.
46. Northwest Log Rules Advisory Group. *Official Rules for the Following Log Scaling and Grading Bureaus: Columbia River, Grays Harbor, Northern California, Puget Sound, Southern Oregon, Yamhill*; Northwest Log Rules Advisory Group: Eugene, OR, USA, 1998; 48p.
47. Hoibo, O.A.; Turnblom, E.C. Models of knot characteristics in young coastal U.S. Douglas-fir: Are the effects of tree and site data visibly rendered in the annual ring width pattern at breast height? *For. Prod. J.* **2017**, *67*, 29–38.
48. Todoroki, C.L.; Lowell, E.C.; Kantavichai, R. Growth and mortality in response to climatic extremes and competition in thinning trials of Douglas-fir. manuscript in preparation.

© 2018 by the authors. Licensee MDPI, Basel, Switzerland. This article is an open access article distributed under the terms and conditions of the Creative Commons Attribution (CC BY) license (http://creativecommons.org/licenses/by/4.0/).

forests

MDPI

Article

Acoustic Velocity—Wood Fiber Attribute Relationships for Jack Pine Logs and Their Potential Utility

Peter F. Newton

Canadian Wood Fiber Centre, Canadian Forest Service, Natural Resources Canada, Sault Ste. Marie, ON P6A 2E5, Canada; peter.newton@canada.ca; Tel.: +1-705-541-5615

Received: 18 October 2018; Accepted: 23 November 2018; Published: 30 November 2018

Abstract: This study presents an acoustic-based predictive modeling framework for estimating a suite of wood fiber attributes within jack pine (*Pinus banksiana* Lamb.) logs for informing in-forest log-segregation decision-making. Specifically, the relationships between acoustic velocity (longitudinal stress wave velocity; v_l) and the dynamic modulus of elasticity (m_e), wood density (w_d), microfibril angle (m_a), tracheid wall thickness (w_t), tracheid radial and tangential diameters (d_r and d_t, respectively), fiber coarseness (c_o), and specific surface area (s_a), were parameterized deploying hierarchical mixed-effects model specifications and subsequently evaluated on their resultant goodness-of-fit, lack-of-fit, and predictive precision. Procedurally, the data acquisition phase involved: (1) randomly selecting 61 semi-mature sample trees within ten variable-sized plots established in unthinned and thinned compartments of four natural-origin stands situated in the central portion the Canadian Boreal Forest Region; (2) felling and sectioning each sample tree into four equal-length logs and obtaining twice-replicate v_l measurements at the bottom and top cross-sectional faces of each log (n = 4) from which a log-specific mean v_l value was calculated; and (3) sectioning each log at its midpoint and obtaining a cross-sectional sample disk from which a 2 × 2 cm bark-to-pith radial xylem sample was extracted and subsequently processed via SilviScan-3 to derive annual-ring-specific attribute values. The analytical phase involved: (1) stratifying the resultant attribute—acoustic velocity observational pairs for the 243 sample logs into approximately equal-sized calibration and validation data subsets; (2) parameterizing the attribute—acoustic relationships employing mixed-effects hierarchical linear regression specifications using the calibration data subset; and (3) evaluating the resultant models using the validation data subset via the deployment of suite of statistical-based metrics pertinent to the evaluation of the underlying assumptions and predictive performance. The results indicated that apart from tracheid diameters (d_r and d_t), the regression models were significant ($p \leq 0.05$) and unbiased predictors which adhered to the underlying parameterization assumptions. However, the relationships varied widely in terms of explanatory power (index-of-fit ranking: w_t (0.53) > m_e > s_a > c_o > w_d >> m_a (0.08)) and predictive ability (s_a > w_t > w_d > c_o >> m_e >>> m_a). Likewise, based on simulations where an acoustic-based w_d estimate is used as a surrogate measure for a Silviscan-equivalent value for a newly sampled log, predictive ability also varied by attribute: 95% of all future predictions for s_a, w_t, c_o, m_e, and m_a would be within ±12%, ±14%, ±15%, ±27%, and ±55% and of the true values, respectively. Both the limitations and potential utility of these predictive relationships for use in log-segregation decision-making, are discussed. Future research initiatives, consisting of identifying and controlling extraneous sources of variation on acoustic velocity and establishing attribute-specific end-product-based design specifications, would be conducive to advancing the acoustic approach in boreal forest management.

Keywords: end-product-based fiber attribute determinates; longitudinal stress wave velocity; mixed-effects hierarchical linear models; predictive performance

1. Introduction

The Canadian forest sector has been increasingly embracing an aspirational trivariate management proposition for which the goal is to maximize end-product value while simultaneously realizing volumetric yield and ecological sustainability objectives (sensu [1,2]). Tangential to this transformative shift is the increased apprehension regarding the quality and associated end-product potential of the increasing wood volumes harvested from more intensely managed second-growth forests [3]. Among the many prerequisites required for realizing this goal and addressing knowledge gaps in second-growth fiber quality, is the provision of enhanced in-forest intelligence in regards to the forecasting of end-product potential at the time of harvest or immediately afterwards (n., in-forest generically refers to all forest operations conducted or decisions made before mill-processing commences inclusive of operational felling areas, landings and log sorting yards).

End-product forecasts can be used to inform and optimize log-segregation, allocation and merchandizing decision-making thus contributing to the potential realization of the value maximization objective [4–6]. More precisely, the end-product potential of the logs extracted from the main stem of individual coniferous trees is a function of (1) external morphological stem features (e.g., diameter, height, taper, sweep, crook, and eccentricity), and (2) internal anatomical characteristics (e.g., microfibril angle, tracheid wall thickness, tracheid radial and tangential diameters) and associated physical properties (e.g., modulus of elasticity, wood density, fiber coarseness and specific surface area) of the xylem tissue. Various performance measures which are used to define and classify the overall type and grade of derived products have been shown to be explicitly linked to these internal fiber-based attributes. Although only stiffness and wood density measures are currently used in machine stress grading systems for solid wood products (e.g., dimensional lumber [7]), microfibril angle, tracheid cell wall thickness, radial and tangential tracheid diameters, fiber coarseness and specific surface area, are also important determinates of end-product quantity and quality [8] (sensu Table 1). Thus, as the fiber supply increases in diversity with the arrival of wood from density manipulated forests (e.g., pre-commercially and/or commercially thinned natural-origin stands, and plantations) combined with increasing pressures to find economic efficiencies within the upper portion of the forest products supply chain, provision of explicit information on these additional attributes may become consequential.

Table 1. Product-based performance measures and their relationship with fiber attributes for boreal conifers.

Product Category	Performance Measure	Relationship with Fiber Attribute [a]
Biomass (e.g., pellets)	Calorific value	$\propto$ xylem density
Pulp and paper (e.g., paperboards, newsprint, facial tissues, and specialized coated papers)	Tensile strength	$\propto$ (tracheid wall thickness)$^{-1}$, specific surface area
	Tear strength	$\propto$ fiber coarseness
	Stretch	microfibril angle
	Bulk	$\propto$ tracheid wall thickness, (tracheid diameter)$^{-1}$
	Light scattering	$\propto$ (tracheid wall thickness)$^{-1}$
	Collapsibility	$\propto$ tracheid wall thickness
	Yield	$\propto$ xylem density
Solid wood and composites (e.g., dimensional lumber; glulam-based beams)	Strength	$\propto$ xylem density, (microfibril angle)$^{-1}$
	Stiffness	$\propto$ xylem density, modulus of elasticity, (microfibril angle)$^{-1}$
Poles and squared timbers (e.g., utility poles and solid wood beams)	Strength	$\propto$ xylem density, (microfibril angle)$^{-1}$
	Stiffness	$\propto$ xylem density, modulus of elasticity, (microfibril angle)$^{-1}$

[a] Generic-based inferences derived from generalized end-product-specific performance metric—attribute relationships for boreal conifers (sensu [8]).

Attribute determination for use in forecasting end-product potential deploying destructive sampling approaches can be logistically challenging, time consuming and expensive (e.g., in-forest extracting of 12 mm diameter xylem cores followed by Silviscan-based laboratory processing and testing). Conversely, non-destructive sampling methods in which attributes can be estimated indirectly through their relationship with acoustic velocity has been shown to be viable alternative [9–12]. More specifically, in-forest acoustic-based sampling tools provide forest practitioners with an ability to estimate the dynamic modulus of elasticity within harvested logs and standing trees. The dynamic modulus of elasticity is a wood stiffness measure that is used as a surrogate measure of its static counterpart (static modulus of elasticity). This latter static measure is commonly employed along with maximum knot size, sweep and physical dimensions, to categorize solid wood products into specific grade classes [7,9,13]. Thus, the ability to forecast one of the key underlying determinates of end-product potential within the forest at the time of harvest or soon after, has important utility in terms of informing segregation, allocation and merchandizing decision-making [6].

Mathematically, as derived from engineering principles, the dynamic modulus of elasticity (MOE_{dyn} denoted m_e in this study; GPa) of a log can be expressed as a function of the density-weighted velocity of a longitudinal stress wave (v_l; km/s) that propagates through the xylem tissue upon its generation arising from a mechanically induced impact on one of the open cross-sectional log faces (Equation (1) and denoted the primary relationship herewith; [12]).

$$m_e = f\left(w'_d v_l^2\right) \tag{1}$$

where w'_d is the green (fresh) wood density (kg/m^3) of the log's xylem tissue. The dynamic modulus of elasticity has also been shown to be correlated with other attributes underlying end-product potential [14–16].

More specifically, based on extracted clear xylem samples obtained from black spruce (*Picea mariana* (Mill) B.S.P.), red pine (*Pinus resinosa* Ait.) and jack pine (*Pinus banksiana* Lamb.) trees growing in the central North America, Silviscan-derived estimates of wood density (oven-dried wood density denoted w_d in this study; kg/m^3), microfibril angle (MFA denoted m_a in this study; °), tracheid cell wall thickness (w_t; µm), radial (d_r; µm) and tangential (d_t; µm) tracheid diameters, fiber coarseness (c_o; µg/m) and specific surface area (s_a; m^2/kg), have been shown to be correlated with the dynamic modulus of elasticity (Table 2). Statistically significant ($p \leq 0.05$) (1) directly proportional relationships between m_e and w_d, w_t and c_o ($m_e \propto w_d, w_t, c_o$), and (2) indirectly proportional relationships between m_e and m_a, d_r, d_t and s_a $\left(m_e \propto m_a^{-1}, d_r^{-1}, d_t^{-1}, s_a^{-1}\right)$, have been established for these species (Table 2). Supporting correlative evidence has also been reported for non-boreal conifers. For example, a directly proportional correlative relationship between m_e and wood density (r = 0.75) and an inversely proportional relationship between m_e and m_a (r = −0.83) has been reported for Silviscan-derived attribute estimates obtained from clear wood samples extracted from 76 radiata pine (*Pinus radiata* D. Don.) boards [13]. Based on this collective correlative evidence, an empirical-based expansion of the acoustic-based inferential framework was proposed for boreal conifer logs [15], as summarized in Table 2. Since wood density is also one of the principal end-product determinates (sensu Table 1) and analytically required for acoustic-based attribute predictions (e.g., Equation (1); Table 2), a simplified directly proportional relationship between acoustic velocity and wood density was included within this framework (i.e., $w_d \propto v_l^2$). Collectively, this expanded acoustic inferential framework represents a more encompassing analytical platform for forecasting commercially relevant wood quality attributes than previous univariate approaches solely based on the primary relationship (Equation (1)).

Table 2. Linear associations between the dynamic modulus of elasticity and other Silviscan-derived wood quality attributes for 3 boreal conifers and the resultant acoustic-based relationship inferred.

Attribute	Association with Dynamic Modulus of Elasticity as Measured by the Pearson Product Moment Correlation Coefficient [a]			Statistical Inference	Empirical Linkage to Acoustic Velocity [b]
	Black Spruce	Red Pine	Jack Pine		
Wood density	0.7765 *	0.7585 *	0.6717 *	$m_e \propto w_d$	$w_d \propto v_l^2$
Microfibril angle	−0.8981 *	−0.8075 *	−0.7101 *	$m_e \propto m_a^{-1}$	$m_a \propto \left(w_d v_l^2\right)^{-1}$
Tracheid wall thickness	0.6765 *	0.6871 *	0.6648 *	$m_e \propto w_t$	$w_t \propto w_d v_l^2$
Radial tracheid diameter	−0.4477 *	−0.3833 *	−0.3169 *	$m_e \propto d_r^{-1}$	$d_r \propto \left(w_d v_l^2\right)^{-1}$
Tangential tracheid diameter	−0.3037 *	−0.0886	−0.0814	$m_e \propto d_t^{-1}$	$d_t \propto \left(w_d v_l^2\right)^{-1}$
Fiber coarseness	0.2044	0.4385 *	0.5412 *	$m_e \propto c_o$	$c_o \propto w_d v_l^2$
Specific surface area	−0.5812 *	−0.6355 *	−0.6368 *	$m_e \propto s_a^{-1}$	$s_a \propto \left(w_d v_l^2\right)^{-1}$

[a] Species-specific bivariate linear associations between Silviscan-determined accumulative area-weighted mean fiber attributes as previously presented in Table 2 of Newton [16]: Pearson product moment correlation coefficient for the relationship between the dynamic modulus of elasticity and each attribute at breast-height (1.3 m) for 50 semi-mature black spruce trees [14], 54 mature red pine trees [16], and 61 semi-mature jack pine trees (this study) where * denotes a significant correlation at the 0.05 probability level. [b] Based on the primary $m_e \propto w_d v_l^2$ relationship for all attributes except wood density.

Although these statistical-based secondary relationships lack the causal underpinnings of the primary relationship (sensu [17]), the empirical results to date have been supportive. Specifically, applying this analytical framework to red pine logs, revealed that statistically viable acoustic-based relationships could be established for five of the eight attributes examined (m_e, w_d, w_t, c_o and s_a) [15]. However, the applicability of this expanded framework of acoustic-based wood attribute relationships to other intensely managed softwood species is largely unknown. Furthermore, even the most fundamental acoustic velocity—attribute relationship (Equation (1)) has yet to be parameterized for most of the commercially important Canadian boreal conifers (e.g., an "acoustic velocity" keyword search for articles published within Canada's primary applied journal (Forestry Chronicle) was unsuccessful in identifying previous research in this field). Conversely, other forest regions, such as New Zealand, United States of America, Australia, Europe, and Asia, have adapted this acoustic-based innovation pathway in order improve segregation decision-making (e.g., [18,19]). Hence, the evaluation of the acoustic approach and the provision of prediction equations for the estimating a suite of key attributes underlying end-product potential for jack pine, could contribute to addressing this innovation void. Principally, by providing the forest practitioner with the prerequisite prediction equations, in-forest segregation decision-making could be improved and potentially yield overall efficiency gains within the upper portion of the jack pine forest products supply chain. Consequently, the objective of this study was to investigate the empirical applicability of the expanded acoustic-based inferential framework by examining the nature, strength and predictability of the relationships between acoustic velocity and the dynamic modulus of elasticity, wood density, microfibril angle, tracheid cell wall thickness, radial and tangential tracheid diameters, fiber coarseness and specific surface area, specifically for jack pine.

2. Materials and Methods

2.1. Sample Stands, Plot Establishment and Sample Tree Selection

Two geographically separated jack pine thinning experiments that were previously established in northeastern (denoted the Sewell site) and northcentral (denoted the Tyrol site) regions of Ontario, were selected for sampling. The experimental treatments were representative of the crop planning strategy historically followed in Ontario for this species. Specifically, allowing jack pine to naturally regenerate following a stand-replacing disturbance and if sufficiently successful in terms of stocking levels and free-to-grow status, (1) implementing precommercial thinning in order to moderate overall site occupancy and encourage individual tree growth thereby reducing the time-to-operability status in order to mitigate the effects of projected wood supply deficits, or (2) implementing a temporal sequence of thinning treatments (precommercial and commercial thinning) in order to optimize site occupancy and maximize end-product potentials throughout the rotation [20].

At the Sewell site, sample trees were selected within 6 sample plots that were established in 3 fire-origin jack pine stands (2 plots/stand). These approximately 53-year-old stands were situated on sites of medium-to-good quality (mean site index of 18 m at a breast-height age of 50 [21]) and geographically located within Forest Section B.7—Missinaibi-Cabonga of the Canadian Boreal Forest Region [22]. The soils and topography were characterized as deep (>1 m) coarse-to-medium textured sandy types situated on gently undulating terrain. Silviculturally, the stands were subjected to 1 of 3 density manipulation treatments yielding 3 unique crop plans: (1) natural stand development with no density management (unthinned); (2) precommercial thinned (PCT) at age 11 (1971); and (3) PCT at age 11 followed by a light pseudo-commercial thinning (CT) at age 43 (2003). Procedurally, for the first stand, sample trees were selected within 2 previously established 0.06 ha circular monitoring plots. For these 2 plots, a stratified random sample protocol was used to select sample trees: the observed diameter frequency distribution at the time of sampling was stratified into 3 size classes from which 1 or 2 trees per class were selected. However, to preserve the original sample design within the remaining stands, temporary prism-based variable-size plots where established adjacent to 2 of the existing

long-term monitoring plots within the second and third stands. Deploying the observed diameter frequency distribution derived from the prism sweeps, 3 size classes were similarly formulated from which 1 or 2 trees per class were selected. In total, 31 jack pine sample trees were selected at the Sewell site: 3 stands × 2 plots/stand × 3 size classes/plot × 1–2 trees/size class.

At the Tyrol site, sample trees were selected within 4 0.07 ha circular sample plots that were established in 2 fire-origin jack pine stands. These stands were situated on sites of good-to-excellent quality (mean site index of 21 m at a breast-height age of 50 [21]), geographically located within Forest Section B9 (Superior) of the Canadian Boreal Forest Region [22], and approximately 73 years of age when sampled. The soils and topography were characterized as deep (>1 m) finely textured sandy types on gently undulating terrain. Silviculturally, the stands were subjected to 2 density manipulation treatments: PCT at an age of approximately 20 (1962) followed by a light pseudo-CT treatment at an age of approximately 56 (1998). A size-based stratified random sample protocol was used to select trees resulting in approximately 2–3 trees being chosen from each of the 3 size (diameter) classes. In total 30 jack pine sample trees were selected from the Tyrol site: 2 stands × 2 plots/stand × 3 size classes/plot × 2–3 sample trees/size class. In summary, a total of 61 sample trees were selected from the 2 experimental areas which were grown under a range of density management regimes reflective of past and current forest management practices for this species and region (e.g., unthinned, PCT, PCT+CT).

2.2. Sample Tree Measurements, Stem Analysis Procedures, Log-Based Acoustic Measurements and Disk Sampling

Prior to felling and sectioning each sample tree using destructive stem analysis, diameter at breast-height (1.3 m) outside-bark diameter (D_b; cm), total height (H_t; m) and height-to-live crown (H_c; m) measurements were obtained. Note, all measurements and destructive sampling were completed on the trees at Sewell and Tyrol sites at the conclusion of the 2013 and 2015 growing seasons, respectively. The destructive stem analysis protocol consisted of felling each sample tree at stump height (0.3 m), delimbing the stem and then topping the stem at an 80% relative height position. The stem was then sectioned into 0%–20%, 20%–40%, 40%–60% and 60%–80% percentile-based log-length intervals employing a percent height sampling protocol. Immediately thereafter, the velocity of a mechanically induced longitudinal stress wave propagating throughout each log was measured using a Director HM200 acoustic velocity resonance tool (Fibre-gen Inc., Christchurch, New Zealand; www.fibre-gen.com). Specifically, a twice-replicated set of v_l (km/s) measurements were obtained at the bottom and top of each log from which an arithmetic mean value was calculated. Log lengths, ambient air, and xylem temperatures were also taken at the time of each acoustic velocity measurement.

For each tree, cross-sectional samples were then extracted from the center of each log, corresponding to the relative height positions of 10%, 30%, 50% and 70%. The samples were placed in temporary cold storage within 8 h of sectioning and then transported to a permanent cold storage (<0 °C) facility until further processing. Overall, the deployed sampling design yielded 124 cross-sectional disks from the Sewell site (1 disk/log × 4 logs/tree × 31 trees) and 120 cross-sectional disks from the Tyrol site (1 disk/log × 4 logs/tree × 30 trees). Due to logistical challenges during field sampling at the Sewell site, however, one of the cross-sectional samples had to be disregarded. Hence a final total of 243 cross-sectional disk samples obtained from the midpoint position on each of the 243 sample logs were available for analysis. Table 3 summarizes the mensuration characteristics of the standing sample trees prior to felling. The trees from both sites exhibited a similar degree of variation for each measured characteristic as quantified by the coefficient of variation. Diameter and live crown ratio ($(H_t - H_c)/H_t$) exhibited the greatest amount of variation given that a size-based stratified random sampling protocol was used to select the sample trees (e.g., trees from all 3 diameter size-groups (small, medium, and large) where included). The minimal degree of age variation is largely due to the even- aged nature of the sampled stands. Table 4 provides a descriptive summary of the derived logs in terms of their dimensions and associated acoustic velocity measurements.

Table 3. Descriptive statistical summary of the mensuration characteristics of the 61 sample trees by site (n = 31 and 30 for Sewell and Tyrol, respectively).

Variable	Site	Mean	Standard Error	Minimum	Maximum	CV [a] (%)
Diameter at breast-height (cm)	Sewell	18.8	2.11	14.7	22.6	11.2
	Tyrol	24.4	2.17	19.8	29.1	8.9
Breast-height age (year)	Sewell	50	0.96	47	51	1.9
	Tyrol	69	1.27	66	71	1.9
Total height (m)	Sewell	21.1	1.26	18.3	22.9	6.0
	Tyrol	22.2	1.57	19.5	24.6	7.1
Live crown ratio (%)	Sewell	26.1	4.50	15.0	35.3	17.3
	Tyrol	28.2	7.20	14.1	41.5	25.5

[a] Coefficient of variation.

Table 4. Descriptive statistical summary of the dimensions of the 243 sample logs and associated acoustic velocity measurements by log position (n = 243 of which 61, 61, 61 and 60 were first, second, third and fourth positioned logs, respectively).

Variable	Log [a]	Mean	Median	Standard Error	Minimum	Maximum	CV [b] (%)
Log length (m)	1st	4.30	4.36	0.04	3.48	5.00	7.7
	2nd	4.28	4.35	0.04	3.47	4.91	7.8
	3rd	4.28	4.37	0.04	3.18	4.91	7.9
	4th	4.25	4.37	0.06	2.27	4.89	10.8
Mean log diameter (inside-bark; cm)	1st	19.49	19.39	0.35	13.70	26.92	14.1
	2nd	16.97	17.03	0.31	10.89	21.76	14.4
	3rd	14.38	14.56	0.28	9.41	19.25	15.4
	4th	11.30	10.99	0.26	7.54	15.71	17.5
Longitudinal stress wave velocity (v_l; km/s)	1st	3.59	3.58	0.02	3.20	4.29	5.2
	2nd	3.59	3.62	0.03	3.15	4.32	5.5
	3rd	3.39	3.42	0.02	2.86	4.12	6.0
	4th	3.08	3.08	0.02	2.69	3.72	6.0

[a] Proceeding upwards from the stump to the stem apex, 1st, 2nd, 3rd and 4th denotes the ordinal position of the first, second, third and fourth log extracted from the main stem of the 61 jack pine sample trees. [b] Coefficient of variation.

2.3. Silviscan-3 Estimation of Fiber Attributes and Preliminary Computations

A transverse 2 cm × 2 cm bark-to-pith-to-bark sample was extracted along the geometric mean diameter of each of the frozen cross-sectional disks. Annual area-weighted ring measures of m_e, w_d, m_a, w_t, d_r, d_t, c_o and s_a were determined along one of the transverse pith- to-bark radii using the SilviScan-3 system. SilviScan-3 analyses yields a set of commercially relevant fiber attribute estimates through the deployment of an integrated hardware-software processing system involving automatic image acquisition and analysis (cell scanner), X-ray densitometry, and X-ray diffractometry technologies. In this study, the following attribute estimates were used from the Silviscan-3 analysis: (1) wood density as measured at a 25 µm resolution and 8% moisture content (dry basis) and determined following the removal of resins using X-ray densitometry (i.e., $w_d = f$ (intensity of incident and transmitted X-ray beams; sample thickness; and X-ray travel distance); [23,24]); (2) microfibril angle as determined via X-ray diffraction patterns (i.e., $m_a = f$ (variance of the cellulose-I 002 azimuthal X-ray diffraction pattern; and dispersion of the microfibril orientation distribution); [25]); (3) dynamic modulus of elasticity as determined from a combination of X-ray densitometry and diffraction measurements (i.e., $m_e = f$ (X-ray densitometry density estimate; and coefficient of variation of the normalized intensity profile); [26]); and (4) fiber dimensions and derived metrics consisting of tracheid wall thickness, radial and tangential tracheid diameters, fiber coarseness and specific surface area as determined using the results from the image analyses (radial and tangential diameters) in combination with the wood density estimate (sensu [27]).

Computationally, deploying the annual area-weighted ring estimates for m_e, w_d, m_a, w_t, d_r, d_t, c_o and s_a and proceeding in a pith-to-bark direction, an attribute-specific cumulative area-weighted moving average value was calculated for each of the 243 radial sequences (Equation (2)).

$$F = \frac{\sum_{i=1}^{I} f_i a_i}{\sum_{i=1}^{I} a_i} \quad (2)$$

where F is the cumulative moving area-weighted fiber attribute average for each sequence, a_i is the Silviscan-3-determined area of the ith annual ring (mm^2; $i = 1, \ldots, I$; I = total cambial age), and f_i is the mean Silviscan-3-determined fiber attribute value within the ith annual ring. Table 5 provides an attribute-specific descriptive statistical summary by log position, inclusive of measures of central tendency (arithmetic means and medians), ranges (minimums and maximums) and relative variation measures (coefficients of variation).

Table 5. Descriptive statistical summary of the fiber attributes of by log position (n = 243 of which 61, 61, 61 and 60 were first, second, third and fourth positioned logs, respectively).

Variable	Log [a]	Mean	Median	Minimum	Maximum	CV [b] (%)
Modulus of elasticity (m_e; GPa)	1st	12.72	12.68	8.59	16.73	15.0
	2nd	12.81	12.95	8.24	16.16	14.2
	3rd	12.38	12.82	7.93	15.89	13.7
	4th	11.33	11.57	7.14	14.57	12.7
Wood density (w_d; kg/m^3)	1st	430.38	421.66	372.88	489.67	6.5
	2nd	416.48	418.68	337.88	482.02	6.6
	3rd	407.47	405.99	359.76	467.79	6.0
	4th	394.23	391.66	356.95	442.25	5.1
Microfibril angle (m_a; °)	1st	12.98	12.79	7.49	19.71	21.1
	2nd	11.47	10.95	6.33	19.23	22.7
	3rd	11.25	10.92	6.24	17.84	22.6
	4th	12.52	12.21	6.84	20.23	22.8
Tracheid wall thickness (w_t; µm)	1st	2.70	2.67	2.35	3.16	7.6
	2nd	2.60	2.60	2.08	3.01	7.8
	3rd	2.52	2.49	2.22	2.92	7.3
	4th	2.39	2.37	2.17	2.77	5.9
Tracheid radial diameter (d_r; µm)	1st	30.80	30.90	28.51	33.00	3.7
	2nd	30.75	30.95	28.69	32.74	3.5
	3rd	30.52	30.68	27.99	32.79	3.7
	4th	30.03	30.18	26.44	31.97	4.1
Tracheid tangential diameter (d_t; µm)	1st	27.87	27.93	26.41	29.88	2.4
	2nd	28.13	28.13	26.89	30.25	2.5
	3rd	28.10	28.16	26.53	29.72	2.5
	4th	27.97	27.99	26.38	29.63	2.6
Fiber coarseness (c_o; µg/m)	1st	406.02	406.67	360.44	471.20	6.8
	2nd	395.23	394.97	339.39	447.85	7.1
	3rd	383.33	383.76	328.30	455.34	7.2
	4th	364.51	365.10	311.38	420.68	6.3
Specific surface area (s_a; m^2/kg)	1st	314.32	315.76	275.59	351.46	6.4
	2nd	322.71	321.31	284.37	372.46	6.4
	3rd	328.16	327.71	287.81	366.30	6.4
	4th	338.15	341.99	297.17	369.33	5.0

[a] Proceeding upwards from the stump to the stem apex, 1st, 2nd, 3rd and 4th denotes the ordinal position of the first, second, third and fourth log extracted from the main stem of the 61 jack pine sample trees. [b] Coefficient of variation.

2.4. Preliminary Data Stratification for Cross-Validation Assessment

To minimize the potential effects of spatial correlation arising from the selection of the multiple logs from the same sample tree while at the same time providing a validation data subset, the full data set consisting of 243 m_e, w_d, m_a, w_t, d_r, d_t, c_o, s_a—v_l observational pairs was systematically subdivided into calibration and validation data subsets of approximately equal size. This involved randomly selecting from each sample tree a sequential set of measurements consisting of either those associated with the 1st and 3th positioned logs or those associated with the 2nd and 4th positioned logs. The resultant pairs were then allocated to either the calibration or validation subsets. At the conclusion of this stratification process, the calibration and validation data subsets were comprised of 122 and 121 m_e, w_d, m_a, w_t, d_r, d_t, c_o, s_a—v_l observational pairs, respectively. As presented in Table 6, the acoustic velocity measurements and attribute values within the subsets were very similar in terms of measures of central tendency, magnitudes, and relative variation. A further similarly structured comparative assessment of the data subsets by log position and location (not shown) also confirmed the equivalency between the data subsets.

Table 6. Descriptive statistical summary of the calibration (n = 122 logs) and validation (n = 121 logs) data subsets.

Variable	Data Subset	Mean	Minimum	Maximum	CV [a] (%)
Longitudinal stress wave velocity (v_l; km/s)	Calibration	3.42	2.74	4.32	7.8
	Validation	3.41	2.69	4.29	8.8
Modulus of elasticity (m_e; GPa)	Calibration	12.28	7.14	16.57	14.8
	Validation	12.34	7.93	16.73	14.7
Wood density (w_d; kg/m^3)	Calibration	412.41	343.02	489.67	6.9
	Validation	412.02	337.88	482.02	6.8
Microfibril angle (m_a; °)	Calibration	12.10	6.84	19.23	21.7
	Validation	12.01	6.24	20.23	24.3
Tracheid wall thickness (w_t; µm)	Calibration	2.56	2.14	3.13	8.6
	Validation	2.55	2.08	3.16	8.3
Tracheid radial diameter (d_r; µm)	Calibration	30.59	27.99	33.00	3.8
	Validation	30.47	26.44	32.74	3.9
Tracheid tangential diameter (d_t; µm)	Calibration	28.01	26.41	29.88	2.5
	Validation	28.02	26.38	30.25	2.5
Coarseness (c_o; µg/m)	Calibration	388.35	318.32	459.90	8.1
	Validation	386.38	311.38	471.20	7.7
Specific surface area (s_a; m^2/kg)	Calibration	325.22	278.70	369.90	6.8
	Validation	326.36	275.59	372.46	6.4

[a] Coefficient of variation.

2.5. Specifying Functional Forms and Parameterization Methods Utilized

Deploying the expanded acoustic-based inferential framework, the Silviscan-derived (1) m_e, m_a, w_t, d_r, d_t, c_o and s_a estimates were expressed as a function of the Silviscan-derived wood density estimates and HM200-based acoustic velocity measures (m_e, m_a, w_t, d_r, d_t, c_o, $s_a = f\left(w_d v_l^2\right)$), and (2) w_d estimates were expressed solely as a function of HM200-based acoustic velocity measures ($w_d = f\left(v_l^2\right)$). Statistically, the model specification procedure consisted of assessing the results from extensive graphical and correlation analyses to determine the most appropriate functional form for each of these 8 relationships. Employing the full data set, bivariate scatterplots were used to determine the degree of linearity between the each dependent and independent variable (i.e., m_e, m_a, w_t, d_r, d_t, c_o, and s_a versus $w_d v_l^2$, and w_d versus v_l^2). A visual interpretation of the graphics for m_e, w_d, m_a, w_t, c_o, and s_a indicated mostly linear trends whereas there were no detectable trends for d_r and d_t. Consequently, log-linear, log-log and power-based transformed relationships were also examined for d_r and d_t using both scatterplots and statistical measures of association. However, the graphical trends and related

measures of linear association (Pearson moment correlation coefficient) from this supplementary analysis did not reveal the presence of viable linear relationships.

Similar to the approach used for quantifying acoustic—attribute relationships for red pine logs (i.e., [15]), a two-level hierarchical mixed-effects linear model specification consisting of fixed and random effects was used (sensu [28]). Specifically, at the first level, log-specific mean attribute values were expressed as a linear function of the density-weighted or density-unweighted acoustic velocity (Equation (3)).

$$F_{(k')_l} = \beta_{0_l(k')} + \beta_{1(k')}\left(w_{d_l} v_{l_i}^2\right) + \varepsilon_{(k')_l} \tag{3a}$$

$$F_{(w_d)_l} = \beta_{0_l(w_d)} + \beta_{1(w_d)}\left(v_{l_l}^2\right) + \varepsilon_{(w_d)l} \tag{3b}$$

where $F_{(k')_l}$ is the cumulative area-weighted moving average value for the k'th attribute where k' = m_e, m_a, w_t, d_r, d_t, c_o or s_a for the lth log, $F_{(w_d)l}$ is the cumulative area-weighted moving average wood density value for the lth log, v_{l_l} is the mean acoustic velocity value for the lth log, $\beta_{0_l(k)}$ is a first-level random effects intercept parameter specific to the kth attribute ($k = k'$ attributes and w_d inclusive) that is allowed to vary across the L logs, $\beta_{1(k)}$ are first-level fixed effects slope parameter specific to the kth attribute, and $\varepsilon_{(k)_l}$ is a random error term specific to the kth attribute for the lth log. The random errors ($\varepsilon_{(k)_l}$) are assumed to be independent, uncorrelated and have constant variance. The second level expressed the first-level intercept parameter as a function of a grand mean plus a random error term whereas the slope parameter was considered a fixed effect (Equations (4a) and (4b), respectively).

$$\beta_{0(k)_l} = \gamma_{0(k)} + u_{0(k)_l} \tag{4a}$$

$$\beta_{1(k)} = \gamma_{1(k)} \tag{4b}$$

where $\gamma_{0(k)}$ and $\gamma_{1(k)}$ are attribute-specific grand mean values and $u_{0(k)_l}$ is an attribute-specific random error term specific to the lth log. The final mixed-effects model specifications were derived by combining the level one- and two-level expressions into a single model (i.e., Equation (5)).

$$F_{(k')_l} = \gamma_{0(k')} + \gamma_{1(k')}\left(w_{d_l} v_{l_l}^2\right) + u_{0(k')_l} + \varepsilon_{(k')_l} \tag{5a}$$

$$F_{(w_d)_l} = \gamma_{0(w_d)} + \gamma_{1(w_d)}\left(v_{l_l}^2\right) + u_{0(w_d)_l} + \varepsilon_{(w_d)_l} \tag{5b}$$

Given the complex error structures, the parameter estimates and model statistics were obtained via the deployment of the hierarchical linear and nonlinear modeling software program HLM7 [29]. Statistically, the program provides empirical-Bayes first-level parameter estimates for each randomly varying coefficient (intercept term), generalized least squares-based estimates for second-level terms, and maximum likelihood estimates for the variance and covariance components. Procedurally, employing the observational pairs from the calibration data subset, the models were parameterized and subsequently assessed on their compliance with the underlying statistical assumptions. Based on the protocol developed by Raudenbush and Bryk [28], this evaluation included testing the (1) constant variance assumption among first stage residuals, and (2) presence of significant random effects as determined via testing the null hypothesis ($u_0 \neq 0$) versus the alternative hypothesis ($u_0 = 0$). Park's homogeneity test was used to evaluate the constant variance assumption for each of the significant regression relationships (sensu [30]). This involved regressing the first stage Bayes residual values (logarithmic square values; dependent variable) against the predictive variable values (logarithmic values; independent variable) using a simple linear regression model specification, and then testing the null hypothesis that the resultant slope parameter estimate was not significantly different from zero at the 0.01 probability level. Resultant slope values not significantly different from zero were supportive of the homoscedasticity assumption. Conversely, slope values significantly different from zero are suggestive of the presence of heteroscedasticity (non-constant variance).

Additionally, given the potential effect of spatial correlation on statistical inference in terms of producing inefficient estimators without the minimum variance best linear unbiased estimator property when present, the spatial correlation among the empirical-Bayes residuals derived from the first-level models was assessed. The approach consisted of employing residual regressions in order to detect the presence of a first-order spatial correlation scheme among adjacent residuals for logs sampled from the same tree (i.e., either the 1st and 3rd log pair or the 2nd and 4th log pair): i.e., fitting the relationship $e_{l+2} = \hat{\rho} e_l + v_a$ where e_l and e_{l+2} are the residual values for the lth and lth + 2 ordinal positioned log, respectively (1st and 3rd ordinal log, or 2nd and 4th ordinal log, respectively), $\hat{\rho}$ is the first-order spatial correlation coefficient estimate ($-1 \leq \hat{\rho} \leq +1$), and v_a is a random error term [30]. For significant ($p \leq 0.01$) regression relationships, the resultant $\hat{\rho}$ estimate reflected the magnitude of the first-order spatial correlation. Otherwise, for regressions that were not significant, spatial correlation was assumed to be absent and the hence the independence assumption was not rejected. The presence of potential outliers or influential observations, systematic lack-of-fits, and non-constant variance was also assessed through the examination of predictor—residual error bivariate scatterplots.

These selected specifications acknowledge the potential log-to-log variation in relationships that may be present and hence the intercept term was allowed to vary randomly. However, the slope term was treated as fixed. This latter constraint was established during the preliminary model specification phase by initially treating both the intercept and slope terms as random. In cases were convergence could not be achieved, the model specification was changed by defining the intercept as fixed and the slope as random and vice versa. Overall, the results indicated that (1) convergence could not be achieved when both terms were treated as random irrespective of the relationship, (2) convergence could not be achieved when the intercept term was treated as fixed and the slope was treated as random for all relationships but that for wood density, and (3) convergence for all relationships was only achieved when the slope was treated as fixed and the intercept term was treated as random. These statistical results were used to inform the selection of the final model specifications (i.e., Equations (5a) and (5b)) and hence were considered the most applicable for the sample population used.

2.6. Goodness-of-fit, Lack-of-fit, and Predictive Ability of Fitted Models

The parameterized models were evaluated based on goodness-of-fit, lack-of-fit, and predictive ability employing the validation data subset. More specifically, the proportion of variability in the dependent variable (kth attribute) explained by the parameterized model as measured by the index-of-fit squared statistic ($I^2_{(k)}$), was used as a goodness-of-fit metric (Equation (6)). Parameterized relationships which had mean absolute bias ($\overline{B}_{a(k)}$; Equation (7)) or mean relative bias ($\overline{B}_{r(k)}$; Equation (8)) that were significantly ($p \leq 0.05$) different from zero as determined through the use of the 95% confidence intervals (Equation (9)), where considered as demonstrating a consequential lack-of-fit. The linear regression relationship between the observed and predicted values was employed as a secondary lack-of-fit measure in terms of detecting systematic bias (sensu [31]). Based on Reynolds [32] statistical framework in combination with Gribko and Waint [33] SAS macro program extension, prediction and tolerance intervals for absolute and relative error where used to quantify the predictive accuracy of the parameterized relationships (Equations (10) and (11), respectively).

$$I^2_{(k)} = 1 - \frac{\sum_{l=1}^{n_{(k)}} \left(V_{(k)_l} - \hat{V}_{(k)_l} \right)^2}{\sum_{l=1}^{n_{(k)}} \left(V_{(k)_l} - \overline{V}_{(k)_\cdot} \right)^2} \tag{6}$$

$$\overline{B}_{a(k)} = \frac{\sum_{l=1}^{n_{(k)}} \left(V_{(k)_l} - \hat{V}_{(k)_l} \right)}{\sum_{l=1}^{n_{(k)}} l} \quad (7)$$

$$\overline{B}_{r(k)} = \frac{\sum_{l=1}^{n_{(k)}} 100 \frac{\left(V_{(k)_l} - \hat{V}_{(k)_l} \right)}{V_{(k)_l}}}{\sum_{l=1}^{n_{(k)}} l} \quad (8)$$

$$\overline{B}_{a,r(k)} \pm \frac{S_{a,r(k)} \cdot t_{(n_{(k)}-1,0.975)}}{\sqrt{n_{(k)}}} \quad (9)$$

$$\overline{B}_{a,r(k)} \pm \sqrt{1/n_{(k)} + 1/n_p} \cdot S_{a,r(k)} \cdot t_{(n_{(k)}-1,0.975)} \quad (10)$$

$$\overline{B}_{a,r(k)} \pm g(\lambda, n_{(k)}, P') \cdot S_{a,r(k)} \quad (11)$$

where $V_{(k)_l}$ and $\hat{V}_{(k)_l}$ are the observed and predicted values, respectively, for the kth attribute within the lth sample log belonging to the validation data subset, $n_{(k)}$ is the number of predicted-observed pairs specific to the kth attribute within the validation data subset, $S_{a,r(k)}$ is the standard deviation of the absolute ($S_{a(k)}$) or relative ($S_{r(k)}$) biases specific to the kth attribute, respectively, $t_{(n_{(k)}-1,0.975)}$ is the 0.975 quantile of the t-distribution with $n_{(k)} - 1$ degrees of freedom specific to the kth attribute, n_p is the number of future predictions under evaluation (n_p = 1; individual log level), and g is a normal distribution tolerance factor specifying the probability (λ; i.e., 0.05) that a specified minimum proportion (i.e., 95%) of the distribution of errors (P') will be contained within the stated tolerance interval.

2.7. Predictive Performance when Deploying Acoustic-Derived Wood Density Estimates

Given the practical reality of not having access to Silviscan-equivalent wood density estimates when acoustic sampling, necessitated the evaluation of the density-weighted acoustic relationships when a surrogate acoustic-derived w_d estimate is used. Procedurally, this involved (1) generating a density estimate for each log within the validation data subset utilizing the parameterized wood density prediction model in combination with the acoustic velocity measurement, (2) given (1), deploying the resultant density estimate along with its acoustic velocity measurement to generate attribute predictions for each of the successfully parameterized models, and (3) using the observed and predicted values to calculate (i) mean absolute and relative biases along with associated 95% confidence intervals, and (ii) prediction and tolerance error intervals. The computations used to generate the mean absolute and relative biases and associated confidence intervals, and the prediction and tolerance error intervals, are similar to those described above (i.e., Section 2.6; Equations (7)–(11)).

3. Results

3.1. Attribute—Acoustic Velocity Relationships: Parameter Estimates, Regression Statistics and Tenability of Associated Assumptions

The resultant parameter estimates, regression statistics and validation metrics for assessing compliance with underlying assumptions for the attribute-specific acoustic velocity relationships, as described by the mixed-effects model specifications (Equation (5)), are given in Table 7. The successful parameterization of 6 out of the 8 relationships assessed (m_e, w_t, m_a, c_o, s_a = $f\left(\hat{\gamma}_{0,1}, w_d v_l^2\right)$ and $w_d = f\left(\hat{\gamma}_{0,1}, v_l^2\right)$) in terms of the (1) statistical significance of the parameter estimates and random effect term, (2) proportion of variability in the dependent variables explained (I^2), and (3) compliance with the independence and constant variance assumptions underlying the parameterization approach used, as assessed by the degree of spatial correlation among adjacent level

one residuals employing regression analysis and Park's homogeneity of variance test [30], respectively, confirmed the applicability of the chosen mixed-effects regression specification in quantifying the attribute—acoustic velocity relationships for jack pine.

Table 7. Attribute-specific regression results for the mixed-effects model specification (Equation (5)): parameter estimates, regression statistics and compliance indicators.

Relationship	Parameter Estimates [a]		Regression Statistics and Compliance Indices				
	$\hat{\gamma}_0$	$\hat{\gamma}_1$	Degrees of Freedom [b] (n_{reg}, n_{res})	I^2 [c]	Random Effects [d]	Homogeneity of Variance [e]	Spatial Correlation [f]
$m_e - w_d v_l^2$	6.5439	0.001194	1, 120	0.466	*	H_0	H_0
$w_d - v_l^2$	321.6483	7.7201	1, 120	0.315	*	H_0	H_0
$m_a - w_d v_l^2$	15.0699	−0.00063	1, 120	0.079	*	H_0	H_0
$w_t - w_d v_l^2$	1.8190	0.000150	1, 120	0.603	*	H_0	H_0
$d_r - w_d v_l^2$	30.6445	-0.000037^{ns}	1, 120	-	-	-	-
$d_t - w_d v_l^2$	28.2502	-0.000048^{ns}	1, 120	-	-	-	-
$c_o - w_d v_l^2$	300.0200	0.017790	1, 120	0.456	*	H_0	H_0
$s_a - w_d v_l^2$	388.1280	−0.012724	1, 120	0.497	*	H_0	H_0

[a] $\hat{\gamma}_0$ is a random effect intercept parameter estimate specific to the kth attribute and $\hat{\gamma}_1$ is fixed effect slope parameter estimate specific to the kth attribute. Note, parameter estimates not significantly ($p > 0.05$) different from zero are superscripted by ns. [b] Degrees of freedom for regression (n_{reg}) and residual error (n_{res}). [c] I^2 is the index-of-fit squared (Equation (6)). [d] Non-significant ($p > 0.05$) and significant ($p \leq 0.05$) random effects are denoted ns and *, respectively (i.e., testing the null hypothesis that $u_0 = 0$ versus the alternative hypothesis $u_0 \neq 0$ in Equation (5)). [e] Non-rejection and rejection of the constant variance assumption at the 0.01 probability level are denoted H_0 and H_1, respectively, as determined from Park's test for homoscedasticity (see text for details). [f] Non-rejection and rejection of the independence assumption (spatially uncorrelated residuals) at the 0.01 probability level are denoted H_0 and H_1, respectively, as determined from the residual regression approach ([30]; see text for details).

Specifically, for these fitted relationships, the intercept and slope parameter estimates and the random effect terms were significantly ($p \leq 0.05$) different from zero, and the percentage of variation explained varied from a relatively low minimum value of 8% for m_a to a relatively moderate maximum value of 60% for w_t. The values for the remaining relationships ordered by magnitude of I^2, were as follows: 32% for w_d, 46% for c_o, 47% for m_e and 50% for s_a. The lack of significant ($p \leq 0.01$) regression relationships among adjacent residuals for the log pairs derived from the same sample trees were indicative of the absence of spatial correlation effects (sensu [29]). Furthermore, the constant variance assumption was not rejected given the results of Park's test for homoscedasticity along with the interpretation of the Bayes residual error—predictor bivariate scatterplots. Note, during the initial parameterizations, examination of the circular-shape data point clusters within the residual error—predictor scatterplots, did reveal the presence of 2 potential outliers or influential observations (i.e., these observational pairs were visually apart from the concentrated residual cloud within the scatterplots for attributes m_e, w_d, m_a, w_t, c_o, and s_a). Thus a review of the field records and laboratory procedures in terms of identifying possible data recording errors, compiling errors or incorrect processing procedures for these suspect data pairs was implemented. Additionally, the attribute values for the other logs sampled from the suspect trees were also examined. Although this inquiry revealed the absence of recording or processing errors, the measurements for the suspect log within the calibration data subset and another one from the same sample tree but within the validation data subset, were substantially different from the measurements for the other logs within their respective data subsets. Based on the acknowledgment that these attributes may be occasionally influenced by uncontrollable and largely undetectable sources of variation such as complex internal knot distributions within logs, it was concluded that these suspect observations should be removed. Consequently, the calibration and validation data subsets were reduced by one observational pair each yielding a final total of 121 and 120 attribute-specific—acoustic velocity observational pairs within calibration and validation data subsets, respectively.

The attribute—acoustic velocity observational pairs within the calibration data subset for each of the 8 relationships evaluated are presented in Figure 1A,B. The successfully parameterized models are also superimposed on the observational pairs where applicable. Examination of the subgraphs for the attributes that were not successfully parameterized by the mixed-effects model specification (i.e., d_r and d_t; Table 7), reinforced the lack of a functional relationship between each of these attributes and density-weighted acoustic velocity: i.e., random cloud of the d_r–$w_d v_l^2$ and d_t–$w_d v_l^2$ observational pairs that were devoid of any obvious linear or nonlinear relationship. Conversely, for the attributes that were successfully parameterized by the mixed-effects model specification (i.e., m_e, m_a, w_d, w_t, c_o, and s_a; Table 7) which are superimposed on their respective subgraphs confirmed the statistical findings (i.e., relationships were unbiased and in accord with the m_e–$w_d v_l^2$, w_d–v_l^2, m_a–$w_d v_l^2$, w_t–$w_d v_l^2$, c_o–$w_d v_l^2$ and s_a–$w_d v_l^2$ linear trends).

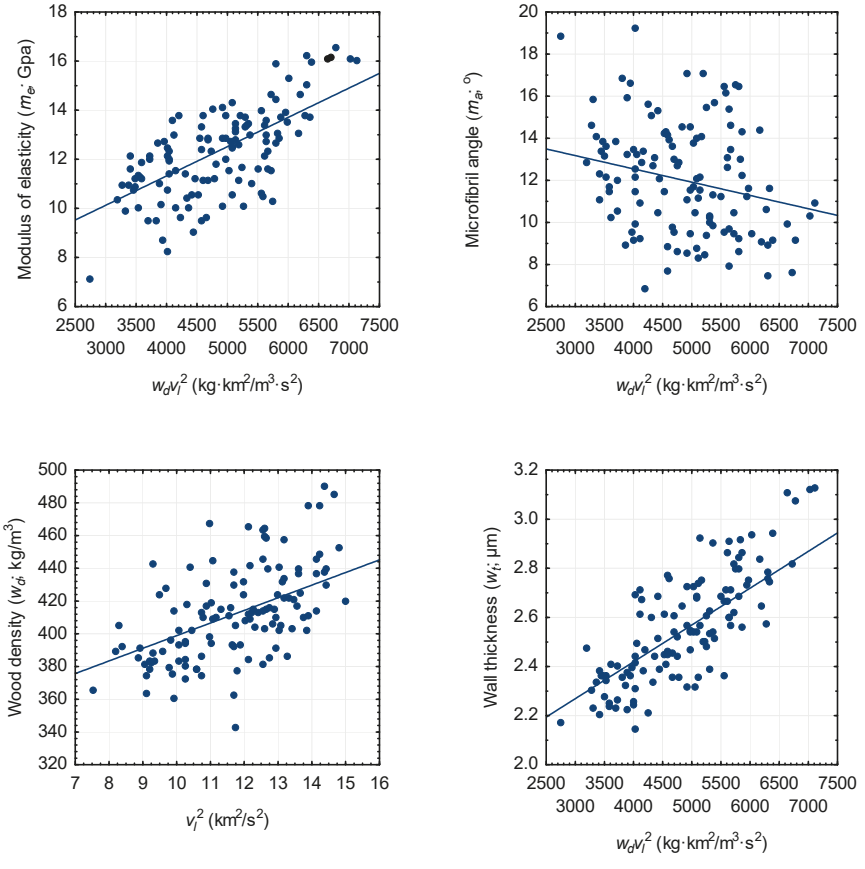

(**A**)

Figure 1. *Cont.*

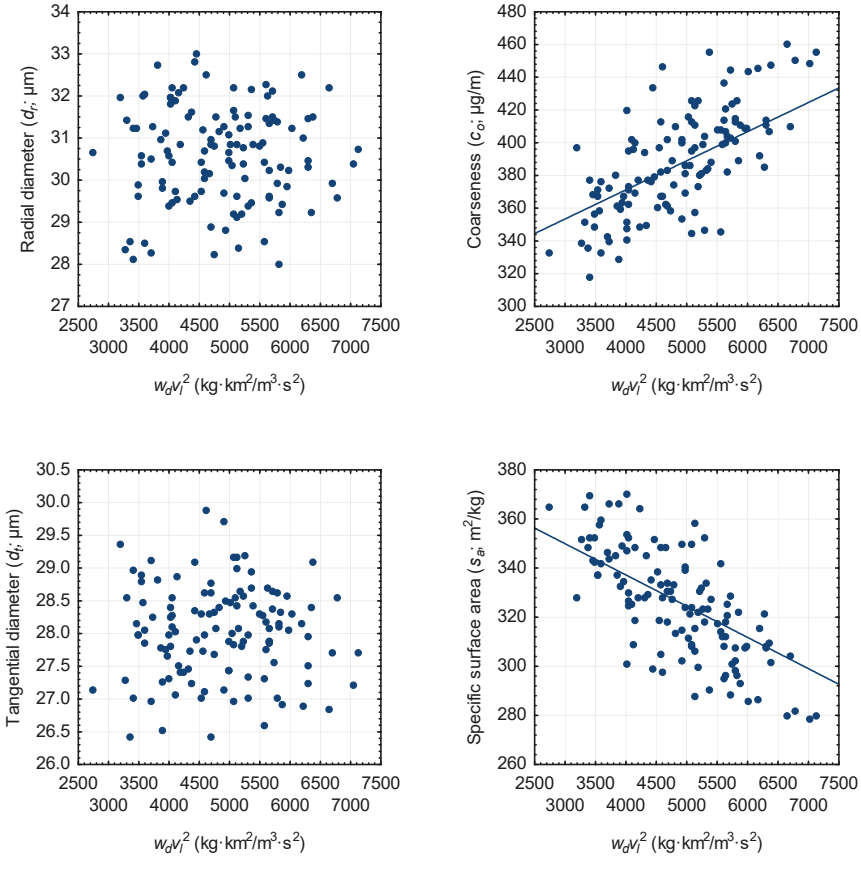

(**B**)

Figure 1. Scatterplots illustrating the relationship between each attribute and density-weighted and density-unweighted acoustic velocity (v_l) for the jack pine logs within the calibration data subset: (**A**) $m_e = f(w_d v_l^2)$, $w_d = f(v_l^2)$, $m_a = f(w_d v_l^2)$, and $w_t = f(w_d v_l^2)$ relationships; and (**B**) $d_r = f(w_d v_l^2)$, $d_t = f(w_d v_l^2)$, and $c_o = f(w_d v_l^2)$ and $s_a = f(w_d v_l^2)$ relationships. The parameterized model is denoted by solid line (Table 7).

3.2. Goodness-of-fit and Lack-of-fit Assessment

The goodness-of-fit evaluation consisted of assessing the magnitude of the variability explained by the parameterized models when applied to the validation data subset. Specifically, the I^2 statistic was calculated for the acoustic-based m_e, w_d, m_a, w_t, c_o and s_a mixed-effects models (Table 8). Results indicated that the models explained a relatively low to moderate level variation (ordered by magnitude): 8% for m_a, 30% for w_d, 43% for c_o, 44% for s_a, 53% for m_e and 58% for w_t. In agreement with expectation, the values for 5 of 6 attributes were slightly less than those observed for the relationships parameterized using the calibration data subset (cf. Table 7 versus Table 8). The exception being that of the result for m_e which was slightly greater than that derived from the calibration data subset. Based on the regression results for the linear relationship between the observed and predicted values, there was insufficient evidence to indicate systematic lack-of-fit for any of the 6 parameterized relationships: i.e., intercept and slope values were not significant ($p > 0.01$) different from zero and unity, respectively

(sensu [31]). Similarly, based on the mean absolute biases and their associated 95% confidence intervals, there was no evidence of lack-of-fit for any of the 6 relationships (Table 8): mean absolute biases were not significantly ($p \leq 0.05$) different from zero as inferred from the 95% confidence intervals. Although approximately equivalent results were obtained when assessing lack-of-fit using mean relative biases, the mean relative bias generated for the m_a relationship was significantly ($p \leq 0.05$) different from zero (Table 8).

The density-weighed and density-unweighted acoustic velocity—attribute observational pairs within the validation data subset for each of the relationships including those that did not exhibit a significant relationship with acoustic velocity, are graphically presented in Figure 2A,B. The parameterized mixed-effects regression relationships derived using the calibration data subset were also superimposed on the m_e, w_d, m_a, w_t, c_o and s_a subgraphs. It was visually evident that the parameterized relationships were representative of the linear trends between the m_e–$w_d v_l^2$, w_d–v_l^2, m_a–$w_d v_l^2$, w_t–$w_d v_l^2$, c_o–$w_d v_l^2$ and s_a–$w_d v_l^2$ observational pairs. The general concordance between the linear trends exhibited by the observational pairs and that established by the regressions, were also suggestive of the absence of systematic bias. For the attributes that were not successfully described by the mixed-effects model specification (i.e., d_r and d_t; Table 7), an examination of the subgraphs reconfirmed the statistical result, that is, there was a random scatter of d_r–$w_d v_l^2$ and d_t–$w_d v_l^2$ observational pairs devoid of discernable linear or nonlinear trends.

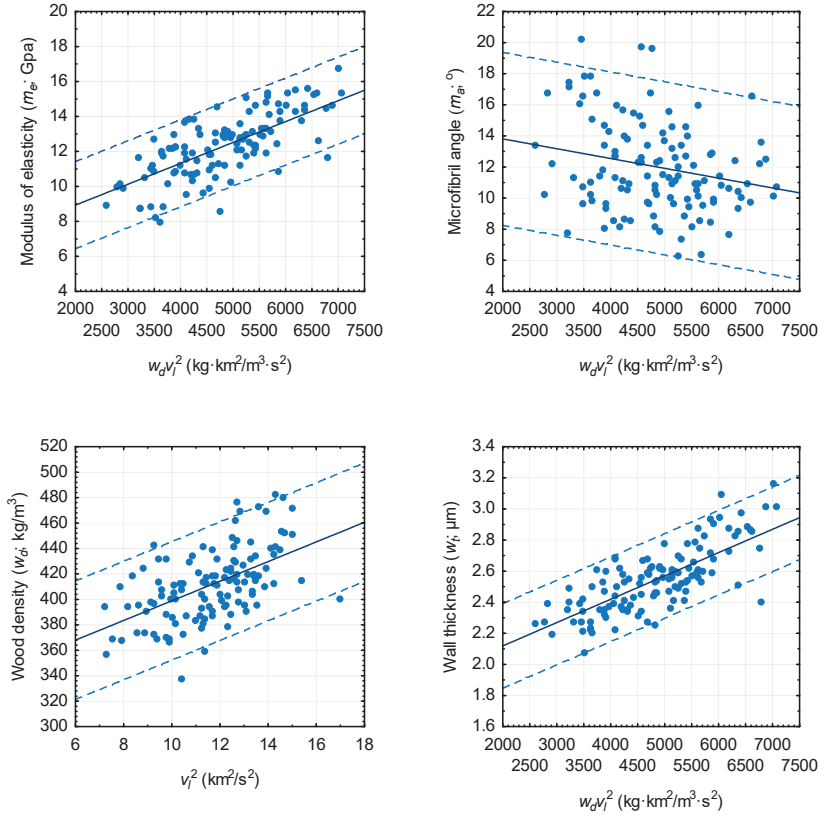

(A)

Figure 2. *Cont.*

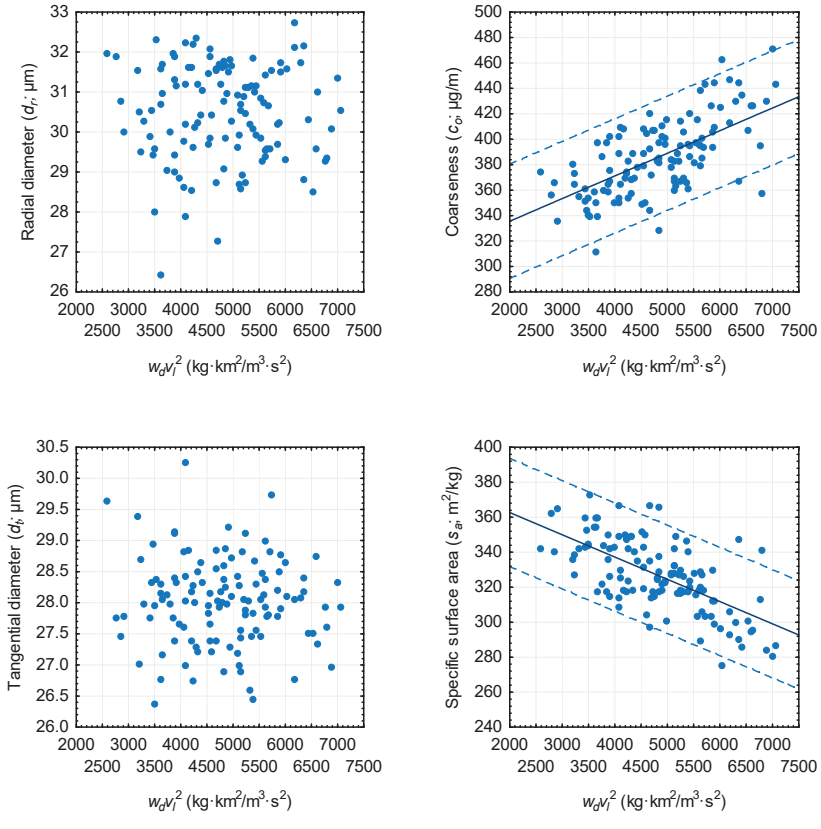

(**B**)

Figure 2. Scatterplots illustrating the relationship between each attribute and density-weighted and density-unweighted acoustic velocity (v_l) for the jack pine logs within the validation data subset: (**A**) $m_e = f(w_d v_l^2)$, $w_d = f(v_l^2)$, $m_a = f(w_d v_l^2)$, and $w_t = f(w_d v_l^2)$ relationships; and (**B**) $d_r = f(w_d v_l^2)$, $d_t = f(w_d v_l^2)$, and $c_o = f(w_d v_l^2)$ and $s_a = f(w_d v_l^2)$ relationships. Note, where applicable, the superimposed parameterized model is denoted by solid line (Table 7) and superimposed contextual 95% prediction error limits are denoted by the parallel dashed lines.

Table 8. Evaluation metrics for the parameterized models: goodness-of-fit, lack-of-fit statistics and predictive ability metrics.

Relationship	Goodness-of-fit Statistic	Hypotheses [b]		Lack-of-fit Measures Absolute [c]		Relative [c] (%)		Predictive Ability: 95% Error Intervals [d] Prediction		Tolerance	
	I^2 [a]	α_0=0	α_1=1	Mean Bias	95% CL	Mean Bias	95% CL	Absolute 95% CL	Relative (%) 95% CL	Absolute 95% CL	Relative (%) 95% CL
$m_e - w_d v_l^2$	0.526	H_0	H_0	−0.031	±0.226	0.986	±2.049	±2.489	±22.543	±2.759	±24.993
$w_d - v_l^2$	0.304	H_0	H_0	−0.125	±4.232	0.292	±1.028	±46.550	±11.306	±51.610	±12.535
$m_a - w_d v_l^2$	0.075	H_0	H_0	0.050	±0.506	5.998 *	±4.553	±5.565	±50.087	±6.170	±55.531
$w_t - w_d v_l^2$	0.583	H_0	H_0	0.004	±0.025	0.151	±0.971	±0.272	±10.679	±0.301	±11.840
$c_o - w_d v_l^2$	0.426	H_0	H_0	−0.399	±4.082	0.250	±1.070	±44.903	±11.764	±49.784	±13.043
$s_a - w_d v_l^2$	0.438	H_0	H_0	0.224	±2.812	0.305	±0.861	±30.937	±9.468	±34.299	±10.497

[a] I^2 is the index-of-fit squared (Equation (6)). [b] Testing the (1) null hypothesis that $\alpha_0 = 0$ versus the alternative hypothesis $\alpha_0 \neq 0$ where H_0 and H_1 denote the non-rejection and rejection of the null hypothesis at the 0.05 probability level, and (2) null hypothesis that $\alpha_1 = 1$ versus the alternative hypothesis $\alpha_1 \neq 1$ where H_0 and H_1 denote the non-rejection and rejection of the null hypothesis at the 0.05 probability level, where α_0 and α_1 are derived from the simple linear ordinary least squares regression relationship between observed (y) and predicted (x) values ($y = \alpha_0 + \alpha_1 x + \varepsilon$ where ε is an error term [31]). [c] Mean absolute (Equation (7)) and relative (Equation (8)) bias and the limits (CL) of the associated 95% confidence interval (Equation (9)) where mean values not significantly ($p > 0.05$) different from zero were indicative of an unbiased relationship (i.e., mean bias ± 95% confidence limits (CL)); note, underlined CL values denote approximations given the presence of significant ($p \leq 0.05$) non-normality within the underlying error distribution; absolute error units are attribute-specific: GPa, kg/m^3, μm, μg/m and m^2/kg for m_e, w_d, m_a, w_t, c_o and s_a, respectively. [d] CL for the 95% prediction and tolerance error intervals for absolute and relative errors (Equations (10) and (11), respectively): mean bias ± 95% CL; specifically, there is a 95% probability that a future error will be within the stated prediction interval and that there is a 95% probability that 95% of all future errors will be within the stated tolerance interval [32,33]; note, underlined CL values denote approximations given the presence of significant ($p \leq 0.05$) non-normality within the underlying error distribution.

3.3. Predictive Ability

The predictive ability of the successfully parameterized mixed-effects models was quantified via the use of prediction and tolerance error intervals (Equations (9) and (10), respectively): mean bias ± 95% confidence limit. The intervals were generated from the absolute and relative bias values generated from the validation data subset. Statistically, these error intervals attempt to quantify the performance of the models when they are actually deployed [32]. Specifically, the prediction intervals quantify the boundaries of the expected range of absolute and relative errors when applying the models for a newly sampled jack pine log (e.g., there is 95% probability that the future error will be within the stated prediction interval). The tolerance intervals quantify the boundaries of the range of the expected population of absolute and relative errors which would be generated from the models when repeatedly deploying them to newly sampled jack pine log populations (e.g., there is 95% probability that 95% of all future errors will fall within the stated tolerance interval).

Accordingly, there is a 95% probability that a future error associated with a m_e, w_d, m_a, w_t, c_o or s_a prediction for a newly sampled jack pine log would be expected to fall within the following absolute and relative intervals (Table 8): (1) $-2.5 \leq m_e$ error (GPa) ≤ 2.5; $-46.7 \leq w_d$ error (kg/m^3) ≤ 46.4; $-5.5 \leq m_a$ error (°) ≤ 5.6; $-0.3 \leq w_t$ error (μm) ≤ 0.3; $-45.3 \leq c_o$ error (μg/m) ≤ 44.5; and $-30.7 \leq s_a$ error (m^2/kg) ≤ 31.2; and (2) $-21.6 \leq m_e$ error (%) ≤ 23.5; $-11.0 \leq w_d$ error (%) ≤ 11.6; $-44.1 \leq m_a$ error (%) ≤ 56.1; $-10.5 \leq w_t$ error (%) ≤ 10.8; $-11.5 \leq c_o$ error (%) ≤ 12.0; and $-9.2 \leq s_a$ error (%) ≤ 9.8. Similarly, based on the tolerance error intervals as presented in Table 8, there is a 95% probability that 95% of all future errors generated from the m_e, w_d, m_a, w_t, c_o and s_a models would fall within the following absolute and relative intervals: (1) $-2.8 \leq m_e$ error (GPa) ≤ 2.7; $-51.7 \leq w_d$ error (kg/m^3) ≤ 51.5; $-6.1 \leq m_a$ error (°) ≤ 6.2; $-0.3 \leq w_t$ error (μm) ≤ 0.3; $-50.2 \leq c_o$ error (μg/m) ≤ 49.4; and $-34.1 \leq s_a$ error (m^2/kg) ≤ 34.5; and (2) $-24.0 \leq m_e$ error (%) ≤ 26.0; $-12.2 \leq w_d$ error (%) ≤ 12.8; $-49.5 \leq m_a$ error (%) ≤ 61.5; $11.7 \leq w_t$ error (%) ≤ 12.0; $-12.8 \leq c_o$ error (%) ≤ 13.3; and $-10.2 \leq s_a$ error (%) ≤ 10.8. Although these intervals also reveal that the parameterized equations would generate unbiased predictions, the level of predictive accuracy attained would vary widely among the attributes (e.g., $s_a > w_t > w_d > c_o >> m_e >>> m_a$ based on the width of relative error tolerance intervals).

3.4. Predictive Performance of Parameterized Models When Deploying Acoustic Generated Wood Density Estimates

Employing the validation data subset, the empirical performance of the density-weighted models in cases where an acoustic-based wood density estimate was used as a surrogate for a Silviscan-based density estimate, was also evaluated. Specifically, based on the functional expressions, m_e, m_a, w_t, c_o, $s_a = f\left(\hat{\gamma}_{0,1}, \hat{w}_d v_l^2\right)$ where $\hat{w}_d$ is derived from the $w_d = f\left(\hat{\gamma}_{0,1}, v_l^2\right)$ relationship, the following set of computations were carried out: (1) inputting the acoustic velocity measurement value for each log in the validation data subset into the parameterized w_d model (Table 7) and generating associated estimates for each attribute; and (2) given (1), treating these resultant attribute estimates as predicted values and the corresponding Silviscan-determined estimates as observed values, absolute and relative biases and associated 95% confidence, and 95% prediction and tolerance intervals, were calculated via the deployment of the computational structure given by Equations (7)–(11).

Upon review of the resulting predictive performance metrics as provided in Table 9, lack-of-fit issues were non-concerning for either of the error measures: 95% confidence intervals indicated that the mean absolute and relative biases were not significantly ($p \leq 0.05$) different from zero. Numerically, the magnitude of error generated when estimating m_e, m_a, w_t, c_o and s_a for a newly sampled jack pine log deploying the acoustic-based density estimate, would be captured within the following absolute and relative prediction error intervals: (1) $-2.8 \leq m_e$ error (GPa) ≤ 2.7; $-5.5 \leq m_a$ error (°) ≤ 5.6; $-0.3 \leq w_t$ error (μm) ≤ 0.3; $-51.8 \leq c_o$ error (μg/m) ≤ 50.9; and $-36.5 \leq s_a$ error (m^2/kg) ≤ 37.0; and (2) $-23.5 \leq m_e$ error (%) ≤ 25.8; $-43.7 \leq m_a$ error (%) ≤ 55.7; $-10.5 \leq w_t$ error (%) ≤ 10.8; $-13.1 \leq c_o$ error (%) ≤ 13.7; and $-10.9 \leq s_a$ error (%) ≤ 11.7. Similarly, the corresponding 95%

tolerance intervals for which 95% of all future errors would be expected to be captured are delineated as follows: (1) $-3.1 \leq m_e$ error (GPa) ≤ 3.0; $-6.1 \leq m_a$ error (°) ≤ 6.2; $-0.3 \leq w_t$ error (μm) ≤ 0.3; $-57.4 \leq c_o$ error (μg/m) ≤ 56.5; and $-40.5 \leq s_a$ error (m^2/kg) ≤ 41.0; and (2) $-26.2 \leq m_e$ error (%) ≤ 28.4; $-49.1 \leq m_a$ error (%) ≤ 61.1; $-11.7 \leq w_t$ error (%) ≤ 12.0; $-14.6 \leq c_o$ error (%) ≤ 15.2; and $-12.2 \leq s_a$ error (%) ≤ 12.9. In summary, these results suggest that the attribute prediction models in which an acoustic-based wood density estimate is deployed, would yield unbiased predictions which would be slightly less precise than that attained when using a Silviscan-derived or equivalent density estimate, and would exhibit a similar among-attribute performance ranking (cf. Table 8 versus Table 9).

4. Discussion

4.1. Hierarchical Mixed-Effects Acoustic-Based Attribute Prediction Models for Jack Pine

The mixed-effects linear model for the primary relationship between the dynamic modulus of elasticity and density-weighted acoustic velocity ($m_e = f\left(\hat{\gamma}_{0,1}, w_d v_l^2\right)$) explained 47% of the variation in the m_e for the logs within the calibration data subset (Table 7) and 53% of the variation in the m_e for the logs within the validation data subset (Table 8). Based on the logs within the validation data subset, the model generated unbiased predictions when assessed using both absolute and relative error measures. The tolerance intervals indicated that 95% of the absolute and relative errors generated from repeatedly applying the parameterized model to a new sample population of jack pine logs would be expected (95% probability level) not to exceed ±2.8 GPa and ±25.0% respectively, when using Silviscan-equivalent w_d estimate (Table 8). For the deployment scenario in which an acoustic-based wood density estimate is employed as a surrogate measure for its Silviscan-based counterpart, the model's predictions would be similarly unbiased (Table 9). However, the predictions would be less precise as evident from the wider tolerance intervals for absolute and relative error that were generated when using the acoustic-based density estimate (i.e., 95% tolerance limits for error of ±3.1 GPa and ±27.3%, respectively; Table 9). Newton [15] reported slightly better results in a similarly structured analysis of red pine logs in terms of explanatory power (e.g., explaining 71% of variation in m_e for red pine logs versus 50% of variation in m_e for jack pine logs) and precision of predictions when deploying either a Silviscan-equivalent estimate of wood density (e.g., relative tolerance error intervals of ±19% for red pine versus ± 25% for jack pine) or acoustic-based estimate (e.g., relative tolerance error intervals of ±19% for red pine versus ± 27% for jack pine).

The results for the mixed-effects linear regression model for the relationship between wood density and acoustic velocity ($w_d = f\left(\hat{\gamma}_{0,1}, v_l^2\right)$), revealed that the parameterized model generated unbiased predictions (Tables 7 and 8). Overall, however, the model performed moderately in terms of (1) explanatory power given that only 32% and 31% of the w_d variation for the logs within the calibration and validation data subsets, respectively, was explained (Tables 7 and 8), and (2) predictive performance given that 95% of absolute and relative errors generated from repeatedly applying the equation to a new sample population of logs would be expected (95% probability level) not to exceed ±51.6 kg/m^3 or ±12.5%, respectively (Table 8). Considerably better results were reported previously for red pine logs [15] in terms of explanatory power (e.g., explaining 80% of variation in w_d for red pine logs versus 31% of variation in w_d for jack pine logs). However, differences in the precision of the predictions were only marginally better (e.g., relative tolerance error intervals of ±10% for red pine versus ± 13% for jack pine).

Table 9. Predictive performance of parameterized models when deploying acoustic-based wood density estimates.

Relationship	Lack-of-fit Measures [a]				Predictive Ability: 95% Error Intervals [b]			
	Absolute		Relative (%)		Prediction (Stand-Level)		Tolerance	
	Mean bias	95% CL [e]	Mean bias	95% CL	Absolute 95% CL	Relative (%) 95% CL	Absolute [b] 95% CL	Relative (%) 95% CL
$m_e - w_d v_l^2$	−0.033	±0.251	1.118	±2.240	±2.756 (±0.562)	±24.640 (±5.028)	±3.055	±27.318
$m_a - w_d v_l^2$	0.051	±0.505	6.000 *	±4.522	±5.554 (±1.129)	±49.738 (±10.111)	±6.158	±55.144
$w_t - w_d v_l^2$	−0.004	±0.025	0.151	±0.971	±0.272 (±0.055)	±10.679 (±2.171)	±0.301	±11.840
$c_o - w_d v_l^2$	−0.440	±4.671	0.300	±1.219	±51.383 (±10.445)	±13.406 (±2.725)	±56.968	±14.863
$s_a - w_d v_l^2$	0.253	±3.340	0.369	±1.027	±36.734 (±7.467)	±11.291 (±2.295)	±40.727	±12.519

[a] Mean absolute (Equation (7)) and relative (Equation (8)) bias and the limits (CL) of the associated 95% confidence interval (Equation (9)) where mean values not significantly ($p > 0.05$) different from zero were indicative of an unbiased relationship; note, underlined CL values denote approximations given the presence of significant ($p \leq 0.05$) non-normality within the underlying error distribution; absolute error units are attribute-specific: GPa, °, µm, µg/m and m^2/kg for m_e, m_a, w_t, c_o and s_a, respectively; and * denotes significant bias. [b] Confidence limits for the 95% prediction and tolerance error intervals for absolute and relative errors (Equations (10) and (11), respectively): mean bias ± 95% CL; specifically, there is a 95% probability that a future error will be within the stated prediction interval and that there is a 95% probability that 95% of all future errors will be within the stated tolerance interval (sensu [32]); notes, (1) absolute error units are attribute-specific as stated above, (2) underlined CL values denote approximations given the presence of significant ($p \leq 0.05$) non-normality within the underlying error distribution, and (3) stand-level CL intervals denote the 95% prediction limits for the mean error generated when group sampling (e.g., assigning a mean attribute estimate to 30-log sample (pile) derived from a single stand).

Although the results for the relationship where microfibril angle is expressed as a function of density-weighted acoustic velocity ($m_a = f(\hat{\gamma}_{0,1}, w_d v_l^2)$) generated unbiased predictions (Tables 7 and 8), the parameterized model exhibited a low level of explanatory power and a relatively high degree of imprecision. Specifically, the model only explained 8% of the variation in m_a for the logs within both the calibration and validation data subsets, respectively (Tables 7 and 8). The predictive intervals indicated that 95% of absolute and relative errors generated from repeatedly applying the equation to a new sample population of logs would be expected (95% probability level) not to exceed (1) ±6.2 ° and ±55.5%, respectively, when using Silviscan-equivalent w_d estimates (Table 8), and (2) ±6.2 ° and ±55.1%, respectively, when deploying acoustic-based wood density estimates. Although these weak results are superior to those obtained previously for red pine logs in which no viable acoustic-based relationship was found for microfibril angle [15], the results are inferior to the level of variation described by the acoustic-based relationship reported in other studies (e.g., 86% for radiata pine logs [6]).

The relationship for cell wall thickness ($w_t = f(\hat{\gamma}_{0,1}, w_d v_l^2)$) exhibited the highest levels of explanatory power as evident from the level of variation explained: 60% and 58% for the calibration and validation data subsets, respectively (Tables 7 and 8). Furthermore, the parameterized model exhibited no lack-of-fit issues and produced unbiased predictions at a relatively high level of precision. Specifically, 95% of absolute and relative errors generated from repeatedly applying the equation to a new sample population of jack pine logs would be expected (95% probability level) to not exceed ±0.3 µm and ±11.8%, respectively, when using Silviscan-equivalent or acoustic generated w_d estimates (Tables 8 and 9). Newton [15] reported a superior result for red pine logs in terms of explanatory power (e.g., explaining 90% of variation in w_t for red pine logs versus 59% of variation in w_t for jack pine logs), but much less so in terms of predictive precision. For example, relative tolerance error intervals of ±9% for red pine versus ±12% for jack pine when deploying a Silviscan-equivalent estimate of wood density, and ±12% for red pine versus ±12% for jack pine when using an acoustic-based estimate. The graphical and statistical results for the relationships in which radial and tangential diameters were expressed as functions of density-weighted acoustic velocity, did not support the existence of viable relationships for these attributes. This result is similar to that obtained for red pine logs (i.e., [15]). Combining these regression results with the observed lack of linear associations exhibited in the

scatterplots (Figures 1 and 2 for jack pine logs; and Figures 1 and 2 for red pine logs in [15]), suggest that these attributes may be intrinsically unrelated to acoustic velocity for these species.

The regression relationships for fiber coarseness and specific surface area (c_o, $s_a = f\left(\hat{\gamma}_{0,1}, w_d v_l^2\right)$) exhibited moderate levels of explanatory power (Tables 7 and 8): (1) 46% and 43% of the variation in fiber coarseness was explained for the logs within the calibration and validation data subsets, respectively; and (2) 50% and 44% of the variation in specific surface area was explained for the logs within the calibration and validation data subsets, respectively. These parameterized models produced unbiased and relative precise predictions when compared with the other attribute models. For the fiber coarseness model, 95% of absolute and relative errors generated from repeatedly applying the parameterized equation to a new sample population of logs would be expected (95% probability level) not to exceed (1) $\pm$49.8 μg/m and $\pm$13.0%, respectively, when using Silviscan-equivalent wood density estimates (Table 8), and (2) $\pm$57.0 μg/m and $\pm$14.9%, respectively, when deploying acoustic-based wood density estimates (Table 9). Similarly, for the model developed for specific surface area, the corresponding precision limits for absolute and relative error were (1) $\pm$34.3 m^2/kg and $\pm$10.5%, respectively, when using Silviscan-equivalent wood density estimates (Table 8), and (2) $\pm$40.7 m^2/kg and $\pm$12.5%, respectively, when deploying acoustic-derived wood density estimates (Table 9).

In relation to acoustic-based prediction of fiber coarseness, Newton [15] reported much improved results for red pine logs in terms of explanatory power (e.g., explaining 81% of variation in c_o for red pine logs versus 44% of variation in c_o for jack pine logs) but again much less so in terms of predictive precision (e.g., relative tolerance error intervals of $\pm$12% for red pine versus $\pm$13% for jack pine when deploying a Silviscan-equivalent estimate of wood density, and $\pm$14% for red pine versus $\pm$15% for jack pine when using an acoustic-based estimate). In comparison of the model developed for predicting specific surface area for red pine logs, the result was considerably superior in terms of explanatory power (e.g., 84% of the variation in s_a explained for red pine logs versus 47% of the variation in s_a explained for jack pine logs). However, similar to the interspecies comparison of the coarseness model, the difference in predictive ability was minimal between the species: (1) relative tolerance error intervals of $\pm$8% for red pine versus $\pm$11% for jack pine when deploying a Silviscan-equivalent estimate of wood density, and (2) $\pm$10% for red pine versus $\pm$13% for jack pine when using an acoustic-based estimate.

4.2. Potential Utility of the Expanded Acoustic-Based Inferential Framework for Jack Pine

Estimation of the modulus of elasticity is of primary importance in log-segregation operations where the objective is to forecast the potential type and grade of extracted solid wood products (e.g., dimension lumber). However, other wood attributes (e.g., wood density, microfibril angle, tracheid dimensions) and derived composite metrics (e.g., fiber coarseness and specific surface area), are also prime determinates of end-product potential (sensu Table 1). Consequently, the expanded acoustic inferential framework presented in this study along with its empirical validation for six of the eight jack pine attributes examined (dynamic modulus of elasticity, wood density, microfibril angle, cell wall thickness, fiber coarseness and specific surface area), yields a more comprehensive system for non-destructive forecasting of end-product potential than systems based solely on wood stiffness (modulus of elasticity). Operationally, however, the in-forest deployment of the parameterized relationships will be largely dependent on the objectives and precision requirements of the end-user. For example, the relative error intervals were quite large for m_e and m_a as exemplified by the resultant tolerance errors of $\pm$25% and $\pm$56%, respectively, when using a Silviscan-equivalent wood density estimate (Table 8), and $\pm$27% and $\pm$55%, respectively, when using an acoustic-based wood density estimate (Table 9). Thus, the ability to stratify individual jack pine logs into narrow-grade class-based acoustic estimates of m_e and m_a would be difficult if not impossible. However, in situations for which the objective is to segregate groups of logs into end-product categories according to their average attribute values, then the magnitude of estimation error associated with the acoustic-based population

mean estimates may be more operationally acceptable. For example, the mean absolute and relative error to be expected when collectively sampling 30 new jack pine logs deploying an acoustic-based wood density estimate would be, respectively, 0.6 GPa and 5% for m_e, and 1° and 10% for m_a (Table 9).

Comparably, the relative tolerance error intervals for w_d, w_t, c_o and s_a were considerably less (i.e., errors in the order of ±10 to ±15% (Table 8)). Thus, depending on the specified width of the w_d, w_t, c_o and s_a intervals the end-user employs to designate logs into specific end-product categories or a binary grade class, differentiating logs according to these attribute predictions may be feasible. Similarly, at the stand-level where the objective is to classify a population of logs in a specific end-product category based on their mean w_d, w_t, c_o or s_a values, the precision of the estimates would be improved considerably. For example, the mean absolute and relative error to be expected when collectively sampling 30 new jack pine logs deploying an acoustic-based wood density estimate would be respectively, 0.1 μm and 2% for w_t, 10.4 μg/m and 3% for c_o, and 7.5 m^2/kg and 2% for s_a (Table 9).

More generally however, based on the explanatory power and precision of acoustic-based attribute prediction models developed to date, increasing the precision of the point-estimates derived from acoustic-based models will be required if they are to be used to stratify individual logs into grade categories given the relatively narrow range of static modulus of elasticity values that currently delineate product grade classes. For example, the mean difference between the 14 machine stress-rated (MSR) lumber grade categories established for Canadian softwood species [34] is approximately 0.7 GPa and hence the explicit stratification of individual logs into such narrow-width grade classes would not be possible given the empirical results to date. Even if it is assumed that the dynamic estimate is equivalent to its static counterpart which in turn is reflective of the actual end-product-based value, the precision of most acoustic-based estimates would be inadequate for stratifying logs into MSR-based classes (e.g., ±3 GPa expected error for individual jack pine logs; Table 9). Thus reducing the number of grade categories from 14 to a smaller number of discrete quality classes based on the expected prediction error range(s) through clustering, and (or) using multiple individual log estimates to generate a mean site, landing or log pile value, may represent a viable alternative when using the acoustic approach in log-segregation operations for jack pine.

Further research into analytical advancements that increase the amount of variability explained and decrease the standard error of estimate, possibly by including covariates within the acoustic-attribute model specification as suggested by Bérubé-Deschênes et al. [35] and Butler et al. [36], may be warranted. Acoustic velocity is known to be affected by a multitude of internal and external factors which includes knot distributions, embedded voids, environmental conditions during acoustic sampling (temperature and moisture conditions), tree size, local competition, and overall site conditions (e.g., [35,37,38]). Provision of operational solutions for minimizing these effects could improve the predictive accuracy of acoustic-based attribute estimation. Recent results examining the effect of xylem temperature and moisture on acoustic velocity within standing semi-mature jack pine trees during the vegetative growing season indicated that acoustic velocity declined in linear fashion with increasing temperature; however, moisture had no appreciable influence [39]. However, the temperature effect was not of consequential significance except when temperatures approached their seasonal extremities. Assuming similar inferences apply to jack pine logs, suggest that acoustic log samplers could treat such variation as a source of random error of minimal importance providing xylem temperatures did not approach their seasonal minimums (<5 °C) or maximums (>30 °C). In cases were temperature effects were of concern, the standardization equation for adjusting acoustic velocities to a reference xylem temperature of 20 °C could be deployed [39].

4.3. Similarities and Differences between Tree and Log Acoustic-Based Attribute Relationships

The time-of-flight acoustic approach to estimating the internal attributes within standing trees employs the dilatational stress wave velocity (v_d) which transverses the breast-height (1.3 m) region of the main stem [40]. This acoustic velocity measurement when weighted by wood density is also related to the modulus of elasticity as described by a functional specification, similar to that given by

Equation (1) (i.e., replacing v_l by v_d). This primary relationship for standing trees can be also potentially expanded to include a similarly structured suite of secondary relationships as that presented in this study for logs (e.g., [16]).

Conceptually, the resonance-based acoustic velocity approach is considered to yield a more representative estimate of the fiber attributes within the xylem tissue than those estimates derived from the time-of-flight approach. This is principally because the mean velocity estimate is derived from many acoustic pulses resonating longitudinally throughout the log rather than the velocity of a single wave front moving between two points within the main stem of a standing tree [41]. The empirical validity of this inference can be partially tested by assessing the differences between the tree and log acoustic-based attribute prediction models parameterized using the same sample tree population. Contrasting the results derived from a companion analysis which assessed the time-of-flight acoustic relationships deploying the same suite of attributes and sample tree population which were measured at the same time [42], revealed that the time-of-flight-based relationships were mostly superior in terms of explanatory power. Specifically, the percentage of attribute variation explained by the dilatational (tree) and longitudinal (log) acoustic relationships were respectively: 71% versus 50% for m_e; 30% versus 31% for w_d; 19% versus 8% for m_a; 66% versus 59% for w_t; 42% versus 44% for c_o; and 61% versus 47% for s_a. However, conversely, in terms of predictive precision, the comparison between the log and tree models revealed minimal differences. The error arising from using a newly sampled acoustic velocity measurement used to estimate m_e, w_d, m_a, w_t, c_o and s_a for standing trees and derived logs would be expected at the 95% confidence level to fall within the respective relative error limits of $\pm$25% versus $\pm$21% for m_e, $\pm$13% versus $\pm$14% for w_d, $\pm$56% versus $\pm$47% for m_a, $\pm$12% versus $\pm$11% for w_t, $\pm$13% versus $\pm$12% for c_o, and $\pm$10% versus $\pm$10% for s_a. These similarities in terms of the predictive performance between the tree and log-based acoustic approaches for estimating attributes within the same species (jack pine) while attaining contrasting results between species (jack pine versus red pine for a given time-of-flight- or resonance-based relationship), suggest that acoustic-based attribute relationships may be intrinsic to a given species irrespective of either of these wave types.

4.4. Advancing Acoustic-Based Attribute Estimation

The resonance-based acoustic approach to estimating internal fiber attributes within logs and associated demonstrations of its utility in segregation, allocation and merchandizing operations have been presented to the forest management community through various case studies (e.g., [41,43,44] and comprehensive literature reviews (e.g., [11,17]). These contributions have mostly focused on the merits of estimating the modulus of elasticity and using it, or its surrogates, to forecast end-product potential. These include (1) treating wood density as a constant and inferring wood stiffness indirectly from acoustic velocity (e.g., implicitly based on the underlying theoretical relationship expressed by Equation (1)), (2) estimating wood stiffness using parameterized regression models in which the dynamic modulus of elasticity is expressed as a function of acoustic velocity and wood density (e.g., explicitly based on the conceptual formulation (Equation (1)), and (3) directly forecasting wood stiffness using relationships that explicitly relate the static modulus of elasticity of a given end-product (e.g., measured using static bending tests of sawn boards) to acoustic velocity. This last approach while the most informative is also the least developed. Consequentially, the full potential of in-forest acoustic-based forecasting of end-product potential has not been fully realized. Determination and quantification of the explicit relationship between log-based acoustic velocity measures and actual performance-based metrics within the derived manufactured end-product are also required. Preliminary results from several studies in which the static modulus of elasticity within dimensional lumber products have been explicitly related to log-based acoustic velocity measures have been positive. These include statistically viable relationships reported for balsam fir (*Abies balsamea* (L.) Mill.) and white spruce (*Picea glauca* (Moench) Voss.) [45], radiata pine [46], Douglas fir ((*Pseudotsuga menziesii* (Mirb.) Franco) [47], and loblolly pine (*Pinus taeda* L.) [48].

Similarly, previous research has shown that several important performance metrics associated with pulp and paper end-products are also empirically related to acoustic velocity measurements taken on logs. Clark et al. [48] found that fiber length, pulp strength and various handsheet properties derived from radiate pine logs varied systematically with acoustic velocity. Bradley et al. [49] demonstrated that the variation in the pulp quality (freeness) for radiata pine logs could be considerably reduced by stratifying the logs according to their acoustic velocity values before processing. Although beyond the scope of this study, establishment of a broader range of more explicit relationships between log-based acoustic velocity measures and attribute-derived performance metrics within actual manufactured end-products, would be an area worthy of further investigation. As these past studies have shown, in-forest acoustic velocity stratification of log populations not only improves segregation efficiency at the time of harvest but also assists in reducing the variation in end-product quality during the manufacturing and merchandizing stages.

In-forest acoustic log grading has been increasingly used to compliment visual-based approaches in the pursuit of deriving economically efficient sorting networks. This remains an iterative and ongoing process in wood allocation decision-making where the objective is to increase operational efficiency within the upstream portion of the forest products supply chain (sensu [50]). Mechanized acoustic sampling has also advanced to the point where onboard resonance tools have been installed directly on harvesting machines where logs are immediately sorted upon bucking according to their end-product potential (e.g., [51]). Although these innovations have advanced the in-forest non-destructive approach to log grading and sorting, the acoustic approach has been largely limited to providing a single measure of internal wood quality, that being wood stiffness. Thus, the confirmatory empirical results presented in this study for jack pine and previous for red pine logs [15] are collectively supportive of an expanded acoustic-based inferential framework in which estimates for a multitude of end-product-based attribute determinates can be attained: e.g., wood density, microfibril angle, tracheid wall thickness, fiber coarseness, and specific surface area, in addition to the dynamic modulus of elasticity (wood stiffness). Although further research is required to fully realize the benefits of this empirical-based framework, the ability to non-destructively forecast a wide array of commercially relevant attributes could have consequential potential utility in advancing the acoustic approach in forest operations.

5. Conclusions

Given the wide spread occurrence of jack pine across the boreal landscape combined with the vast array of potential end-products it can produce, inclusive of solid wood products (e.g., dimensional lumber) and associated mill-work derivatives (window frames, doors, shelving, moldings, and paneling, and composite lumber products such as glulam-based beams, headers and heavy trusses and finger-jointed joists and rafters), and pulp-derived products such as paperboards, newsprint, facial tissues and specialized coated papers [52], the species has become the dominant feedstock species for numerous industrial conversion facilities. However, this diversity of end-products complicates in-forest segregation, allocation, and merchandizing decision-making. Hence the provision of enhanced operational intelligence arising from in-forest forecasts of end-product potential of harvested logs through non-destructive acoustic-based methods, may yield increased efficiencies within the upper portion of the jack pine forest products supply chain. Consequentially, the development and evaluation of a suite of acoustic-based models for predicting the principal attributes governing end-product potential for jack pine as presented in this study, represents an incremental contribution towards more informed decision-making. Specifically, deploying a mixed-effects linear modeling approach combined with cross-validation techniques, viable forecasting models for predicting the dynamic modulus of elasticity, wood density, microfibril angle, cell wall thickness, fiber coarseness and specific surface area were developed. Although these positive results confer additional empirical support for the proposed acoustic-based inferential framework, further research in the areas of accounting for environmentally induced wave variation, specifying

end-product-based design thresholds, and explicitly establishing linkages between log-based attribute estimates and those within recoverable end-products, would be beneficial. Collectively, the results presented here for jack pine not only provides the prerequisite parameterized relationships for improving in-forest segregation and allocation decision-making but also contributes to solidifying the empirical foundation of the expanded acoustic-based inferential framework.

Funding: Canadian Wood Fiber Centre, Canadian Forest Service, Natural Resources Canada.

Acknowledgments: The author expresses his appreciation to: (1) Mike Laporte (retired) of the Canadian Wood Fiber Centre, Canadian Forest Service (CFS), Natural Resources Canada (NRCan), and Gordon Brand of the Great Lakes Forestry Centre, CFS, NRCan for field and laboratory data acquisition support; (2) Dr. Tong and Ny Nelson at FPInnovations Inc., Vancouver, British Columbia, Canada, for completing the SilviScan-3 analysis, (3) Canadian Wood Fiber Centre, CFS, NRCan for fiscal support; and (4) anonymous journal reviewers for constructive and insightful comments and suggestions.

Conflicts of Interest: The author declares no conflict of interest.

References

1. Emmett, B. Increasing the value of our forest. *For. Chron.* **2006**, *82*, 3–4. [CrossRef]
2. Emmett, B. Perspectives on sustainable development and sustainability in the Canadian forest sector. *For. Chron.* **2006**, *82*, 40–43. [CrossRef]
3. Zhang, S.Y.; Chauret, G.; Ren, H.Q.; Desjardins, R. Impact of plantation black spruce initial spacing on lumber grade yield, bending properties and MSR yield. *Wood Fibre Sci.* **2002**, *34*, 460–475.
4. Tsehaye, A.; Buchanan, A.H.; Walker, J.C.F. Sorting of logs using acoustics. *Wood Sci. Technol.* **2000**, *34*, 337–344. [CrossRef]
5. Carter, P.; Briggs, D.; Ross, R.J.; Wang, X. Acoustic testing to enhance western forest values and meet customer wood quality needs. In *Productivity of Western Forests: A Forest Products Focus*; Harrington, C.A., Schoenholtz, S.H., Eds.; Gen. Tech. Rep. PNW-GTR-642; USDA, Forest Service, Pacific Northwest Research Station: Portland, OR, USA, 2005; pp. 121–129.
6. Wang, X.; Carter, P.; Ross, R.J.; Brashaw, B.K. Acoustic assessment of wood quality of raw materials: A path to increased profitability. *For. Prod. J.* **2007**, *57*, 6–14.
7. National Lumber Grades Authority (NLGA). *Standard Grading Rules for Canadian Lumber*; NLGA: Surrey, BC, Canada, 2014.
8. Defo, M. SilviScan-3—A Revolutionary Technology for High-Speed Wood Microstructure and Properties Analysis. Midis de al Foresterie. UQAT. Available online: http://chaireafd.uqat.ca/midiForesterie/pdf/20080422PresentationMauriceDefo.pdf (accessed on 1 October 2018).
9. Wang, X.; Ross, R.J.; Mattson, J.A.; Erickson, J.R. Nondestructive evaluation techniques for assessing modulus of elasticity and stiffness of small-diameter logs. *For. Prod. J.* **2002**, *52*, 79–85.
10. Dickson, R.L.; Raymond, C.A.; Joe, B.; Wilkinson, C.A. Segregation of *Eucalyptus dunnii* logs using acoustics. *For. Ecol. Manag.* **2003**, *179*, 243–251. [CrossRef]
11. Ross, R.J. *Nondestructive Evaluation of Wood*, 2nd ed.; General Technical Report FPL-GTR-238; USDA, Forest Service, Forest Products Laboratory: Madison, WI, USA, 2015; p. 169.
12. Legg, M.; Bradley, S. Measurement of stiffness of standing trees and felled logs using acoustics: A review. *J. Acoust. Soc. Am.* **2016**, *139*, 588–604. [CrossRef] [PubMed]
13. Raymond, C.A.; Joe, B.; Evans, R.; Dickson, R.L. Relationship between timber grade, static and dynamic modulus of elasticity, and Silviscan properties for *Pinus radiata* in New SouthWales. *N. Z. J. For. Sci.* **2007**, *37*, 186–196.
14. Newton, P.F. Development trends of black spruce fibre attributes in maturing plantations. *Int. J. For. Res.* **2016**, 1–12. [CrossRef]
15. Newton, P.F. Predictive relationships between acoustic velocity and wood quality attributes for red pine logs. *For. Sci.* **2017**, *63*, 504–517. [CrossRef]
16. Newton, P.F. Acoustic-based non-destructive estimation of wood quality attributes within standing red pine trees. *Forests* **2017**, *8*, 380. [CrossRef]
17. Wang, X. Acoustic measurements on trees and logs: A review and analysis. *Wood Sci. Technol.* **2013**, *475*, 965–975. [CrossRef]

18. Brashaw, B.K.; Bucur, V.; Divos, F.; Goncalves, R.; Lu, J.; Meder, R.; Yin, Y. Nondestructive testing and evaluation of wood: A worldwide research update. *For. Prod. J.* **2009**, *59*, 7–14.
19. Wang, X.; Senalik, C.A.; Ross, R.J. (Eds.) *20th International Nondestructive Testing and Evaluation of Wood Symposium*; General Technical Report FPL-GTR-249; USDA, Forest Service, Forest Products Laboratory: Madison, WI, USA, 2017; p. 539.
20. McKinnon, L.M.; Kayahara, G.J.; White, R.G. *Biological Framework for Commercial Thinning Evenaged Single-Species Stands of Jack Pine, White Spruce, and Black Spruce in Ontario*; Report TR-046; Ontario Ministry of Natural Resources, Northeast Science and Information Section: Timmins, ON, Canada, 2006; p. 130.
21. Carmean, W.H.; Niznowski, G.P.; Hazenberg, G. Polymorphic site index curves for jack pine in Northern Ontario. *For. Chron.* **2001**, *77*, 141–150. [CrossRef]
22. Rowe, J.S. *Forest Regions of Canada*; Publication No. 1300; Government of Canada, Department of Environment, Canadian Forestry Service: Ottawa, ON, Canada, 1972.
23. Evans, R. Rapid measurement of the transverse dimensions of tracheids in radial wood sections from *Pinus radiata*. *Holzforschung* **1994**, *48*, 168–172. [CrossRef]
24. Siau, J.F. *Wood: Influence of Moisture on Physical Properties*; Virginia Polytechnic Institute and State University, Department of Wood Science and Forest Products: Blacksburg, VA, USA, 1995.
25. Evans, R.; Hughes, M.; Menz, D. Microfibril angle variation by scanning X-ray diffractometry. *Appita* **1999**, *52*, 363–367.
26. Evans, R. Wood stiffness by X-ray diffractometry. In *Characterization of the Cellulosic Cell Wall*; Stokke, D.D., Groom, L.H., Eds.; Wiley: Hoboken, NJ, USA, 2006; pp. 138–146.
27. Evans, R.; Downes, G.; Menz, D.; Stringer, S. Rapid measurement of variation in tracheid transverse dimensions in a radiata pine tree. *Appita* **1995**, *48*, 134–138.
28. Raudenbush, S.W.; Bryk, A.S. *Hierarchical Linear Models: Applications and Data Analysis Methods*, 2nd ed.; Sage: Newbury Park, CA, USA, 2002; p. 485.
29. Raudenbush, S.W.; Bryk, A.S.; Cheong, Y.F.; Congdon, R.T.; Toit, M., Jr. *HLM 7—Hierarchical Linear and Nonlinear Modeling*; Scientific Software International Inc.: Lincolnwood, IL, USA, 2011; p. 360.
30. Gujarati, D.N. *Essentials of Econometrics*, 3rd ed.; McGraw-Hill/Irwin Inc.: New York, NY, USA, 2006; p. 553.
31. Ek, A.R.; Monserud, R.A. Performance and comparison of stand growth models based on individual tree and diameter-class growth. *Can. J. For. Res.* **1979**, *9*, 231–244. [CrossRef]
32. Reynolds, M.R., Jr. Estimating the error in model predictions. *For. Sci.* **1984**, *30*, 454–469.
33. Gribko, L.S.; Wiant, H.V., Jr. A SAS template program for the accuracy test. *Compiler* **1992**, *10*, 48–51.
34. National Lumber Grades Authority (NLGA). *Special Products Standard for Machine Graded Lumber*; NLGA: Surrey, BC, Canada, 2013.
35. Bérubé-Deschênes, A.; Franceschini, T.; Schneider, R. Factors affecting plantation grown white spruce (*Picea glauca*) acoustic velocity. *J. For.* **2016**, *114*, 629–637. [CrossRef]
36. Butler, M.A.; Dahlen, J.; Eberhardt, T.L.; Montes, C.; Antony, F.; Daniels, R.F. Acoustic evaluation of loblolly pine tree-and lumber-length logs allows for segregation of lumber modulus of elasticity, not for modulus of rupture. *Ann. For. Sci.* **2017**, *74*, 1–15. [CrossRef]
37. Kang, H.; Booker, R.E. Variation of stress wave velocity with MC and temperature. *Wood Sci. Technol.* **2002**, *36*, 41–54. [CrossRef]
38. Chauhan, S.S.; Walker, J.C.F. Variations in acoustic velocity and density with age, and their interrelationships in radiata pine. *For. Ecol. Manag.* **2006**, *229*, 388–394. [CrossRef]
39. Newton, P.F. Quantifying the effects of wood moisture and temperature variation on time-of-flight acoustic velocity measures within standing red pine and jack pine trees. *Forests* **2018**, *9*, 527. [CrossRef]
40. Wessels, C.B.; Malan, F.S.; Rypstra, T. A review of measurement methods used on standing trees for the prediction of some mechanical properties of timber. *Eur. J. For. Res.* **2011**, *130*, 881–893. [CrossRef]
41. Wang, X.; Carter, P. Acoustic assessment of wood quality in trees and logs. In *Nondestructive Evaluation of Wood*; Ross, R.J., Ed.; General Technical Report FPL-GTR-238; USDA, Forest Service, Forest Products Laboratory: Madison, WI, USA, 2015; pp. 87–101.
42. Newton, P.F. In-forest acoustic-based prediction of commercially-relevant wood quality attributes within standing jack pine trees. *Forests* **2018**, in preparation.
43. Walker, J.C.F.; Nakada, R. Understanding corewood in some softwoods: A selective review on stiffness and acoustics. *Int. For. Rev.* **1999**, *1*, 251–259.

44. Harris, P.; Petherick, R.; Andrews, M. Acoustic resonance tools. In *Proceedings of the 13th International Symposium on Nondestructive Testing of Wood*; Forest Products Society: Berkeley, CA, USA, 2003; pp. 195–201.
45. Ross, R.J.; McDonald, K.A.; Green, D.W.; Schad, K.C. Relationship between log and lumber modulus of elasticity. *For. Prod. J.* **1997**, *47*, 89–92.
46. Dickson, R.L.; Matheson, A.C.; Joe, B.; Ilic, J.; Owen, J.V. Acoustic segregation of *Pinus radiata* logs for sawmilling. *N. Z. J. For. Sci.* **2004**, *34*, 175–189.
47. Vikram, V.; Cherry, M.L.; Briggs, D.; Cress, D.W.; Evans, R.; Howe, G.T. Stiffness of Douglas-fir lumber: Effects of wood properties and genetics. *Can. J. For. Res.* **2011**, *41*, 1160–1173. [CrossRef]
48. Clark, T.A.; Hartmann, J.; Lausberg, M.; Walker, J.C.F. Fibre characterisation of pulp logs using acoustics. In Proceedings of the 56th Appita Annual Conference, Rotorua, New Zealand, 18–20 March 2002; pp. 17–24.
49. Bradley, A.; Chauhan, S.S.; Walker, J.C.F.; Banham, P. Using acoustics in log segregation to optimise energy use in thermomechanical pulping. *Appita* **2005**, *58*, 306–311.
50. Murphy, G.; Cown, D. Stand, stem and log segregation based on wood properties: A review. *Scand. J. For. Res.* **2015**, *30*, 757–770. [CrossRef]
51. Walsh, D.; Strandgard, M.; Carter, P. Evaluation of the Hitman PH330 acoustic assessment system for harvesters. *Scand. J. For. Res.* **2014**, *29*, 593–602. [CrossRef]
52. Zhang, S.Y.; Koubaa, A. *Softwoods of Eastern Canada: Their Silvics, Characteristics, Manufacturing and End-Uses*; Special Publication SP-526E; FPInnovations: Quebec City, QC, Canada, 2008.

© 2018 by the author. Licensee MDPI, Basel, Switzerland. This article is an open access article distributed under the terms and conditions of the Creative Commons Attribution (CC BY) license (http://creativecommons.org/licenses/by/4.0/).

forests

MDPI

Article

Variations in Orthotropic Elastic Constants of Green Chinese Larch from Pith to Sapwood

Fenglu Liu [1,2], Houjiang Zhang [1,2,*], Fang Jiang [1], Xiping Wang [3] and Cheng Guan [1,2]

[1] School of Technology, Beijing Forestry University, Beijing 10083, China; liufenglu3339@bjfu.edu.cn (F.L.); jf0620@bjfu.edu.cn (F.J.); cguan6@bjfu.edu.cn (C.G.)
[2] Joint International Research Institute of Wood Nondestructive Testing and Evaluation, Beijing Forestry University, Beijing 100083, China
[3] USDA Forest Products Laboratory, Madison, WI 53726, USA; xiping.wang@usda.gov
* Correspondence: hjzhang6@bjfu.edu.cn; Tel.: +86-010-62336925 (ext. 401)

Received: 26 April 2019; Accepted: 23 May 2019; Published: 25 May 2019

Abstract: Full sets of elastic constants of green Chinese larch (*Larix principis-rupprechtii* Mayr) with 95% moisture content at four different cross-section sampling positions (from pith to sapwood) were determined in this work using three-point bending and compression tests. Variations in the material constants of green Chinese larch from pith to sapwood were investigated and analyzed. The results showed that the sensitivity of each elastic constant to the sampling position was different, and the coefficient of variation ranged from 4.3% to 48.7%. The Poisson's ratios ν_{RT} measured at four different sampling positions were similar and the differences between them were not significant. The coefficient of variation for Poisson's ratio ν_{RT} was only 4.3%. The four sampling positions had similar Poisson's ratios ν_{TL}, though the coefficient of variation was 11.7%. The Poisson's ratio ν_{LT} had the greatest variation in all elastic constants with a 48.7% coefficient of variation. A good linear relationship was observed between the longitudinal modulus of elastic E_L, shear modulus of elasticity G_{RT}, Poisson's ratio ν_{RT}, and sampling distance. E_L, G_{RT}, and ν_{RT} all increased with sampling distance R. However, a quadratic relationship existed with the tangential modulus of elasticity E_T, radial modulus of elasticity E_R, shear modulus of elasticity G_{LT}, and shear modulus of elasticity G_{LR}. A discrete relationship was found in the other five Poisson's ratios. The results of this study provide the factual changes in the elastic constants of green wood from pith to sapwood for numerical modelling of stress wave propagation in trees or logs.

Keywords: orthotropic; elastic constants; green larch; compression; three-point bending

1. Introduction

Elastic constants, especially the modulus of elasticity (MOE), which indicate the elastic behavior of wood, are critical parameters for furniture, musical instruments, or wood products, such as plywood, laminated veneer lumber, and cross laminated timber. Numerical simulation is being increasingly used to investigate the propagation of stress wave in standing trees or logs [1–4]. Material elastic constants are required for numerical simulation, especially when defining material properties. Wood, as a complex and anisotropic material, has considerable variations in its mechanical properties from bottom to top, pith to sapwood within a tree. In many studies, wood has been considered an orthotropic material, given its unique and independent material performance in the three principal or orthotropic directions (radial R, tangential T, and longitudinal L) [5–11]. Nine independent elastic constants (reduced from twelve elastic constants according to the symmetry of the stress and strain sensor in orthotropic materials), including three elastic moduli, three shear moduli, and three Poisson's ratios, are required to characterize the elastic behavior of orthotropic materials for mechanical analysis. Wood is also a hygroscopic material, and its mechanical behavior is therefore impacted by variations in moisture

content (MC) [12–16]. Hering et al. determined all the independent elastic properties of European beech wood at different moisture conditions (MC ranged from 8.7% to 18.6%), and results indicated that all elastic parameters, except for Poisson's ratios ν_{TR} and ν_{RT}, show a decrease in stiffness with increasing moisture content [13]. Similarly, Jiang et al. examined the influence of moisture content on the elastic and strength anisotropy of Chinese fir (*Cunninghamia lanceolate* Lamb.) wood and found that, except for Poisson's ratios, all investigated elastic and strength parameters decreased with increasing MC (varied from 10.3% to 16.7%), whereby individual moduli and strength values were affected by the MC to different degrees [14].

Resistance strain gauges and ultrasonic are the two of most commonly used methods determining the elastic constants of wood. As a destructive method, resistance strain gauges are usually used to evaluate the material constants of wood. Sliker first proposed the use of compression and bending tests using strain gauges in wood to determine the elastic constants of materials [6–8]. Many studies had been conducted to verify the feasibility and validity of this method. Li successfully measured the full set of elastic constants for *Fraxinus mandshurica* with 13.4% moisture content via the compression test using strain gauges [9]. Gong estimated the elastic moduli parallel to the grain of *Pinus Massoniana* with 15% MC through strain gauges [10]. Wang et al. determined the full set of material constants for White Birch (*Betula platyphylla* Suk.) with 12% MC using the compression and three-point bending tests [17]. Shao et al. measured the seven elastic constants of *Cunninghamia lanceolata* with 12% MC using electric resistance strain gauges [18]. Aira et al. performed compression tests on dry specimens (around 12% MC) to determine the elastic constants of Scots pine (*Pinus sylvestris* L.) and found the MOE values obtained were greater than the average values for softwoods, and Poisson's ratios obtained parallel to the grain were similar to the values in the literature [19].

Ultrasonic, a rapid and efficient non-destructive method for determining material properties, has drawn increasing attention in wood characteristic measurement. Preziosa et al. first determined the stiffness matrix of wood using the ultrasonic technique [20,21]. Then, Bucur measured the elastic constants of six species (pine, spruce, Douglas-fir, oak, beech, and tulip-tree) in the dry condition, applying ultrasonic to different cubic specimens [22]. Francois proposed the use of a polyhedral specimen with 26 faces for the determination of all the elements in the stiffness matrix from a single specimen to measure the elastic constants of dry wood [23]. Many studies have demonstrated the feasibility of using ultrasonic to measure all the elastic constants from a single specimen of dry wood (MC ranged from 7.5% to 12.3%) from different species, such as *Castanea sativa* Mill., ash (*Fraxinus excelsior* L), beech, *Eucalyptus saligna*, *Apuleia leiocarpa*, and *Goupia glabra* [24–27].

Although the full material constants of wood can be measured by both resistance strain gauges and ultrasonic, the full sets of elastic constants for green wood have rarely been reported in the literature. As wood is often used in a dry state, the elastic constants reported in most published papers for wood are in these conditions [28–31]. This would lead to a poor representation when the elastic constants of dry wood are used for modelling standing trees or green logs. Only Davies et al. investigated and obtained the elastic constants of green *Pinus radiata* wood using compression and tension tests [32]. Davies et al. stated that the mathematical modelling would be more realistic with the material constants of green wood rather than those of dry wood. The variation in elastic constants in cross-sections of green wood from pith to sapwood have not been reported in the literature. Davies et al. only measured the material constants of the corewood and outerwood of *Pinus radiata* instead of elastic constants across whole transverse sections of wood. Although Xavier et al. reported that the two stiffness values (Q_{22} and Q_{66}) of *P. pinaster* varied across three or four different radial positions using the unnotched Iosipescu test, the moisture content of the specimens was 10.4% and only two stiffness values were investigated [33]. Therefore, to the best of our knowledge, no full sets of elastic constants varying from pith to sapwood have been published for green wood. The variations in the mechanical properties of green wood from pith to sapwood have not yet been studied.

The main purpose of this research was to determine the elastic constants of green Chinese larch from pith to sapwood using compression and three-point bending tests, as well as to investigate and

analyze the variations in the mechanical characteristics of green Chinese larch from pith to sapwood. We aimed to obtain basic knowledge about the mechanical properties of wood from pith to sapwood, and to describe standing trees or logs as an orthotropic material in numerical modelling. Use of wood could be optimized in various applications, such as papermaking, furniture, musical instruments, or wood products, according to the measured material performance in different parts of the wood. Standing trees or logs could be modelled more realistically in numerical simulation with the acquired data. The results of this study provide factual elastic constants of green wood from pith to sapwood for numerical modelling of stress wave propagation in trees or logs.

2. Materials and Methods

2.1. Materials

Two Chinese larches (*Larix principis-rupprechtii* Mayr), a common plantation species in Northern China, were harvested from Maojingba National Plantation Farm, located in Longhua County, Chengde City, Hebei Province, China (118°06′05″ E, 41°28′46″ N at approximately 750 m elevation). The trees (coded A and B) aged 40 years were felled and branches were subsequently removed. The diameter at breast height (DBH) values of tree A and tree B were 32 cm and 36 cm, respectively. Then, two 60-cm-long logs were cut from each selected tree at a height of 0.5 m and 1.25 m above the ground. A 15-cm-thick disc for density and moisture content measurements was cut from each tree at a height of 1.1 m above the ground. A total of four 60-cm-long logs and two 15-cm-thick discs were obtained and immediately sealed in plastic wrap. After, these logs and discs were directly transported to the mechanics laboratory in Beijing Forestry University and kept in a condition room at 15 °C and 95% relative humidity.

2.2. Static Testing Method

2.2.1. Specimen Sampling

A schematic of the sawing pattern used to obtain green larch specimens for static testing is presented in Figure 1. Four different sampling positions from pith to sapwood (numbered 1, 2, 3, and 4 in Figure 1 referred to sampling position, defined as P1, P2, P3, and P4 hereinafter, respectively) were chosen to determine the elastic constants at different positions from pith to sapwood in the cross-sections of standing trees and investigate the distribution of elastic constants in the cross-sections of standing trees. As shown in Figure 1, sampling positions P1, P2, and P4 were located at the pith, heartwood, and sapwood, respectively, whereas P3 was located between the heartwood and sapwood. The initial transverse dimension of specimens for static testing in each sampling location was 53 × 53 mm.

Parameter R was used to define the distance between the center of pith and the center of sampling position. Thus, the designed distance R for sampling position P1, P2, P3 and P4 was 13 mm, 56 mm, 76 mm and 132 mm, respectively. It should be noticed that the sampling distance R for P1, P2, P3 and P4 shown in Figure 1 was designed for a log with a DBH ranging from 300 mm to 360 mm. The sampling distance would be different as the DBH of log over 360 mm and need to be changed.

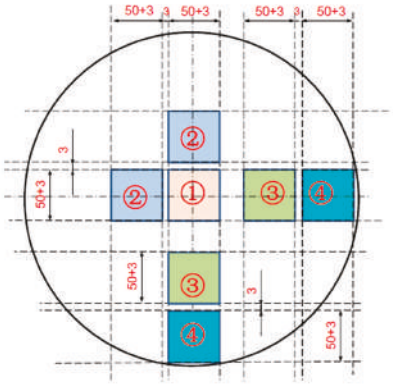

Figure 1. Schematic of sawing pattern for testing specimens. Dashed lines represent the sawing line and the units are millimeters. The extra 3 mm width was the machining allowance. The number 1, 2, 3, and 4 in the yellow, gray, green, and blue area, respectively represent four different sampling positions.

One P1 lumber (53 × 53 × 600 mm), two P2 lumbers (53 × 53 × 600 mm), two P3 lumbers (53 × 53 × 600 mm), and two P4 lumbers (53 × 53 × 600 mm) were obtained from each log according to sampling pattern shown in Figure 1. A total of 4 P1- lumbers, 8 P2- lumbers, 8 P3- lumbers, and 8 P4-lumbers were acquired from four 600-mm-long logs. Then, these were used to prepare the specimens for static testing, including the compression test and three-point bending test, performed according to American Society for Testing Materials (ASTM) D5536-94 [34]. Specimens for static testing were instantly sealed with plastic wrap and stored in the condition room (15 °C and 95% relative humidity) before mechanical testing. The dimensions of the specimens used for static testing are provided in Table 1. Each sampling location (referred to as P1, P2, P3, and P4) all used the same size specimens for static testing. Therefore, the elastic constants of these four different positions (from pith to sapwood) in the cross-section of standing trees could be determined.

Table 1. Dimensions of specimens for static testing.

Static Test	Orientation		Size (mm) (Length × Width × Thickness)	Number of Specimens for One Sampling Position
Compression test	Parallel to grain	Longitudinal (L)	25 × 25 × 100	8
	Perpendicular to grain	Radial (R) Tangential (T) With a 45° to tangential	50 × 50 × 150	8 × 3
Three-point bending test	Parallel to grain	Longitudinal (L)	25 × 25 × 150 25 × 25 × 200 25 × 25 × 250 25 × 25 × 300 25 × 25 × 350	8 8 8 8 8

2.2.2. Compression Test

The four types of test specimens used for the compression test, with wood grain oriented relative to the orthotropic directions and the distribution of strain gauges in specimen, are displayed in Figure 2. Eight clear test specimens of the required shape and orientation were machined from the cut lumber. A total of 128 test specimens (8 replicates × 4 orientations × 4 sampling positions) were used for compression testing. Eight 25 × 25 × 100 mm specimens parallel to the grain (Figure 2a) were used to measure the elastic constants of E_L, ν_{LR}, and ν_{LT}. Eight 50 × 50 × 150 mm specimens perpendicular to the grain radially (Figure 2b) were used to test E_R, ν_{RL}, and ν_{RT}. Eight 50 × 50 × 150 mm specimens perpendicular to the grain tangentially (Figure 2c) were used to evaluate E_T, ν_{TR}, and ν_{TL}.

Eight 50 × 50 × 150 mm specimens inclined at a 45° to the grain (Figure 2d) were used to obtain the shear modulus of elasticity G_{RT}.

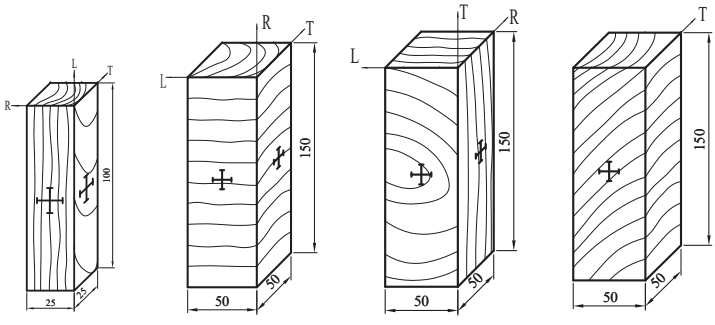

(**a**) (**b**) (**c**) (**d**)

Figure 2. Types of specimens and strain gauges placement for compression test: (**a**) parallel to the grain, (**b**) perpendicular to the grain radially, (**c**) perpendicular to the grain tangentially, and (**d**) inclined at 45°.

Resistance strain gauges were directly bonded to the surfaces of the specimen prior to compression testing. Figure 2a–c show that four strain gauges were placed on each specimen. Two resistance strain gauges were glued perpendicularly to a surface of testing sample, and the other two resistance strain gauges were perpendicularly bonded to the adjacent surface. As shown in Figure 2d, only two strain gauges perpendicularly glued to a surface of specimen were used for compression testing. Strain gauges should be placed close to each other so that measurements record the strain state of the same point with no variability in their elastic properties due to the heterogeneity of wood. The adhesive used has a lower longitudinal stiffness than wood to avoid restricting its free deformation when receiving the external load. The adhesive must simultaneously have a high shear stiffness so that the deformation of strain gauge is not damped by the thickness of the adhesive [19]. RGM-4050-100 (made by Reger Instrument Corporation Limited, Shenzhen City, China), a microcomputer-controlled electronic universal testing machine, was used to conduct the compression test according to ASTM D143-09 [35]. Specimens were loaded at a rate of 0.2 mm/min for compression testing. Modulus of elasticity (E_L, E_R, and E_T), Poisson's ratios (ν_{LR}, ν_{LT}, ν_{RL}, ν_{RT}, ν_{TR}, and ν_{TL}) and shear modulus of elasticity (G_{RT}) were calculated from Equations (1)–(3), respectively.

$$E = \frac{P_n - P_0}{A_0(\varepsilon_n - \varepsilon_0)} \tag{1}$$

where E is the modulus of elasticity (MPa), P_n is the final load (N), P_0 is the initial load (N), A_0 is the cross-section area of specimen (mm^2), ε_n is the final strain, and ε_0 is the initial strain.

$$v = -\frac{\Delta\varepsilon'}{\Delta\varepsilon} \tag{2}$$

where v is the Poisson's ratio of specimen, $\Delta\varepsilon'$ is the lateral strain increase, and $\Delta\varepsilon$ is the axial strain increase.

$$G_{RT} = \frac{\Delta P_{45^\circ}}{2A_0\left(\Delta\varepsilon_x - \Delta\varepsilon_y\right)} \tag{3}$$

where G_{RT} is the shear modulus of elasticity in the RT plane (MPa), A_0 is the cross-section area of the specimen (mm^2), ΔP_{45° is the load increase of the elastic deformation phase on the load-strain

curve (N), $\Delta\varepsilon_x$ is the strain increase along the axis of the specimen, and $\Delta\varepsilon_y$ is the strain increase perpendicular to the axis of specimen.

Since the moisture content has a significant effect on the mechanical properties of wood, the specimens were taken from the condition room and tested in sequence to ensure less variation in the moisture content of specimens. Measurements for each specimen were performed as soon as possible to reduce the impact of the moisture content on the testing results.

2.2.3. Three-Point Bending Test

In the light of ASTM D5536-94, specimens with five different ratios of span to depth were prepared to conduct three-point bending test. We obtained a total of 160 test specimens in total (8 replicates × 5 spans × 4 sampling positions) for the bending tests. The specific size of the specimens, especially the length, are shown in Table 1. The span for each length of specimen was 132 mm, 176 mm, 220 mm, 264 mm, and 308 mm, respectively. Three-point bending tests were conducted using an RGM-4050-100 universal testing machine on the basis of ASTM D143-09. The loading speed of specimens for three-point bending test was 5 mm/min. As above, the specimens for the bending test were successively measured and tested as quickly as possible to reduce the variation in the moisture content of the measured samples. Bending moduli of elasticity (*MOE*) were calculated using Equation (4), and then shear modulus of elasticity (*G*) can be obtained using Equation (5).

$$MOE = \frac{\Delta P l^3}{4\Delta f b h^3} \tag{4}$$

where *MOE* is the bending modulus of elasticity (MPa), ΔP is loading increase (N), Δf is the deflection increase (mm), b is the width of the specimen (mm), h is the thickness of the specimen (mm), and l is the span of the specimen (mm).

$$G = \frac{1.2\Delta(h/l)^2}{\Delta(1/MOE)} \tag{5}$$

where $\Delta(h/l)^2$ is the increase in the square of ratio between the thickness and span and $\Delta(1/MOE)$ is the increase in the reciprocal of the bending modulus of elasticity (mm^2/N). The shear modulus of elasticity G_{LR} was obtained by measuring specimen loaded from radial direction, and the shear modulus of elasticity G_{LT} was obtained by measuring the specimen loaded from tangential direction. Both of them can be calculated using Equations (4) and (5).

3. Results and Discussion

3.1. Twelve Elastic Constants of Green Chinese Larch at Different Sampling Positions

The moisture content (MC) of green Chinese larch was measured in the laboratory using the kiln-dry method, and the average MC of the sample trees was 95%. The average green density of Chinese larch was 625 kg/m^3. Twelve elastic constants of green Chinese larch were calculated using Equations (1)–(4) using the experimental data obtained from three-point bending and compression tests. The elastic constants of the four different sampling positions (P1, P2, P3, and P4) are shown in Table 2. The average values of the elastic moduli in the longitudinal, radial, and tangential directions were 7,629 MPa, 773 MPa, and 362 MPa, respectively. Davies et al. reported that the longitudinal, radial, and tangential elastic moduli of the outerwood in green *Pinus radiata* were 4,360 MPa, 490 MPa, and 250 MPa, respectively. The values for the corewood of green *Pinus radiata* were 3,500 MPa, 260 MPa, and 240 MPa, respectively. The average values of the three elastic moduli obtained from this work were higher than those derived from Davies's research due to the differences in the tested species and tree ages. The longitudinal modulus of elasticity (E_L) increased from 5016 MPa to 10,137 MPa as the sampling distance (R) varied from 13 mm (P1) to 132 mm (P4), respectively. This means that the longitudinal mechanical properties of green Chinese larch increased from pith to sapwood. However, the radial

modulus of elasticity (E_R) initially increased from 628 MPa to 1,154 MPa as the sampling distance changed from 13 mm (P1) to 76 mm (P3) and then decreased to 342 MPa as sampling distance increased to 132 mm (P4). This may indicate a lower radial modulus of elasticity in sapwood. No significant relationship was found between tangential modulus of elasticity (E_T) and sampling distance (R).

The average values of shear moduli in the LR, LT, and RT plane were 428 MPa, 393 MPa, and 450 MPa, respectively. Davies et al. presented the lower values for these three shear moduli, 60 MPa, 110 MPa, 50 MPa in LR, LT, and RT plane for outerwood and 40 MPa, 110 MPa, 20 MPa in LR, LT, and RT plane for corewood, respectively. The average values of ν_{LT}, ν_{LR}, ν_{TL}, ν_{TR}, ν_{RL}, and ν_{RT} Poisson's ratios were 0.30, 0.22, 0.04, 0.60, 0.05, and 0.77, respectively. The corresponding values of these six Poisson's ratios in Davies's paper were 0.60, 0.29, 0.03, 0.33, 0.03, and 0.64 for outerwood and 0.16, 0.46, 0.01, 0.33, 0.05, and 0.54 for corewood, respectively. However, no significant relationship with sampling distance was found for either shear modulus of elasticity or Poisson's ratio.

Table 2. Twelve elastic constants at different sampling locations in cross-sections of green Chinese larch.

Sampling Position	E_L (MPa)	ν_{LT}	ν_{LR}	E_T (MPa)	ν_{TL}	ν_{TR}	E_R (MPa)	ν_{RL}	ν_{RT}	G_{RT} (MPa)	G_{LR} (MPa)	G_{LT} (MPa)
1	5016	0.15	0.13	339	0.04	0.55	628	0.04	0.74	326	538	403
2	5996	0.47	0.34	423	0.05	0.66	967	0.03	0.75	535	339	352
3	9365	0.21	0.15	402	0.04	0.53	1154	0.06	0.79	383	404	371
4	10137	0.36	0.26	282	0.04	0.66	342	0.05	0.81	556	430	446
Mean	7629	0.30	0.22	362	0.04	0.60	773	0.05	0.77	450	428	393
SD [1]	2503	0.15	0.10	64	0.01	0.07	360	0.01	0.03	113	83	41
SE [2]	1252	0.07	0.05	32	0.01	0.04	180	0.01	0.02	57	41	21
COV [3] (%)	32.8	48.7	44.7	17.7	11.7	11.6	46.6	28.7	4.3	25.1	19.4	10.5

[1] SD, standard deviation; [2] SE, standard error; [3] COV, coefficient of variation.

Table 2 shows that the longitudinal modulus of elasticity (E_L) was higher than the radial modulus of elasticity (E_R), and the radial modulus of elasticity (E_R) was greater than the tangential modulus of elasticity (E_T), i.e., $E_L > E_R > E_T$, for all four sampling positions. Similarly, Poisson's ratio ν_{RT} was higher than Poisson's ratio ν_{LT}, and Poisson's ratio ν_{LT} was greater than Poisson's ratio ν_{LR}, i.e., $\nu_{RT} > \nu_{LT} > \nu_{LR}$ at these four sampling locations. These results align with the findings in dry wood [17,18]. Wood is a highly anisotropic material. Thus, different values would be obtained for the same elastic constant due to different sampling positions. Table 2 also shows that the sensitivity of each elastic constant to the sampling position was different, and the corresponding coefficient of variation ranged from 4.3% to 48.7%. Table 3 provides the results of the analysis of variance (ANOVA) for each elastic constant at different sampling positions. Table 3 shows that sampling position had a significant impact both on E_L, G_{RT}, ν_{LT}, and ν_{LR} ($p < 0.05$), whereas no significant effect was found in the other elastic constants ($p > 0.05$). For three MOE, only E_L showed significant differences ($p < 0.05$) in sampling positions with a 32.8% coefficient of variation. Poisson's ratios ν_{RT} measured at four different sampling positions were similar and the coefficient of variation for Poisson's ratio ν_{RT} was only 4.3%, which is in agreement with the insignificant differences between them ($p > 0.05$). The four sampling positions had similar Poisson's ratios ν_{TL} and showed an insignificant difference ($p > 0.05$), though the coefficient of variation was 11.7%. Poisson's ratio ν_{LT} had the greatest variation in all elastic constants with a 48.7% coefficient of variation and showed a significant difference in sampling position ($p < 0.05$). For shear moduli, only G_{RT} showed significant differences ($p < 0.05$) in sampling positions with a 25.1% coefficient of variation.

Table 3. Analysis of variance of elastic constants at different sampling positions.

	Source	Sum of Squares	Degrees of Freedom	Mean Square	*F*-Value	*p*-Value
E_L	Between groups [1]	9.92×10^7	3	3.31×10^7	8.31	0.001
	Within groups	9.55×10^7	24	3.98×10^6		
	Total	1.95×10^8	27			
E_R	Between groups	1.99×10^6	3	6.65×10^5	1.62	0.21
	Within groups	9.84×10^6	24	4.09×10^5		
	Total	1.18×10^7	27			
E_T	Between groups	1.55×10^6	3	5.17×10^5	1.07	0.38
	Within groups	1.16×10^7	24	4.82×10^5		
	Total	1.31×10^7	27			
G_{LR}	Between groups	8.27×10^4	3	2.76×10^4	1.29	0.322
	Within groups	2.56×10^5	12	2.13×10^4		
	Total	3.38×10^6	15			
G_{LT}	Between groups	2.04×10^4	3	6.79×10^4	0.49	0.694
	Within groups	1.65×10^5	12	1.38×10^4		
	Total	1.86×10^5	15			
G_{RT}	Between groups	2.23×10^5	3	7.43×10^4	25.57	3.25×10^{-4}
	Within groups	5.52×10^4	19	2.91×10^3		
	Total	2.78×10^5	22			
v_{LT}	Between groups	0.439	3	0.146	12.14	1.54×10^{-3}
	Within groups	0.290	24	0.012		
	Total	0.729	27			
v_{LR}	Between groups	0.221	3	0.074	12.82	1.12×10^{-3}
	Within groups	0.138	24	0.006		
	Total	0.358	27			
v_{TL}	Between groups	0.006	3	0.002	0.644	0.594
	Within groups	0.072	24	0.003		
	Total	0.078	27			
v_{TR}	Between groups	0.105	3	0.035	1.505	0.239
	Within groups	0.558	24	0.023		
	Total	0.663	27			
v_{RL}	Between groups	0.005	3	0.002	0.974	0.421
	Within groups	0.045	24	0.002		
	Total	0.050	27			
v_{RT}	Between groups	0.024	3	0.008	0.187	0.904
	Within groups	1.040	24	0.043		
	Total	1.065	27			

[1] Groups: there are four groups, i.e., four different sampling positions P1, P2, P3, and P4.

3.2. Vadility of Measured Data

Although the elastic constants of green Chinese larch at the four different sampling positions were obtained through experiments and data processing, the validity of testing data needed further verification. According to the mechanics of composite materials, the elastic constants of orthotropic materials should satisfy the limitations of Maxwell's theorem, as shown in Equations (6) and (7). As mentioned, in many studies, wood is considered an orthotropic material in the three main orthotropic directions. Therefore, the modulus of elasticity and the Poisson's ratio of green larch measured in this research should be satisfied the limitations of Maxwell's theorem.

$$\frac{v_{ij}}{E_i} = \frac{v_{ji}}{E_j} (i, j = \mathrm{L}, \mathrm{R}, \mathrm{T}) \tag{6}$$

$$\left|v_{ij}\right| < \left|\frac{E_i}{E_j}\right|^{\frac{1}{2}} \tag{7}$$

The modulus of elasticity and the Poisson's ratio obtained from P1 sampling position were taken into Equations (6) and (7), and the results showed that these elastic constants from P1 satisfy the limitation of Maxwell's theorem. Similar results were found in the P2, P3, and P4 sampling locations. Table 4 provides the results of Equation (7) at the P1, P2, P3, and P4 sampling locations. These results indicate that acquired data and calculated elastic constants from compression test were both valid and accurate.

Table 4. Results of the limitations of Maxwell's theorem at the four different sampling locations.

Sampling Position	$\lvert v_{LT}\rvert$	$\lvert\frac{E_L}{E_T}\rvert^{\frac{1}{2}}$	$\lvert v_{LR}\rvert$	$\lvert\frac{E_L}{E_R}\rvert^{\frac{1}{2}}$	$\lvert v_{TL}\rvert$	$\lvert\frac{E_T}{E_L}\rvert^{\frac{1}{2}}$	$\lvert v_{TR}\rvert$	$\lvert\frac{E_T}{E_R}\rvert^{\frac{1}{2}}$	$\lvert v_{RL}\rvert$	$\lvert\frac{E_R}{E_L}\rvert^{\frac{1}{2}}$	$\lvert v_{RT}\rvert$	$\lvert\frac{E_R}{E_T}\rvert^{\frac{1}{2}}$
1	0.15	3.85	0.13	2.83	0.04	0.26	0.55	0.73	0.04	0.35	0.74	1.36
2	0.47	3.76	0.34	2.49	0.05	0.27	0.66	0.66	0.03	0.40	0.75	1.51
3	0.21	4.83	0.15	2.85	0.04	0.21	0.53	0.59	0.06	0.35	0.79	1.69
4	0.36	6.00	0.26	5.44	0.04	0.17	0.66	0.91	0.05	0.18	0.81	1.10

However, Maxwell's theorem was only used to verify the validity of the modulus of elasticity and Poisson's ratio and could not be used to confirm the validity of the shear modulus of elasticity. Correlation analysis, consequently, was conducted on experimental data from the three-point bending tests to verify the validity of calculated shear modulus of elasticity. The relationship between the square of ratio between thickness and span $(h/l)^2$ and the reciprocal of bending modulus of elasticity ($1/MOE$) was analyzed both for radial-loaded and tangential-loaded bending tests. The results of correlation analysis for the P1, P2, P3, and P4 sampling positions are presented in Figures 3–6, respectively.

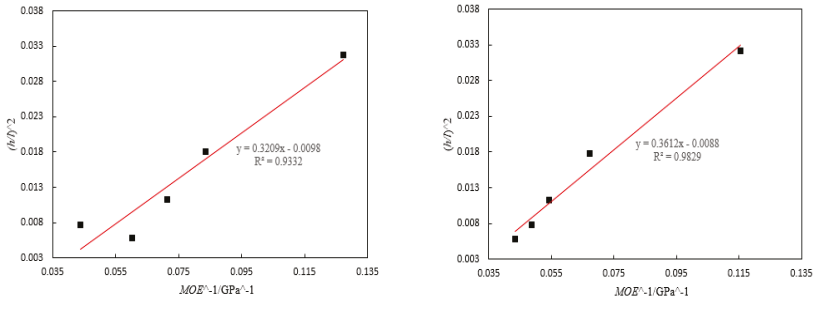

(**a**) (**b**)

Figure 3. Relationship between the reciprocal of bending elastic modulus and the square of the ratio between depth and length (Sampling position 1) for: (**a**) tangential loading and (**b**) radial loading.

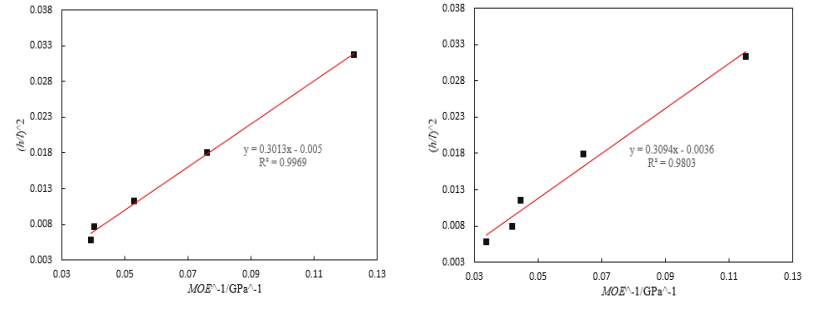

(**a**) (**b**)

Figure 4. Relationship between the reciprocal of bending elastic modulus and the square of the ratio between depth and length (Sampling position 2) for: (**a**) tangential loading and (**b**) radial loading.

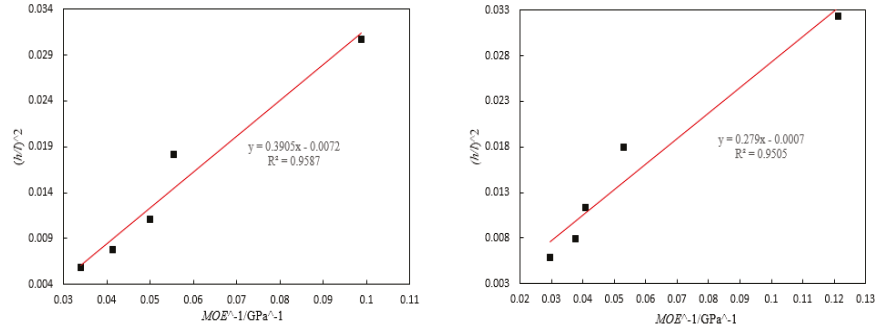

Figure 5. Relationship between the reciprocal of bending elastic modulus and the square of the ratio between depth and length (Sampling position 3) for: (**a**) tangential loading and (**b**) radial loading.

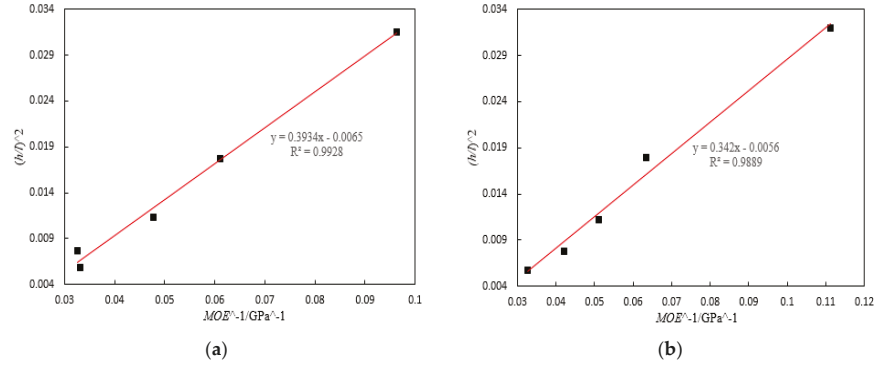

Figure 6. Relationship between the reciprocal of bending elastic modulus and the square of the ratio between depth and length (Sampling position 4) for: (**a**) tangential loading and (**b**) radial loading.

Figures 3–6 show that a linear relationship between the square of ratio in span and depth and the reciprocal of bending modulus of elasticity was found in the four sampling positions both for tangential-loaded and radial-loaded bending tests. The correlation coefficients between the square of the ratio in span and depth and the reciprocal of bending modulus of elasticity for the P1, P2, P3, and P4 sampling positions were all over 0.9 in the tangential-loaded and radial-loaded bending tests. These results indicate that the three-point bending test data and calculated shear modulus of elasticity were both effective and reasonable.

3.3. Variation in Elastic Constants of Wood Cross-Sections

3.3.1. Modulus of Elasticity

Wood is a highly anisotropic material with different mechanical properties throughout its interior. Wood properties change from pith to bark within a tree and differ between trees. Therefore, the mechanical properties, especially the elasticity constants, of wood vary along the cross-section. To investigate the difference and variation in the elastic constants along the cross-section of wood, the relationships between the modulus of elasticity, shear modulus of elasticity, Poisson's ratios, and sampling distance R were analyzed by regression analysis to obtain the variation patterns of the elastic constants along the cross-section of green Chinese larch using the experimental data derived from compression and three-point bending tests.

The results of regression analysis for modulus of elasticity and sampling position are provided in Figure 7 and Table 5. Relationships between sampling distance and the modulus of elasticity for the three principal axes of wood are illustrated in Figure 7. Table 5 displays the corresponding fitting equations and correlation coefficients came from regression analysis.

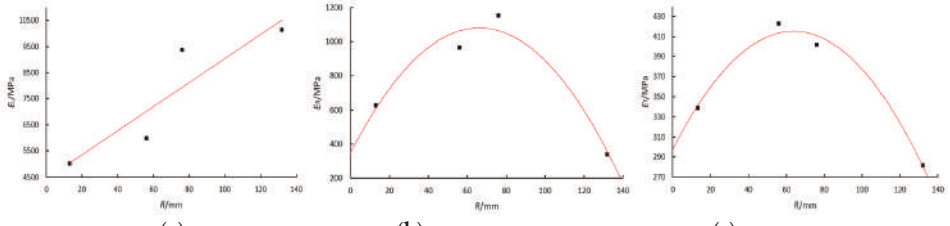

(**a**) (**b**) (**c**)

Figure 7. Relationships between the distance from pith and elastic moduli in the (**a**) longitudinal, (**b**) radial, and (**c**) tangential directions.

Table 5. Mathematical model of elastic moduli in three principle directions and distance from pith.

Modulus of Elasticity	Fitted Equation	Coefficient of Determination (R^2)
E_L	$E_L = 4436.36 + 46.12R$	0.91
E_R	$E_R = 343.25 + 22.27R - 0.17R^2$	0.95
E_T	$E_T = 297.55 + 3.68R - 0.03R^2$	0.98

Figure 7 shows the variation patterns of the three principal moduli of elasticity along the cross-section of the wood. Figure 7a shows that the longitudinal modulus of elasticity (E_L) of green Chinese larch linearly increased with sampling distance. However, a quadratic relationship was observed between the radial modulus of elasticity (E_R) and the sampling distance, as well as for the tangential modulus of elasticity (E_T) and the sampling distance. E_R and E_T both first increased with sampling distance, and then decreased with sampling distances over 70 mm, as shown in Figure 7b,c. E_R and E_T near the bark were significantly lower than in other sampling positions, and even lower than the measured values near the pith. Table 5 shows the linear relationship between the longitudinal modulus of elasticity and sampling distance ($R^2 = 0.91$). Even though a quadratic relationship was found in the tangential and radial moduli of elasticity, both coefficients of determination were higher than 0.95. Little research has been conducted to investigate the variation in elastic constants of wood from pith to sapwood. Only Xavier et al. studied the variation in two stiffness values (Q_{22} and Q_{66}) of dry Maritime pine across the radial position using the unnotched Iosipescu test. They found the transverse stiffness ($Q_{22} = E_R/(1 - \nu_{LR}.\nu_{RL})$) of dry Maritime pine decreased between the radial position r_1 (thirteenth ring, 29% of the radius) and r_2 (nineteenth ring, 46% of the radius), and a progressive increase was observed up to r_4 (forty-third ring, 81% of the radius) [33]. This means that the transverse stiffness decreased from the center to about the middle radius of stem and increased afterward to the outermost positions. The variation pattern of elastic moduli E_R of green Chinese larch measured in this work was different from that of the transverse stiffness Q_{22}. This may be because the transverse stiffness was not only affected by the radial elastic moduli but also by Poisson's ratios ν_{LR} and ν_{RL}. Different moisture contents and tree species may also produce these differences. More data from the same or different species should be acquired to investigate the variation in these three elastic constants in dry or green wood.

3.3.2. Shear Modulus of Elasticity

The results of regression analysis for the shear modulus of elasticity and sampling position are provided in Figure 8 and Table 6. The relationships between sampling distance and the shear modulus

of elasticity are illustrated in Figure 8. Table 6 provides the corresponding fitting equations and correlation coefficients.

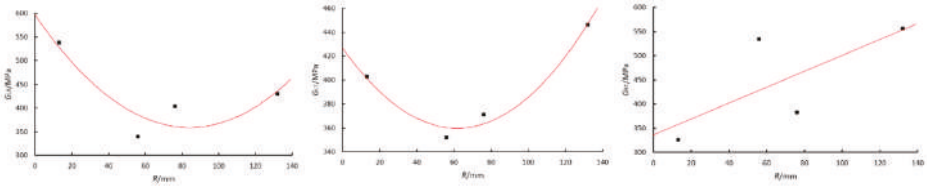

(**a**) (**b**) (**c**)

Figure 8. Relationships between distance from pith and shear moduli in: (**a**) Longitudinal-radial (LR) plane, (**b**) Longitudinal-tangential (LT) plane, and (**c**) Radial-tangential (RT) plane.

Table 6. Mathematical model of shear moduli and distance from pith.

Shear Modulus of Elasticity	Fitted Equation	Coefficient of Determination (R^2)
G_{LR}	$G_{LR} = 597.134 + 64.293R + 0.034R^2$	0.80
G_{LT}	$G_{LT} = 426.009 - 2.155R + 0.018R^2$	0.98
G_{RT}	$G_{RT} = 335.912 + 1.645R$	0.72

Figure 8 shows the variation patterns of the three shear moduli of elasticity (G_{LR}, G_{LT}, and G_{RT}) along the cross-section of wood. Figure 8a,b demonstrate a quadratic relationship between shear modulus of elasticity G_{LR} and sampling distance, as well as for shear modulus of elasticity G_{LT} and sampling distance. Both G_{LR} and G_{LT} first decreased with increasing sampling distance, and then increased at a sampling distance over 70 mm. G_{LR} and G_{LT} near the bark increased compared to the minimum values. However, the shear modulus of elasticity G_{RT} of green Chinese larch linearly increased with sampling distance. Table 6 shows the coefficient of determination for the shear modulus of elasticity G_{RT} and the sampling distance was 0.72, indicating a robust linear relationship between them. Even though a quadratic relationship was found in the shear modulus of elasticity G_{LR} and G_{LT}, their coefficients of determination were 0.80 and 0.98, respectively. The possible interpretation for the relatively lower coefficient of determination (R^2) for G_{RT} could be attributed to the large variability in wood performance especially in the cross-sections. Xavier et al. reported the shear stiffness ($Q_{66} = G_{LR}$) of dry Maritime pine decreased from the center (radial position r_1, 29% of the radius) to around the middle radius of stem (radial position r_2, 46% of the radius), and progressively increased afterward to the outermost positions (r_4, 81% of the radius) [33]. Despite the different moisture content and tree species, the variation in shear moduli G_{LR} along the whole cross-section derived in this research was basically in compliance with the results reported in Xavier's study. No study has reported the variation in the shear moduli G_{LT} and G_{RT} along the whole cross-section of wood, whether dry or green. Therefore, the variation patterns of shear moduli G_{LT} and G_{RT} presented in this paper could be used to describe the shear properties of green wood in LT and RT plane. More data from identical or different species need to be obtained to determine the variation in shear properties of dry or green wood, especially for shear moduli G_{LT} and G_{RT}.

3.3.3. Poisson's Ratio

The results from experimental data (Table 2) showed that the relationship between the values of the Poisson's ratios at the four sampling positions and sampling distance R was relatively discrete, except for Poisson's ratio ν_{RT}. To determine the quantitative relationship between Poisson's ratios and sampling distance R, three extra data points were inserted using interpolation for each Poisson's ratio, apart from ν_{RT}. Thus, the relationships between the Poisson's ratios and sampling distance R were obtained as shown in Figure 9a–f. The corresponding fitting equations are provided in Table 7.

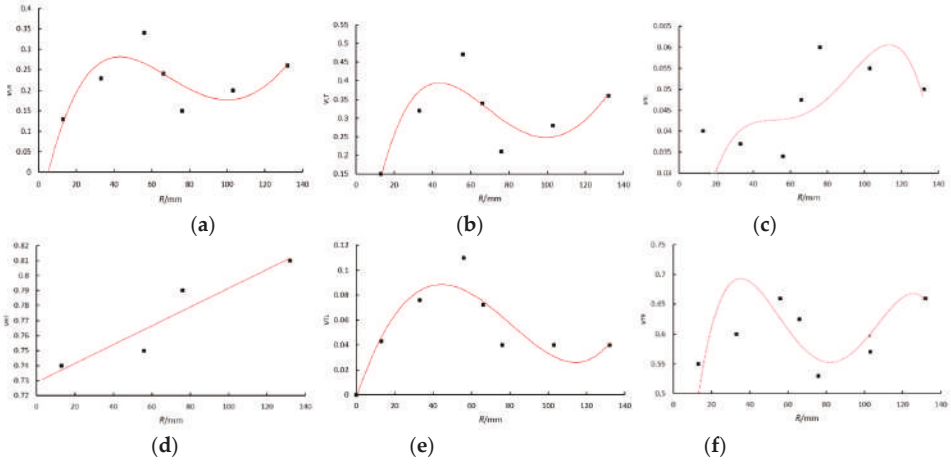

Figure 9. Relationships between distance from pith and Poisson's ratio of: (**a**) ν_{LR}, (**b**) ν_{LT}, (**c**) ν_{RL}, (**d**) ν_{RT}, (**e**) ν_{TL}, and (**f**) ν_{TR}.

Figure 9 shows the variation patterns of the six Poisson's ratios along the cross-section of the green wood. Figure 9d depicts the linear relationship between the Poisson's ratio ν_{RT} and sampling distance. Poisson's ratio ν_{RT} gradually increased with sampling distance. However, for the other five Poisson's ratios, there was a discrete relationship between the Poisson's ratio and sampling distance R. For Poisson's ratios ν_{LR}, ν_{LT}, and ν_{TR}, the values first increased at sampling distances lower than 50 mm and then significantly decreased as sampling distance varied from 50 mm to about 80 mm. When the sampling distance was over 80 mm, the values of Poisson's ratio increased with sampling distance again. However, similar results were not found for Poisson's ratios ν_{RL} and ν_{TL}. The values of the Poisson's ratios determined in this study irregularly changed with sampling distance probably due to the variation in moisture content, density, or microfibril angle in different parts of the wood. In general, no significant variation patterns were found in these five Poisson's ratios. Davies et al. estimated six Poisson's ratios both in outerwood and corewood from green *Pinus radiata* and no significant difference between outerwood and corewood was found [32]. Therefore, we still do not understand the variation patterns of the Poisson's ratios along wood cross-sections, and few researchers have evaluated the variation in the Poisson's ratios along the whole cross-section of dry or green wood. Therefore, more efforts are required to investigate the variation patterns of Poisson's ratio in the entire cross-section of dry or green wood.

Table 7. Mathematical model of Poisson's ratios and distance from pith.

Poisson's Ratio	Fitted Equation
ν_{LR}	$\nu_{LR} = -0.0078 + 0.0138R - 2.112 \times 10^{-4}R^2 + 8.8643\times10^{-7}R^3 - 3.155 \times 10^{-8}R^4$
ν_{LT}	$\nu_{LT} = -0.0124 + 0.0172R - 2.2671 \times 10^{-4}R^2 + 5.2757 \times 10^{-7}R^3 + 2.8007 \times 10^{-9}R^4$
ν_{RL}	$\nu_{RL} = 0.0044 + 0.00276R - 7.1388\times10^{-5}R^2 + 7.7972 \times 10^{-7}R^3 + 2.8887 \times 10^{-9}R^4$
ν_{RT}	$\nu_{RT} = 0.7312 + 6.2191R$
ν_{TL}	$\nu_{TL} = -0.0023 + 0.0046R - 6.7872 \times 10^{-5}R^2 + 1.9557\times10^{-3}R^3 + 5.4162 \times 10^{-10}R^4$
ν_{TR}	$\nu_{TR} = 0.028 + 0.0471R - 0.0011R^2 + 1.0274 \times 10^{-5}R^3 - 3.155 \times 10^{-8}R^4$

4. Conclusions

The objective of this study was to investigate the variation in the mechanical properties, especially elastic constants, of green Chinese larch from pith to sapwood. The conclusions are as follows:

(1) The relationships between longitudinal modulus of elasticity (E_L), radial modulus of elasticity (E_R), and tangential modulus of elasticity (E_T) were $E_L > E_R > E_T$ for all four sampling positions. Similarly, $\nu_{RT} > \nu_{LT} > \nu_{LR}$ were found for Poisson's ratios ν_{RT}, ν_{LT}, and ν_{LR} at the four sampling locations. These results align with the reported findings in dry wood.

(2) The sensitivity of each elastic constant to the sampling position was different, and the coefficient of variation ranged from 4.3% to 48.7%. The Poisson's ratios ν_{RT} measured at the four different sampling positions were similar and the differences between them were not significant. The coefficient of variation for Poisson's ratio ν_{RT} was only 4.3%. The four sampling positions had similar Poisson's ratios ν_{TL}, though the coefficient of variation was 11.7%. The Poisson's ratio ν_{LT} had the greatest variation in all elastic constants with a 48.7% in coefficient of variation.

(3) We found a good linear relationship between the longitudinal modulus of elastic E_L, shear modulus of elasticity G_{RT}, Poisson's ratio ν_{RT} and the distance from pith. E_L, G_{RT}, and ν_{RT} all increased with sampling distance R. However, a quadratic relationship existed in the tangential modulus of elasticity E_T, radial modulus of elasticity E_R, shear modulus of elasticity G_{LT}, shear modulus of elasticity G_{LR}, and the distance from pith. A discrete relationship was found in the other five Poisson's ratios.

Author Contributions: F.L. wrote the original draft of the manuscript and performed most of test and analysis work. H.Z. and C.G. supervised the research team and provided some ideas to research as well as revised the manuscript. F.J. provided the main idea of experiments and assisted with the experiments. X.W. conceived the project and provided technical guidance to the research.

Funding: This project was supported by "the Fundamental Research Funds for the Central Universities (NO. BLX201817)", China Postdoctoral Science Foundation (NO. 2018M641225), the Special Research Funds for Public Welfare (NO. 201304512) and the National Natural Science Foundation of China (No. 31328005).

Acknowledgments: The authors wish to thank Jianzhong Zhang for his grateful assistance of conducting the experiments.

Conflicts of Interest: The authors declare no conflict of interest.

References

1. Feng, H.L.; Li, G.H. Stress wave propagation model and simulation in non-destructive testing of wood. *J. Syst. Simul.* **2009**, *21*, 2373–2376.
2. Feng, H.L.; Li, G.H.; Fang, Y.M.; Li, J. Stress wave propagation modeling and application in wood testing. *J. Syst. Simul.* **2010**, *22*, 1490–1493.
3. Yang, X.C.; Wang, L.H. Study on the propagation theories of stress wave in log. *Sci. Silvae Sin.* **2005**, *41*, 132–138.
4. Liu, F.L.; Jiang, F.; Wang, X.P.; Zhang, H.J.; Yang, Z.H. *Stress Wave Propagation in Larch Plantation Trees—Numerical Simulation*; USDA Forest Service, Forest Products Laboratory, General Technical Report, FPL-GTR-239; USDA, Forest Products Laboratory: Madison, WI, USA, 22–25 September 2015; pp. 418–427.
5. Bodig, J.; Jayne, B.A. *Mechanics of Wood and Wood Composites*; Van Nostrand Reinhold Company, Inc.: New York, NY, USA, 1982; p. 712.
6. Sliker, A. A method for predicting non-shear compliance in the RT plane of wood. *Wood Fiber Sci.* **1988**, *20*, 44–45.
7. Sliker, A. Orthotropic strains in compression parallel to grain tests. *For. Prod. J.* **1985**, *35*, 19–26.
8. Sliker, A. A measurement of the smaller Poisson's ratios and related compliance for wood. *Wood Fiber Sci.* **1989**, *21*, 252–262.
9. Li, W.J. Elasticity and drying stresses of wood. *J. Nanjing Technol. Coll. For. Prod.* **1983**, *6*, 115–122.
10. Gong, M. A study of wood elastic parameters parallel to grain in compression test by using resistance strain gages. *Sci. Silvae Sin.* **1995**, *31*, 190–191.
11. Zhang, F.; Li, L.; Zhang, L. Study of the determination of the elastic constants and mechanical property parameters of five kinds of wood commonly used in furniture. *For. Mach. Woodwork. Equip.* **2012**, *40*, 16–19.
12. Skaar, C. *Wood-Water Relations*; Springer: Berlin Heidelberg, German, 1988.

13. Hering, S.; Keunecke, D.; Niemz, P. Moisture-dependent orthotropic elasticity of beech wood. *Wood Sci. Technol.* **2012**, *46*, 927–938. [CrossRef]
14. Jiang, J.; Bachtiar, E.V.; Lu, J.; Niemz, P. Moisture-dependent orthotropic elasticity and strength properties of Chinese fir wood. *Eur. J. Wood Wood Prod.* **2017**, *68*, 927–938. [CrossRef]
15. Ozyhar, T.; Hering, S.; Sanabria, S.; Niemz, P. Determining moisture-dependent elastic characteristics of beech wood by means of ultrasonic waves. *Wood Sci. Technol.* **2013**, *47*, 329–341. [CrossRef]
16. Bachtiar, E.V.; Sanabria, S.J.; Mittig, J.P.; Niemz, P. Moisture-dependent elastic characteristics of walnut and cherry wood by means of mechanical and ultrasonic test incorporating three different ultrasound data evaluation techniques. *Wood Sci. Technol.* **2017**, *51*, 47–67. [CrossRef]
17. Wang, L.Y.; Lu, Z.Y.; Shen, S.J. Study on twelve elastic constants values of Betula platyphylla Suk. wood. *J. Beijing For. Univ.* **2003**, *25*, 64–67.
18. Shao, Z.P.; Zhu, S. Study on determining the elastic constants of wood of Cunninghamia lanceolata by means of electric resistance-strain gauges. *J. Anhui Agric. Univ.* **2001**, *28*, 32–35.
19. Aira, J.R.; Arriaga, F.; Íñiguez-González, G. Determination of the elastic constants of Scots pine (*Pinus sylvestris* L.) wood by means of compression tests. *Biosyst. Eng.* **2014**, *126*, 12–22. [CrossRef]
20. Preziosa, C. Méthode de déTermination des Constantes éLastiques du Matériau Bois Par Utilisation des Ultrasons (Method for Determining Elastic Constants of Wood Material by Use of Ultrasound). Ph.D. Thesis, Université d'Orléans, Orléans, France, 1982.
21. Preziosa, C.; Mudry, M.; Launay, J.; Gilletta, F. Détermination des constantes élastiques du bois par une méthode acoustique goniométrique. (Determination of the elastic constants of wood by an acoustic method using immersion). *CR Acad. Sci. Paris Série II* **1981**, *293*, 91–94.
22. Bucur, V.; Archer, R.R. Elastic constants for wood by an ultrasonic method. *Wood Sci. Technol.* **1984**, *18*, 255–265. [CrossRef]
23. Francois, M.L.M. Identification des symétries matérielles de matériaux anisotropes (Identification of the Material Symmetries of Anisotropic Materials). Ph.D. Thesis, Université Pierre et Marie Curie-Paris VI, Paris, France, 1995.
24. Goncalves, R.; Trinca, A.J.; Pellis, B.P. Elastic constants of wood determined by ultrasound using three geometries of specimens. *Wood Sci. Technol.* **2014**, *48*, 269–287. [CrossRef]
25. Longo, R.; Delaunay, T.; Laux, D.; El Mouridi, M.; Arnould, O.; Le Clézio, E. Wood elastic characterization from a single sample by resonant ultrasound spectroscopy. *Ultrason* **2012**, *52*, 971–974. [CrossRef]
26. Majano-Majano, A.; Fernandez-Cabo, J.L.; Hoheisel, S.; Klein, M. A test method for characterizing clear wood using a single specimen. *Exp. Mech.* **2012**, *52*, 1079–1096. [CrossRef]
27. Vazquez, C.; Gonçalves, R.; Bertoldo, C.; Bano, V.; Vega, A.; Crespo, J.; Guaita, M. Determination of the mechanical properties of Castanea sativa Mill. using ultrasonic wave propagation and comparison with static compression and bending methods. *Wood Sci. Technol.* **2015**, *49*, 607–622. [CrossRef]
28. Yang, N.; Zhang, L. Investigation of elastic constants and ultimate strengths of Korean pine from compression and tension tests. *J. Wood Sci.* **2018**, *64*, 85–96. [CrossRef]
29. Dahmen, S.; Ketata, H.; Ben Ghozlen, M.H.; Hosten, B. Elastic constants measurement of anisotropic Olivier wood plates using air-coupled transducers generated Lamb wave and ultrasonic bulk wave. *Ultrasonics* **2010**, *50*, 502–507. [CrossRef]
30. Nadir, Y.; Nagarajan, P.; Midhun, A.J. Measuring elastic constants of Hevea brasiliensis using compression and Iosipescu shear test. *Eur. J. Wood Wood Prod.* **2014**, *72*, 749–758. [CrossRef]
31. Yoshihara, H.; Ohta, M. Estimation of the shear strength of wood by uniaxial-tension tests of off-axis specimens. *J. Wood Sci.* **2000**, *46*, 159–163. [CrossRef]
32. Davies, N.T.; Altaner, C.M.; Apiolaza, L.A. Elastic constants of green Pinus radiata wood. *N. Z. J. For. Sci.* **2016**, *46*, 399. [CrossRef]
33. Xavier, J.; Avril, S.; Pierron, F.; Morais, J. Variation of transverse and shear stiffness properties of wood in a tree. *Compos. Part A Appl. Sci. Manuf.* **2009**, *40*, 1953–1960. [CrossRef]

34. ASTM D5536-94. *Standard Practice for Sampling Forest Trees for Determination of Clear Wood Properties*; ASTM International: West Conshohocken, PA, USA, 1994.
35. ASTM D143-09. *Standard Test Method for Small Clear Specimens of Timber*; ASTM International: West Conshohocken, PA, USA, 2009.

© 2019 by the authors. Licensee MDPI, Basel, Switzerland. This article is an open access article distributed under the terms and conditions of the Creative Commons Attribution (CC BY) license (http://creativecommons.org/licenses/by/4.0/).

forests

MDPI

Article

Intra-Ring Wood Density and Dynamic Modulus of Elasticity Profiles for Black Spruce and Jack Pine from X-Ray Densitometry and Ultrasonic Wave Velocity Measurement †

Wassim Kharrat [1], Ahmed Koubaa [2,*], Mohamed Khlif [3] and Chedly Bradai [3]

[1] Centre de Recherche sur les Matériaux Renouvelables, Université Laval, Ville de Québec, QC G1V 0A6, Canada
[2] Institut de Recherche sur les Forêts, Université du Québec en Abitibi-Témiscamingue, Rouyn-Noranda, QC J9X 5E4, Canada
[3] Laboratoire des Systèmes électromécaniques (LASEM), École Nationale d'ingénieurs de Sfax, Sfax 3038, Tunisia
* Correspondence: ahmed.koubaa@uqat.ca; Tel.: +01-819-761-0971 (ext. 2579)
† This manuscript is part of an M.S. thesis by the first author, available online at depositum.uqat.ca.

Received: 30 May 2019; Accepted: 4 July 2019; Published: 9 July 2019

Abstract: Currently, ultrasonic measurement is a widely used nondestructive approach to determine wood elastic properties, including the dynamic modulus of elasticity (DMOE). DMOE is determined based on wood density and ultrasonic wave velocity measurement. The use of wood average density to estimate DMOE introduces significant imprecision: Density varies due to intra-tree and intra-ring differences and differing silvicultural treatments. To ensure accurate DMOE assessment, we developed a prototype device to measure ultrasonic wave velocity with the same resolution as that provided by the X-ray densitometer for measuring wood density. A nondestructive method based on X-ray densitometry and the developed prototype was applied to determine radial and intra-ring wood DMOE profiles. This method provides accurate information on wood mechanical properties and their sources of variation. High-order polynomials were used to model intra-ring wood density and DMOE profiles in black spruce and jack pine wood. The transition from earlywood to latewood was defined as the inflection point. High and highly significant correlations were obtained between predicted and measured wood density and DMOE. An examination of the correlations between wood radial growth, density, and DMOE revealed close correlations between density and DMOE in rings, earlywood, and latewood

Keywords: ultrasonic wave velocity measurement; nondestructive assessment; wood mechanical properties; intra-ring variation; dynamic modulus of elasticity

1. Introduction

"Wood quality is the resultant of physical and chemical characteristics possessed by a tree or a part of a tree that enable it to meet the property requirements for different end products" [1]. Wood density is considered to be the most important wood quality attribute. It is one of the most widely used parameters to predict the mechanical and other physical properties of wood, such as dimensional stability [2]. However, wood density and all its related wood quality attributes are highly variable, with multiple sources of variation, including differences within and between trees, between sites, and between genetic origins. This high variability is due to genetic, environmental, and physiological factors [3,4]. In a same species, variations in wood density also result from variations in anatomical characteristics such as earlywood and latewood width. Wood density is generally

defined as the ratio of the wood mass to volume, and is expressed in kilograms per cubic meter (kg/m^3). However, this definition does not consider variations in wood density due to biological processes such as earlywood and latewood formation, juvenile wood formation, or environmental conditions. Modern nondestructive measurement methods such as X-ray densitometry are widely used to assess wood quality variations due to biological processes (intra-ring and inter-ring variation), genetic sources, and environmental conditions (e.g., tree-to-tree, site-to-site, and silvicultural treatments).

Intra-ring wood density profiles obtained with X-ray densitometry are generally used to calculate ring density (RD), earlywood density (EWD), latewood density (LWD), ring width (RW), earlywood width (EWW), and latewood width (LWW). These parameters have been determined for many wood species, such as European oak [5], black spruce [2], and *Thuja occidentalis* [6]. Intra-ring wood density profiles are used to determine the use-specific suitability of wood, especially for high value-added applications [5,7]. Intra-ring wood density variation can also indicate wood uniformity and provide information about the wood growth process and the wood fiber yield [7,8].

Earlywood and latewood properties depend on the earlywood–latewood transition point (E/L). Several methods have been reported in the literature to determine the E/L, notably Mork's index [9]. There are at least two interpretations of Mork's index [10]. According to the first, the E/L is obtained when the double wall thickness becomes greater than or equal to the width of the cell lumen. Under the second interpretation, the E/L is obtained when the double cell wall thickness multiplied by two becomes greater than or equal to the lumen width. While this index, using either interpretation, is arbitrary and time-consuming to measure, it allows consistent determination of earlywood and latewood features.

Because Mork's index is based on the double wall thickness and the lumen diameter, these anatomical wood features must be measured in individual growth rings on microscopic slides or using indirect microscopic procedures [11]. In addition, this method is difficult to integrate into X-ray computations. Good agreement was found between earlywood and latewood features determined by three methods: Mork's index, threshold density, and the maximum derivative [12]. However, use of Mork's index and the maximum derivative produced better estimates of physiological variations compared to threshold density. Intra-ring wood density profiles are generally modelled to define the earlywood–latewood transition. Pernestål et al. [8] and Ivkovic et al. [13] used modified spline functions to model intra-ring wood density profiles. The E/L transition was defined using a numerical derivative method. Koubaa et al. [2] demonstrated that high-order polynomial functions consider both profile and intra-ring density variation for E/L estimation. These functions gave consistent estimates of the E/L transition point, with correlation coefficients between measured and predicted density well above 0.90 for the six order polynomial. These results are significant, because modelled intra-ring wood density profiles can simplify the modelling of final wood product properties [13].

While wood density is considered to be the most important wood quality attribute, elastic properties are also important, especially for engineering design purposes [14]. The wood dynamic modulus of elasticity (DMOE), being an elastic constant that describes wood mechanical behavior, is computed from the wood density and the ultrasonic wave velocity [15]. Ultrasonic wave velocity measurement is one of the most widely used nondestructive methods to assess the strength properties of living trees, logs, sawn timbers, and wood-based materials, due to its rapidity, flexibility, portability, cost-effectiveness, and ease of use [16–19]. Wood DMOE has been determined using ultrasonic wave velocity parallel to the grain direction and wood density based on the mass-to-volume ratio of specimens [15,18–21]. However, no study to date has investigated intra-ring wood DMOE profiles to determine variations between earlywood and latewood DMOE. A nondestructive method based on X-ray densitometry and ultrasonic wave velocity measurement was proposed to determine intra-ring wood DMOE profiles.

The objectives of this study were therefore to (1) develop a nondestructive method to determine intra-ring wood DMOE profiles; (2) model intra-ring wood density and DMOE profiles in black spruce and jack pine wood using high-order polynomial functions [2]; (3) determine radial variations in ring

wood density and ring DMOE; and (4) analyze correlations between wood radial growth, density, and DMOE.

2. Materials and Methods

X-ray densitometry provides intra-ring wood density profiles and determines both annual ring width and wood density components. Intra-ring wood ultrasonic velocity profiles were determined using the developed prototype and a Sonatest Masterscan ultrasonic flaw detector. The superposition of these two profiles is a nondestructive method to obtain the intra-ring wood DMOE profile.

2.1. Study Materials

The experimental material used in this study consisted of subsamples from previous studies on the wood quality of jack pine [22] and black spruce [23] sampled from even-aged stands in the Abitibi region of Québec, Canada. Eight black spruce and eight jack pine trees were used. Discs taken at breast height were used in this study. Bark-to-bark samples passing through the pith were extracted from each disc. Thin strips (15 to 20 mm wide and 1.57 to 1.9 mm thick) were sawn from each sample. The sawn strips were extracted with cyclohexane/ethanol (2:1) solution for 24 h and then with distilled water for another 24 h to remove extraneous compounds [24]. After extraction, the strips were air-dried under restraint to prevent warping. Samples were then conditioned to 8% equilibrium moisture content before measurement. The same samples were used to determine wood density and ultrasonic wave propagation time. In this study, a nondestructive method based on X-ray densitometry and ultrasonic wave velocity measurement was used to determine intra-ring wood density and DMOE variation.

2.2. Wood Ring Density and Width Measurement

Ring density (RD) and ring width (RW) were measured for each ring using a QTRS-01X Tree-Ring Scanner (Quintek Measurement Systems, Knoxville, TN, USA). The QTRS passes thin strips from increment cores through an accurately collimated soft X-ray beam using a precisely controlled stepping system and linear bearing carriage. Video images of both the wood sample surface and the X-ray density graph are displayed at the same scale on the screen. A linear resolution step size of 40 μm was used for the X-ray densitometry. Rings from pith to bark were scanned in air-dry condition to estimate the basic wood density (ovendry weight/green volume) for each ring. Ring density (RD) and ring width (RW) for each ring were determined based on intra-ring microdensitometer profiles. Incomplete or false rings and rings with compression wood or branch tracers were eliminated from the analysis. Matlab software (R2016a, the MathWorks, Inc., Natick, MA, USA) was used to determine the intra-ring wood density profiles at 40 μm resolution.

2.3. Wood Ultrasonic Wave Velocity Measurement

An in-house prototype device was developed for measuring the ultrasonic wave propagation time with the same resolution as that used for the wood density measurement by X-ray densitometry (40 μm). The prototype (Figure 1) consists of a motorized linear translation stage that holds the sample and is controlled by a microcontroller. The ultrasonic wave propagation time in the wood sample is measured between the ultrasonic transmitter (Spot Weld Transducer) and the receiver transducers (Fingertip Contact Transducer CF) at 40 μm resolution. The ultrasonic transducers are mounted in parallel to two mini motorized actuators to ensure constant pressure during measurement.

Following the X-ray densitometry density measurement, nondestructive ultrasonic wave propagation measurement was applied to the same samples using a Masterscan 380 (Sonatest Inc., San Antonio, TX, USA) equipped with 10 MHz frequency transducers. Ultrasonic waves were applied to the samples through two transducers (transmitting and receiving). A coupling agent (Vaseline original petroleum jelly) was used to aid the transmission of the transducer pulses into the test specimens.

A correction factor (C_f; s) was applied to calculate the ultrasonic wave velocity in the wood samples to take into consideration the transport time of the electric waves within the measuring circuit.

A Plexiglas sample having the same thickness as the wood samples (2 mm) was used as a reference to determine the correction factor (Equation (1)) [20,25]. The ultrasonic velocity (V; m/s) was then calculated using Equation (2):

$$C_f = t_r - (d_r / v_r) \quad (1)$$

$$V = d/(T - C_f) \quad (2)$$

where d is the thickness of the wood sample (m), T is the ultrasonic wave propagation time (s), t_r is the wave propagation time through the reference Plexiglas core (s), d_r is the thickness of the reference Plexiglas core (m), and v_r is the wave velocity in the reference Plexiglas core (2670 m/s).

The dynamic modulus of elasticity (DMOE; MPa) based on the ultrasonic method was determined using the following one-dimensional wave equation:

$$\mathrm{DMOE} = \rho \times V^2 \times 10^{-6}. \quad (3)$$

where ρ is the wood density measured by X-ray densitometry (kg/m^3) and V is the ultrasonic wave velocity calculated using Equation (1).

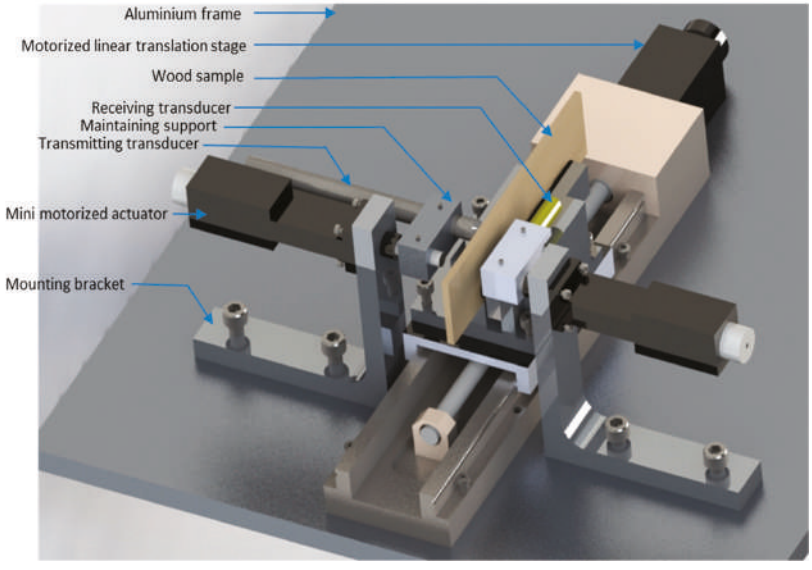

Figure 1. Prototype device for measuring the ultrasonic wave propagation time.

2.4. Modelling Intra-Ring Wood Density and Dynamic Modulus of Elasticity Profiles

In this study, we used 6th order polynomial functions to model intra-ring wood density and DMOE profiles for black spruce and jack pine wood (Equation (4)).

$$R = a_0 + a_1 RW + a_2 RW^2 + a_3 RW^3 + a_4 RW^4 + a_5 RW^5 + a_6 RW^6 \quad (4)$$

where R is the ring density or ring DMOE, RW is the ring width in proportion, and a_i are the parameters to be estimated.

The E/L transition was defined as the inflection point obtained from the within-ring density and DMOE profiles. The E/L transition is obtained by equalling the second derivative of the polynomial function to zero (Equation (5)). For a 6th order polynomial function, the second derivative gives 4 solutions, but only one solution is of interest. Certain restrictions were specified in the Matlab

program to obtain this unique solution. These restrictions specify that the solution should be included in a positive slope and in the range of 40 to 90% of the ring width proportion. If more than one solution is obtained, the highest value among the solutions is chosen.

$$d^2R/dRW^2 = 2a_2 + 6a_3RW + 12a_4RW^2 + 20a_5RW^3 + 30a_6RW^4 \quad (5)$$

2.5. Statistical Analysis

For both softwood species (black spruce and jack pine), the correlations between the wood radial growth, density, and DMOE components were determined using R software (Version 2.15.0 R, R Development Core Team, 2012, Vienna, Austria).

3. Results and Discussion

Typical X-ray density and DMOE profiles for jack pine wood are shown in Figure 2. Both the within-ring and radial pattern variation in these properties are shown.

3.1. Intra-Ring Wood Density and Dynamic Modulus of Elasticity Profiles

Figure 3 shows the within-ring variation in wood density and DMOE for black spruce and jack pine, revealing similar within-ring density patterns between the two species. Wood density and DMOE increase slowly in earlywood to reach a maximum in latewood. Both properties decrease thereafter at about mid-latewood width to reach a minimum at the boundary between two growth rings. The similarity between intra-ring density and DMOE profiles confirms the close relationship between wood density and wood stiffness, even at the intra-ring level. Some slight differences between the intra-ring density and DMOE profiles appear in earlywood. Thus, the intra-ring wood density profiles increase more slowly in earlywood compared to the DMOE profiles, which show a relatively sharp increase. Similar patterns of within-ring density variation were obtained by Koubaa et al. [2] for black spruce and by Ivkovic et al. [13] for Norway spruce and Douglas fir.

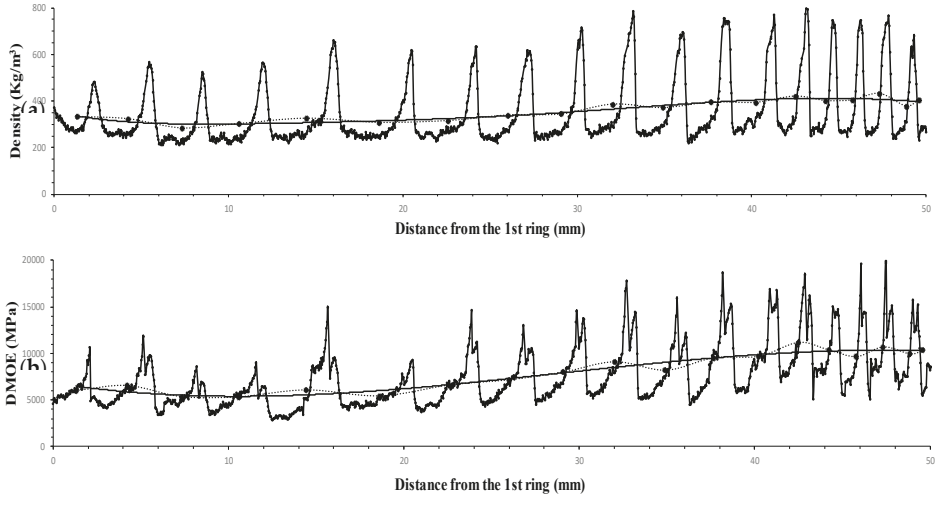

Figure 2. Examples of jack pine profiles showing radial variation in: (**a**) Wood density and (**b**) DMOE in (from ring 2 to 19).

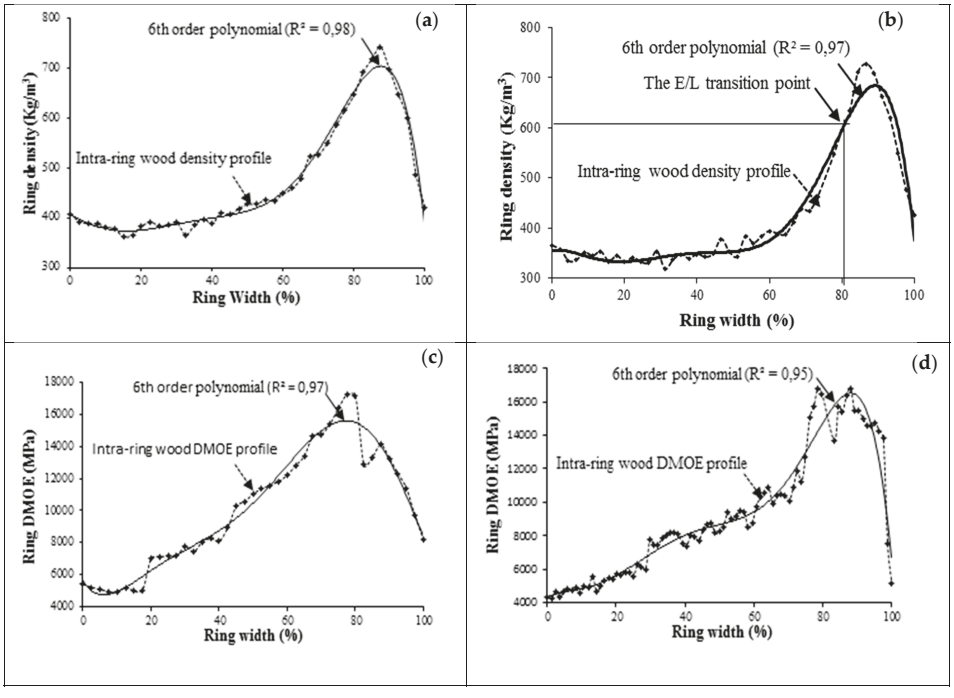

Figure 3. Examples of within-ring profiles and the fits obtained with the 6th order polynomials for: (**a**) Ring density in black spruce; (**b**) ring density in jack pine; (**c**) DMOE in Black spruce; and (**d**) DMOE in Jack pine.

The same 6th polynomial function modeling approach suggested by Koubaa et al. [2] was used to model within-ring density and DMOE profiles for the black spruce and jack pine samples in this study. Figure 3 illustrates the fitness of the 6th order polynomials for the intra-ring density and DMOE profiles for both softwoods species: (a) Black spruce and (b) jack pine. Table 1 confirms the fitness. The correlation coefficients obtained between the measured and predicted ring density data range from 0.88 to 1.00, with an average well above 0.95. These results indicate that these models can well describe intra-ring wood density profiles obtained from black spruce and jack pine, and probably other softwood species, as the coefficients are in good agreement with those obtained by Koubaa et al. [2] for black spruce.

Table 1 also indicates that high-order polynomials fit well the intra-ring DMOE profiles for black spruce and jack pine. The correlation coefficients obtained between measured and predicted DMOE data using the 6th order polynomial models range from 0.80 to 0.99, with an average well above 0.90 (Table 1). These results indicate that high-order polynomials can describe DMOE profiles well for these two softwoods.

The measured elastic properties of wood material yield essential information for the understanding of bonding at a very fine structural level [14]. As the elastic properties describe the mechanical behavior of wood, it is mandatory to determine intra-ring wood DMOE profiles. Moreover, modelled intra-ring wood DMOE profiles can serve as effective prediction tools for wood mechanical behavior.

3.2. The Earlywood–Latewood Transition

Table 2 shows that wood density at the E/L transition point (Figure 3b) (E/L transition density) as defined by the inflexion point method presents large variation for black spruce (Figure 4a) and jack

pine (Figure 4b). The radial variation pattern for the E/L transition density in black spruce (Figure 4a) is similar to that reported by Koubaa et al. [2], and is characterized by large variation with no specific trend. In contrast, the radial variation for the E/L transition in jack pine (Figure 4b) is characterized by a steady increase in juvenile wood and a tendency to level off in mature wood. Similar radial variation patterns for the E/L wood transition were observed by Park et al. [22].

Table 1. Average, standard variation (between parenthesis) and range of Pearson's coefficient of determination between measured and predicted within-ring density and DMOE values from the 6th order polynomial models for different rings for black spruce and jack pine.

	Ring from Pith			
	5	10	15	20
Wood density profiles				
Black spruce				
Average profiles	0.96 (0.02)	0.97 (0.02)	0.96 (0.02)	0.97(0.02)
Range	0.88–0.99	0.91–0.99	0.91–0.99	0.92–1.00
Jack pine				
Average profiles	0.96 (0.02)	0.95 (0.02)	0.97 (0.02)	0.98 (0.01)
Range	0.92–0.98	0.90–1.00	0.89–0.99	0.96–0.99
Dynamic modulus of elasticity profiles				
Black spruce				
Average profiles	0.92 (0.03)	0.94 (0.04)	0.95 (0.03)	0.95 (0.02)
Range	0.82–0.99	0.88–0.99	0.86–0.99	0.91–0.99
Jack pine				
Average profiles	0.89 (0.04)	0.93 (0.02)	0.93 (0.03)	0.94 (0.02)
Range	0.80–0.97	0.88–0.98	0.82–0.99	0.91–0.99

Within a same ring, the E/L transition also shows substantial variation in the true measures, as indicated by the relatively large standard errors (Figure 4a,b, Table 2). For example, the E/L transition density for the 10th annual ring from the pith varies from 541 to 655 kg/m^3 and from 548 to 672 kg/m^3 in black spruce and jack pine, respectively (Table 2). These results concur with the findings by Koubaa et al. [26] for black spruce and by Park et al. [22] for jack pine. Earlywood and latewood density defined by this method also show large variation. Thus, for a same annual ring, earlywood density ranges from 383 to 432 kg/m^3 for black spruce and from 318 to 367 kg/m^3 for jack pine.

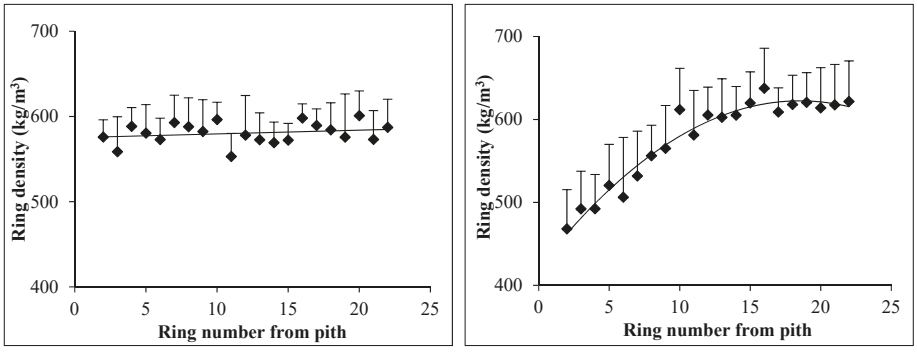

Figure 4. Radial variation in E/L transition density (bars indicate the standard error) for (**a**) black spruce and (**b**) jack pine.

As shown in Table 2, wood density is variable at the E/L transition point for black spruce and jack pine. For black spruce, the average wood density at the E/L transition point is variable and higher

than the 590 kg/m^3 reported by Koubaa et al. [2], as well as the threshold wood density of 540 kg/m^3 used for black spruce in X-ray densitometry programs. The results for jack pine are similar: The E/L transition density is variable and higher than the threshold density typically used for jack pine in X-ray densitometry programs. As the wood density at the E/L transition point, as defined by the inflexion point method, is variable and higher than the threshold wood density, the average earlywood and latewood width and density as defined by the inflexion point method will differ from those defined by the threshold method, for both black spruce and jack pine. Earlywood width defined by the inflexion point method will be greater, whereas latewood width will be smaller. Consequently, the latewood proportion defined by the inflexion point method will be lower. These results confirm the findings by Koubaa et al. [2] that the E/L transition point varied greatly among individual growth rings and that the use of a predetermined fixed threshold wood density does not reflect the variation in intra-ring wood density profiles across growth rings in a species.

Table 2. Average (Av), range (Ra), and standard variation for ring width, wood density, and wood DMOE at the earlywood–latewood transition and in earlywood and latewood, as defined by the inflexion method for different rings.

	Black Spruce			**Jack Pine**		
	Ring Number from the Pith					
	5	**10**	**20**	**5**	**10**	**20**
			Earlywood width			
Av (mm)	1.32 (0.37)	1.26 (0.35)	1.02 (0.20)	2.65 (0.27)	2.05 (0.31)	1.23 (0.32)
Ra (mm)	0.69–1.95	0.81–1.88	0.72–1.37	2.05–3.17	1.40–2.74	0.87–2.09
			Latewood width			
Av (mm)	0.39 (0.12)	0.30 (0.08)	0.23 (0.06)	0.58 (0.06)	0.50 (0.06)	0.38 (0.10)
Ra (mm)	0.22–0.61	0.15–0.48	0.16–0.31	0.47–0.67	0.44–0.58	0.25–0.63
			Earlywood density			
Av (kg/m^3)	415 (27)	403 (14)	385 (17)	316 (16)	340 (13)	331 (22)
Ra (kg/m^3)	376–491	383–432	344–418	296–348	318–367	295–359
			Latewood density			
Av (kg/m^3)	637 (47)	673 (20)	692 (36)	612 (58)	734 (89)	726 (62)
Ra (kg/m^3)	578–729	568–796	591–746	502–769	605–856	581–798
			Density at the earlywood latewood transition			
Av (kg/m^3)	580 (33)	596 (20)	600 (29)	520 (49)	612 (49)	614 (48)
Ra (kg/m^3)	536–653	541–655	547–649	433–623	548–672	482–674
			Earlywood dynamic modulus of elasticity			
Av (GPa)	11.2 (2.5)	11.1 (1.6)	11.8 (2.6)	6.4 (0.8)	9.9 (1.2)	10.7 (1.9)
Ra (GPa)	8.3–17.6	6.5–13.7	8.2–15.3	5.2–8.1	7.9–1.2	8.0–1.4
			Latewood dynamic modulus of elasticity			
Av (GPa)	14.8 (2.4)	15.2 (2.5)	17.9 (2.4)	10.6 (1.6)	14.6 (1.0)	16.3 (3.6)
Ra (GPa)	11.9–21.7	10.3–18.8	14.0–22.1	8.1–12.1	12.9–16.9	11.9–21.0
			Dynamic modulus of elasticity at the earlywood latewood transition			
Av (GPa)	13.4 (2.1)	13.6 (1.9)	15.4 (1.9)	9.8 (1.4)	12.9 (1.2)	14.9 (1.9)
Ra (GPa)	10.4–17.7	9.3–15.8	13.1–18.4	6.4–12.2	11.2–15.9	11.2–17.1

The same method was used to determine earlywood DMOE (EWDMOE), latewood DMOE (LWDMOE), and DMOE at the earlywood–latewood transition (Figure 5a,b). Thus, the wood DMOE at the E/L transition for the 10th annual ring varied from 9261 to 15,798 MPa for black spruce and from 11,162 to 15,950 MPa for jack pine. For the same annual ring, EWDMOE ranged from 6500 to 13,652 MPa for black spruce and from 7946 to 11,613 MPa for jack pine. LWDMOE also showed large variation: From 10,327 to 18,792 MPa for black spruce and from 12,873 to 16,916 MPa for jack pine (Table 2). The radial DMOE patterns at the E/L transition for black spruce (Figure 5a) and jack pine (Figure 5b) are shown. As shown in Figure 4a, the radial variation pattern for the E/L transition density in black spruce is characterized by large variation with no specific trend. Similar radial variation patterns for the E/L transition density were observed by Koubaa et al. [2]. In contrast, for jack pine,

the radial variation pattern for the E/L transition density is characterized by a steady increase in juvenile wood and a tendency to level off in mature wood (Figure 4b). The radial variation pattern for the E/L transition DMOE in black spruce (Figure 5a) is similar to jack pine (Figure 5b) characterized by a linear increase. These results confirm the importance of measuring ring density and RDMOE separately in order to obtain a more detailed characterization of wood mechanical behavior.

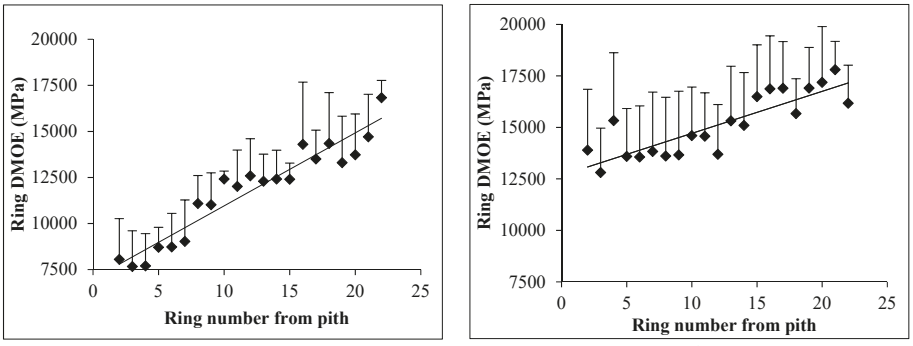

Figure 5. Radial variation in E/L transition DMOE (bars indicate the standard error) for (**a**) black spruce ad (**b**) jack pine.

Figure 6 illustrates the close relationship between the transition DMOE measured for the earlywood–latewood transition density and the transition DMOE, as defined by the inflexion point method for all tested samples (black spruce and jack pine). A linear regression curve ($y = 1.06x$) was obtained. Student's t test was applied and results indicated no significant differences between the transition DMOE calculated for the earlywood–latewood transition density and the transition DMOE as defined by the inflexion point method calculated from DMOE data. These results reaffirm the close relationship between wood density and wood mechanical properties, and particularly wood DMOE.

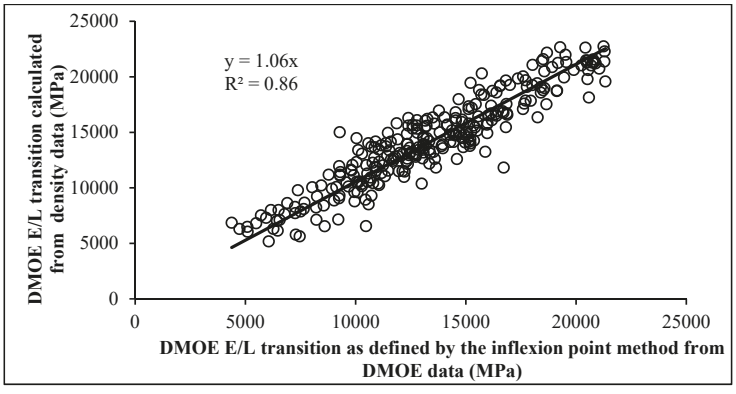

Figure 6. Relationship between transition DMOE calculated at the earlywood–latewood (E/L) transition density and transition DMOE, as defined by the inflexion point method for black spruce and jack pine.

3.3. Radial Variation in Ring Wood Density and Ring Dynamic Modulus of Elasticity

The mean values for intra-ring density over all samples for both black spruce (a) and jack pine (b) are shown in Figure 7a,b, respectively. The radial variation pattern for wood density is similar to that reported by Park et al. [22] for jack pine, Koubaa et al. [26] for black spruce, and Grabner et al. [24]

for European larch. The ring density is relatively high near the pith and decreases thereafter to reach a minimum in the transition zone leading into the mature wood, where a slow and steady increase is observed. Earlywood density (Figure 7a) decreases rapidly from a maximum near the pith to a low value in the transition zone. The density decreases slowly thereafter with age [26]. Latewood density (Figure 7a) increases almost linearly to a maximum at about ring 13, then levels off in the transition zone and the mature wood [22]. Similar typical variation patterns are seen for DMOE (Figure 8a,b). Ring DMOE increases with tree age, then levels off beyond the 13th ring. A similar radial variation pattern for DMOE was previously reported for hybrid poplar [25]. However, no study to date has investigated radial variation in earlywood and latewood DMOE (EWDMOE and LWDMOE). RDMOE and LWDMOE increase almost linearly in juvenile wood to a maximum at about ring 15, then decrease slowly thereafter through the outer rings in mature wood (Figure 8a,b).

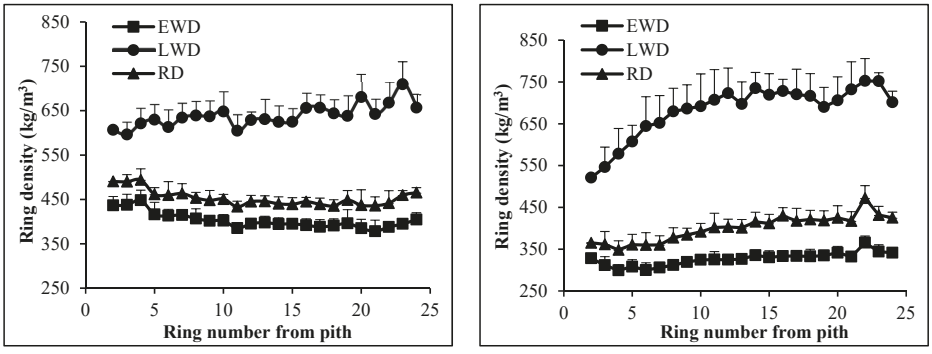

Figure 7. Radial variation in ring density (RD), earlywood density (EWD), and latewood density (LWD) for (**a**) black spruce and (**b**) jack pine.

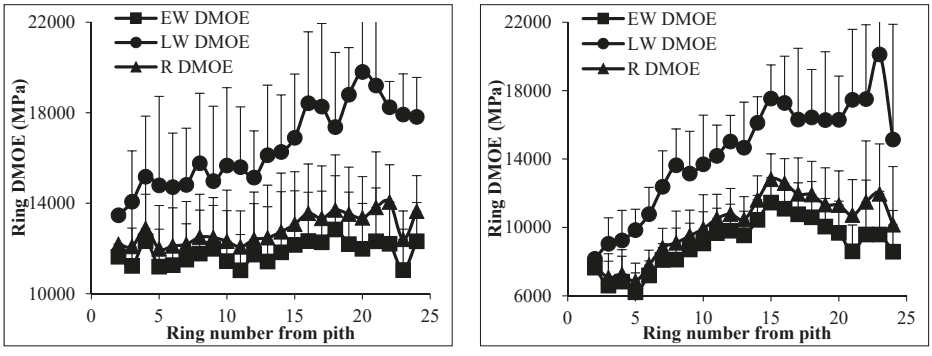

Figure 8. Radial variation in ring dynamic modulus of elasticity (RDMOE), earlywood dynamic modulus of elasticity (EWDMOE), and latewood dynamic modulus of elasticity (LWDMOE) for (**a**) black spruce and (**b**) jack pine.

3.4. Relationships between Growth, Density, and Elastic Properties

The developed prototype enabled determining relationships between ultrasonic velocity and wood density in rings, earlywood, and latewood (Figures 9 and 10). The coefficient of determination for the linear correlation between RD measured with X-ray densitometry and ring ultrasonic velocity obtained from the developed prototype was $R^2 = 0.66$ using black spruce and jack pine data (Figure 9).

Moderate linear correlations were also obtained between ring, earlywood, and latewood density and ultrasound speed of propagation for Jack pine (Figure 10) and black spruce (not shown).

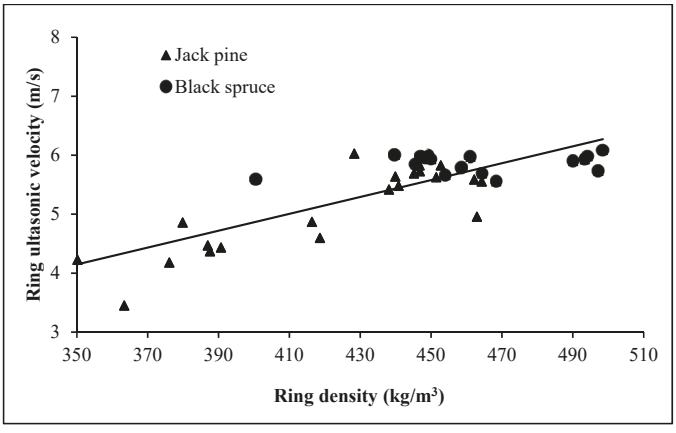

Figure 9. Relationship between ring density and ring ultrasonic velocity for black spruce and jack pine.

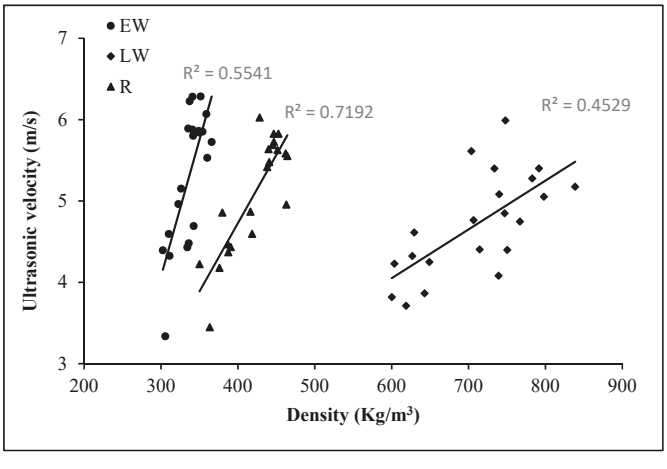

Figure 10. Relationships between wood density and ultrasonic velocity in rings (R), earlywood (EW), and latewood (LW) for jack pine.

Table 3 indicates that ring density is positively correlated with earlywood and latewood density. However, for both softwood species, the correlations between ring density and earlywood density are higher than between ring density and latewood density. These results concur with previous studies of black spruce [27]. Ring DMOE shows similar results. Thus, for both black spruce and jack pine, the correlations between ring DMOE and earlywood DMOE are higher than those between ring DMOE and latewood DMOE. The close correlations between DMOE and density shown in Table 3 are due to the fact that the DMOE is obtained from density (Equation (3)). Table 3 also shows a negative and statistically significant correlation between RDMOE and RW. Similar results were found for both earlywood and latewood. In contrast, high positive relationships were found between RDMOE and both earlywood and latewood DMOE, for both softwood species (Table 3). These results have practical implications for a considerably accurate, nondestructive determination of wood density, growth, and stiffness from small samples.

Table 3. Pearson's coefficient of correlations between the different traits for black spruce (upper row) and jack pine (lower row).

	RW	EWW	LWW	RD	EWD	LWD	RDMOE	EWDMOE	LWDMOE
RW		0.98 ***	0.81 ***	−0.21 *	0.00 ns	−0.36 *	−0.37 *	−0.29 *	−0.49 **
EWW	0.99 ***		0.73 ***	−0.25 *	−0.03 ns	−0.32 *	−0.38 *	−0.30 *	−0.49 **
LWW	0.82 ***	0.77 ***		−0.02 ns	0.08 ns	−0.49 **	−0.31 *	−0.25 *	−0.50 **
RD	−0.69 **	−0.72 ***	−0.42 **		0.91 ***	0.37 *	0.45 **	0.44 **	0.33 *
EWD	−0.58 **	−0.58 **	−0.39 *	0.85 ***		0.11 ns	0.40 **	0.46 **	0.18 ns
LWD	−0.50 **	−0.49 **	−0.52 **	0.75 ***	0.48 **		0.18 ns	0.09 ns	0.49 **
RDMOE	−0.65 **	−0.66 ***	−0.48 **	0.79 ***	0.65 **	0.66 ***		0.98 ***	0.85 ***
EWDMOE	−0.60 **	−0.61 **	−0.44 **	0.73 ***	0.65 **	0.57 **	0.98 ***		0.75 ***
LWDMOE	−0.61 **	−0.60 **	−0.55 **	0.74 **	0.54 **	0.80 ***	0.89 ***	0.78 ***	

* Significant at $\alpha = 0.05$; ** Significant at $\alpha = 0.01$; *** Significant at $\alpha = 0.001$; ns not significant. RW: ring width, EWW: earlywood width, LWW: latewood width, RD: ring density, EWD: earlywood density, LWD: latewood density, RDMOE: ring dynamic modulus of elasticity, EWDMOE: earlywood dynamic modulus of elasticity, LWDMOE: latewood dynamic modulus of elasticity.

4. Practical Implications

For this study, we developed a rapid nondestructive method to determine wood density and the dynamic modulus of elasticity (DMOE) based on X-ray densitometry and ultrasonic wave velocity measurement. This method was used to determine earlywood and latewood properties in order to obtain a more detailed characterization of wood mechanical behavior. Only a few studies have investigated earlywood and latewood elastic properties [28–32]. Roszyk et al. [29] reported that latewood modulus of elasticity (MOE) is higher than earlywood MOE for scots pine at low moisture content (8%). Similar results were obtained for Spruce wood [*Picea abies (L.) Karst*] [31] and loblolly pine [28–32] with an important increase in MOE values with the growth of annual rings. However, the preparation of initial and final wood samples was quite complicated and required perfectly parallel annual rings. Different methods have been used to retrieve two adjacent earlywood and latewood bands of 1 mm thick for loblolly pine [28–32]. Moliński et al. [31] reported that two adjacent wood samples were cut out from the region in which the borders of annual rings were straight lines parallel to the longer axis of the plank to obtain two earlywood and latewood samples of 200 µm in thickness for Spruce wood. Thus, it is important to use a rapid nondestructive method with easily prepared samples to determine wood intra-ring mechanical properties, which have direct impacts on wood processing performance. In fact, understanding mechanical properties variations at the earlywood-latewood scale will eventually allow a better knowledge of wood's areas of weakness in order to optimize the performance of wood products. At the wood processing industry scale, this information would be important for mechanical pulping processes where the pulping and refining energies and wood fractioning are closely related to the fiber characteristics including earlywood and latewood mechanical properties [33]. Similarly, oriented strand board (OSB) manufacturing and properties are directly related to earlywood and latewood mechanical properties [28,34]. The results of this study further confirm that ultrasonic measurement can be used to determine the elastic constants of wood with considerable accuracy (0.04 mm). Indeed, the relationships found between ultrasonic wave velocity, density, and wood stiffness demonstrate the experimental efficiency of ultrasonic measurement [35]. Whereas several studies have investigated relationships between static and dynamic MOE in wood [15,19,20,36] and have found significant linear correlations between them, only a few studies have investigated relationships between wood DMOE and wood density [37,38]. For example, linear correlations ($r = 0.70$) were found between DMOE and wood density for *Eucalyptus delegatensis* [39].

The relationships between tree growth and wood properties, especially in terms of mechanical properties, are critical for effective forest management strategies [19,39]. Russo et al. [39] reported that the effects of silvicultural practices (different intensities of thinning) on wood quality can be identified using acoustic measurement to assess the MOED of standing trees with non-destructive method in Calabrian pine. The authors demonstrated that using a low intensity of thinning induced better tree wood quality. In boreal species, enhanced growth through tree improvement programs or

intensive forest management strategies can significantly diminish the wood mechanical properties due to several biological factors, including increased earlywood proportion and the production of larger cells with thinner walls. Several anatomical and physical characterization studies have clearly demonstrated the impact of intensive forest management strategies on earlywood, latewood, and overall wood properties [40]. Nevertheless, the impact of intensive forest management on wood mechanical properties has received relatively little attention due to sample size constraints, the destructive nature of characterization tests, and the lack of effective tools for rapid, nondestructive characterization of these properties at the ring level. Nondestructive assessment is essential for understanding the impact of intensive forest management practices on wood mechanical properties as well as the physiological and biological processes involved in wood strength development [39]. The method developed here allows nondestructive measurement of intra-ring wood DMOE and provides deeper insights into wood strength development and its relationships to growth and wood density. As shown in Table 3, radial profiles enable investigating relationships between wood radial growth, density, and elastic properties in rings, earlywood, and latewood.

5. Conclusions

Based on the results of this study, the following conclusions can be drawn:

(1) Intra-ring wood dynamic modulus of elasticity (DMOE) profiles can be determined using a nondestructive method based on X ray densitometry and ultrasonic wave velocity measurement.

(2) Sixth order polynomials can well describe intra-ring wood density and dynamic modulus of elasticity profiles in black spruce and jack pine.

(3) The inflexion point method can be used to determine with considerable accuracy the earlywood–latewood transition density and DMOE in black spruce and jack pine.

(4) For black spruce and jack pine, the correlation coefficients between wood density and wood DMOE were positive and statistically significant in rings, earlywood, and latewood. Furthermore, high positive correlations were obtained between ring DMOE and both earlywood and latewood DMOE.

Author Contributions: Conceptualization, A.K., W.K., C.B. and M.K.; methodology, W.K. and A.K.; formal analysis, W.K. and A.K.; investigation, W.K. and A.K.; resources, A.K.; data curation, W.K. and A.K.; writing—original draft preparation, W.K.; writing—review and editing, A.K., M.K., C.B.; supervision, A.K., C.B. and M.K.; project administration, A.K.; funding acquisition, A.K.

Funding: This research was funded by the Canada Research Chair Program, Grant number: 557752; MITACS Grant number: IT04397 and Natural Resources Canada, CWFC 2017-2018.

Acknowledgments: The authors are grateful to Gilles Villeneuve and Williams Belhadef for their invaluable technical assistance. The authors also thank Besma Bouslimi and Zahia Ait-Si-Said for assistance with X-ray density measurements. Thanks also to Margaret McKyes for linguistic editing.

Conflicts of Interest: The authors declare no conflict of interest. The funders had no role in the design of the study; analyses, interpretation of data; in the writing of the manuscript, or in the decision to publish the results.

References

1. Mitchell, H. *A Concept of Intrinsic Wood Quality and Nondestructive Methods for Determining Quality in Standing Timber*; Forest Service, U.S. Report No 2233; Forest Products Laboratory: Madison, WI, USA, 1961.
2. Koubaa, A.; Tony Zhang, S.Y.; Makni, S. Defining the transition from earlywood to latewood in black spruce based on intra-ring wood density profiles from X-ray densitometry. *Ann. For. Sci.* **2002**, *59*, 511–518. [CrossRef]
3. Panshin, A.J.; De Zeeuw, C. *Textbook of Wood Technology*; McGraw-Hill Book Co: New York, NY, USA, 1980; p. 772.
4. Rozenberg, P.; Franc, A.; Bastien, C.; Cahalan, C. Improving models of wood density by including genetic effects: A case study in Douglas-Fir. *Ann. For. Sci.* **2001**, *58*, 385–394. [CrossRef]
5. Zhang, S.Y.; Nepveu, G.; Owoundi, R.E. Intratree and intertree variation in selected wood quality characteristics of European oak (Quercus petraea and Quercus robur). *Can. J. For. Res.* **1994**, *24*, 1818–1823. [CrossRef]

6. Bouslimi, B.; Koubaa, A.; Bergeron, Y. Anatomical properties in *Thuja occidentalis*: Variation and relationship to biological processes. *IAWA J.* **2014**, *35*, 363–384. [CrossRef]
7. Zobel, B.J.; Van Buijtenen, J.P. *Wood Variation: Its Causes and Control*; Springer: Berlin, Germany, 1989; p. 363.
8. Pernestal, K.; Jonsson, B.; Larsson, B. A simple model for density of annual rings. *Wood Sci. Technol.* **1995**, *29*, 441–449. [CrossRef]
9. Mork, E. Die qualität des fichtenholzes unterbesonderer rücksichtnahme auf schleif-und papierholz. *Papier-Fabrikant* **1928**, *26*, 741–747.
10. Denne, M.P. Definition of latewood according to Mork (1928). *IAWA Bull.* **1988**, *10*, 59–62. [CrossRef]
11. Evans, R.; Gartside, G.; Downes, G. Present and prospective use of Silviscan for wood microstructure analysis. In Proceedings of the 49th Appita Annual General Conference proceedings 1995, Hobart, Australia, 2–7 April 1995; pp. 91–96.
12. Barbour, R.J.; Bergqvist, G.; Amundson, C.; Larsson, B.; Johnson, J.A. New methods for evaluating intra-ring X-ray densitometry data: Maximum derivative methods as compared to Mork's index. In Proceedings of the CTIA/IUFRO International Wood Quality Workshop, Quebec, QC, Canada, 18–22 August 1997; p. 61.
13. Ivkovic, M.; Rosenberg, P. A method for describing and modelling of within-ring wood density distribution in clones of three coniferous species. *Ann. For. Sci.* **2004**, *61*, 759–769. [CrossRef]
14. Bucur, V.; Archer, R.R. Elastic constants for wood by an ultrasonic method. *Wood Sci. Technol.* **1984**, *18*, 255–265. [CrossRef]
15. Hassan, K.T.; Horacek, P.; Tippner, J. Evaluation of stiffness and strength of Scots Pine wood using resonance frequency and ultrasonic techniques. Dynamic test of wood. *BioResources* **2013**, *8*, 1634–1645. [CrossRef]
16. Najafi, S.K.; Bucur, V.; Ebrahimi, G. Elastic constants of particleboard with ultrasonic technique. *Mater. Lett.* **2005**, *59*, 2039–2042. [CrossRef]
17. Brashaw, B.K.; Bucur, V.; Divos, F.; Gonçalves, R.; Lu, J.; Meder, R.; Pellerin, R.F.; Potter, S.; Ross, R.J.; Wang, X.; et al. Nondestructive testing and evaluation of wood: A Worldwide Research Update. *For. Prod. J.* **2009**, *59*, 7–13.
18. Chiu, C.M.; Lin, C.H.; Yang, T.H. Application of nondestructive methods to evaluate mechanical Properties of 32-Year Old Taiwan Incense Cedar (*Calocedrus formosana*) wood. *BioResources* **2013**, *8*, 688–700. [CrossRef]
19. Proto, A.R.; Macri, G.; Bernardini, V.; Russo, D.; Zimbalatti, G. Acoustic evaluation of wood quality with a non destructive method in standing trees: A first survey in Italy. *IForest* **2017**, *10*, 700–706. [CrossRef]
20. Yang, J.L.; Fortin, Y. Evaluating strength properties of *Pinus radiata* from ultrasonic measurements on increment cores. *Holzforschung* **2001**, *55*, 606–610. [CrossRef]
21. Horáček, P.; Tippner, J. Nondestructive evaluation of static bending properties of Scots Pine wood using stress wave technique. *Wood Res.* **2012**, *57*, 359–366.
22. Park, Y.I.D.; Koubaa, A.; Brais, S.; Mazerolle, M.J. Effects of cambial age and stem height on wood density and growth of jack pine grown in boreal stands. *Wood Fib. Sci.* **2009**, *41*, 346–358.
23. Ourais, M. Variations intra-arbres de la largeur du cerne, de la masse volumique du bois et des propriétés morphologiques des trachéides de l'épinette noire (*Picea Mariana* (MILL.) B.S.P) avant et après traitements sylvicoles. Master's Thesis, Université du Québec en Abitibi-Témiscamingue, Rouyn-Noranda, QC, Canada, 2012.
24. Grabner, M.; Wimmer, R.; Gierlinger, N.; Evans, R.; Downes, G. Heartwood extractives in larch and effects on X-ray densitometry. *Can. J. Res.* **2005**, *35*, 2781–2786. [CrossRef]
25. Hernández, R.; Koubaa, A.; Beaudoin, M.; Fortin, Y. Selected mechanical properties of fast-growing poplar hybrid clones. *Wood Fib. Sci.* **1998**, *30*, 138–147.
26. Koubaa, A.; Isabel, N.; Zhang, S.Y.; Beaulieu, J.; Bousquet, J. Transition from juvenile to mature wood in black spruce *(Picea Mariana* (Mill.) B.S.P.). *Wood Fib. Sci.* **2005**, *37*, 445–455.
27. Koubaa, A.; Zhang, S.Y.; Isabel, N.; Beaulieu, J.; Bousquet, J. Phenotypic correlations between juvenile-mature wood density and growth in black spruce. *Wood Fib. Sci.* **2000**, *32*, 61–71.
28. Jeong, G.Y.; Zink-Sharp, A.; Hindman, D.P. Tensile properties of earlywood and latewood from lobolly pine (*Pinus taeda*) using digital image correlation. *Wood Fib. Sci.* **2009**, *41*, 51–63.
29. Roszyk, E.; Molinski, W.; Kaminski, M. Tensile properties along the grains of earlywood and latewood of scots pine (*Pinus Sylvestris* L.) in dry and wet state. *BioResources* **2016**, *11*, 3027–3037. [CrossRef]
30. Cramer, S.; Kretschmann, D.; Lakes, R.; Schmidt, T. Earlywood and latewood elastic properties in loblolly pine. *Holzforschung* **2005**, *59*, 531–538. [CrossRef]

31. Moliński, W.; Roszyk, E.; Puszyński, J. Variation in mechanical properties within individual annual ring of the resonance spruce wood [*Picea abies (L.) Karst*]. *Dev. Ind.* **2014**, *65*, 215–223.
32. Mott, L.; Groom, L.; Shaler, S. Mechanical properties of individual southern pine fibers. Part II. Comparison of earlywood and latewood fibers with respect to tree height and juvenility. *Wood Fib. Sci.* **2002**, *34*, 221–237.
33. Vehniäinen, A. Single Fiber Properties—A Key to the Characteristic Defibration Patterns from Wood to Paper Fibers. Ph.D. Thesis, Helsinki University of Technology, Helsinki, Finland, 2008.
34. Jeong, G.Y.; Hindman, D.P. Modeling differently oriented loblly pine strands incorporating variating intraring properties using a stochastic finite element method. *Wood Fib. Sci.* **2010**, *42*, 51–61.
35. Ross, R.J. *Nondestructive Evaluation of Wood*, 2nd ed.; Forest Products Laboratory, Forest Service, WI: U.S, General Technical Report FPL-GTR-238; Department of Agriculture: Madison, WI, USA, 2015.
36. Sales, A.; Candian, M.; De Salles Cardin, V. Evaluation of the mechanical properties of Brazilian lumber *(Goupia glabra)* by nondestructive techniques. *Constr. Build. Mater.* **2011**, *25*, 1450–1454. [CrossRef]
37. Evans, R.; Ilic, J. Rapid prediction of wood stiffness from microfibril angle and density. *For. Prod. J.* **2001**, *51*, 53–57.
38. Lasserre, J.; Mason, E.G.; Watt, M.S.; Moore, J.R. Influence of initial planting spacing and genotype on microfibril angle, wood density, fiber properties and modulus of elasticity in *Pinus radiata D*. Don corewood. *For. Ecol. Manag.* **2009**, *258*, 1924–1931. [CrossRef]
39. Russo, D.; Marziliano, P.A.; Macri, G.; Proto, A.R.; Zimbalatti, G.; Lambardi, F. Does Thinning Intensity Affect Wood Quality? An Analysis of Calabrian Pine in Southern Italy Using a Non-Destructive Acoustic Method. *Forests* **2019**, *10*, 303. [CrossRef]
40. Wang, X.; Ross, R.J.; McClellan, M.; Barbour, R.J.; Erickson, J.R.; Forsman, J.W.; McGinnis, G.D. Nondestructive evaluation of standing trees with a stress wave method. *Wood Fib. Sci.* **2001**, *33*, 522–533.

© 2019 by the authors. Licensee MDPI, Basel, Switzerland. This article is an open access article distributed under the terms and conditions of the Creative Commons Attribution (CC BY) license (http://creativecommons.org/licenses/by/4.0/).

forests

MDPI

Article

Use of Time-of-Flight Ultrasound to Measure Wave Speed in Poplar Seedlings

Fenglu Liu [1,2], Pengfei Xu [1,2], Houjiang Zhang [1,2,*], Cheng Guan [1,2], Dan Feng [1,2] and Xiping Wang [3]

[1] School of Technology, Beijing Forestry University, Beijing 100083, China
[2] Joint International Research Institute of Wood Nondestructive Testing and Evaluation, Beijing Forestry University, Beijing 100083, China
[3] USDA Forest Service, Forest Products Laboratory, Madison, WI 53726-2398, USA
* Correspondence: hjzhang6@bjfu.edu.cn; Tel.: +86-10-6233-6925

Received: 28 June 2019; Accepted: 9 August 2019; Published: 13 August 2019

Abstract: In this study, 145 poplar (*Populus* × *euramericana cv.*'74/76') seedlings, a common plantation tree species in China, were selected and their ultrasonic velocities were measured at four timepoints during the first growth year. After that, 60 poplar seedlings were randomly selected and cut down to determine their acoustic velocity, using the acoustic resonance method. The effects of influencing factors such as wood green density, microfibril angle, growth days, and root-collar diameter on acoustic speed in seedlings and the relationship between ultrasonic speed and acoustic resonance speed were investigated and analyzed in this work. The number of specimens used for investigating growth days and root-collar diameter was 145 in both cases, while 60 and two specimens were used for investigating wood density and the microfibril angle, respectively. The results of this study showed that the ultrasonic speed of poplar seedlings significantly and linearly increased with growth days, within 209 growing days. The ultrasonic velocity of poplar seedlings has a high and positive correlation with growth days, and the correlation was 0.99. However, no significant relationship was found between the ultrasonic velocity and root-collar diameter of poplar seedlings. Furthermore, a low and negative relationship was found between wood density and ultrasonic speed ($R^2 = 0.26$). However, ultrasonic velocity significantly decreased with increasing microfibril angle (MFA) in two seedlings, and thus MFA may have an impact on ultrasonic speed in poplar seedlings. In addition, ultrasonic velocity was found to have a strong correlation with acoustic resonance velocity ($R^2 = 0.81$) and a good correlation, $R^2 = 0.75$, was also found between the dynamic moduli of elasticity from ultrasonic and acoustic resonance tests. The results of this study indicate that the ultrasonic technique can possibly be used to measure the ultrasound speed of young seedlings, and thus early screen seedlings for their stiffness properties in the future.

Keywords: ultrasonic speed; poplar seedlings; acoustic resonance; density; microfibril angle; root-collar diameter

1. Introduction

Trees grown in plantation forests are expected to have a high average value of stiffness (i.e., a high modulus of elasticity (MOE)), a low microfibril angle (MFA), and a low shrinkage propensity to distort, thus yielding lumber or other wood products with a high quality, as well as resulting in a high average grade out-turn [1]. The genetics have a significant impact on whether the tree can produce an acceptable yield of wood products, such as lumbers. Therefore, it is extremely desirable to be able to select young seedlings that are more likely to produce better wood products and, hence, can be grown to maturity in the knowledge that they will be more valuable [1]. Many studies show that for juvenile wood, MFA decreases with age [2,3]. There are many studies showing that it is possible to

enable an early selection of trees that yield better wood quality. For example, Donaldson and Burdon found that it may be possible to effectively select for desirable MFA, starting from ring 1 [4]. Similarly, Dungey et al. found that it was possible to early select for high stiffness (MOE) in *Pinus radiata* D. Don, around rings 4 to 8 at breast height [5]. In addition, Nakada studied *Cryptomeria japonica* D. Don and found an effective selection method and improvement in average log stiffness at an early age (5 years old). He also suggested that it was worth developing an early selection for tree quality [6]. Moreover, Watt et al. (2010) suggested that *P. radiata* clones with high average stiffness can be selected from trees aged 5 years [7]. Emms et al. stated that the early screening of tree quality has benefits to the forestry industry, potentially yielding better wood quality [1,8].

Acoustic techniques such as longitudinal stress waves, acoustic resonance, and ultrasound have been used to determine the mechanical properties of wood materials for many years [9,10]. Since the acoustic speed of wood materials is related to their stiffness, the measurement of acoustic speed in wood still receives much attention from researchers [11–13]. For instance, the acoustic speeds measured by longitudinal stress waves, acoustic resonance or ultrasound are widely used to evaluate the quality of standing trees and to assess the mechanical performance of logs and lumbers and further sort their grades in terms of measured MOE [14–19]. Therefore, acoustic technologies including longitudinal stress waves, acoustic resonance, and ultrasound have been well developed for standing trees, logs, lumbers, and other wood products. For seedlings, however, few acoustic techniques are applied to evaluate their wood quality. There is a lack of interest in the mechanical properties of seedlings and methods for quality evaluation; hence, there are few studies on acoustic speed measurement and wood quality assessment for seedlings. Only Emms et al. measured the acoustic speeds in 2-year-old *Pinus radiata* seedlings, using a longitudinal-wave time-of-flight prototype that they built and an acoustic resonance technique [1,8]. They found that this longitudinal-wave time-of-flight acoustic technique may be able to become a novel technique for non-damaging measurement of acoustic speed in seedlings, and that the technique shows good promise as a rapid and cost-effective tool for early screening of wood quality. Furthermore, they suggest that the measurement of acoustic speed in seedlings has benefits to the forestry industry, potentially enabling the early selection of trees that yield better quality wood. Huang et al. used the stress-wave technique to measure the stiffness properties of seedlings, and Divos et al. conducted seedling segregation by acoustic velocity using stress-wave devices [20,21]. Therefore, more efforts are still needed to find a proper acoustic technique for non-destructive measurement of sound speed, and to establish a comprehensive evaluation method for the quality of seedlings.

It is well-known that acoustic speed is related to the important quality properties of wood, such as stiffness, referred to as MOE, grain angle and the MFA of the S2 layer in the cell wall. Therefore, it is necessary to accurately measure acoustic speed in seedlings and to investigate the influencing factors on acoustic speed, since this will help to improve the reliability and accuracy of assessment for the quality of seedlings via acoustic techniques. However, there are few reports about acoustic speed measurement in seedlings using acoustic technology, especially for ultrasound, and no reports were found for studying the influencing factors on acoustic speed in seedlings. As mentioned previously, only Emms et al. conducted acoustic speed measurement on *Pinus radiata* seedlings, using longitudinal waves and an acoustic resonance technique [1,8]. Huang et al. used the stress-wave method to test the mechanical properties of seedlings, and Divos et al. performed seedling segregation according to stress-wave acoustic velocity [20,21]. Therefore, to the best of our knowledge, no research on acoustic speed measurement for seedlings using ultrasound was found, and no paper investigating influencing factors, such as wood density, MFA, growth days, and root-collar diameter (commonly used to visually evaluate the physical and mechanical properties of seedlings, and subsequently to grade the quality of seedlings), on acoustic speed has been published for seedlings. It is, hence, highly desirable to measure sound speed in seedlings with the application of an ultrasonic technique and to investigate the influencing factors on ultrasonic propagation speed in seedlings.

The poplar is a common plantation tree species in China, and poplar plantations provide an important raw material for papermaking, plywood, fiberboard, paper matches, sanitary chopsticks, and the packaging industry. The research work presented in this paper aimed to measure the ultrasonic propagation velocity in poplar (*Populus* × *euramericana cv.'74/76'*) seedlings, and to analyze the effect of various influencing factors such as wood density, MFA, growth days, and root-collar diameter on acoustic speed in seedlings. The results of this paper will provide some basic insights for the early screening of seedlings for their stiffness properties, using ultrasonic technology, and for developing a rapid evaluation method of poplar seedling wood quality in the future.

2. Materials and Methods

2.1. Materials

A total of 22 rows of poplar seedlings (*Populus* × *euramericana cv.'74/76'*) growing in the nursery base of Beijing Forestry University were planted at an initial spacing of 80 cm (row interval) × 30 cm (column interval), on April 10th. Then, 105 days later, 145 poplar seedlings numbered in sequence from P-001 to P-145 were randomly selected from the nursery base to conduct ultrasonic speed testing for the first time. After that, poplar seedlings were cut down, and a *l* (mm)-long specimen was cut from each green seedling using a portable electric saw. The extracted stem length, *l* is given by the equation

$$L = 15 \times d + 100 \quad (1)$$

where *d* (mm) is the root-collar diameter of the poplar seedling, and 100 mm is a reserved length of the specimen for density measurement. A total of 60 *l* (mm)-long specimens were obtained to perform acoustic resonance tests and density determination. These 60 specimens were immediately sealed by plastic wraps and directly transported to the wood nondestructive evaluation and testing laboratory in Beijing Forestry University, where they were kept in a condition room to maintain the green condition for poplar seedlings prior to acoustic resonance testing. A 15 × *d* (mm)-long specimen and two 50-mm-long specimens (one from the top and the other one from the bottom) were cut from one l (mm)-long poplar seedling specimen. A total of 60 15 × *d* (mm)-long specimen were obtained to conduct acoustic resonance tests. It was found that 15 × *d* (mm) is the optimal length for specimen to perform acoustic resonance tests, therefore, the ratio of length to diameter of specimen for acoustic resonance tests was 15 in this paper. Moreover, 60 50-mm-long specimens from the top of l (mm)-long poplar seedling specimen and 60 50-mm-long specimens from bottom, in total, were acquired and used to determine the green density of poplar seedlings by the water immersion method [22,23].

Additionally, two poplar seedlings, numbered P-146 and P-147, in the nursery were randomly chosen to determine the microfibril angle of seedlings. Five 30-mm-thick lines, named as A, B, C, D, and E, were marked on the poplar seedlings at the heights of 10, 50, 90, 130, and 170 cm above the base of seedling, respectively, as shown in Figure 1a. The ultrasonic speed between two discs, such as AB, BC, CD, or DE, was tested and recorded prior to being felled using a Fakopp Ultrasonic Timer (Sopron, Hungary) with a frequency of 90 kHz. After that, these two poplar seedlings were felled down and five discs, i.e., A, B, C, D, and E, were cut from each seedling. In order to obtain the specimens used for MFA measurement, at first, a 2-cm-wide strip was symmetrically taken from one disc along the pith from north to south direction. Then, a 2-cm-wide strip was symmetrically cut along the pith from east to west direction to obtain a specimen with a thickness of 0.2 cm (see Figure 1b). Finally, a total of 42 specimens measuring 2 (longitudinal) × 1.5 (tangential) × 0.15 (radial) cm obtained from the P-146 poplar seedling, and 28 specimens from the P-147 poplar seedling, were used to conduct the determination of the MFA of seedlings. These specimens were numbered as, e.g., P-146-A-1, where P-146 is the number of the poplar seedling, the letter A represents the number of the disc, and 1 means the number of the sampling position, as shown in Figure 1b. Specimens obtained from discs A, B, C, and D of P-146 poplar seedlings are shown in Figure 1c. Bruker D8 ADVANCE (Stuttgart, Germany), an X-ray diffractometer, was used in this paper to measure the MFA of specimens.

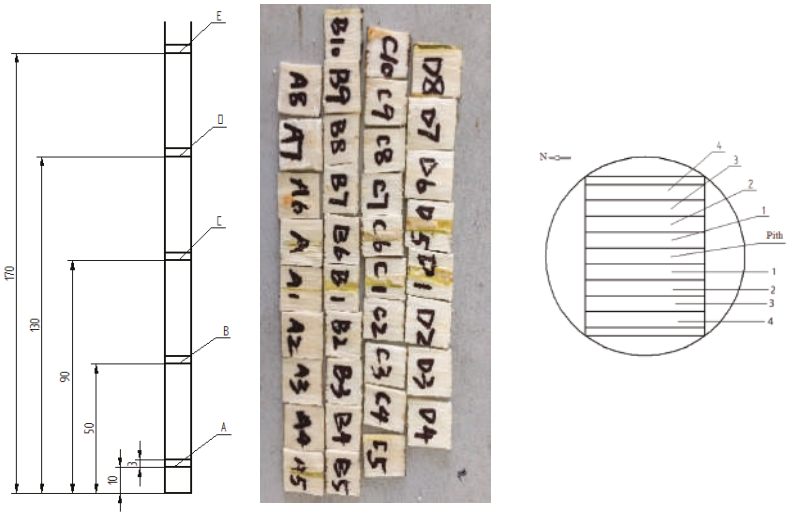

(**a**) (**b**) (**c**)

Figure 1. Schematic diagram of specimen preparation for MFA measurement: (**a**) disc sample position; (**b**) specimen sampling from cross-section; (**c**) specimens from discs A, B, C, and D of P-146 poplar seedlings.

2.2. Methods

2.2.1. Ultrasonic Method

A Fakopp ultrasonic timer, an ultrasonic instrument made in Hungary, was utilized to implement ultrasonic testing on poplar seedlings in situ. This ultrasonic tool is composed of two piezoelectric sensors with cables and one electronic box, as shown in Figure 2. These two sensors, a starter sensor and a receiver sensor, are placed on the same side of the seedling stem. The starter sensor, in field ultrasonic testing, was placed at a height of 200 mm above the ground. The receiver sensor was aligned with the starter sensor, and the distance between them was L (mm), namely measuring distance, seen in Figure 3a. Then, the ultrasonic propagation time for detection distance (L) from the starter sensor to the receiver sensor was displayed on the hand-held box. Three readings were recorded for each seedling, and then the average propagation time was used to calculate the corresponding ultrasonic velocity. Figure 3b shows the factual tests in situ using the Fakopp ultrasonic timer.

It should be noted that testing distance, L, was still uncertain due to the attenuation of ultrasound propagating in the seedling stems. Generally, a long distance between the starter and receiver sensors was necessary to fully reflect the wood properties of seedlings. However, if the test distance was too large, the ultrasonic pulse signal became weakened as the propagation distance increased. As a result, the receiver sensor did not trigger the timer, and thus no reading was recorded. Therefore, before ultrasonic testing, a pre-experiment was conducted to determine the proper detection distance between the two sensors when measuring ultrasonic velocity in poplar seedling stems. Six poplar seedlings with root-collar diameters ranging from 5 mm to 9 mm were selected to perform the pre-experiment using ultrasonic tools. In the pre-experiment, the detection distance, L, was set to a series of values, i.e., 65, 165, 265, 365, 465, 565, 665, 765, 865, and 965 mm. Then, the ultrasonic propagation time was

measured for these 10 various testing distances. Moreover, the ultrasonic velocity in the seedling stems was calculated according to Equation (2).

$$v_u = \frac{L}{T - t_0} \times 1000 \quad (2)$$

where v_u is the ultrasonic velocity (m/s), L is the detection distance (mm), T is the transit time appearing on the ultrasonic instrument (s), and t_0 = 6.1 s is the time correction, which is the transit time inside the two sensors [24]. $T - t_0$ represents the true ultrasonic wave traveling time at the detection distance L in the seedling stems. Ultimately, the proper detection distance for ultrasonic testing was determined based on wave velocities at different measuring distances.

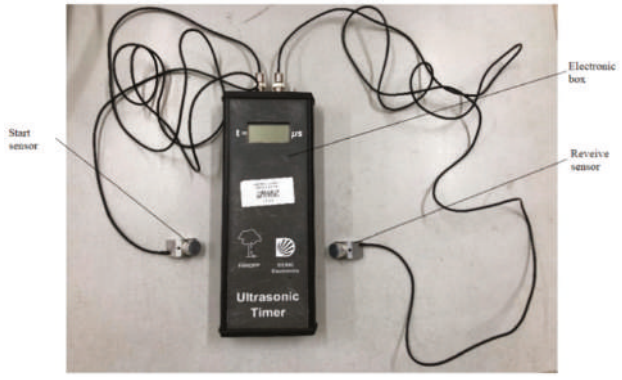

Figure 2. Fakopp ultrasonic timer.

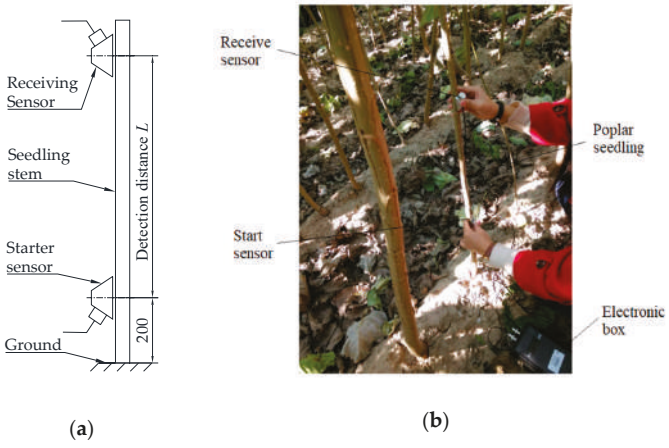

Figure 3. Ultrasonic propagation time measuring method: (**a**) Schematic diagram, (**b**) Field tests.

Once the proper detection distance (L) was identified, the ultrasonic propagation times of 145 seedling samples were measured, and then the ultrasonic propagation velocity of each seedling was calculated using Equation (2). To reduce the effect of environmental factors, the ultrasonic tests for the measurement of 145 seedlings were all completed on the same day. Simultaneously, the root-collar diameters of the seedlings were measured and recorded. A Vernier caliper was used in this step. Two diameters, perpendicular to each other such as east-west and north-south, at the starting point were measured and averaged. Then, the average was denoted as the final root-collar diameter. A total

of four timepoints of ultrasonic testing were performed on July 24, September 2, September 20, and November 5 in 2018, respectively—i.e., 105, 145, 165, and 209 days after the seedlings were planted.

2.2.2. Acoustic Resonance Method

Acoustic resonance techniques have been used to determine the stiffness of construction materials for a long time. In many respects, acoustic resonance techniques may obtain more useful results, as is evident by the correlations between time-of-flight measurement results on stems and resonance results on logs [25]. Acoustic resonance techniques are more accurate and repeatable than time-of-flight techniques [26], and generally do not require calibration and do not greatly depend on how the operator performs the measurements. The acoustic resonance test, a kind of stress-wave method, was performed in this part to be compared with the ultrasonic experiment described previously.

An acoustic resonance testing system (as shown in Figure 4), comprised of a hammer, two strings, a microphone (Type 2671, Brüel & Kjær, Copenhagen, Denmark), a signal amplifier (Type 1704, Brüel & Kjær, Copenhagen, Denmark) and a data acquisition card (Type USB-6218, National Instruments Corporation, Austin, TN, USA), was used to carry out acoustic resonance tests. As can be seen in Figure 3, the seedling specimens were hung with two strings, and the resonance signal generated by the hammer acted on one end of specimens, with a parallel direction. Then, the acoustic resonance signal was collected by the microphone, and afterwards transmitted to the amplifier and the data acquisition (DAQ) card. Finally, the signal was input to a computer for signal processing and analyzing. 60 15 × *d* (mm)-long specimens cut from the seedling samples used for the ultrasonic tests were applied for the acoustic resonance tests to measure the periodic frequency of acoustic propagation in seedling specimens. Consequently, the acoustic velocity was determined through Equation (3).

$$V_a = 2l_a f = 30df \tag{3}$$

where v_a is acoustic velocity, l_a is the length of specimen, d is the root-collar diameter of poplar seedlings and f is the frequency of resonance signal traveling between two ends of specimen. Furthermore, to compare with the modulus of elasticity (MOE) from the ultrasonic and acoustic resonance method, the dynamic MOE of these 60 seedling specimens derived from ultrasonic tests and acoustic resonance tests were calculated according to the determined density and measured transmitting velocity using the following equation.

$$E_d = \rho v^2 \tag{4}$$

where E_d is the dynamic MOE of the seedling sample (Pa), v is the wave velocity measured by either the ultrasonic test or the acoustic resonance test (m/s), and ρ is the green density of the sample (kg/m^3). It should be noticed that the acoustic test was conducted on only one occasion, on 24 July in 2018, i.e., 105 days after the seedlings were planted.

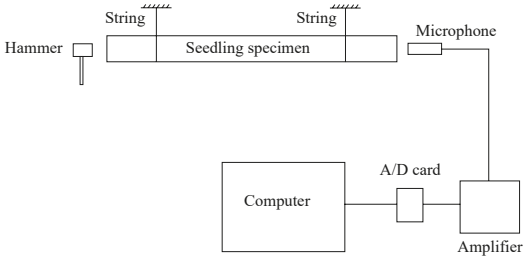

Figure 4. Test setup of the acoustic resonance method.

2.2.3. Density Measurement

A water immersion method was used to determine the green density of poplar seedlings. A total of 60 100-mm-long specimens were applied for the determination of their density. Firstly, two 50-mm-long specimens used for density measurement were cut from the top and bottom of each l-mm-long specimen, and then these two specimens were marked as top and bottom, respectively. After that, the mass of the top 50-mm-long specimen, marked as m (g), was scaled and recorded using an electronic balance (see Figure 5a). A beaker with water inside was placed on the scale, and then a slim pin was vertically immersed in the water until the marked position, as shown in Figure 5b. Thus, the total mass of the beaker with the water and the immersed slim pin, marked as m_0 (g), was scaled and recorded by the electronic balance. Finally, the slim pin was inserted into the top 50-mm-long specimen at a depth of about 1 cm, and then this top specimen was immersed in the beaker until the same position marked on the slim pin, as seen in Figure 5c. Afterwards, the total mass of the beaker with the water, top specimen and immersed slim pin was scaled and recorded, and marked as m_1 (g).

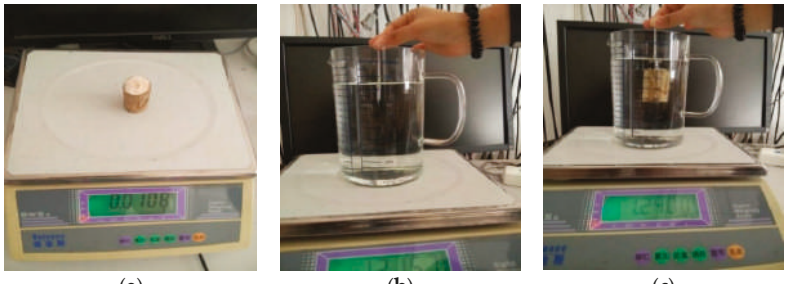

(**a**) (**b**) (**c**)

Figure 5. Density measurement for a 50-mm-long specimen: (**a**) the mass of m, (**b**) the mass of m_0, (**c**) the mass of m_1.

Since the density of water is 1 g/cm^3, the density of the top specimen can be calculated from the Equation (5). Similarly, the density of the bottom specimen can be determined by the above steps and calculated using Equation (5). Therefore, the average density value of the top and bottom specimens was the green density of a poplar seedling specimen. It should be noted that the density measurement method described in this paper only works for wood which has a lower density than water. Another denser liquid, such as mercury, can be used for certain sapwood specimens that have greater densities than water.

$$\rho = \frac{m}{(m_1 - m_0) \cdot 1 \text{ g/cm}^3} \quad (5)$$

3. Results and Discussion

3.1. Proper Detection Distance for Ultrasonic Tests

Figure 6 shows the relationship between detection distance and ultrasonic velocity for six different seedling samples, i.e., P002, P004, P005, P006, P007, and P008. The root-collar diameters of these six seedling samples, in sequence, were 8.1, 5.9, 6.8, 9.0, 7.1, and 7.2 mm. It can be obviously observed from Figure 6 that no ultrasonic velocity values were obtained when the detection distance was over 765 mm for the P004 seedling. A similar result was also found in the P005 seedling when the detection distance was greater than 865 mm. This may be due to smaller root-collar diameters in the P004 and P005 seedlings (5.9 mm and 6.8 mm, respectively) compared with the other four seedling samples. Ultrasonic propagation time could not be measured as the root-collar diameter was too small.

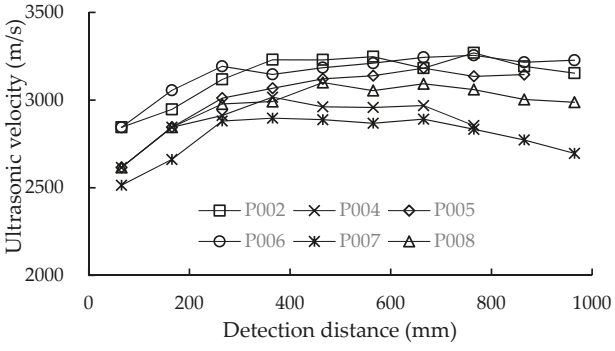

Figure 6. Relationship between detection distance and ultrasonic velocity.

It can be seen from Figure 6 that the ultrasonic velocities of the six seedlings all significantly increased when the detection distance changed from 65 mm to 265 mm. For the P004 and P007 seedlings, the ultrasonic velocities both remained basically stable when the detection distance increased from 265 mm to 665 mm, and then linearly decreased once the test distance went beyond 665 mm. For the P002 and P008 seedlings, the ultrasonic velocity generally remained steady when the detection distance was larger than 265 mm. However, for P005 and P006, the ultrasonic velocity slightly increased when the detection distance was larger than 265 mm. Therefore, the proper detection distance for the ultrasonic test should be chosen from 265 mm to 665 mm. Considering the convenience and feasibility of experimental tests, the detection distance used in this paper was ultimately set to 365 mm. The ultrasonic wave speeds shown in the following were all measured at a test distance of 365 mm.

3.2. Ultrasonic Velocity and Root-Collar Diameters of Poplar Seedlings

The measured ultrasonic velocities and root-collar diameters of poplar seedlings from tests conducted on July 24, September 2, September 20, and November 5 in the same year, 2018, respectively, are given in Table 1. The values in brackets besides average root-collar diameter and velocity are standard deviations. The average root-collar diameter of 145 seedling samples obtained from four different test dates was 15.98 mm, 20.88 mm, 22.06 mm, and 22.60 mm, respectively. A fast growth rate was observed in average root-collar diameter from July 24 to September 2. In contrast, a lower growth rate was found from September 20 to November 5. This means that poplar seedlings may have a fast growth rate from July to September, and a low growth rate from September to November. Moreover, a low growth rate was also found from September 2 to September 20 due to the shorter growth days.

Ultrasonic velocity, apparently, was increased with growth days. Moreover, in the first (July 24), second (September 2), third (September 20), and fourth (November 5) ultrasonic tests, the maximum values of average ultrasonic velocity—i.e., 1995, 2518, 2703, and 2953 m/s, respectively—were all found in poplar seedlings with a root-collar diameter between 10 mm and 20 mm. The minimum values of average velocity from the first ultrasonic test were found in poplar seedlings with a root-collar diameter between 20 mm and 30 mm. However, for the second and third tests, the minimum values of average velocity were presented in poplar seedlings with a root-collar diameter over 30 mm. Meanwhile, the poplar seedlings with a root-collar diameter of less than 10 mm had the minimum values of average ultrasonic velocity.

Table 1. Results of ultrasonic velocity and root-collar diameter for 145 poplar seedlings.

Date	Root-Collar Diameter	Number	Average Root-Collar Diameter	Maximum Root-Collar Diameter	Minimum Root-Collar Diameter	Average Velocity	Maximum Velocity	Minimum Velocity
	(mm)		(mm)	(mm)	(mm)	(m/s)	(m/s)	(m/s)
24 July	$d \leq 10$	15	8.4(1.5)	10.0	4.9	1921(219)	2241	1675
	$10 < d \leq 20$	101	15.4(2.9)	20.0	10.3	1995(123)	2269	1680
	$20 < d \leq 30$	29	21.9(1.4)	25.0	20.1	1919(122)	2087	1748
2 September	$d \leq 10$	5	8.0(1.5)	9.4	5.7	2435(116)	2520	2283
	$10 < d \leq 20$	56	15.4(2.6)	20.0	10.2	2518(153)	2747	2136
	$20 < d \leq 30$	79	24.9(2.7)	29.9	20.2	2315(122)	2707	1996
	$d > 30$	5	31.6(1.1)	33.3	30.5	2145(88)	2283	2041
20 September	$d \leq 10$	5	8.0(1.6)	9.7	5.7	2509(137)	2667	2404
	$10 < d \leq 20$	49	15.4(2.6)	19.5	10.2	2703(125)	2923	2327
	$20 < d \leq 30$	73	25.1(2.7)	29.6	20.1	2484(134)	2833	2228
	$d > 30$	18	31.8(1.6)	35.0	30.1	2328(57)	2404	2188
5 November	$d \leq 0$	5	8.4(1.4)	9.9	6.8	2669(281)	2855	2555
	$10 < d \leq 20$	48	15.6(2.6)	19.9	10.2	2953(107)	3234	2707
	$20 < d \leq 30$	71	25.4(2.8)	29.8	20.5	2884(133)	3353	2629
	$d > 30$	21	32.5(1.7)	36.3	30.1	2741(92)	2971	2573

Figure 7 shows the results of the statistical analysis for ultrasonic velocities measured on July 24 and November 5. It can be clearly found from Figure 7 that the ultrasonic velocities of poplar seedlings measured on November 5 were significantly greater than those tested on July 24, maybe due to the longer growth days or the changes in wood density throughout the growing season. In addition, as shown in Figure 7a, the majority of ultrasonic velocities in the first test (July 24) were concentrated near the average velocity (1974 m/s) and ranged from 1825 m/s to 2025 m/s. Moreover, for the fourth test (November 5), the majority of ultrasonic velocities were likewise concentrated near the average ultrasonic velocity (2881 m/s), but ranged from 2680 m/s to 3160 m/s.

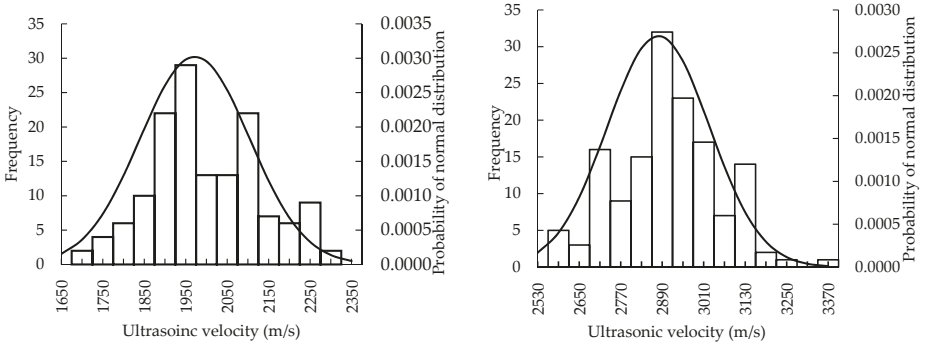

Figure 7. Results of statistical analysis for ultrasonic velocities: (**a**) test on July 24; (**b**) test on November 5.

3.3. Relationships Between Ultrasonic Velocity and Influencing Factors

3.3.1. Growth Days

The effect of growth days on ultrasonic speed in poplar seedlings was analyzed, and the relationships between ultrasonic velocity and growth days are illustrated in Table 2 and Figure 8. The results of the statistical analysis for ultrasonic velocity and growth days are summarized in Table 2. The upper limit of velocity is the wave speed value at the position of positive 3σ in the ultrasonic velocity probability distribution histogram. Conversely, the lower limit of velocity is the value at the position of negative 3σ in the ultrasonic velocity probability distribution histogram. As can be seen in Table 2, the average ultrasonic velocities of poplar seedlings were 1972, 2365, 2540, and 2879 m/s, corresponding to 105, 145, 165, and 209 growth days. The ultrasonic speed of poplar seedlings increased with growth days, within 209 growing days. This result means that the growth days may play a positive role in the ultrasonic velocity of poplar seedlings. Similarly, the growth days have a positive influence on the upper limit of velocity and the lower limit of velocity. The upper limit wave speed increased from 2368 to 3323 m/s, and the lower limit wave speed increased from 1576 to 2434 m/s, when growth days increased from 105 to 209 days.

Table 2. Results of statistical analysis for ultrasonic velocity and growth days.

Date	Number of Trees	Growth Days	Average Velocity	Standard Deviation	Upper Limit of Velocity	Lower Limit of Velocity
			(m/s)		(m/s)	(m/s)
24 July	145	105	1972	132	2368	1576
2 September	145	145	2365	166	2865	1866
20 September	145	165	2540	183	3087	1992
5 November	145	209	2879	148	3323	2434

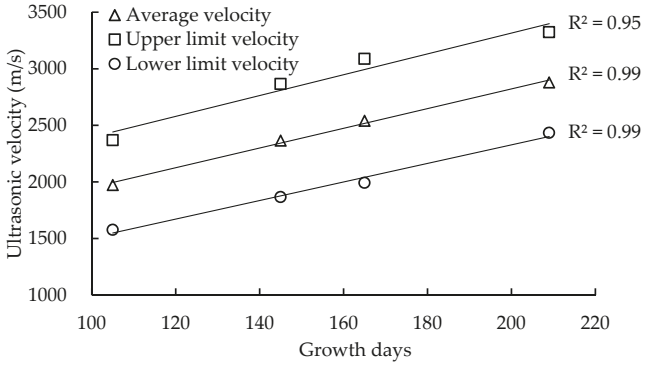

Figure 8. Relationship between ultrasonic velocity and growth days.

Figure 8 shows the results of the correlation analysis between the ultrasonic velocities and seedling growth days. It can be seen from Figure 8 that the average velocity, upper limit of velocity and lower limit of velocity were all linearly increased with growth days, within 209 growing days. There are good correlations between these three kinds of ultrasonic velocities and growth days, and the correlations (R^2) between the average velocity, upper limit of velocity, lower limit of velocity, and the growth days were 0.99, 0.95, and 0.99, respectively. There was a dramatic difference in the ultrasonic velocities of seedlings at different growth days. This is may be due to the fact that the mechanical properties of poplar seedlings gradually become better as growth days increase, resulting in an increase in ultrasonic wave velocity. Therefore, it could be predicted that the ultrasonic velocity of seedlings would continually increase with growth days due to the underlying changes in density or other wood properties. Growth days, thus, may play an important role in the ultrasonic speed of early stage poplar seedlings, especially within 209 growth days. However, it should be noted that the ultrasonic velocity is likely changing due to the underlying changes in density or other wood properties, and not directly due to more growing days. Underlying factors such as moisture content, MFA, wood density, and other wood properties are also likely to have a role in the development of mechanical properties that affect the ultrasonic velocity.

3.3.2. Root-Collar Diameter

It is necessary to investigate the effect of root-collar diameter on ultrasonic velocity and then to determine the relationship between root-collar diameter and ultrasonic speed. In general, the root-collar diameter of seedlings increased with growth days (i.e., the age of seedlings). As showed in Figure 8, the ultrasonic velocity in seedlings linearly increased with increasing growth days. Thereby, it could be speculated that ultrasonic speed may increase with increasing root-collar dimeter of seedlings. However, from the relationships between the ultrasonic velocity and root-collar diameter of poplar seedlings provided in Figure 9, it can be observed that for the four different test dates, the ultrasonic velocity kept relatively stable as the root-collar diameter of poplar seedlings increased. There was no significant correlation between ultrasonic velocity and root-collar diameter in this paper. In other words, it seems that ultrasonic speed does not increase with root-collar diameter.

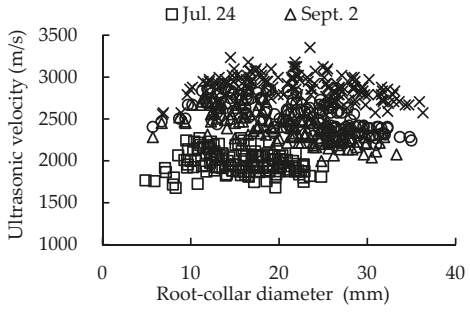

Figure 9. Relationship between the ultrasonic velocity and root-collar diameter of seedlings.

In addition, it was found that the overall ultrasonic velocities measured on November 5 were the highest among the four timepoints of ultrasonic tests, while the test on July 24 obtained the lowest velocity. Ultrasonic velocity was overall increased with growth days, which is consistent with the results shown in Figure 8. Therefore, the root-collar diameter of seedlings did not show a significant effect on ultrasonic velocity in this work. More data from the same or diverse seedlings species, however, still need to be acquired to further verify the effect of root-collar diameter on ultrasonic speed and the relationship between them.

3.3.3. Density

Wood density is also often utilized to assess the mechanical and physical performance of seedlings, and then to classify the quality of seedlings. Accordingly, it is essential to learn the impact of density on ultrasonic velocity in poplar seedlings and the correlation between wood density and ultrasonic speed.

Figure 10 shows the relationship between the density of seedlings and ultrasonic velocity. It can be seen from Figure 10 that ultrasonic velocity overall tends to decrease with increasing density of seedlings. However, a low value of correlation (R^2 = 0.26) was found between ultrasonic velocity and density. Therefore, the relation between ultrasonic speed and the density of seedlings was not significant. This poor relation may be contributed to by the fact that ultrasound speed not only depends on density, but also on other factors such as MFA, grain angle, and the age of seedlings.

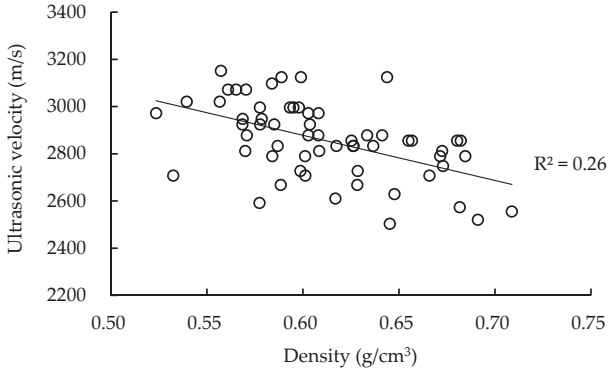

Figure 10. Relationship between the ultrasonic velocity and density of poplar seedlings.

The effect of wood density on acoustic speed has been investigated and reported in many studies. However, two contrasting results were found in the relationship between density and acoustic speed. Some studies reported a negative relationship between wood density and acoustic velocity. Isik et al., for instance, found a low but negative correlation for air-dry density and acoustic velocity in *Pinus taeda*,

and the corresponding correlation coefficient was −0.2 [27]. Hasegawa et al. showed that the ultrasonic wave velocities of Japanese cedar and Japanese cypress both linearly decreased with air-dry density, and the correlation coefficients were −0.83 and −0.74, respectively [28]. However, other studies indicated a positive relation between wood density and acoustic speed. Krauss et al., for example, reported a low but positive relation for density and ultrasonic velocity in Scots pine, and the correlation was 0.15 [29]. Chen et al. and Lachenbruch et al. both found a moderate and positive relationship for green density and ultrasonic speed, and the correlations were 0.46 in Norway spruce and 0.33 in Douglas fir, respectively [12,30]. Moreover, Blackburn et al. and Ribeiro et al. found that acoustic speed greatly increased with wood basic density, and the correlations were 0.75 for *Eucalyptus nitens* and 0.84 for *Pinus taeda* [31,32]. The results of the present paper were basically in accordance with those reported in Isik et al.'s work. Therefore, density may have an influence on ultrasonic speed. More efforts definitely need to be put into the investigation of the impact of density on ultrasonic speed and the correlations between ultrasonic velocity and density in identical or different seedling species. It may help to early select the better-quality seedlings with high average values of stiffness, if the effect of wood density on ultrasonic velocity were comprehensively understood.

3.3.4. Microfibril Angle

The microfibril angle of the S2 cell wall layer is an important parameter of wood. Many studies have showed that the microfibril angle was highly related to the mechanical properties of wood and acoustic speed, for logs and lumbers [33]. The stiffness—i.e., modulus of elasticity—and the acoustic velocity of wood decreased as the microfibril angle increased. Therefore, it is necessary to figure out the effect of microfibril angle on ultrasonic velocity in poplar seedlings and the relationship between MFA and ultrasonic speed.

Microfibril angles measured at different positions (1, 2, 3, 4, ... as shown in Figure 1b) of one disc were averaged and used as the microfibril angle of this disc. Then, the average of the microfibril angle of discs A and B is taken as the microfibril angle between disc A and B. Similarly, the microfibril angles between B and C, C and D, and D and E can be obtained. Thus, the ultrasonic speeds for sections AB, BC, CD, and DE and their corresponding microfibril angles were used to analyze the correlations between them. Figure 11 shows the relationship between the microfibril angle of seedlings and ultrasonic velocity. It can be seen from Figure 11 that ultrasonic velocity significantly decreased with increasing microfibril angle of seedlings. The correlation (R^2) between ultrasonic velocity and MFA for poplar seedling P-146 was 0.69, which is lower than that for poplar seedling P-147 (R^2 = 0.89). Therefore, the relation between ultrasonic speed and MFA is of great interest for these two seedlings, and MFA may have an impact on ultrasonic speed in poplar seedlings. More seedling specimens are definitely needed to verify this relationship and confirm the effect of MFA on ultrasonic velocity.

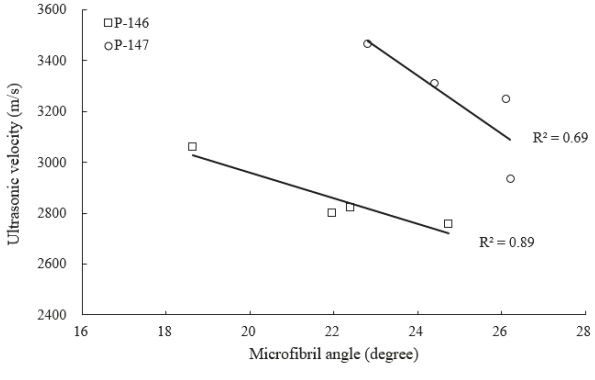

Figure 11. Relationship between the ultrasonic velocity and microfibril angle of poplar seedlings.

MFA has been reported to have a significant and negative relation with acoustic velocity for wood materials such as logs and lumbers in many studies. Krauss et al., for example, found a negative relationship (R^2 = 0.71) between the ultrasonic wave velocity and MFA of Scots pine [29]. Chen et al. reported a very high but negative relationship (R^2 = 0.98) between acoustic velocity and MFA in Norway spruce [30]. Isik et al. and Lachenbruch et al. both observed that acoustic velocity greatly decreased with increasing MFA, and the correlations were 0.70 and 0.69 for *Pinus taeda* and Douglas fir, respectively [12,27]. Moreover, Hasegawa et al. showed that for Japanese cedar, the correlation between ultrasonic wave velocity and MFA was 0.90, and 0.82 for Japanese cypress. They suggested that MFA greatly affects the ultrasonic wave velocity in softwood [28]. The results of the present paper are consistent with their reported results.

3.4. Comparison with the Results of Acoustic and Ultrasonic Tests

Figure 12 shows the relationship between ultrasonic velocity and acoustic resonance velocity in the 60 poplar seedlings. The average ultrasonic velocity and acoustic velocity for these 60 poplar seedlings were 3114.8 m/s and 2856.7 m/s, respectively. The standard deviations of ultrasonic velocity and acoustic velocity were 159.53 and 164.68, respectively. The average ultrasonic velocity was approximately 9.1% (i.e., 260 m/s) higher than the average acoustic velocity. In addition, it can be seen from Figure 12 that there was a significant relationship between ultrasonic velocity and acoustic velocity, and the correlation (R^2) was 0.81. Similar results have been reported by other researchers as well [1,23]. The acoustic resonance method is generally recognized as a reliable and accurate method for measuring the sound speed of wood material, such as logs and lumbers. Therefore, the prominent relationship between ultrasonic and acoustic velocity may indicate that the ultrasonic method can be used to measure the ultrasonic sound speed of poplar seedlings.

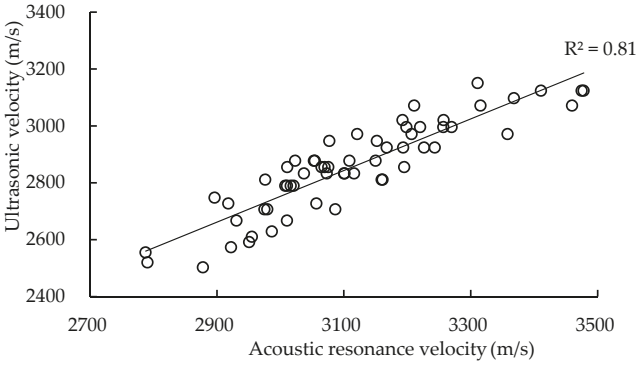

Figure 12. Relationship between ultrasonic velocity and acoustic resonance velocity.

Figure 13 presents the relationship between the dynamic MOE results obtained from ultrasonic and acoustic tests carried out in 60 seedlings. The average dynamic MOE values derived from the ultrasonic and acoustic tests for these 60 poplar seedlings were 5.92 and 4.98 GPa, respectively. The standard deviations of dynamic MOE derived from the ultrasonic and acoustic methods were 0.48 and 0.36, respectively. The average dynamic MOE from the ultrasonic test was approximately 18.87% (i.e., 0.94 GPa) higher than that from the acoustic test. Additionally, it can be observed from Figure 13 that there was a good relationship between dynamic MOE from the ultrasonic test and the acoustic test, and the correlation (R^2) was 0.75. It is well known that the dynamic elastic modulus measured by the acoustic method can be well used to predict the static elastic modulus of wood. Therefore, this means that the dynamic elastic modulus measured by the ultrasonic method may be able to be used for predicting the static elastic modulus of wood, especially for young seedlings, due to the noticeable relationship between dynamic MOE results from ultrasonic and acoustic tests. However,

there is still a lot of work that needs to be done to investigate whether the ultrasonic method could be potentially utilized to evaluate the quality of young seedlings. Moreover, if ultrasound could be applied to the early selection of seedlings, the quality of standing trees and wood-based products may be improved because of the good quality of the young seedlings. Although good quality young seedlings do not guarantee good quality standing trees, they are a good start to cultivate the high properties of plantation trees.

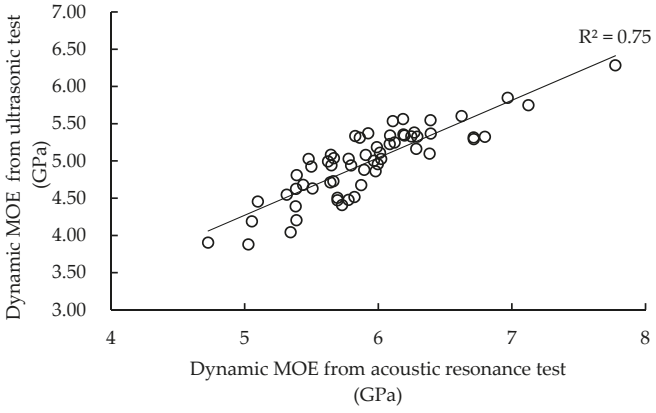

Figure 13. Relationship between dynamic MOE values from ultrasonic and acoustic resonance tests.

4. Conclusions

The aim of this study was to investigate the application of ultrasonic speed measurement to poplar (*Populus* × *euramericana cv.'74/76'*) seedlings, a common plantation species in China, and to gain some basic insights for the future early selection of poplar seedlings with high wood quality. The conclusions are as follows:

- The proper detection distance for the ultrasonic method to be applied to poplar seedlings is ranged from 265 mm to 665 mm, and 365 mm was used in this study.
- There were good correlations (R^2 = 0.99) between the average ultrasonic velocities and growth days. Ultrasonic speed increased with growth days, within 209 growing days. However, almost no relationship was found between the ultrasonic velocities and the root-collar diameters of seedlings, i.e., ultrasonic speed does not seem to increase with increasing root-collar diameter.
- Even though ultrasonic velocity, in general, decreases with increasing density, the density of seedlings showed a weak influence on ultrasonic speed due to the low correlation between them (R^2 = 0.26). However, ultrasonic velocity significantly decreased with the increasing microfibril angle of seedlings. The relations between ultrasonic speed and MFA are of great interest for the two sample seedlings, and MFA may have an impact on ultrasonic speed in poplar seedlings. More seedling specimens are definitely needed to verify this relationship and confirm the effect of MFA on ultrasonic velocity.
- There was a significant relationship between ultrasonic velocity and acoustic velocity, and a similar result was also found in the dynamic MOE values derived from the acoustic resonance test and the ultrasonic test, respectively.
- Other influencing factors that were excluded in this paper—such as MFA, temperature, and moisture content—need to be studied in future research to investigate their effect on ultrasonic velocity in seedlings.

Author Contributions: F.L. rewrote and revised the manuscript as well as conducted part of data analysis work. P.X. conducted part of analysis work and wrote the original draft of the manuscript. H.Z. and C.G. supervised the

research team and provided some ideas to research as well as revised the manuscript. D.F. performed most of test and analysis work. X.W. revised the manuscript.

Funding: This project was supported by "the Fundamental Research Funds for the Central Universities (no. BLX201817)", China Postdoctoral Science Foundation (no. 2018M641225) and the National Natural Science Foundation of China (no. 31328005).

Acknowledgments: The authors wish to thank Jianhua Hao for his grateful assistance of planting the seedlings.

Conflicts of Interest: The authors declare no conflict of interest. The funders had no role in the design of the study; in the collection, analyses, or interpretation of data; in the writing of the manuscript, or in the decision to publish the results.

References

1. Emms, G.W.; Nanayakkara, B.; Harrington, J.J. Application of longitudinal-wave time-of-flight sound speed measurement to Pinus radiata seedlings. *Can. J. For. Res.* **2013**, *43*, 750–756.
2. Huang, Y.H.; Zhao, R.J.; Fei, B.H. Variation patterns of microfibril angle for Chinese fir wood. *J. Northwest For. Univ.* **2007**, *22*, 119–122.
3. Sun, D.Y.; Yang, W.X.; Liu, Q.L.; Fang, S.Z. A study on geographic variation in wood microfibril angle of *Cyclocarya paliurus*. *J. Nanjing For. Univ. Nat. Sci. Ed.* **2018**, *42*, 81–85.
4. Donaldson, L.A.; Burdon, R.D. Clonal variation and repeatability of microfibril angle in Pinus radiata. *N. Z. J. For. Sci.* **1995**, *25*, 164–174.
5. Dungey, H.S.; Matheson, A.C.; Kain, D.; Evans, R. Genetics of wood stiffness and its component traits in Pinus radiata. *Can. J. For. Res.* **2006**, *36*, 1165–1178.
6. Nakada, R. Within-tree variation of wood characteristics in conifers and the anatomical characteristics specific to very young trees. In *The Compromised Wood Workshop 2007*; University of Canterbury: Christchurch, New Zealand, 2007; pp. 51–67.
7. Watt, M.S.; Sorensson, C.; Cown, D.J.; Dungey, H.S.; Evans, R. Determining the main and interactive effect of age and clone on wood density, microfibril angle, and modulus of elasticity for Pinus radiata. *Can. J. For. Res.* **2010**, *40*, 1550–1557.
8. Emms, G.; Harrington, J.J. A novel technique for non-damaging measurement of sound speed in seedlings. *Eur. J. For. Res.* **2012**, *131*, 1449–1459.
9. Hearmon, R.F.S. The influence of shear and rotatory inertia on the free flexural vibration of wooden beams. *Br. J. Appl. Phys.* **1958**, *9*, 381–388. [CrossRef]
10. Bucur, V. *Acoustics of Wood*; CRC Press: Boca Raton, FL, USA, 1995.
11. Yin, Y.F.; Nagao, H.; Liu, X.L. Mechanical properties assessment of *Cunninghamia lanceolata* plantation wood with three acoustic-based nondestructive methods. *J. Wood Sci.* **2010**, *56*, 33–40.
12. Lachenbruch, B.; Johnson, G.R.; Downes, G.M.; Evans, R. Relationships of density, microfibril angle, and sound velocity with stiffness and strength in mature wood of Douglas-fir. *Can. J. For Res.* **2010**, *40*, 55–64.
13. Todoroki, C.L.; Lowell, E.C.; Dykstra, D. Automated knot detection with visual post-processing of Douglas-fir veneer images. *Comput. Electron. Agric.* **2010**, *70*, 163–171.
14. Chauhan, S.S.; Walker, J.C.F. Variations in acoustic velocity and density with age, and their interrelationships in radiata pine. *For. Ecol. Manag.* **2006**, *229*, 388–394.
15. Toulmin, M.J.; Raymond, C.A. Developing a sampling strategy for measuring acoustic velocity in standing Pinus radiata using the treetap time of flight tool. *N. Z. J. For Sci.* **2007**, *37*, 96–111.
16. Lindstrom, H.; Reale, M.; Grekin, M. Using non-destructive testing to assess modulus of elasticity of Pinus sylvestris trees. *Scand. J. For. Res.* **2009**, *24*, 247–257.
17. Gerhards, C. Longitudinal stress-waves for lumber stress grading: Factors affecting applications: State of the art. *For. Prod. J.* **1982**, *32*, 20–25.
18. Tsehaye, A.; Buchanan, A.H.; Walker, J.C.F. Sorting of logs using acoustics. *Wood Sci. Technol.* **2000**, *34*, 337–344.
19. Carter, P.; Chauhan, S.S.; Walker, J.C.F. Sorting logs and lumber for stiffness using director HM200. *Wood Fibre Sci.* **2006**, *38*, 49–54.
20. Huang, C.L.; Lambeth, C.C. Methods for Determining Potential Characteristics of a Specimen Based on Stress Wave Velocity Measurements. U.S. Patent Application No. 7340958, 11 March 2008.

21. Divos, F. Acoustic tools for seedling, tree and log selection. Presented at the The Future of Quality Control for Wood & Wood Products—COST Action E53, Edinburgh, UK, 4–7 May 2010.
22. ASTM G2395-17. *Standard Test Methods for Density and Specific Gravity (Relative Density) of Wood and Wood-Based Materials*; ASTM International: West Conshohocken, PA, USA, 2017.
23. GB/T1933-2009. *Method for Determination of the Density of Wood*; Standardization Administration of China: Beijing, China, 2009.
24. *Ultrasonic Timer User's Guide*; FAKOPP: Budapest, Hungary, 2008.
25. Wang, X.P.; Ross, R.J.; Carter, P. Acoustic evaluation of wood quality in standing trees. Part I. Acoustic wave behavior. *Wood Fiber Sci.* **2007**, *39*, 28–38.
26. Chauhan, S.S.; Entwistle, K.M.; Walker, J.C.F. Differences in acoustic velocity by resonance and transit-time methods in an anisotropic laminated wood medium. *Holzforschung* **2005**, *59*, 428–434.
27. Isik, F.; Mora, C.R.; Schimleck, L.R. Genetic variation in *Pinus taeda* wood properties predicted using non-destructive techniques. *Ann. For. Sci.* **2011**, *68*, 283–293.
28. Hasegawa, M.; Takata, M.; Matsumura, J.; Oda, K. Effect of wood properties on within-tree variation in ultrasonic wave velocity in softwood. *Ultrasonics* **2011**, *51*, 296–302. [CrossRef] [PubMed]
29. Krauss, A.; Kudela, J. Ultrasonic wave propagation and Young's modulus of elasticity along the grain of Scots pine wood (Pinus Sylvestris L.) varying with distance from the pith. *Wood Res.* **2011**, *56*, 479–488.
30. Chen, Z.Q.; Karlsson, B.; Lundqvist, S.O.; Maria, R.G.G.; Olsson, L.; Wu, H.X. Estimating solid wood properties using Pilodyn and acoustic velocity on standing trees of Norway spruce. *Ann. For. Sci.* **2015**, *72*, 499–508.
31. Blackburn, D.; Farrell, R.; Hamilton, M.; Volker, P.; Harwood, C. Genetic improvement for pulpwood and peeled veneer in *Eucalyptus nitens*. *Can. J. For. Res.* **2012**, *42*, 1724–1732.
32. Ribeiro, P.G.; Goncalez, J.C.; Goncalves, R.; Teles, R.F.; Souza, F.D. Ultrasound waves for assessing the technological properties of *Pinus caribaea* var *hondurensis* and *Eucalyptus grandis* wood. *Maderas Cienc. Tecnol.* **2013**, *15*, 195–204.
33. Cown, D.J.; Hebert, J.; Ball, R. Modelling Pinus radiata lumber characteristics. Part 1: Mechanical properties of small clears. *N. Z. J. For. Sci.* **1999**, *29*, 203–213.

© 2019 by the authors. Licensee MDPI, Basel, Switzerland. This article is an open access article distributed under the terms and conditions of the Creative Commons Attribution (CC BY) license (http://creativecommons.org/licenses/by/4.0/).

forests

MDPI

Article

Machinability Study of Australia's Dominate Plantation Timber Resources

Nathan J. Kotlarewski [1,*], Mohammad Derikvand [1,2], Michael Lee [3] and Ian Whiteroad [4]

1 Australian Research Council Centre for Forest Value, University of Tasmania, Launceston TAS 7250, Australia; Mohammad.Derikvand@utas.edu.au
2 Department of Civil Engineering, Aalto University, 02150 Espoo, Finland
3 Centre for Sustainable Architecture with Wood, University of Tasmania, Launceston 7250, Australia; M.W.Lee@utas.edu.au
4 ARTEC Australia Pty Ltd., Launceston 7250, Australia; Ian.Whiteroad@artec.net.au
* Correspondence: Nathan.Kotlarewski@utas.edu.au; Tel.: +61-3-6324-4473

Received: 9 August 2019; Accepted: 14 September 2019; Published: 16 September 2019

Abstract: This study tested the machinability of three major timber species grown in Tasmania, Australia, under different resource management schemes: plantation fiber-managed hardwood (*Eucalyptus globulus* Labill. and *Eucalyptus nitens* Maiden) and plantation sawlog-managed softwood (*Pinus radiata* D. Don). *P. radiata* was used as a control to identify significant differences in machining fibre-managed plantation timber against sawlog-managed plantation timber with numerically controlled computer technology and manually fed timber production techniques. The potential to fabricate architectural interior products such as moldings with plantation fiber-managed hardwood timber that is high in natural features was the focus of this study. Correlations between wood species, variation in moisture content, and density of individual machinability characteristics were analyzed to determine factors impacting the overall quality of plantation wood machinability. Correlations between species and within species groups from the resulting machinability tests are highlighted and discussed. The results indicate that the machinability of sawlog-managed softwood *P. radiata* is superior in some circumstances to fiber-managed hardwood *E. globulus* and *E. nitens* specimens, according to the American Society for Testing and Materials D1666-11.

Keywords: machinability; Eucalyptus; plantation timber; fiber-managed hardwoods

1. Introduction

Australia has close to one million hectares of plantation hardwood eucalypt species managed for pulplog production. The two major hardwood species grown under this management scheme are *Eucalyptus globulus* Labill., of which 52.7% is predominately grown in Western Australia and the Green Triangle region, followed by *Eucalyptus nitens* Maiden, of which 25.2% is predominately grown in Tasmania (a smaller proportion of the Tasmanian plantation estate for both species is also managed for sawlogs). In addition, there are over one million hectares of planation softwood species managed for sawlog production throughout Australia. *Pinus radiata* D. Don accounts for 74.5% of this estate, which is grown predominately in the Green Triangle region and the Murray Valley (Tasmania also has an established estate of this resource [1]).

In this study, different machinability characteristics of the three major plantation timber species in Australia (*E. globulus*, *E. nitens*, and *P. radiata*) have been evaluated and statistically compared to determine new applications for hardwood plantation resources in machine-manufactured products. With the current supply of planation hardwoods in Australia en masse, and a rise in demand for timber products in the built environment driven by state wood encouragement policies, there is an opportunity to utilize hardwood pulplogs to produce value-added architectural products with

advanced manufacturing technologies such as computer numerically controlled (CNC) machinery. The key driver for this research is refocusing hardwood plantation resources into higher-value sawn board applications for furniture and architectural products. To design and manufacture such products, the suitability of processing pulplog with CNC or manually operator-controlled technologies is needed to determine: (i) the machinability of timber derived from pulplogs according to the American Society for Testing and Materials (ASTM) D1666-11 (Standard Test Methods for Conducting Machining Tests on Wood and Wood-Based Materials, 2011) [2] and (ii) the timber properties that most affect the quality of finish for each species.

Utilizing low-quality and low-value plantation logs has been a global topic for a long time [3]. In recent times, *Eucalypts* have attracted much attention for improving the genetics for solidwood production [4] and utilization in value-added materials and product research [5], particularly mass-timber product development such as nail-laminated beams [6] and cross-laminated timber paneling [7]. Traditional wood products (board and veneer), engineered wood products (glulam) and wood-based panels (particleboard and medium-density fiberboard) have revolutionized the way wood is used in the built environment. Wood used in an appearance application relies on a high-quality surface finish to accommodate its final use [8], as well as the application of paints or lamella overlays. The literature consists of various machinability studies that investigate the quality of wood product surface finishes. Not surprisingly, a vast majority of the literature focus on homogeneous wood products such as medium density fiberboard and chipboards due to controllable conditions and less-variable moisture content (MC) and densities [9–11]. Considering these factors, it is of interest to determine the machinability properties of highly variable processed plantation solidwood. How wood specimens are assessed is also a widely presented topic in the literature [12]. Visual assessment has been the standardized procedure for some time now, and new technologies are increasingly being employed to validate quality and compare results [13]. Some researchers go beyond the parameters of ASTM D1666-11, adapting and capturing more data than specified such as the temperature of test specimen after sanding [14] to validate or conclude their findings. Other researchers focus entirely on specific machinability tests such as drilling [15] to advance knowledge. There has also been research conducted in the literature to determine the effects of wood modifications such as thermal treatments on wood machinability [16].

Key variables with any wood machining are cutting speed, feed direction, depth of cut, cutting tool (type and its sharpness) and quality of treatments applied to wood specimens (such as heat or chemical treatment). In addition, the literature states that anatomical characteristics such as species, MC, grain direction, sapwood/hardwood, and density affect the quality of surface machinability [17–19]. New manufacturing knowledge is needed to determine appropriate techniques and commercial processors for the incorporation and potential use of pulplog resources in high-value architectural products, as well as applications to encourage their use in current markets to fulfil demand.

2. Materials and Methods

2.1. Plantation Timber

The studied timber species included *E. nitens* and *E. globulus* obtained from unthinned and unpruned fiber-managed hardwood plantation resources (from Nook and Trowutta, Tasmania, respectively) for pulplog production in northern Tasmania. These two hardwood pulplog timber species were compared to softwood sawn-board timber obtained from a plantation *P. radiata* resource in Tasmania, Australia. A summary of the three species management schemes, ages and densities is given in Table 1.

Table 1. Species sample data.

Specie	Management Scheme	Age (years)	Average Small End Diameter (mm)	Sample Density Range (kg/m^3)	Number of Specimens
E. nitens Maiden	Pulplog	16	345	395–741 (523 *)	54
E. globulus Labill.	Pulplog	26	403	409–763 (544 *)	54
P. radiata D. Don	Sawlog	30	N/A	444–604 (521 *)	53

* Average specimen density.

The variation in species heterogeneity such as density, presented in Table 1, highlights key characteristics of hardwood species managed under pulplog management schemes. Both hardwood species' density ranges were much wider than *P. radiata*. Specimens prepared for *E. nitens* and *E. globulus* were plainsawn for best recovery. A total of 54 specimens were prepared randomly from ungraded boards for both eucalypt species and varied in origin from each log, deriving from 140-, 120- and 90-mm dressed boards. A maximum of six specimens were machined from individual boards for all species (Figure 1).

Figure 1. Six samples machined from individual boards.

For the varying board widths in the hardwood specimens, three sets of six samples were machined from 140-, 120- and 90-mm dressed boards. A total of 53 specimens were prepared for *P. radiata*, all of which derived from utility grade 90-mm dressed boards. All boards designated for sample machining were randomly selected during final processing as run of the mill production to reflect market supply. Prior to testing, boards were stored in a joinery workshop environment at 10 °C (± 4 °C) and 40% (± 5%) relative humidity. This range of environmental conditions (in Tasmania, Australia) was set to test typical joinery workshop environments in which secondary manufacturing commonly takes place, thus allowing a true representation of timber MC in local manufacturing and in service.

2.2. Machinability Tests

The machining tests conducted in this study complied with ASTM D1666-11 (2011), with the exception of choice in tooling for CNC operations. All CNC tests were conducted at the Discipline of Architecture and Design, University of Tasmania. The tests conducted included boring, routing, shaping, mortising, and an additional test to determine biscuit boring (doweling) for a more contemporary reference in timber joinery. Each specimen was subjected to boring, routing, and shaping tests. Only a selected number of specimens for each species were subjected to mortising and biscuit boring, as initial results were consistent in machinability quality.

2.3. Tooling and Speed/Feed Rates

All boring and routing tests were conducted with a solid carbide, 9.5-mm, 3-flute roughing spiral cutter and finished with a solid carbide, 8-mm, 2-flute compression cutter. A spindle speed of 15,000 revolutions per minute (RPM) and feed rate of 6350 mm/min were used (the standard spindle speed for boring tests is 3600 RPM). The choice in tooling and spindle speeds represented a typical entry-level combination of available tooling in timber joinery workshops for CNC machining. Boring and routing profiles were cut in two passes: first, full depth conventional milling was performed with the roughing tool, leaving 1.6-mm clearance from the finish surface before climb milling with the compression cutter to remove the 1.6 mm overcut. New tools were used for each species. The intention of this change in the standard method was to determine the resilience in timber machinability quality in contemporary industry practice. This was further substantiated and compared with the use of sawlog-managed softwood as a control to determine significant discrepancies between fibre-managed hardwood test results. Mortising tooling complied with the standard (13-mm hollow chisel drill), as did the spindle speed (3600 RPM), which was hand fed by peck drilling on a pedestal drill. Specimen-shaping was conducted on a table router with a no-load spindle speed of 27,000 RPM. The shaping with the table router was done with a 2-flute face-molding carbide tip with a ball bearing guide for profiling. The specimens on the side grain were shaped via hand feeding in two passes due to the depth of the profile. The equipment used to machine biscuit dowels was a Festool DF 500 DOMINO, which cuts the timber stock in a pendulum motion and therefore no spindle speed was recorded. Chip thickness was not measured in any tests. The mortising, shaping, and biscuit-boring introduced a variable of unreliable human-controlled feed rates in comparison with CNC machining. To minimize this variable, one operator conducted each human feed test to maintain consistency in test conditions. This research acknowledges the differences between numerically controlled feed rates and human feed rates, although the intention of this research is still an investigation of the machinability of hardwood plantation resources in commercially mass-produced repetitive machining versus niche one-off productions.

2.4. Scoring and Results Analysis

All specimens were graded according to the visual examination classification in ASTM D1666-11 (2011) on the bases of six grades, namely, G0 (defect-free), G1 (excellent), G2 (good), G3 (fair), G4 (poor), and G5 (very poor). While this method of machinability grading is qualitative and context-specific, depending on the product's intended use, two industry-experienced wood machinists with years of sawing, machining, and grading Tasmanian hardwoods were used to visually grade the specimens for each species according to ASTM D1666-11 (2011) and Australian Standard (AS) 2796.3. Grading was conducted using a photo studio lighting kit (Figure 2).

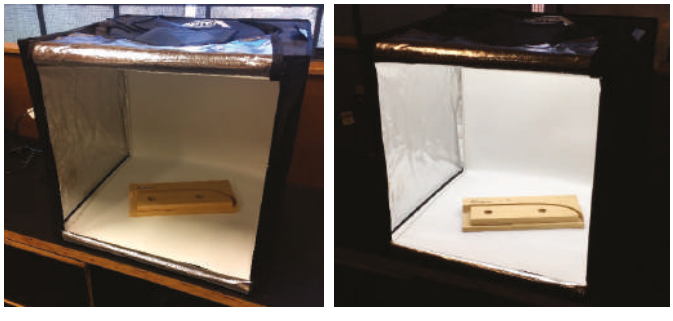

Figure 2. Photo studio lighting kit used to grade specimens.

No mechanical or scanning techniques were employed to measure the precision of the visual grading evaluation. A combination of visual and tactile evaluations was employed to determine specimen surface quality as indicated by the existing literature [12,20]. Most of the machining quality was notable by eye and touch, as visual grading provides a rapid and complete analysis of surface quality [21]. The micro-level assessment of surface quality was deemed irrelevant, as products' appearances would normally be graded for Australian markets according to AS 2796. The grade given to each specimen was based on commercially acceptable appearance parameters for high-value architectural products. Commercially acceptable parameters were determined by referencing AS 2796.3 Appendix D, Table D1: "Limits of the machining imperfections and surface finish imperfection on exposed surfaces of hardwood timber for furniture components" [21]. Where specimen tests resulted in surface imperfections, a grade of G2 (good) to G5 (very poor) was given. Specimens with no imperfections were graded as G0 (defect-free) to G1 (excellent). These parameters were also determined by the consistency of surface finish and visually graded using the examples in ASTM D166 and the literature [22]. This process was used to justify allocated grades and to identify significant discrepancies between the resulting specimens within each species and against each species.

2.5. Statistical Analyses

The significance of differences between the machinability characteristics of the three wood species in this study were statistically analyzed via Chi-Square testing using IBM SPSS Statistics software (version 23, IBM Corporation, New York, USA). The Analysis of Variance (ANOVA) and Duncan's multiple range test were used for determining the differences between the three species with respect to density and MC. The correlations between machinability characteristics with the variations in density and MC were determined using Pearson's correlation test (interval by interval). All the statistical analyses were conducted at 0.05 significance level.

3. Results

3.1. Statistical Analyses of Density and MC between Species

The ANOVA results indicated no significant difference between the densities of the three species in this study ($p > 0.05$), which enabled a statistical comparison between the machinability characteristics. The difference between MC values in the three species, however, was significant ($p < 0.05$). The difference between the density and MC of *E. nitens* and *P. radiata* was less than 0.4% and 2.3%, respectively. The average density and MC of *E. globulus* samples were respectively 4.2% and 3.9% higher than that of *E. nitens*, and 4.6% and 1.5% higher than *P. radiata*. The variations in the density and MC values of the test samples within each species can be seen in Figures 3–5.

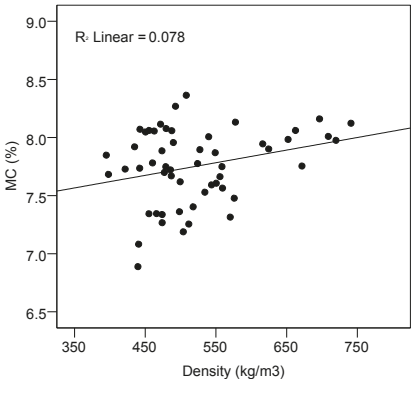

Figure 3. Variation in moisture content and density of *E. nitens* samples.

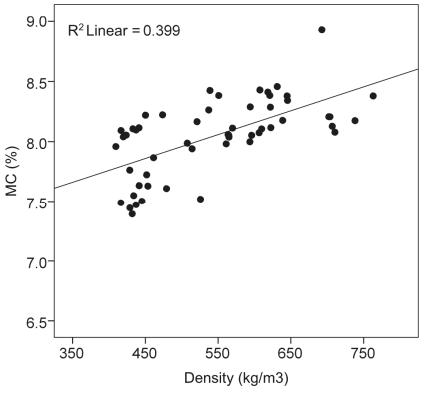

Figure 4. Variation in moisture content and density of *E. globulus* samples.

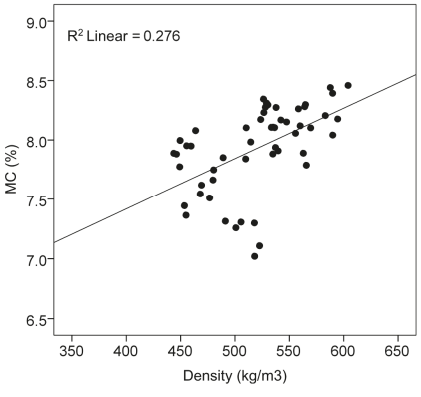

Figure 5. Variation in moisture content and density of *P. radiata* samples.

3.2. Statistical Analyses of Machinability Results between Species

The test results obtained with respect to routing end grain (fuzzy and raised) and boring (crushing, fuzzy, and smoothness) indicated that the test samples from the three species were all defect-free with consistent quality (having a grade of G0). These test results are therefore not presented in this study. The results of the statistical analyses for the remaining machinability characteristics are presented. No statistically significant difference was found between the three species with respect to raised routing side grain, chipped routing end grain, chipped shaping side grain, boring tear-out and biscuit bore (crushed and chipped) ($p > 0.05$). Statistically significant differences were found between the three species for routing side grain (fuzzy and chipped), shaping side grain (raised and fuzzy), mortising (crushing, tearing and smoothness) and fuzzy biscuit-bore grain ($p < 0.05$).

The grading results of the machinability characteristics for each species sample are shown in Tables 2–7. The values with the most important contributions to the statistical significance for each characteristic are highlighted in grey where applicable (indicating the differences within species and between species). All the *E. nitens* and *P. radiata* samples received a G0 grade (defect-free) for routing side grain (Table 2). The fuzzy routing side grain (Figure 6), was more variable within the *E. globulus* samples, with more than 37% of the samples having a grade between G1 to G4. There was no significant difference between the *E. nitens* and *P. radiata* samples with respect to the chipped routing side grain. The number of samples with a grade worse than G0 were significantly higher in *E. globulus* compared to *E. nitens* and *P. radiata*.

Table 2. Grading results according to routing side grain.

Routing Side Grain Results			Routing Side Grain (Raised)			Routing Side Grain (Fuzzy)				Routing Side Grain (Chipped)					Total
			Grade 0	Grade 1	Grade 2	Grade 0	Grade 1	Grade 2	Grade 3	Grade 4	Grade 0	Grade 1	Grade 2	Grade 3	
Species	*E. nitens*	Count	53	1	0	54	0	0	0	0	49	1	1	3	54
		Standardised residual	0.2	−0.3	−1	1	−1.3	−1.9	−1	−0.6	0	1.1	−1.2	1	
	E. globulus	Count	49	2	3	34	5	11	3	1	44	0	8	2	54
		Standardised residual	−0.4	0.6	2	−1.9	2.6	3.8	2	1.1	−0.7	−0.6	2.9	0.2	
	P. radiata	Count	52	1	0	53	0	0	0	0	53	0	0	0	53
		Standardised residual	0.2	−0.3	−1	1	−1.3	−1.9	−1	−0.6	0.7	−0.6	−1.7	−1.3	
Total		Count	154	4	3	141	5	11	3	1	146	1	9	5	161

Table 3. Grading results according to routing end grain.

Routing End Grain Results			Routing End Grain Chipped		Total
			Grade 0	Grade 2	
Species	*E. nitens*	Count	53	1	54
		Standardised residual	−0.1	1.1	
	E. globulus	Count	54	0	54
		Standardised residual	0	−0.6	
	P. radiata	Count	53	0	53
		Standardised residual	0	−0.6	
Total		Count	160	1	161

Table 4. Grading results according to shaping side grain.

Shaping Side Grain Results			Shaping Side Grain (Raised)				Shaping Side Grain (Fuzzy)				Shaping Side Grain (Chipped)						Total
			Grade 0	Grade 1	Grade 2	Grade 3	Grade 0	Grade 1	Grade 2	Grade 3	Grade 0	Grade 1	Grade 2	Grade 3	Grade 4	Grade 5	
Species	*E. nitens*	Count	42	6	6	0	54	0	0	0	47	1	1	2	1	2	54
		Standardised residual	−0.9	1.4	2.4	−0.6	1.2	−2.2	−1.7	−0.6	−0.2	0.4	0	0.6	−0.5	1	
	E. globulus	Count	48	4	1	1	47	0	6	1	44	1	2	2	4	1	54
		Standardised residual	0	0.4	−0.9	1.1	0.2	−2.2	1.7	1.1	−0.6	0.4	1	0.6	1.8	0	
	P. radiata	Count	53	0	0	0	36	14	3	0	53	0	0	0	0	0	53
		Standardised residual	0.9	−1.8	−1.5	−0.6	−1.4	4.4	0	−0.6	0.8	−0.8	−1	−1.1	−1.3	−1	
Total		Count	143	10	7	1	137	14	9	1	144	2	3	4	5	3	161

Table 5. Grading results according to boring.

Boring Results			Boring Tear-Out			Total
			Grade 0	Grade 2	Grade 3	
Species	*E. nitens*	Count	54	0	0	54
		Standardised residual	0.1	−0.6	−0.6	
	E. globulus	Count	52	1	1	54
		Standardised residual	−0.2	1.1	1.1	
	P. radiata	Count	53	0	0	53
		Standardised residual	0.1	−0.6	−0.6	
Total		Count	159	1	1	161

Table 6. Grading results according to mortising.

Mortising Results			Mortising (Crushing)				Mortising (Tearing)				Mortising (Smoothness)		Total
			Grade 2	Grade 3	Grade 4	Grade 5	Grade 2	Grade 3	Grade 4	Grade 5	Grade 4	Grade 5	
Species	*E. nitens*	Count	0	20	10	0	0	20	9	1	0	30	30
		Standardised residual	−1.4	1.2	1.5	−2.5	−1.4	0.8	0.2	−1.2	−1.4	0.4	
	E. globulus	Count	0	2	9	19	0	6	16	8	0	30	30
		Standardised residual	−1.4	−3.4	1.1	5	−1.4	−2.6	2.7	2.9	−1.4	0.4	
	P. radiata	Count	6	24	0	0	6	24	0	0	6	24	30
		Standardised residual	2.8	2.2	−2.5	−2.5	2.8	1.8	−2.9	−1.7	2.8	−0.8	
Total		Count	6	46	19	19	6	50	25	9	6	84	90

Table 7. Grading results according to biscuit boring.

Biscuit Bore Results			Biscuit Bore (Crushed)		Biscuit Bore (Fuzzy)				Biscuit Bore (Chipped)		Total
			Grade 0	Grade 3	Grade 0	Grade 1	Grade 2	Grade 3	Grade 0	Grade 4	
Species	*E. nitens*	Count	30	0	0	0	0	30	29	1	30
		Standardised residual	0.1	−0.6	−1.5	−0.8	−2.5	2.1	−0.1	0.4	
	E. globulus	Count	29	1	7	0	4	19	29	1	30
		Standardised residual	−0.1	1.2	3.1	−0.8	−0.9	−0.4	−0.1	0.4	
	P. radiata	Count	30	0	0	2	15	13	30	0	30
		Standardised residual	0.1	−0.6	−0.5	1.6	3.4	−1.7	0.1	−0.8	
Total		Count	89	1	7	2	19	62	88	2	90

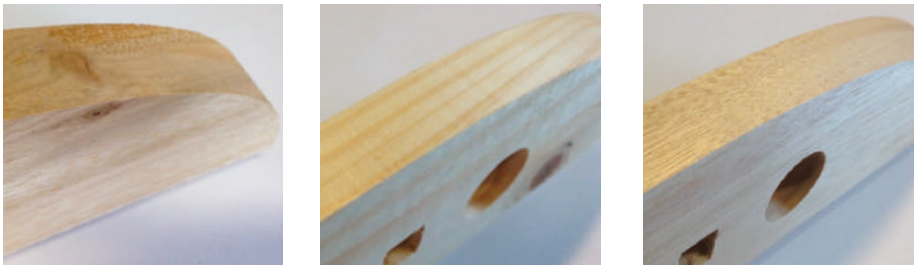

(**a**) (**b**) (**c**)

Figure 6. Examples of *E. globulus* (**a**) with a grade of G4 (poor) and *P. radiata* (**b**) and *E. nitens* (**c**) with a grade of G0 (excellent) for fuzzy routing side grain.

Routing end grain (Figure 7) divided the *E. nitens* samples into grades of G0 and G2; however, no statistically significant difference was found between the three species with respect to the chipped routing end grain (Table 3). This machinability characteristic was less sensitive among the species.

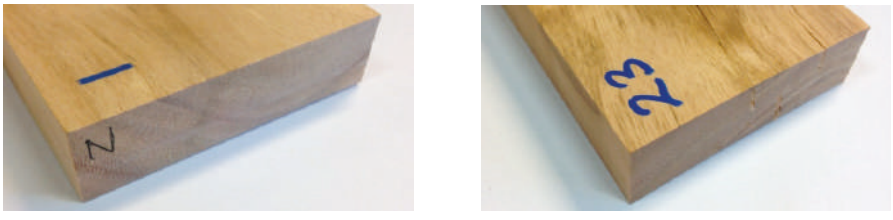

(**a**) (**b**)

Figure 7. Examples of *E. nitens* with grades of G0 (excellent) (**a**) and G2 (good) (**b**) for routing end grain.

The grading results of the samples with respect to shaping side grain are shown in Table 4. For both shaping side grains (raised or chipped), *P. radiata* displayed a better finish quality than *E. nitens* and *E. globulus*, with 100% defect-free results. The *E. nitens* samples, however, had the highest fuzzy shaping side grain quality compared to *P. radiata* and *E. globulus*, with 100% of the samples being graded as G0. None of the test samples from the three species had any grade worse than G3 with respect to shaping side grain (raised or fuzzy) (Figure 8).

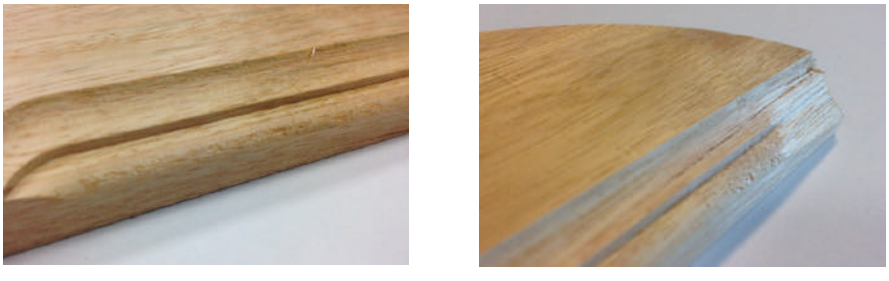

(**a**) (**b**)

Figure 8. Examples of *E. globulus* with a grade of G2 (good) for fuzzy shaping side grain (**a**) and *E. nitens* with a grade of G5 (very poor) for chipped shaping side grain (**b**).

All the *E. nitens* and *P. radiata* samples were graded as G0 with respect to boring tear-out (Table 5). Only two samples from *E. globulus* had a grade worse than G0, a difference that was not statistically significant (Figure 9).

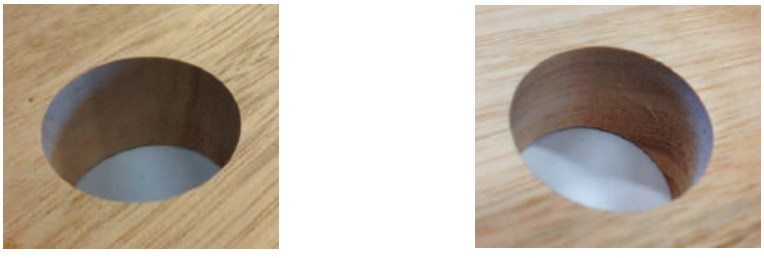

(**a**) (**b**)

Figure 9. Examples of *E. nitens* with a grade of G0 (excellent) (**a**) and *E. globulus* with a grade of G2 (good) (**b**) for boring tear-out.

The results indicated that mortising quality is significantly correlated to the wood species (Table 6), with *P. radiata*, *E. nitens*, and *E. globulus* having the best to the worst overall mortising qualities, respectively (Figure 10). There was no statistically significant difference between *E. nitens* and *E. globulus* in respect to mortising smoothness, whereas *P. radiata* had significantly better mortising smoothness than both eucalypt species. All *E. nitens* and *E. globulus* samples had a G5 grade for mortising smoothness.

(**a**) (**b**) (**c**)

Figure 10. Examples of *E. nitens* (**a**) and *E. globulus* (**b**) with grades of G5 (very poor), and *P. radiata* (**c**) with a grade of G2 (good) for mortising (tearing).

The *E. nitens* samples had the worst quality when graded based on biscuit bore (Table 7), with 100% of the samples being graded as G3 (Figure 11). More than 30% of the *E. globulus* samples were defect-free (G0), which made a high contribution to the statistical significance between the three species. The three species had almost the same quality when the biscuit bore (crushed and chipped) was used as the grade-determining parameter. The *E. globulus* samples showed more variations in the fuzzy biscuit-bore grain compared to the other two species.

(**a**) (**b**) (**c**)

Figure 11. Examples of *E. nitens* (**a**) with a grade of G3 (fair) for fuzzy biscuit-bore grain and *E. globulus* (**b**) and *P. radiata* (**c**) with a grade of G2 (good).

4. Discussion

The findings in this research intend to demonstrate appropriate new applications for hardwood plantation resources in machine-manufactured products. The following sections validate opportunities where hardwood plantation resources could serve as appropriate materials of choice.

4.1. Statistical Analyses of Density and MC Within Species

The results indicate a higher variability in the machinability of the *E. nitens* and *E. globulus* specimens compared to that of *P. radiata*. Part of this is because of the variation in the density of the samples and its influence on the results obtained. A possible physical phenomenon that explains the variation in machinability results—due to the degree of changes in densities—could relate to the management of the resource that was initially intended for pulplog production. The variations in MC for *E. nitens* specimens showed no significant correlation with any of the studied machinability characteristics ($p > 0.05$). The variations in specimen densities, however, had significant correlations with chipped routing end grain, raised shaping side grain and mortising (crushing and tearing) ($p < 0.05$). For *E. globulus*, the variation in MC values had significant correlations with fuzzy routing side grain and fuzzy shaping side grain ($p < 0.05$). In addition, the variations in specimen densities also had significant correlations with fuzzy routing side grain, fuzzy shaping side grain and mortising (tearing) ($p < 0.05$). For *P. radiata*, the variations in MC values had significant correlations with mortising (crushing, tearing, and smoothness) ($p < 0.05$) and the variations in specimen densities showed no statistically significant correlation with the studied machinability characteristics.

4.2. Routing End Grain and Boring

Despite being managed for pulplog production, machinability tests of *E. nitens* and *E. globulus*—as well as sawlog *P. radiata*—for routing end grain (fuzzy and raised), boring (crushing, fuzzy, and smoothness), resulted in defect-free specimens. Both pulplog resources were out-graded in quality of finish by *P. radiata* due to chipping in the end grain (*E. nitens*) and tear-out from boring (*E. globulus*). Expectedly, chipping and tear-out were present in the fiber-managed plantation species given that the nature of the resource to break apart is a direct reason for its use in pulp production. The chipping observation could be due to the long fiber lengths when machined perpendicular to the grain, and the tear-out evident in boring (also perpendicular to the grain) may be caused by pulling fibers. Regardless, the results suggest that either species would be an acceptable choice for products such as cabinetry or acoustic panels that require end-grain routing or a degree of good and better surface boring for fixtures or perforations, particularly where high-quality surface finishes are essential. Extra care in machining could mitigate chipping or tear-out from the pulplog resources. As suggested in ASTM D1666-11 (2011), a roughing cut offset by 1.6 mm then finished in a final pass can ensure that any edge damaged in roughing is removed for a better surface finish. As previously highlighted in this study, two solid carbide tools—one for roughing and the other for finishing—were used to ensure that

the best surface quality could be achieved. In addition, the roughing cut was conventional milling and the finishing cut was climb milling. Generally, optimal surface qualities were achieved directly parallel and perpendicular to the wood grain, and most raised grain, fuzzing, and chipping were at tangent angles following a parabola specimen shape as set out in ASTM D-1666.

4.3. Routing Side Grain and Shaping

E. nitens and *P. radiata* samples showed better routing qualities on the side grain than *E. globulus*. Once again, *P. radiata* out-graded both pulplog resources, and *E. nitens* out-graded *E. globulus*. In line with routing end grain, chipping appears to have been dominant for both hardwood species, particularly towards the edge of a specimen. This could have been caused by the length of wood fiber in plantation *Eucalyptus*, which typically results in pulling out or tearing more stock material than intended by machining. Similarly, fuzzy routing side grain for *E. globulus* was the greatest reason for the downgrading of these specimens. The results of shaping on the side grain also suggest that *E. globulus* and *P. radiata* are less desirable for architectural applications such as moldings where high-quality surface finishes are necessary. In comparison, shaping on the side grain of *E. nitens* resulted in raised grain.

4.4. Mortising and Biscuit Boring

P. radiata out performed *E. nitens* and *E. globulus*, however the results for all species were far from perfect, with no tests resulting in a defect-free grade (G0). This may suggest that following the defined test method set out in ASTM D1666-11 (2011) for mortising is not an ideal form of joinery. The results also suggest that the surface hardness of the tested species could have been low, and therefore the observed crushing by compression and tearing could have been mitigated by a change in choice of tooling. Consideration should be made, however, of the fact that grading of the mortise refers to an internal surface that is not seen in final products such as assembled furniture. As an alternative to mortise and tenon joinery, boring via CNC fabrication would be an acceptable alternative, as substantiated in the boring tests. In keeping with the grading standards set out in ASTM D1666-11 (2011), this study considered the quality in surface finish from biscuit boring, a more contemporary approach to joinery with dowels. All species performed exceptionally well against crushing and chipping. In this test, it was fuzzy grain that was the dominate grade-reducing feature. This may have been due to the pendulum motion of the biscuit dowel cutter. Regardless, the extrusion generated in this test—like a mortise—is internal, and not seen in a product's finally assembly. Moreover, the fuzzy grain caused by the biscuit borer could advantageously improve the retention of the biscuit dowel and glue for furniture or table tops.

4.5. Other Considerations

Another reason for the higher variability in the machinability of the *E. nitens* and *E. globulus* specimens compared to that of *P. radiata* could be that the pulplog specimens were selected randomly from ungraded timber boards high in natural features. Considering this, there could be a high potential to improve the machinability of these plantation species by making use of an appropriate timber grading system that would allow proper resources to be selected for appropriate higher-value products. Although *E. nitens* and *E. globulus* specimens were derived from pulplog resources, the results suggest that in some applications these species are appropriate alternatives for products where hardwood species are desirable or in demand.

The physical phenomena observed in *E. globulus* and *E. nitens*, such as the tearing, fuzzing, and chipping throughout the test specimens, could be related to fiber length, elasticity, hardness, and ductility of the pulp resources [23]. *E. globulus* is known for its high density, high coarseness, and high fiber-length [23], which contribute to its use in pulp production; however, these properties also render the resource useful for raw forest products as well as other composite and engineering forest products [23]. Carefully considered machining processes to mitigate chipping and tearing

parallel and perpendicular to wood grains may improve and reduce the quantity of machining defects in these hardwood species. This could be as simple as including lead-ins and -outs, making helical cuts, and programming multiple steps to mitigate visible fibre damage to value-added timber products. Future research could investigate these multiple variables to identify processes or techniques to avoid when machining plantation *Eucalyptus* species.

All species demonstrated both a high-quality and less-than-favorable surface finished with both CNC and manual machining techniques. Where possible, any automated system that is replicable and controllable is ideal for consistency in quality. This research suggests that both forms of machining can produce acceptable finishes for architectural value-added products.

Further research on the machinability of *Eucalyptus* pulplogs could consider the origin of specimens from log and tree positions, as well as the orientations of cuts. The impact of surface and internal checking could also be investigated to determine if these characteristics impact chipping and tear-out from various machinability tests conducted on fiber-managed hardwood resources. Furthermore, the impact of live and dead knots on machinability properties could be investigated to determine the acceptable presence of different types of knots on the appearance of products that are routed, shaped, or bored.

5. Conclusions

The aim of this study was to determine the machinability of Tasmanian plantation fibre-managed hardwood *Eucalyptus globulus* and *Eucalyptus nitens* and to evaluate their potential use in architectural interior products such as moldings, as well as other timber products such as furniture. Plantation sawlog-managed softwood *Pinus radiata* was used as a control reference given its acceptable quality and use in a wide range of architectural and product applications.

- The results in this study suggest that fibre-managed plantation hardwood *E. nitens* and *E. globulus* have the same machinability qualities (with no statistically significant difference) as sawlog-managed *P. radiata* for routing end grain (fuzzy, raised, and chipped), boring (crushing, fuzzy, smoothness, and tear-out), raised routing side grain, chipped shaping side grain, and biscuit bore (crushed and chipped). In products and applications where secondary manufacturing involves routing (end grain and side grain), boring, shaping, and biscuit boring, producers can expect acceptable machinability qualities that would allow the use of fibre-managed plantation hardwoods as an alternative to sawlog-managed plantations softwoods.
- No statistically significant difference was observed between *E. nitens* and *E. globulus* except when routing side grain (fuzzy and chipped), shaping side grain (raised and fuzzy), mortising (crushing and tearing), and fuzzy biscuit-bore grain were used as the grade-determining parameters.
- The correlations between the variations in density and machinability characteristics of *E. nitens* and *E. globulus* were statistically significant, whereas no significant correlations existed between the variations in density and machinability of *P. radiata*.

5.1. E. nitens

- The machinability characteristics of *E. nitens* were statistically comparable to *P. radiata* in all cases except for shaping side grain (raised and fuzzy), mortising (crushing, tearing, and smoothness) and fuzzy biscuit-bore grain.
- The studied *E. nitens* samples received the worst grades among the studied timber species when graded against raised shaping side grain and fuzzy biscuit-bore grain as the grade-determining parameters.
- The machinability of the *E. nitens* samples was significantly better than both *E. globulus* and *P. radiata* in respect to fuzzy shaping side grain.
- The *E. nitens* had better quality than *E. globulus* in respect to routing side grain (fuzzy and chipped), fuzzy shaping side grain, mortising (crushing and tearing), and fuzzy biscuit-bore grain.

- Unlike *P. radiata* and *E. globulus*, the variations in the MC of the samples had no important correlation with the machinability characteristics of *E. nitens*.

5.2. E. globulus

- The machinability characteristics of *E. globulus* were statistically comparable to *P. radiata* in all cases except for routing side grain (fuzzy and chipped), fuzzy shaping side grain, mortising (crushing, tearing, and smoothness) and fuzzy biscuit-bore grain.
- The only cases in which the *E. globulus* samples showed significantly better qualities than *P. radiata* were fuzzy shaping side grain and fuzzy biscuit-bore grain.

Author Contributions: Conceptualization, N.K.; formal analysis, N.K. and M.D.; investigation, N.K. and M.D.; methodology, N.K., M.D., M.L., and I.W.; resources, N.K. and M.L.; validation, N.K., M.D., M.L. and I.W.; writing—original draft preparation, N.K.; writing—review and editing, N.K, M.D. and M.L.

Funding: This research was funded by the Australian Research Council, Centre for Forest Value, University of Tasmania, TAS, Australia, grant number IC150100004. The APC was funded by the Australian Research Council, Centre for Forest Value, University of Tasmania, TAS, Australia.

Acknowledgments: The authors would like to thank Trevor Innes (TimberLink Australia) for supplying the sawn-board *P. radiata* for this study; Forico Pty Ltd. for providing the fibre-managed hardwood logs; and Britton Timbers for milling, drying, and dressing the fiber-managed hardwood resources.

Conflicts of Interest: The authors declare no conflict of interest. The funders had no role in the design of the study; in the collection, analyses, or interpretation of data; in the writing of the manuscript, or in the decision to publish the results.

References

1. Australian Bureau of Agricultural and Resource Economics and Sciences (ABARES). Australian Plantation Statistics 2017 Update, Australian Bureau of Agricultural and Resource Economics and Sciences, Canberra, August 2017. CC BY 3.0. Available online: https://data.gov.au/dataset/ds-dga-a1fcbbec-807c-438e-b8fd-db1a9a93f887 (accessed on 4 October 2018).
2. American Society for Testing and Materials (ASTM). *Standard Test Methods for Conducting Machining Tests of Wood and Wood-Base Materials*; ASTM D1666-11; ASTM International: West Conshohocken, PA, USA, 2011; 23p.
3. Zobel, B. The changing quality of the world wood supply. *Wood Sci. Technol.* **1984**, *181*, 1–17. [CrossRef]
4. Hamilton, M.G. The Genetic Improvement of Eucalyptus Globulus and Eucalyptus Nitens for Solidwood Production. Ph.D. Dissertation, University of Tasmania, Newnham, Australia, 2007.
5. Dugmore, M.; Nocetti, M.; Brunetti, M.; Naghizadeh, Z.; Wessels, C.B. Bonding quality of cross-laminated timber: Evaluation of test methods on Eucalyptus grandis panels. *Constr. Build. Mater.* **2019**, *211*, 217–227. [CrossRef]
6. Derikvand, M.; Kotlarewski, N.; Lee, M.; Jiao, H.; Chan, A.; Nolan, G. Short-term and long-term bending properties of nail-laminated timber constructed of fast-grown plantation eucalypt. *Constr. Build. Mater.* **2019**, *211*, 952–964. [CrossRef]
7. Pangh, H.; Hosseinabadi, H.Z.; Kotlarewski, N.; Moradpour, P.; Lee, M.; Nolan, G. Flexural performance of cross-laminated timber constructed from fibre-managed plantation eucalyptus. *Constr. Build. Mater.* **2019**, *208*, 535–542. [CrossRef]
8. Aguilera, A.; Martin, P. Machining qualification of solid wood of *Fagus silvatica* L. and *Piceaexcelsa* L.: Cutting forces, power requirements and surface roughness. *Holz Als Roh-Und Werkst.* **2001**, *59*, 483–488. [CrossRef]
9. Aguilera, A.; Meausoone, P.J.; Martin, P. Wood material influence in routing operations: The MDF case. *Eur. J. Wood Wood Prod.* **2000**, *58*, 278–283. [CrossRef]
10. Lin, R.J.; van Houts, J.; Bhattacharyya, D. Machinability investigation of medium-density fibreboard. *Holzforschung* **2006**, *60*, 71–77. [CrossRef]
11. Szymanowski, K.; Gorski, J.; Czarniak, P.; Wilkowski, J.; Podziewski, P.; Cyrankowski, M.; Morek, R. Machinability index of certain types of chipboards. In *Forestry and Wood Technology; Annals of Warsaw*; Warsaw University of Life Sciences Press: Warsaw, Poland, 2015; p. 90.

12. Goli, G.; Sandak, J. Proposal of a new method for the rapid assessment of wood machinability and cutting tool performance in peripheral milling. *Eur. J. Wood Wood Prod.* **2016**, *74*, 867–874. [CrossRef]
13. Sütçü, A. Investigation of parameters affecting surface roughness in CNC routing operation on wooden EGP. *BioResources* **2012**, *8*, 795–805. [CrossRef]
14. Moya-Roque, R.; Tenorio-Monge, C.; Salas-Garita, C.; Berrocal-Jiménez, A. Evaluation of wood properties from six native species of forest plantations in Costa Rica. *Bosque* **2016**, *37*, 71–84. [CrossRef]
15. Podziewski, P.; Szymanowski, K.; Górski, J.; Czarniak, P. Relative Machinability of Wood-Based Boards in the Case of Drilling–Experimental Study. *BioResources* **2018**, *13*, 1761–1772. [CrossRef]
16. Ratnasingam, J.; Ioras, F. Effect of heat treatment on the machining and other properties of rubberwood. *Eur. J. Wood Wood Prod.* **2012**, *70*, 759–761. [CrossRef]
17. Laina, R.; Sanz-Lobera, A.; Villasante, A.; López-Espí, P.; Martínez-Rojas, J.A.; Alpuente, J.; Sánchez-Montero, R.; Vignote, S. Effect of the anatomical structure, wood properties and machining conditions on surface roughness of wood. Maderas. *Cienc. Y Tecnol.* **2017**, *19*, 203–212. [CrossRef]
18. Thoma, H.; Peri, L.; Lato, E. Evaluation of wood surface roughness depending on species characteristics. Maderas. *Cienc. Y Tecnol.* **2015**, *17*, 285–292. [CrossRef]
19. Aguilera, A.; Zamora, R. Surface roughness in sapwood and heartwood of Blackwood (*Acacia melanoxylon* R. Br.) machined in 90-0 direction. *Eur. J. Wood Wood Prod.* **2009**, *67*, 297–301. [CrossRef]
20. Ramanakoto, M.F.; Andrianantenaina, A.N.; Ramananantoandro, T.; Eyma, F. Visual and visuo-tactile preferences of Malagasy consumers for machined wood surfaces for furniture: Acceptability thresholds for surface parameters. *Eur. J. Wood Wood Prod.* **2017**, *75*, 825–837. [CrossRef]
21. Standards Australia. *Australian Standard 2796 Timber—Hardwood—Sawn and Milled Products Part 3: Timber for Furniture Components*; Standards Associations of Australia: Sydney, NSW, Australia, 1999; reconfirmed in 2016.
22. Goli, G.; Marchal, R.; Negri, M.; Costes, J.P. Surface quality: Comparison among visual grading and 3D roughness measurements. In Proceedings of the 15th International Wood Machining Seminar, Los Angeles, CA, USA, 30 July–1 August 2001.
23. Carrillo-Varela, I.; Valenzuela, P.; Gacitúa, W.; Mendonca, R.T. An Evaluation of Fiber Biometry and Nanomechanical Properties of Different Eucalyptus Species. *BioResources* **2019**, *14*, 6433–6446. [CrossRef]

© 2019 by the authors. Licensee MDPI, Basel, Switzerland. This article is an open access article distributed under the terms and conditions of the Creative Commons Attribution (CC BY) license (http://creativecommons.org/licenses/by/4.0/).

forests

MDPI

Article

Artificial Neural Network Modeling for Predicting Wood Moisture Content in High Frequency Vacuum Drying Process

Haojie Chai [1], Xianming Chen [2], Yingchun Cai [1] and Jingyao Zhao [1,*]

[1] Ministry of Education, Key Laboratory of Bio-Based Material Science and Technology, College of Material Science and Engineering, Northeast Forestry University, Harbin 150040, China; nefuchj@163.com (H.C.); caiyingchunnefu@163.com (Y.C.)

[2] College of Information and Computer Engineering, Northeast Forestry University, Harbin 150040, China; chenxianming@nefu.edu.cn

* Correspondence: zjy_20180328@nefu.edu.cn; Tel./Fax: +86-451-8219-1002

Received: 5 December 2018; Accepted: 26 December 2018; Published: 29 December 2018

Abstract: The moisture content (MC) control is vital in the wood drying process. The study was based on BP (Back Propagation) neural network algorithm to predict the change of wood MC during the drying process of a high frequency vacuum. The data of real-time online measurement were used to construct the model, the drying time, position of measuring point, and internal temperature and pressure of wood as inputs of BP neural network model. The model structure was 4-6-1 and the decision coefficient R^2 and Mean squared error (Mse) of the training sample were 0.974 and 0.07355, respectively, indicating that the neural network model had superb generalization ability. Compared with the experimental measurements, the predicted values conformed to the variation law and size of experimental values, and the error was about 2% and the MC prediction error of measurement points along thickness direction was within 2%. Hence, the BP neural network model could successfully simulate and predict the change of wood MC during the high frequency drying process.

Keywords: neural network; high frequency drying; moisture content; wood

1. Introduction

Wood MC (moisture content) is one of the crucial indicators in the drying process as it has a direct impact on the stability of wood drying quality, and a reasonable control of MC can help in meeting the various quality requirements of actual wood products [1]. High frequency vacuum drying is a joint drying technology with a fast drying rate, low energy consumption, and low environmental pollution [2], and is in widespread use throughout the wood drying industry [3]. However, due to the interference of high frequency electromagnetic fields, the traditional MC online monitoring device cannot be used normally, which makes the online prediction and effective detection of wood MC problematic [4]. Therefore, the research on the prediction model of wood MC is of great significance in the high frequency drying process.

The wood structure is complex and it is difficult to establish a precise mathematical model through mathematical mechanism. An accurate control of MC requires precise mathematical models. The high frequency vacuum drying of wood is a non-linear, complex drying process, which is difficult to accurately express, control, or implement by using general mathematical methods [5]. The concept of BP (Back Propagation) neural network comes from the biological system of brain, which is composed of numerous neurons that are connected to each other through synapses that process information. The neural network has decent characteristics for predicting nonlinear complex systems [6,7], and the model reflects the intrinsic connection of experimental data after a finite

number of iterative calculations. It is not only strong at processing nonlinearity, self-organizing adjustment, adaptive learning, and fault-tolerant anti-noise [8–10] but also can effectively deal with nonlinear and complex fuzzy processes. An effective network prediction model can be established without any assumption or theoretical relationship analysis, based on the historical data and powerful self-organization integration capabilities [11,12].

Artificial neural networks are increasingly being used for modeling in the field of wood science. For instance, in the field of wood drying, Avramidis (2006) [13] predicted the drying rate of wood based on neural network construction model; Zhang Dongyan (2008) [14] constructed a neural network model for predicting wood MC during conventional drying; İlhan Ceylan (2008) [15] used neural network models to study wood drying characteristics; Watanabe (2013, 2014) [16,17] employed artificial neural network model to predict the final moisture content of Sugi (*Cryptomeria japonica*) during drying and evaluate the drying stress on the wood surface. Ozsahin (2017) [18] utilized artificial neural networks to successfully predict the equilibrium moisture content and specific gravity of heat-treated wood. The artificial neural networks are widely used in the study of conventional drying characteristics, stress monitoring, and MC prediction of wood [19]; however, the use of neural networks to predict changes in the wood MC during high frequency drying has been rarely studied.

Hence, in order to provide a predictive model for the control of wood MC during high frequency drying, based on the BP neural network algorithm and using the real-time online measurement data, drying time, location of measuring point, and internal temperature and pressure of wood as the input to neural network model, the changes in the wood MC can be predicted. Also, the feasibility and prediction accuracy of the model was analyzed.

2. Materials and Methods

2.1. On-Line Monitoring of Wood Internal Temperature and Pressure

Some uniform and defect-free Mongolian pine (*Pinus sylvestris* var. *mongholica* Litv.) were selected. The 200 mm ends were removed at both ends of the test piece, and the specifications were 120 × 120 × 500 mm specimens after sawing and planning, and the initial moisture content was 50%. As shown in Figure 1, five temperature pressure measuring points were uniformly preset at the center of the sample in the thickness direction. Drilling holes on the side of specimen with a 4 mm drill bit to depth of 60 mm (seeing Figure 1 for specific locations). Each measuring point was embedded with one of the pressure and temperature fiber sensors, and the locations where the sensors were in contact with the surface of wood were coated with silica gel to ensure good sealing. The data was recorded online through the optical fiber sensors.

As shown in Figure 2, 1 is drying tank of high frequency vacuum with the diameter of 650 mm and length of 1350 mm; 2 and 4 are upper and lower plates respectively; and 3 is test material. The high frequency generator oscillates at the frequency of 27.12 MHz and outputs the effective power of 1 kW, which is powered by the center of electrode plate length.

During the drying process, the wood control temperature was set to 55 °C, the ambient pressure was set to 8 kPa, and the control of high frequency output time was set to stop for 2 min after a continuous oscillation for 7 min. In the early stage of drying, wood was quickly taken out and weighed after every 4 h, the real-time MC of wood was calculated, and the pressure and temperature values of five measuring points before the sample was taken out were recorded. In the middle stage of drying, the data were recorded once every 8 h; while, in the later stage of drying, the data were recorded once every 12 h.

The drying was carried out for 204 h until wood MC was dried to 11.56%. The experiment was stopped and a total of 135 data were recorded.

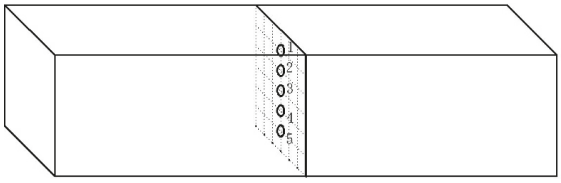

Figure 1. Diagram of the wood tested sample and location of the sensors. (1 is the upper layer measuring point; 2 is the upper middle layer measuring point; 3 is the core layer measuring point; 4 is the lower middle layer measuring point; and 5 is the lower layer measuring point).

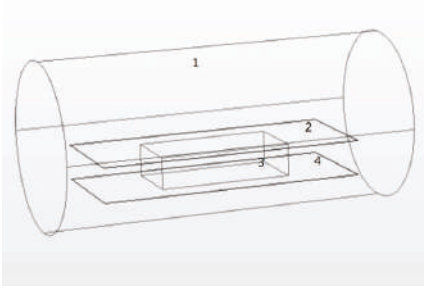

Figure 2. Drying tank of high frequency vacuum.

2.2. BP Neural Network Model

The BP (Back Propagation) model is currently the most studied and widely used artificial neural network model [20]. It has a powerful nonlinear mapping ability and the qualities of human intelligence such as self-learning, adaptive, associative memory, and parallel information processing. It can imitate the human brain nervous system to store, retrieve, and process the information with an excellent fault tolerance, and is extremely suitable for modeling and control of complex systems [21]. The Python language has a rich and powerful class library. It is an interpreted, interactive, and pure object-oriented scripting programming language that combines the best design principles and ideas of several different languages and is widely used in various fields of software development and application programming. Therefore, this paper built the BP neural network model using Python language programming.

2.2.1. Determination of Neuron Number

The neural network prediction model in this paper uses a three-layer feedforward network structure, which includes an input layer, a hidden layer, and an output layer [22]. The hidden layer can be further divided into a single hidden layer and multiple hidden layer according to the layer number. The multiple hidden layer is composed of multiple single hidden layers. Compared with a single hidden layer, a multiple hidden layer has a stronger generalization ability and higher prediction accuracy, but the training time is longer. The selection of hidden layers should be considered comprehensively based on the network accuracy and training time. For a simple mapping relationship, in case the network accuracy meets the requirements, the single hidden layer can be selected to speed up the process. For a complex mapping relationship, the multiple hidden layer can be selected to enhance the network prediction accuracy. Therefore, according to the research requirements, the study chose a single hidden layer.

The number of hidden neurons also has a certain impact on the network [23]. The neuron number in the hidden layer is directly related to the predictive power of network model. If the number is too high, it will not only increase the network training time but also the network will not converge to the target error, resulting in an over-fitting. If the number is too small, the model training will be

insufficient and would not be able to completely express the relationship between the input variables and output parameters, thus affecting the predictive ability of the model. Therefore, the determination of neuron number in hidden layer is particularly critical [24].

The optimal neurons number was determined via trial and error method [5]. The neuron number in hidden layer was set to 4~10, and the learning error and epoch of different nodes were tested by network training. The optimal node was obtained by comparison analysis.

2.2.2. Data Normalization

The data obtained during the experiment were randomly divided into two data sets: a training group and a test group. The 101 test data of the training group accounted for 75% of the total data, while 34 data of the test group accounted for 25% of the total data.

Each input sample usually has different physical meanings and dimensions; hence, in order to make each input sample have an equally important position and also to prevent the adjustment of the weight into the flat area of error, the input sample needs to be normalized [5]. In addition, as the neurons of the BP neural network adopt the Sigmoid transfer function and the output is between [0, 1], it is also necessary to normalize the output samples (Equation (1)).

$$X' = \frac{X - X_{\min}}{X_{\max} - X_{\min}} \tag{1}$$

where X' is the X normalization value; $X_{\max}$ and $X_{\min}$ are the maximum and minimum values of X, respectively.

The neurons in each layer are only connected to the neurons in the adjacent layer and there is no connection between the neurons in each layer. Also, there is no feedback connection between the neurons in each layer. The input signal first propagates forward to the hidden node and then through the transformation function. The output information of the hidden node is propagated to the output node and the output result is given after processing. In general, the Sigmoid transfer function (Equation (2)) is used on all nodes of hidden layer. In the output layer, all nodes use the linear transfer function Pureline.

$$f = \frac{1}{1 + e^{-x}} \tag{2}$$

where f represents the neuron output value and x represents the neuron input value.

2.2.3. Model Performance Analysis

In the model correlation test, the model was evaluated by using the determination coefficient R^2 and Mse (Mean squared error) of the training sample [25].

The determination coefficient R^2 is defined as:

$$R^2 = \frac{\sum_{i=1}^{n} (t_i - p_i)^2}{\sum_{i=1}^{n} t_i^2 \sum_{i=1}^{n} p_i^2}. \tag{3}$$

The Mean square error (Mse) is calculated as [12]:

$$Mse = \frac{1}{n} \sum_{n=1}^{n} (t_i - p_i)^2 \tag{4}$$

where t_i (i = 1, 2, . . . , n) is the predicted value of the ith sample, p_i (i = 1, 2, . . . , n) is the true value of the ith sample, and n is the total number of all samples. The decision coefficient is in [0, 1], and the closer the value to 1, the better the model performance, and the closer to 0, the worse the model performance. The smaller the sample Mean square error, the better the prediction performance and the better the model performance. The learning efficiency is set to 0.01.

3. Results and Discussion

3.1. Determination of Neuron Number

The corresponding relationship between the neuron number of hidden layer and the training error and epoch of neural network is shown in Figure 3. When the node number of hidden layer is 6, the training error is the smallest at 0.07355, and the epoch is 17, the network training is faster. These results show that the neural network model has superb generalization ability at this time [26]; hence, the node number of hidden layer is determined to be 6. According to the node number of hidden layer, the structure of neural network is shown in Figure 4.

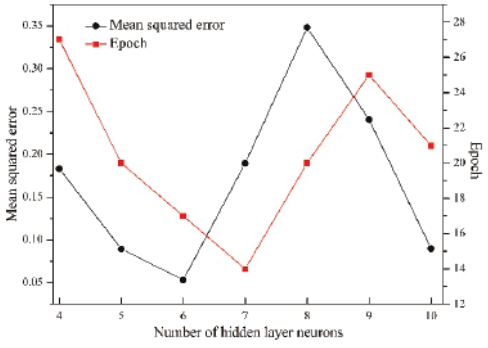

Figure 3. Correspondence between the network error and the number of hidden layer neurons.

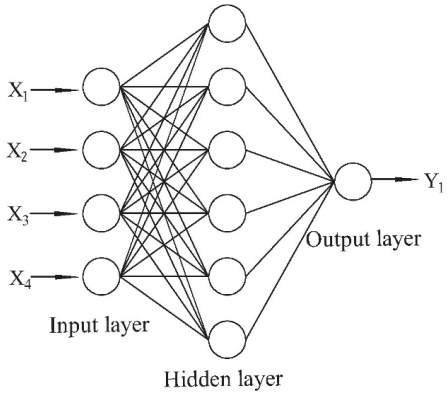

Figure 4. BP (Back Propagation) neural network structure diagram (X_1: drying time; X_2: measuring point position; X_3: temperature; X_4: pressure; Y_1: MC (moisture content)).

3.2. Model Performance Analysis

The training regression map for the BP neural network is shown in Figure 5. The linear regression equation between experimental and the predicted value is y = 0.948x + 1.24 while the determination coefficient R^2 is 0.974. These results indicate that the experimental and predicted values fit well. The BP neural network model has a good performance and can explain 97% of the above experimental values [24].

The predicted fitted curve for the neural network is shown in Figure 6. The remaining 25% of the samples are predicted and compared with the experimental values. The predicted values are consistent

with the variation and size of the experimental values. Initially, the BP neural network model can simulate and predict the change of wood MC during high frequency drying.

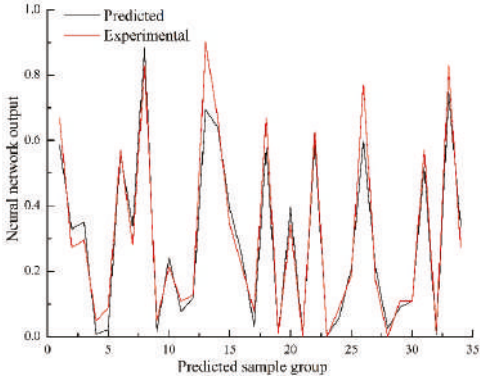

Figure 5. Training regression graph of BP neural network.

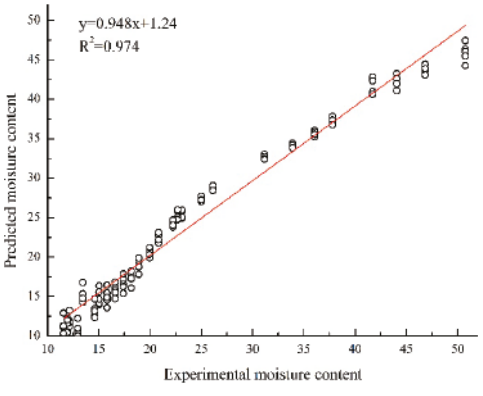

Figure 6. Prediction fitting curve of BP neural network.

3.3. Prediction of Moisture Content Change

During the drying process of wood, the free water is primarily discharged along the large capillary system above the fiber saturation point. The bound water in cell wall is mainly discharged along the microcapillary system below the fiber saturation point. The bound water is affected by the hydroxyl interaction force in the amorphous region of cell wall [27]. In the early stage of drying, there is a short accelerated drying section. The energy of high frequency radiation is basically used to raise the temperature of wood, and the drying rate is gradually increased from zero. The middle stage of drying is constant-speed drying section. The energy of high frequency radiation is basically used to evaporate the moisture in wood. The MC decreases rapidly and exhibits constant-speed drying tendency. This stage basically completes the evaporation process of moisture in wood. In the later stage of drying, there is less water in wood, and the evaporation rate of moisture and the drying rate of wood gradually decrease [28].

The experimental data is input into the trained model for simulation verification. Figure 7 presents the curve of predicted and experimental values with time. In the early stage of drying, the predicted values are slightly lower than the experimental values; in the middle stage of drying, the predicted values are slightly higher than the experimental values; and in the later stage of drying, the predicted values have a slight wave motion, but overall the value is basically the same as the experimental values.

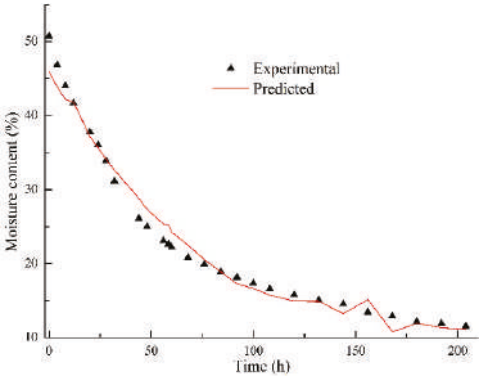

Figure 7. Simulation results of BP neural network.

Figure 8 displays the predicted error curve for the neural network (error = experimental value − predicted value [29]). The overall error range is −4%~6% and most of the data is concentrated between −2%~2%, which can basically meet the requirements of prediction accuracy in wood drying.

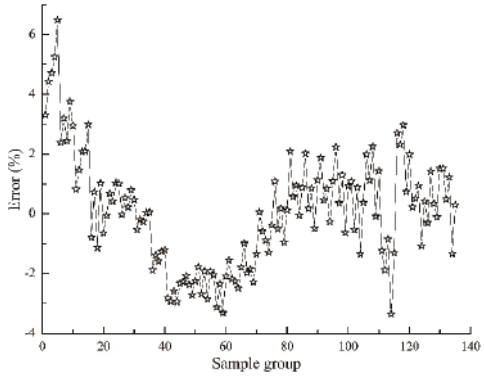

Figure 8. Prediction error of BP neural network.

Overall, the predicted data could basically reflect the change trend of MC during the high frequency drying process. The prediction error is about 2%, which proves the feasibility of BP neural network model in MC prediction. Moreover, if the external environmental parameters in the high frequency drying process and the relevant parameters of wood itself are known, the trained neural network model can be used to predict the MC change, thereby eliminating the complicated experimental detection process and saving time and cost [30].

3.4. Analysis of Stratified Moisture Content Prediction Error

Figure 9 shows the MC prediction error of measurement points along thickness direction. In the early and later stage of drying, the error is positive and the predicted values are slightly less than the experimental values. In the middle stage of drying, the error is negative and the predicted values are slightly larger than the experimental values. Among these, the error in the middle stage of drying is the largest, followed by the early and later stage of drying. In the early and middle stage of drying, along the thickness direction of test material, from top to bottom, the error increases firstly, then decreases, then increases, and then decreases. The results show M-type trend with no clear law, and the error of the upper surface measurement point is the smallest. In the later stage of drying, along the thickness

direction of the test material, from top to bottom, the error is firstly reduced, then increased, and then decreased, while the error at the upper intermediate layer is the smallest.

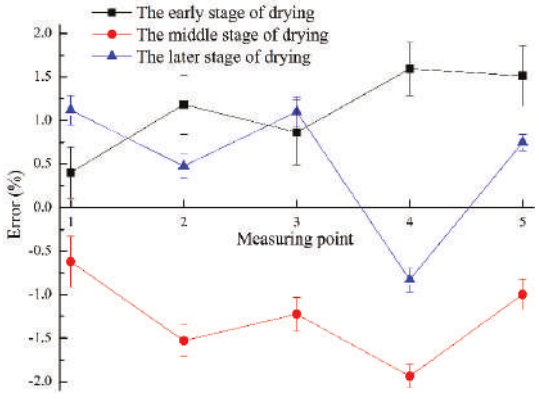

Figure 9. Error analysis of stratified moisture content prediction.

Due to the difference in material properties at different locations of the wood and the degree of electromagnetic radiation, the prediction accuracy of each measurement point is different. But overall, the prediction error of MC of each layer is less than 2%, indicating that the prediction accuracy of each measurement point is good and can meet the demand for stratified moisture content prediction.

4. Conclusions

The BP neural network was used to simulate the wood MC during the high frequency drying process. The drying time, the location of measuring point, and the internal temperature and pressure of the wood were taken as input variables, while the wood MC was the output variable, 101 test data of the training group accounted for 75% of the total data, while 34 data of the test group accounted for 25% of the total data. The results showed that when the number of hidden layer of neurons was six, the neural network training error was the smallest and the BP neural networks had better stability. The error between the predicted and the experimental values was about 2% and the stratified moisture content prediction error was within 2%, which the model could well simulate the change trend of wood MC during the drying process. In general, although the performance of wood varies greatly and the complex relationship has not been completely elucidated, the proposed neural network model is reliable and has a good predictive power.

Author Contributions: H.C. and X.C. conceived and designed the experiments; J.Z. performed the experiments; H.C. and Y.C. analyzed the data and wrote the paper.

Funding: The Fundamental Research Funds for the Central Universities (Grant No. 2572018BB08) and the National Natural Science Foundation of China (Grant No. 31670562), financially supported this research.

Acknowledgments: The authors thank Zhiqiang Huang for the technical support in the computer field.

Conflicts of Interest: The authors declare no conflict of interest.

References

1. Xie, J. Study on Larch Wood Drying Models by Artificial Neural Network. Master's Thesis, Northeast Forestry University, Harbin, China, 2013.
2. Chai, H.J. Development and Validation of Simulation Model for Temperature Field during High Frequency Heating of Wood. *Forests* **2018**, *9*, 327. [CrossRef]
3. Kong, F.X. Study on Technique of Radio-Frequency Vacuum Drying for Oak Veneer. *J. Northeast. For. Univ.* **2018**, *6*, 46.

4. Li, X.J. *Characteristics of Microwave Vacuum Drying of Wood and Mechanism of Thermal and Mass Transfer*; China Environmental Science Press: Beijing, China, 2009; p. 65. ISBN 9787802099890.
5. Yu, H.M. Study on Drying Mathematical Model of Hawthorn Using Microwave Coupled with Hot Air and Drying Machine Design. Ph.D. Thesis, Jilin University, Changchun, China, 2015.
6. Zhou, P. *MATLAB Neural Network Design and Application*; Tsinghua University Press: Beijing, China, 2013; p. 153. ISBN 9787302313632.
7. Poonnoy, P.; Tansakul, A. Artificial Neural Network Modeling for Temperature and Moisture Content Prediction in Tomato Slices Undergoing Microwave-Vacuum Drying. *J. Food Sci.* **2007**, *72*, E042–E047. [CrossRef] [PubMed]
8. Sablani, S.S.; Kacimov, A. Non-iterative estimation of heat transfer coefficients using artificial neural network models. *Int. J. Heat Mass Transf.* **2005**, *48*, 665–679. [CrossRef]
9. Rai, P.; Majumdar, G.C. Prediction of the viscosity of clarified fruit juice using artificial neural network: A combined effect of concentration and temperature. *J. Food Eng.* **2005**, *68*, 527–533. [CrossRef]
10. Shyam, S.; Sablani, M. Using neural networks to predict thermal conductivity of food as a function of moisture content, temperature and apparent porosity. *Food Res. Int.* **2003**, *36*, 617–623.
11. Hagan, M.T. *Neural Network Design*; PWS Publishing Company: Boston, MA, USA, 1996.
12. Fu, Z. Artificial neural network modeling for predicting elastic strain of white birch disks during drying. *Eur. J. Wood Wood Prod.* **2017**, *75*, 949–955. [CrossRef]
13. Wu, H.W.; Stavros, A. Prediction of Timber Kiln Drying Rates by Neural Networks. *Dry Technol.* **2006**, *24*, 1541–1545. [CrossRef]
14. Zhang, D.Y. Neural network prediction model of wood moisture content for drying process. *Sci. Silva Sin.* **2008**, *44*, 94–98.
15. İlhan, C. Determination of Drying Characteristics of Timber by Using Artificial Neural Networks and Mathematical Models. *Dry Technol.* **2008**, *26*, 1469–1476.
16. Watanabe, K. Artificial neural network modeling for predicting final moisture content of individual Sugi (*Cryptomeria japonica*) samples during air-drying. *J. Wood Sci.* **2013**, *59*, 112–118. [CrossRef]
17. Watanabe, K. Application of Near-Infrared Spectroscopy for Evaluation of Drying Stress on Lumber Surface: A Comparison of Artificial Neural Networks and Partial Least Squares Regression. *Dry Technol.* **2014**, *32*, 590–596. [CrossRef]
18. Ozsahin, S. Prediction of equilibrium moisture content and specific gravity of heat treated wood by artificial neural networks. *Eur. J. Wood Wood Prod.* **2018**, *76*, 563–572. [CrossRef]
19. Aghbashlo, M. Application of Artificial Neural Networks (ANNs) in Drying Technology: A Comprehensive Review. *Dry Technol.* **2015**, *33*, 1397–1462. [CrossRef]
20. Zhang, Z.Y. Research on Load Forecasting Analysis of Wuhai Power Grid Based on Artificial Neural Network BP Algorithm. Master Thesis, University of Electronic Science and Technology of China, Sichuan, China, 2008.
21. Bi, W. Research and Design of a Wood Drying Control System Based on Artificial Neural Network. Master's Thesis, Jilin University, Changchun, China, 2011.
22. MATLAB Chinese Forum. *30 Case Analysis of MATLAB Neural Network*; Beijing University of Aeronautics and Astronautics Press: Beijing, China, 2010.
23. Liu, T.Y. Improvement Research and Application of BP Neural Network. Master's Thesis, Northeast Agricultural University, Harbin, China, 2011.
24. Fu, Z.Y. Study on Dry Stress and Strain of Birch Tree in Conventional Drying Process. Ph.D. Thesis, Northeast Forestry University, Harbin, China, 2017.
25. Zhang, T. Prediction Model of Moisture Content of Ginger Hot Air Drying Based on BP Neural Network and SVM. Master's Thesis, Inner Mongolia Agricultural University, Hohhot, China, 2014.
26. Xu, X. Nonlinear fitting calculation of wood thermal conductivity using neural networks. *Zhejiang Univ. (Eng. Sci.)* **2007**, *41*, 1201–1204.
27. Gao, J.M. *Wood Drying*, 1st ed.; Science Press: Beijing, China, 2008; p. 10. ISBN 9787030205179.
28. Allegretti, O. Nonsymmetrical drying tests—Experimental and numerical results for free and constrained spruce samples. *Dry Technol.* **2018**, *36*, 1554–1562. [CrossRef]

29. Cai, Y.C. *Wood High Frequency Vacuum Drying Mechanism*; Northeast Forestry University Press: Harbin, China, 2007.
30. Wang, Y. Prediction of Wood Moisture Content Based on BP Neural Network Optimized by SAGA. *Tech. Autom. Appl.* **2013**, *32*, 4–6.

© 2018 by the authors. Licensee MDPI, Basel, Switzerland. This article is an open access article distributed under the terms and conditions of the Creative Commons Attribution (CC BY) license (http://creativecommons.org/licenses/by/4.0/).

forests

MDPI

Article

Multi-Scale Evaluation of the Effect of Phenol Formaldehyde Resin Impregnation on the Dimensional Stability and Mechanical Properties of *Pinus Massoniana* Lamb.

Xinzhou Wang [1], Xuanzong Chen [1], Xuqin Xie [2], Shaoxiang Cai [1], Zhurun Yuan [1] and Yanjun Li [1,*]

[1] College of Materials Science and Engineering, Nanjing Forestry University, Nanjing 210037, China
[2] Dehua Tubao New Decoration Material Co., Ltd., Zhejiang 313200, China
* Correspondence: lalyj@njfu.edu.cn; Tel.: +86-025-85428507

Received: 1 July 2019; Accepted: 27 July 2019; Published: 31 July 2019

Abstract: The local chemistry and mechanics of the control and phenol formaldehyde (PF) resin modified wood cell walls were analyzed to illustrate the modification mechanism of wood. Masson pine (*Pinus massoniana* Lamb.) is most widely distributed in the subtropical regions of China. However, the dimensional instability and low strength of the wood limits its use. Thus, the wood was modified by PF resin at concentrations of 15%, 20%, 25%, and 30%, respectively. The density, surface morphology, chemical structure, cell wall mechanics, shrinking and swelling properties, and macro-mechanical properties of Masson pine wood were analyzed to evaluate the modification effectiveness. The morphology and Raman spectra changes indicated that PF resin not only filled in the cell lumens, but also penetrated into cell walls and interacted with cell wall polymers. The filling and diffusing of resin in wood resulted in improved dimensional stability, such as lower swelling and shrinking coefficients, an increase in the elastic modulus (E_r) and hardness (H) of wood cell walls, the hardness of the transverse section and compressive strength of the wood. Both the dimensional stability and mechanical properties improved as the PF concentration increased to 20%; that is, a PF concentration of 20% may be preferred to modify Masson pine wood.

Keywords: *Pinus massoniana* Lamb.; phenol formaldehyde resin; wood impregnation; wood properties; cell-wall mechanics

1. Introduction

Pinus massoniana Lamb., commonly known as Masson pine, is one of the most widely distributed tree species in the subtropical regions of China [1]. The wood from Masson pine planted forests has become an important industrial raw material for wide commercial use such as wood construction, wood-based panels, and polymer composites due to the beautiful wood grain, good adaptability to the environment, and shorter growth cycle [2,3]. However, as one of the common fast-growing tree species, Masson pine wood also presents drawbacks which limit its practical application, such as low dimensional stability, softness, and low bio-durability [4,5]. In the past few decades, a number of modification methods have been proposed to enhance the quality and high value-added utilization of plantation wood, including thermal or densification treatment, surface coating, and chemical impregnation [6–10]. Above all, chemical impregnation under vacuum or pressure has been proven to be an effective method to improve the properties of the wood. Among the existing chemical modification methods, impregnating and curing the wood with resins appears to especially promote the industrial utilization of wood [11,12].

Phenol formaldehyde (PF) resin is a popular thermosetting agent that forms a three dimensional structure via cross-linking reactions after curing, which are extensively used in exterior grade

wood-based panels for its excellent performance, including water resistance and chemical stability [13–15]. It has therefore been widely used to improve dimensional stability and strength and prolong the service life of wood for indoor and outdoor use [16–18]. To date, changes in physical, mechanical, and chemical properties of chemically modified wood have been intensively analyzed at the macro scale [19,20]. The modified wood achieved high dimensional and stiffness stability and biological resistance. Monomers such as methyl methacrylate, styrene-methyl methacrylate and styrene-glycidyl methacrylate have been utilized for wood modification and have proven that the monomers not only filled in the cell lumens, but also penetrated into the cell walls [21,22]. However, for a pre-polymer like PF resin with a higher molecular weight, it is still unclear whether it can penetrate into cell wall or not, or what the accompanied influence on the cell wall would be. In particular, only limited attempts have been made to find out the correlations between chemical, physical, and mechanical performance between the cell wall- and macro-level to indicate the contribution of cell wall modification. Nanoindentation (NI) has been successfully applied for measuring the mechanics of wood cell walls including modulus of elasticity, hardness, etc. [23–25] and the Raman spectra technique can detect the local chemical structure of wood cell walls [26], which facilitates in situ characterization of the effects of PF resin impregnation on wood cell walls.

The purpose of this study was to characterize the properties of PF resin modified Masson pine wood for enriching the fundamental theory of wood chemical modification, which may benefit the modification process. For this purpose, the changes in morphology, local chemical structure and mechanics at the cell wall level and the density, dimensional stability, and mechanical properties at the macro-scale of Masson pine wood after PF resin impregnation were analyzed using scanning electron microscopy (SEM), Raman, NI, and conventional physical and mechanical test instruments, respectively.

2. Materials and Methods

2.1. Materials

Wood samples were obtained from 40-year-old Masson pine (*Pinus massoniana* Lamb.) wood harvested from plantation forestry located in Fujian Province, China. Wood blocks with the dimensions 20 mm^3 × 20 mm^3 × 160 mm^3 and 50 mm^3 × 50 mm^3 × 70 mm^3 (longitudinal × tangential × radial) were cut from the sapwood around the 21st growth ring. The initial moisture content was about 11%. A commercial phenol formaldehyde (PF) resin (Dynea Co., Ltd., Guangdong, China) with a solid content of 48% and a viscosity of 150 mPa·s at 25 °C was used in this experiment.

2.2. Impregnation Treatment

The wood samples were oven-dried at 103 ± 2 °C until a constant weight was achieved, and the weight was determined before impregnation. The PF resin was diluted with distilled water into resin concentrations of 15%, 20%, 25%, and 30% for separate treatments. Twenty replicate samples in each treatment group were conducted in a stainless-steel chamber under a vacuum of 0.09 MPa for 30 min and then at 0.8 MPa for 2 h. After impregnation, the samples were air-dried at room temperature for 48 h after removing the excess resin on the surface, and then were cured at a temperature of 130 °C for 2 h in an oven.

2.3. Determination of Weight Percent Gain and Density

The oven-dried weight and volume of the 20 replicate samples with the dimensions 20 mm^3 × 20 mm^3 × 20 mm^3 (L × T × R) cut from the PF resin modified wood were determined to calculate the oven-dried density and weight percent gain (WPG) of the samples. The WPG was calculated according to Equation (1):

$$WPG\ (\%) = \frac{W_1 - W_0}{W_0} \times 100\% \quad (1)$$

where W_1 is the oven-dried weight of the modified wood and W_0 is the oven-dried weight of the control wood.

2.4. Morphology Observation

Both the cross-section and tangential section of the surfaces of the control and modified wood samples were observed using scanning electron microscopy (SEM, JSM-7600F, JEOL Japan Electronics Co., Ltd., Japan) at an accelerating voltage of 20 kV.

2.5. Raman Measurement

The local chemical distribution analysis in the transversal section of the control and modified wood samples was analyzed by a laser Raman spectrometer (DXR532, Thermo Fisher Scientific Inc., USA) equipped with a linear-polarized 780 nm laser. The cross-sections of the wood samples were sliced by an ultra-microtome (Leica MZ6, Germany) with a thickness of 20 μm and then placed on glass slides covered with glass coverslips. All spectra were collected in the range of 1800 cm^{-1} to 600 cm^{-1}.

2.6. Dimensional Stability Analysis

The dimensions (L × T × R) of the control and modified wood samples were measured under three different moisture contents (> fiber satruated point, air-dried, and oven-dried) to analyze the dimensional stability according to the testing procedure of Chinese National Standards (GB/T 1932-2009 and GB/T 1934.2-2009). For determination of shrinkage, samples were soaked in distilled water at 20 °C until the dimension was constant, and then the wet samples were conditioned at 20 °C and relative humidity (RH) of 65%, and finally the air-dried samples were dried in an oven at 103 °C until a constant weight was achieved. In contrast, the determination of swelling was processed in reverse order. The swelling coefficient (α), shrinkage coefficient (β), anti-swelling efficiency (ASE), and anti-shrinking efficiency (ASE') can be calculated by Equations (2)–(13):

$$\alpha_w\ (\%) = \frac{l_w - l_0}{l_0} \times 100\% \quad (2)$$

$$\alpha_{max}\ (\%) = \frac{l_{max} - l_0}{l_0} \times 100\% \quad (3)$$

$$\alpha_{Vw}\ (\%) = \frac{V_w - V_0}{V_0} \times 100\% \quad (4)$$

$$\alpha_{Vmax}\ (\%) = \frac{V_{max} - V_0}{V_0} \times 100\% \quad (5)$$

$$ASE_w\ (\%) = \frac{\alpha_{Vw(c)} - \alpha_{Vw(m)}}{\alpha_{Vw(c)}} \times 100\% \quad (6)$$

$$ASE_{max}\ (\%) = \frac{\alpha_{Vmax(c)} - \alpha_{Vmax(m)}}{\alpha_{Vmax(c)}} \times 100\% \quad (7)$$

where α_w and α_{max} are the linear swelling coefficient from oven-dried to air-dried and from oven-dried to wet, respectively; l_{max}, l_w, and l_0 are the length in the tangential and radial directions of wet, air-dried, and oven-dried samples, respectively; similarly, α_{Vw} and α_{Vmax} are the volumetric swelling coefficients; V_{max}, V_w, and V_0 are the volume of samples at different moisture conditions; $\alpha_{Vw(c)}$ and $\alpha_{Vmax(m)}$ are the volumetric swelling coefficient of the control and modified wood samples, respectively.

$$\beta_{max}\ (\%) = \frac{l_{max} - l_0}{l_{max}} \times 100\% \quad (8)$$

$$\beta_w\ (\%) = \frac{l_{max} - l_w}{l_{max}} \times 100\% \quad (9)$$

$$\beta_{Vmax}\ (\%) = \frac{V_{\max} - V_0}{V_{\max}} \times 100\% \tag{10}$$

$$\beta_{Vw}\ (\%) = \frac{V_{\max} - V_{\mathrm{w}}}{V_{\max}} \times 100\% \tag{11}$$

$$ASE'_{max}\ (\%) = \frac{\beta_{Vmax(c)} - \beta_{Vmax(m)}}{\beta_{Vmax(c)}} \times 100\% \tag{12}$$

$$ASE'_{w}\ (\%) = \frac{\beta_{Vw(c)} - \beta_{Vw(m)}}{\beta_{Vw(c)}} \times 100\% \tag{13}$$

where $\beta_{\max}$ and β_{w} are the linear shrinking coefficient from oven-dried to air-dried and from oven-dried to wet, respectively; $l_{\max}$, l_{w}, and l_0 are the length in the tangential and radial directions of oven-dried, air-dried, and wet samples, respectively; similarly, $\beta_{V\max}$ and $\beta_{V\mathrm{w}}$ are the volumetric shrinking coefficients; $V_{\max}$, V_{w}, and V_0 are the volume of samples at different moisture conditions; $\beta_{V\max(\mathrm{m})}$ and $\beta_{V\mathrm{w}(\mathrm{c})}$ are the volumetric shrinking coefficients of the control and modified wood samples, respectively.

2.7. Mechanical Property Testing

Wood samples with the dimensions 5 mm^3 × 5 mm^3 × 10 mm^3 (T × R × L) were obtained for nanoindentation (NI) to evaluate the effect of modification on the wood cell wall. The transverse section of the samples was polished by an ultra-microtome with a diamond knife (Micro Star Tech Inc., Huntsville, AL, USA). As shown in Figure 1, the cell wall mechanics of both the control and modified wood, which had been equilibrated at 20 °C and 65% RH for 48 h, were measured by using a Hysitron TriboIndenter system (Hysitron Inc., USA) equipped with scanning probe microscopy (SPM). Testing was operated with the load function: loading, holding at the peak load of 400 μN, and unloading for 5 s, respectively. About 30 valid indents were obtained to calculate the reduced elastic modulus (E_{r}) and hardness (H) based on Equations (14) and (15) introduced by Oliver and Pharr [27]:

$$H = \frac{P_{\max}}{A} \tag{14}$$

where $P_{\max}$ is the peak load, and A is the projected contact area of the tips at peak load.

$$E_r = \frac{\sqrt{\pi}}{2\beta}\frac{S}{\sqrt{A}} \tag{15}$$

where E_{r} is the combined elastic modulus; S is initial unloading stiffness; and β is a correction factor correlated to indenter geometry (β = 1.034).

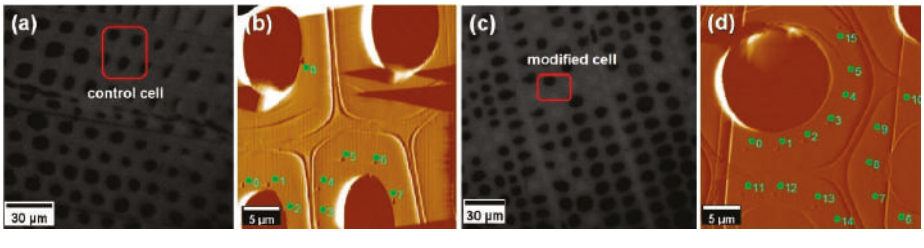

Figure 1. Microscope images showing the positioning of indents: (**a**) and (**c**) optical micrograph of the transverse section of wood samples; (**b**) and (**d**) scanning probe microscopy (SPM) images of wood cell walls after nanoindentation (NI).

The Janka hardness of a transverse section and the compressive strength parallel to the grain of the wood was determined in accordance with GB/T 1941-2009 and GB/T 1935-2009 standards, respectively. The dimensions of the samples were 30 mm^3 × 20 mm^3 × 20 mm^3 (L × T × R). A total of 20 replicate

samples for each treatment were conditioned until they reached a moisture content of approximately 12% before testing.

3. Results and Discussion

3.1. Weight Percent Gain and Density

Figure 2 shows the weight percent gain (WPG) and density of the control and modified wood samples. It can be observed that the WPG and density increase with increasing PF concentration. Density was positively correlated with WPG, which gradually increased by 34.7% and 39.6% as compared to the control when the PF concentration was 30%, respectively. The increased density of the samples was mainly attributed to the filling of the cell lumens with PF resin. Meanwhile, the lower increased rate of density than that of WPG may due to the swelling of cell wall filled with PF resin. However, both the WPG and density increased slowly when the PF concentration was above 20%. In a previous study, the viscosity of the solution has been found to affect the penetration in wood [28,29]. That is, higher concentration PF resin could decrease the permeability of the resin in wood.

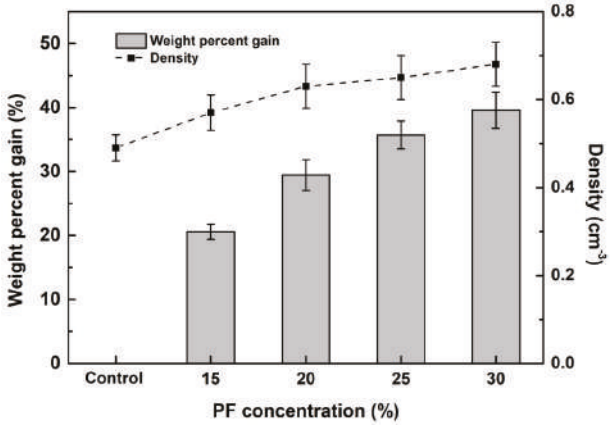

Figure 2. Weight percent gain (WPG) and density of the control and modified wood. PF = phenol formaldehyde.

3.2. Morphological Analysis

The scanning electron microscopy images of the cross-sectional and tangential-sectional surfaces of the wood samples are shown in Figure 3. The presence of the polymeric structure of PF resin can be easily noted in many cell lumens and pits (Figure 3d,f). During impregnation in Masson pine wood, the chemicals entered the interior of the wood primarily through the wood tracheids and then circulated through the pits in an axial and transverse direction [10,26]. Under the action of exterior pressure, the PF molecules freely diffused into the intercellular spaces of the wood. It also can be observed that there is no obvious boundary between the wood cell wall and the filled PF resin, which may indicate that some PF resin has penetrated into the cell wall and that they interact with each other well. Furthermore, some cracks appear on the cell walls that are not filled with resin; however, the surface of the cell walls filled with resin was smoother and more compact after drying. This finding illustrates that the penetration of resin into the cell wall can enlarge the differences in shrinkage properties of the filled and unfilled cell walls and might be responsible for the cracks between them (Figure 3e).

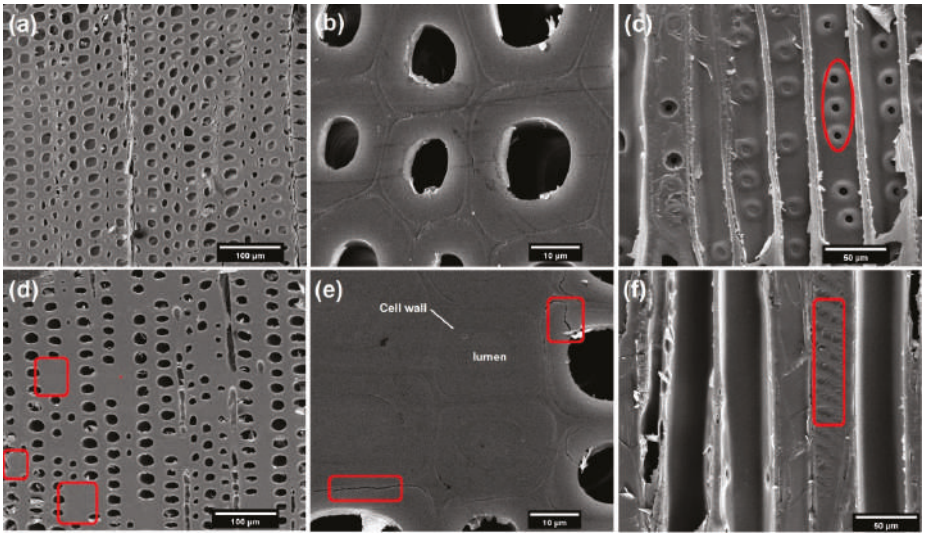

Figure 3. Micrographs of the cross-sections of (**a**,**b**) the control wood, (**d**,**e**) the wood modified by PF resin, and tangential-section of (**c**) the control wood, (**f**) the modified wood.

3.3. Local Chemical Analysis by Raman

Raman was used to detect the local chemical groups to confirm the possible interactions between the wood cell wall materials and the resin. Figure 4 shows the typical spectra for the control wood cell wall, PF resin within the lumen, and cell wall filled with resin. The spectra with black and blue color in Figure 4 indicate that the chemical nature of the native cell wall material is clearly different from the cured PF resin. Wood cell walls are mainly composed of cellulose, hemicelluloses, and lignin. The bands at 1091 cm^{-1} , 1336 cm^{-1} , and 1376 cm^{-1} on the black IR spectra corresponded to the C-O stretching and flexural vibrations in cellulose and hemicellulose, and the absorption at 1595 cm^{-1} and 1656 cm^{-1} arises from the non-conjugated and conjugated C=C stretching vibrations in the aromatic ring of the phenol in lignin [30–32]. For phenol formaldehyde resin, the intensive band at 1607 cm^{-1} originates from the C=C stretching vibration in the aromatic ring of the phenol, while the bands at 1287 cm^{-1} and 778 cm^{-1} are attributable to the biphenyl C-C bridge stretching vibration and C-H flexural vibration in the aromatic ring. It is intriguing that a number of spectral modifications appeared on the spectra with red color for the modified cell wall, although the general aspect of the spectra remained unchanged. The intensity of the C=C stretching and C-O stretching at 1656 cm^{-1} , 1376 cm^{-1}, and 1336 cm^{-1} decreased significantly, while some new bands at 1287 cm^{-1} and 778 cm^{-1} appeared as compared to the control cell wall, which can be attributed to the penetration of PF resin into the cell wall [33,34]. Moreover, a relatively broader band between 1150 cm^{-1} and 1100 cm^{-1} appeared in the spectra of modified wood, corresponding to the asymmetric stretching vibration of C-O-C aliphatic ether, which is in agreement with the literature that the chemical reactions of the -OH groups of wood and PF resin occurred at the cell wall level [35,36].

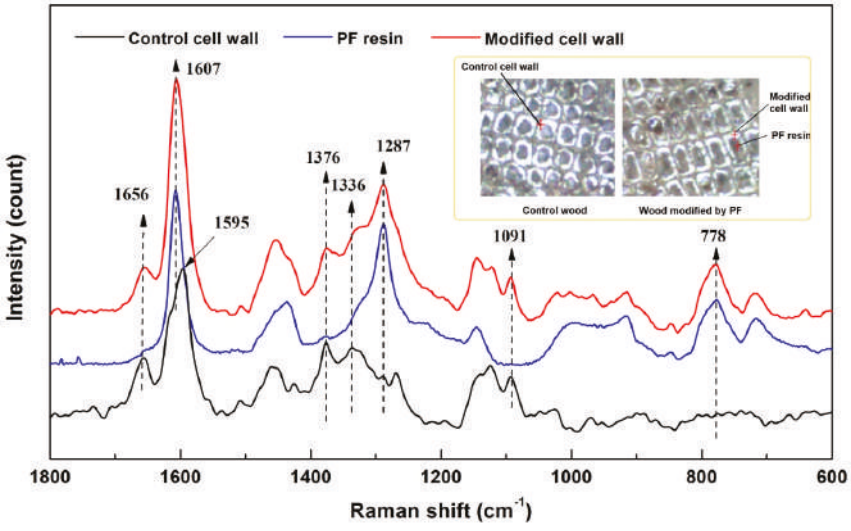

Figure 4. Raman spectra of the control and modified wood.

3.4. Dimensional Stability

The swelling and shrinking coefficients (α and β) of the control and chemically modified wood samples under different moisture conditions are presented in Figure 5. The swelling and shrinking coefficients of wood with the changing moisture content (MC) between oven-dried and air-dried conditions (α_w and β_w) were primarily measured to evaluate the dimensional stability of wood applied on locations with low equilibrium moisture content. Both the α_w and β_w in the radial direction were about half of that in the tangential direction, resulting from the anatomical structures such as the limitation of xylem ray, the difference of lignin content in the radial and tangential cell wall, etc. [10]. The α_w and β_w decreased significantly at first and then kept stable with an increase in PF resin concentration in comparison with the control, indicating that chemical treatment could effectively improve wood dimensional stability [19]. The radial, tangential, and volumetric α_ws of wood modified by PF resin with 20% concentration were about 45%, 58%, and 54% lower than that of the control, respectively. However, the β_w became stable when the PF concentration was beyond 15%, indicating that PF resin concentrations ranging from 15% to 20% are better for wood impregnation.

As applied in areas with a larger moisture content range, such as outdoors, the swelling and shrinking coefficients of wood with the changing MC between oven-dried and wet conditions (α_{max} and β_{max}) need to be analyzed too. It can be observed from Figure 5c and 5d that the effect of PF resin impregnation on the α_{max} and β_{max} is similar to that of α_w and β_w; that is, the dimensional stability of wood can be modified effectively by the PF resin at concentrations below 20%. The radial, tangential, and volumetric β_{max}s of wood modified by PF resin at 20% concentration decreased by about 49%, 50%, and 51%, respectively. Moreover, both the α_{max} and β_{max} were almost twice as high as the α_w and β_w, respectively, which can be attributed to the different moisture content. The MC of air-dried wood is approximately 12–15%, which is half of the fiber saturation point (FSP). Generally, the hygroscopic water located within the cell wall plays the most important role on the dimension stability rather than the free water occupied in the cell lumen or other macro-voids.

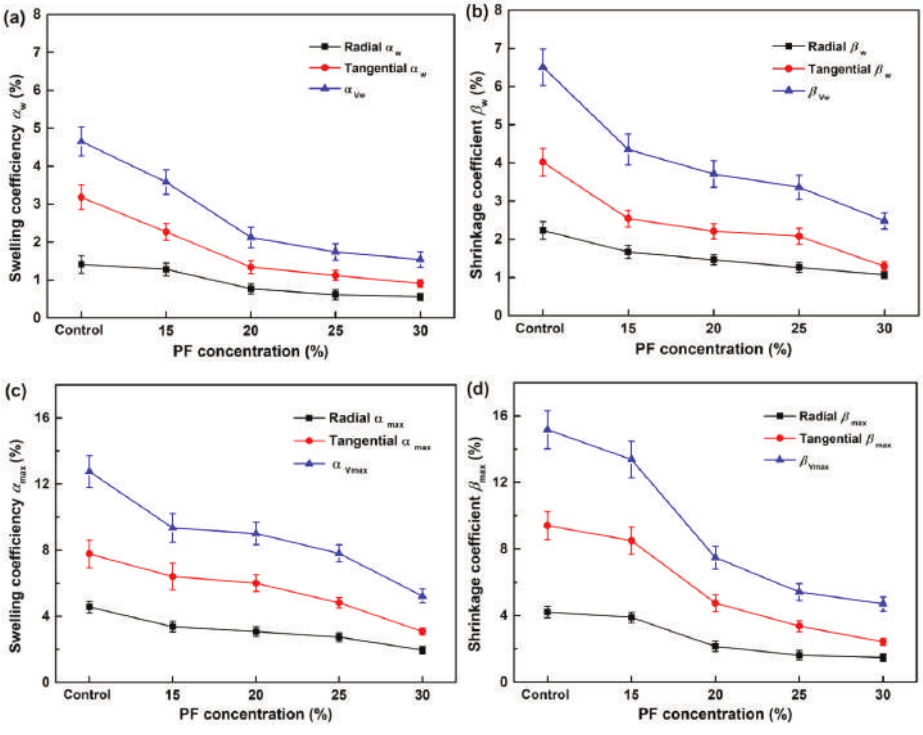

Figure 5. The swelling and shrinking coefficients of the control and modified wood: (**a**) and (**b**) swelling and shrinking coefficients from oven-dried to wet; (**c**) and (**d**) swelling and shrinking coefficients from oven-dried to air-dried.

The anti-swelling efficiency (ASE) and anti-shrinking efficiency (ASE') were positively affected by the PF resin concentration (Figure 6). The ASE_w and ASE'_w initially increased at a concentration of 20% and then kept stable or only increased slightly with a further increase in concentration. The ASE_w and ASE'_w of the wood treated with 20% PF resin reached 54% and 50%, respectively. The deposition of PF in the cell walls reduced the space within the cell walls, which could be occupied by water in untreated wood. In addition, the reduction in swelling and shrinking of the modified wood could be partly attributed to cross-linking of particle cell wall polymers [37,38]. However, the ASE_{max} and ASE'_{max} of the wood kept increasing with the increased concentration and reached the maximum of 59% and 62% as PF resin concentration increased to 30%. As the MC of wood exceeded the FSP, the free voids in the wood provided space for free water, which also affected the swelling and shrinking. Thus, the higher WPG attributed to the higher PF resin concentration could occupy more free space and finally increase the ASE_{max} and ASE'_{max}. The ASE_w and ASE'_w of the wood treated with 20% PF resin is close to the maximum ASE_{max} and ASE'_{max}, indicating that the lower concentration PF resin is suitable for treating the wood utilized in areas with small MC range.

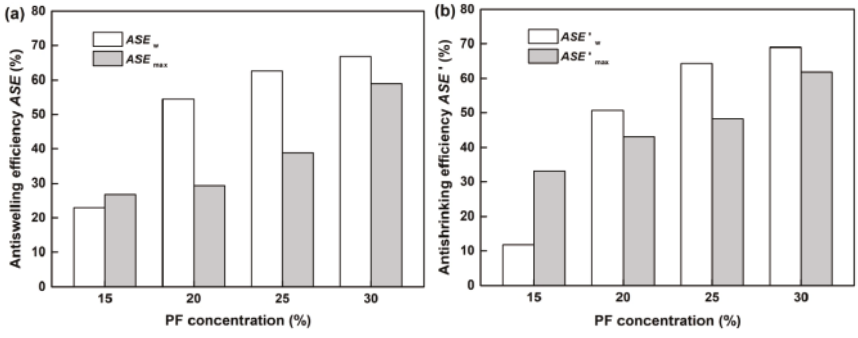

Figure 6. The anti-swelling and anti-shrinking efficiency of the modified wood: (**a**) anti-swelling efficiency; (**b**) anti-shrinking efficiency.

3.5. Micro-Mechanics of Wood Cell Walls

The longitudinal reduced elastic modulus (E_r) and hardness (H) of the control and modified wood cell walls are presented in Figure 7, respectively. It is remarkable that the E_r and H values increased after impregnation by PF resin. For instance, the E_r and H values of the wood cell walls modified with PF resin at 15% concentration increased by about 24.9% and 47.3%, which further confirmed the results of the Raman measurements that some PF molecules penetrated into the cell wall successfully. The filling of the voids and the cross-linking of -OH groups of the wood polymer with the resins may reinforce the cell wall [39,40]. However, the cell wall mechanics increased slowly and even decreased accompanying the increase in PF resin concentration. The E_r and H of the wood cell walls modified by 30% PF resin were 8.7% and 11.6% lower than that of the cell wall modified by 20% PF, which can be easily interpreted as a result of the increasing bulking effects attributed to the deposition of resin in the cell walls at higher WPG.

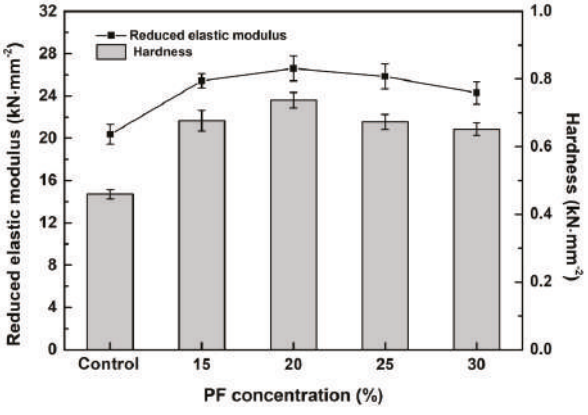

Figure 7. The reduced elastic modulus and hardness of the control and modified wood cell walls.

3.6. Macro-Mechanics of Wood

Figure 8 shows the hardness of the transverse section and the compressive strength parallel to grain of the control and modified wood at the macro-level. The initial hardness and compressive strengths of the control wood are 39.5 N·mm^{-2} and 49.1 N·mm^{-2} , respectively. Both the hardness and compressive strength gradually increased with an increase in PF resin concentration, reaching the maximum of 54.9 N·mm^{-2} and 59.7 N·mm^{-2} with a concentration of 30%. The higher filling degree of the wood voids led to a higher density, which mainly contributed to the improved hardness and

compressive strength after curing of the PF resin [41]. In addition, the increased mechanics of wood cell walls induced by the chemical modification also played an important role to achieve the desired modification effect. However, as the PF concentration was above 20%, the hardness and compressive strength kept stable, which was in agreement with the results of dimensional stability and cell wall mechanics. That is, the PF concentration of 20% may be preferred to modify Masson pine wood.

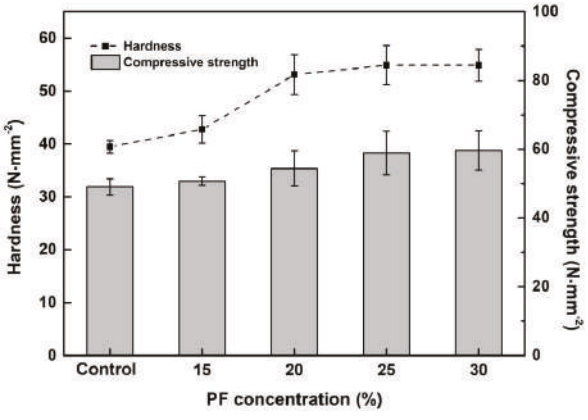

Figure 8. The compressive strength and hardness of the control and modified wood.

4. Conclusions

The effects of PF resin impregnation on the density, dimensional stability, mechanical strength, and microscopic chemical and mechanical properties of Masson pine wood were determined in this paper. PF resin was impregnated into the wood cell lumen and diffused into the cell walls, as verified by scanning electron microscopy and Raman spectrum. Swelling and shrinking coefficients were significantly reduced while the anti-swelling and anti-shrinking efficiency of wood were improved accompanying the increase in PF resin concentration. The inter-reaction between the resin and cell walls made a positive contribution to the cell wall mechanics of wood cell walls. The elastic modulus (E_r) and hardness (H) of the wood cell walls modified by 15% PF resin increased by about 24.9% and 47.3% as compared to the control. Both the increased density attributed to the filling of resin in cell lumens and cell walls and the improved cell wall mechanics resulted in the remarkable increase in hardness and the compress strength of wood. However, both the dimensional stability and mechanical properties improved slowly as the PF concentration was above 20%; that is, the PF concentration of 20% may be preferred to modify Masson pine wood.

Author Contributions: X.W. conceived and designed the experiments; X.C. and S.C. performed the experiments; X.C., X.X., and Z.Y. analyzed the data; X.W. wrote the paper, with revisions by Y.L.

Acknowledgments: The authors would like to gratefully acknowledge the financial support from the Natural Science Foundation of Jiangsu Province (BK20180774), Natural Science Foundation of China (31570552), and Key University Science Research Project of Jiangsu Province (17KJA220004).

Conflicts of Interest: The authors declare no conflict of interest.

References

1. Gu, H.; Wang, J.; Ma, L.; Shang, Z.; Zhang, Q. Insights into the BRT (Boosted Regression Trees) method in the study of the climate-growth relationship of Masson pine in subtropical China. *Forests* **2019**, *10*, 228. [CrossRef]
2. He, Q.; Zhan, T.; Ju, Z.; Zhang, H.; Hong, L.; Brosse, N.; Lu, X. Influence of high voltage electrostatic field (HVEF) on bonding characteristics of Masson (*Pinus massoniana* Lamb.) veneer composites. *Eur. J. Wood Wood Prod.* **2019**, *77*, 105–114. [CrossRef]

3. Ge, S.; Ma, J.; Jiang, S.; Liu, Z.; Peng, W. Potential use of different kinds of carbon in production of decayed wood plastic composite. *Arab. J. Chem.* **2018**, *11*, 838–843. [CrossRef]
4. Wang, X.; Chen, X.; Xie, X.; Wu, Y.; Zhao, L.; Li, Y.; Wang, S. Effects of thermal modification on the physical, chemical and micromechanical properties of Masson pine wood (*Pinus massoniana* Lamb.). *Holzforschung* **2018**, *72*, 1063–1070. [CrossRef]
5. Li, W.; Wang, H.; Ren, D.; Yu, Y.; Yu, Y. Wood modification with furfuryl alcohol catalysed by a new composite acidic catalyst. *Wood Sci. Technol.* **2015**, *49*, 845–856. [CrossRef]
6. Altgen, M.; Hofmann, T.; Militz, H. Wood moisture content during the thermal modification process affects the improvement in hygroscopicity of Scots pine sapwood. *Wood Sci. Technol.* **2016**, *50*, 1–15. [CrossRef]
7. Gaff, M.; Babiak, M.; Kačík, F.; Sandberg, D.; Turčani, M.; Hanzlík, P.; Vondrová, V. Plasticity properties of thermally modified timber in bending—The effect of chemical changes during modification of European oak and Norway spruce. *Compos. Part B Eng.* **2019**, *165*, 613–625. [CrossRef]
8. Shi, J.; Lu, Y.; Zhang, Y.; Cai, L.; Shi, S.Q. Effect of thermal treatment with water, H_2SO_4 and NaOH aqueous solution on color, cell wall and chemical structure of poplar wood. *Sci. Rep.* **2018**, *8*, 17735. [CrossRef]
9. Wu, Y.; Wu, J.; Wang, S.; Feng, X.; Chen, H.; Tang, Q.; Zhang, H. Measurement of mechanical properties of multilayer waterborne coatings on wood by nanoindentation. *Holzforschung* **2019**. [CrossRef]
10. Cai, M.; Fu, Z.; Cai, Y.; Li, Z.; Xu, C.; Xu, C.; Li, S. Effect of impregnation with maltodextrin and 1,3-dimethylol-4,5-dihydroxyethyleneurea on Poplar wood. *Forests* **2018**, *9*, 676. [CrossRef]
11. Gérardin, P. New alternatives for wood preservation based on thermal and chemical modification of wood-a review. *Ann. For. Sci.* **2016**, *73*, 559–570. [CrossRef]
12. Sandberg, D.; Kutnar, A.; Mantanis, G. Wood modification technologies—A review. *iForest* **2017**, *10*, 895–908. [CrossRef]
13. Li, W.; Jan, V.D.B.; Dhaene, J.; Zhan, X.; Mei, C.; Van Acker, J. Investigating the interaction between internal structural changes and water sorption of mdf and OSB using X-ray computed tomography. *Wood Sci. Technol.* **2018**, *52*, 701–716. [CrossRef]
14. Yue, K.; Chen, Z.; Lu, W.; Liu, W.; Li, M.; Shao, Y.; Tang, L.; Wan, L. Evaluating the mechanical and fire-resistance properties of modified fast-growing Chinese fir timber with boric-phenol-formaldehyde resin. *Constr. Build. Mater.* **2017**, *154*, 956–962. [CrossRef]
15. Sun, S.; Zhao, Z. Influence of acid on the curing process of tannin-sucrose adhesives. *BioResources* **2018**, *13*, 7683–7697. [CrossRef]
16. Shams, M.I.; Morooka, T.; Yano, H. Compressive deformation of wood impregnated with low molecular weight phenol formaldehyde (PF) resin V: Effects of steam pretreatment. *J. Wood Sci.* **2006**, *52*, 389–394. [CrossRef]
17. Khalil, H.A.; Amouzgar, P.; Jawaid, M.; Abdullah, C.; Issam, A.; Zainudin, E.; Paridah, M.T.; Hassan, A. Physical and thermal properties of microwave-dried wood lumber impregnated with phenol formaldehyde resin. *J. Compos. Mater.* **2013**, *47*, 3565–3571. [CrossRef]
18. Biziks, V.; Bicke, S.; Militz, H. Penetration depth of phenol-formaldehyde (PF) resin into beech wood studied by light microscopy. *Wood Sci. Technol.* **2018**, *53*, 165–176. [CrossRef]
19. Deka, M.; Saikia, C.N. Chemical modification of wood with thermosetting resin: Effect on dimensional stability and strength property. *Bioresour. Technol.* **2000**, *73*, 179–181. [CrossRef]
20. Özçifçi, A. Impacts of impregnation with boron compounds on the bonding strength of wood materials. *Constr. Build. Mater.* **2008**, *22*, 541–545. [CrossRef]
21. Devi, R.R.; Ali, I.; Maji, T. Chemical modification of rubber wood with styrene in combination with a crosslinker: Effect on dimensional stability and strength property. *Bioresour. Technol.* **2003**, *88*, 185–188. [CrossRef]
22. Yildiz, U.C.; Yildiz, S.; Gezer, E.D. Mechanical properties and decay resistance of wood-polymer composites prepared from fast growing species in Turkey. *Bioresour. Technol.* **2005**, *96*, 1003–1011. [CrossRef]
23. Gindl, W.; Schoberl, T. The significance of the elastic modulus of wood cell walls obtained from nanoindentation measurements. *Compos. Part A* **2004**, *35*, 1345–1349. [CrossRef]
24. Wimmer, R.; Lucas, B.N.; Tsui, T.Y.; Oliver, W.C. Longitudinal hardness and young's modulus of spruce tracheid secondary walls using nanoindentation technique. *Wood Sci. Technol.* **1997**, *31*, 131–141. [CrossRef]

25. Yu, Y.; Fei, B.; Wang, H.; Tian, G. Longitudinal mechanical properties of cell wall of *Masson pine* (Pinus massoniana Lamb) as related to moisture content: A nanoindentation study. *Holzforschung* **2011**, *65*, 121–126. [CrossRef]
26. Ali, E.M. Modification of spruce wood by UV-crosslinked PEG hydrogels inside wood cell walls. *React. Funct. Polym.* **2018**, *131*, 100–106.
27. Oliver, W.C.; Pharr, G.M. An improved technique for determining hardness and elastic modulus using load and displacement sensing indentation experiments. *J. Mater. Res.* **1992**, *7*, 1564–1583. [CrossRef]
28. Xie, Y.; Xiao, Z.; Grüneberg, T.; Militz, H.; Hill, C.A.; Steuernagel, L.; Mai, C. Effects of chemical modification of wood particles with glutaraldehyde and 1,3-dimethylol-4,5-dihydroxyethyleneurea on properties of the resulting polypropylene composites. *Compos. Sci. Technol.* **2010**, *70*, 2003–2011. [CrossRef]
29. Xie, Y.; Fu, Q.; Wang, Q.; Xiao, Z.; Militz, H. Effects of chemical modification on the mechanical properties of wood. *Eur. J. Wood Wood Prod.* **2013**, *71*, 401–416. [CrossRef]
30. Tjeerdsma, B.F.; Militz, H. Chemical changes in hydrothermal treated wood: FTIR analysis of combined hydrothermal and dry heat-treated wood. *Holz Roh. Werkst.* **2005**, *63*, 102–111. [CrossRef]
31. González-Peña, M.M.; Curling, S.F.; Hale, M.D. On the effect of heat on the chemical composition and dimensions of thermally-modified wood. *Polym. Degrad. Stab.* **2009**, *94*, 2184–2193. [CrossRef]
32. Kotilainen, R.A.; Toivanen, T.J.; Alén, R.J. FTIR monitoring of chemical changes in softwood during heating. *J. Wood Chem. Technol.* **2000**, *20*, 307–320. [CrossRef]
33. Krajnc, M.; Poljanšek, I. Characterization of phenol-formaldehyde prepolymer resins by in line FTIR spectroscopy. *Acta Chim. Slov.* **2015**, *52*, 238–244.
34. De, D.; Adhikari, B.; De, D. Grass fiber reinforced phenol formaldehyde resin composite: Preparation, characterization and evaluation of properties of composite. *Polym. Adv. Technol.* **2007**, *18*, 72–81. [CrossRef]
35. Wang, X.; Deng, Y.; Li, Y.; Kjoller, K.; Roy, A.; Wang, S. In situ identification of the molecular-scale interactions of phenol-formaldehyde resin and wood cell walls using infrared nanospectroscopy. *RSC Adv.* **2016**, *6*, 76318–76324. [CrossRef]
36. Paris, J.L.; Kamke, F.A.; Xiao, X. X-ray computed tomography of wood-adhesive bondlines: Attenuation and phase-contrast effects. *Wood Sci. Technol.* **2015**, *49*, 1185–1208. [CrossRef]
37. Yelle, D.J.; Ralph, J. Characterizing phenol-formaldehyde adhesive cure chemistry within the wood cell wall. *Int. J. Adhes. Adhes.* **2016**, *70*, 26–36. [CrossRef]
38. Wang, J.; Laborie, M.P.G.; Wolcott, M.P. Correlation of mechanical and chemical cure development for phenol–formaldehyde resin bonded wood joints. *Thermochimica Acta* **2011**, *513*, 20–25. [CrossRef]
39. Jakes, J.E.; Hunt, C.G.; Yelle, D.J.; Lorenz, L.; Hirth, K. Synchrotron-based X-ray fluorescence microscopy in conjunctionwith nanoindentation to study molecular-scale interactions of phenol-formaldehyde in wood cell walls. *ACS Appl. Mater. Interfaces* **2015**, *7*, 6584–6589. [CrossRef]
40. Kuai, B.; Wang, X.; Lv, C.; Xu, K.; Zhang, Y.; Zhan, T. Orthotropic tension behavior of two typical chinese plantation woods at wide relative humidity range. *Forests* **2019**, *10*, 516. [CrossRef]
41. Olaniran, S.O.; Michen, B.; Mora Mendez, D.F.; Wittel, F.K.; Bachtiar, E.V.; Burgert, I.; Markus, R. Mechanical behaviour of chemically modified *Norway spruce* (Picea abies L. karst.): Experimental mechanical studies on spruce wood after methacrylation and in situ polymerization of styrene. *Wood Sci. Technol.* **2019**, *53*, 425–445. [CrossRef]

© 2019 by the authors. Licensee MDPI, Basel, Switzerland. This article is an open access article distributed under the terms and conditions of the Creative Commons Attribution (CC BY) license (http://creativecommons.org/licenses/by/4.0/).

forests

MDPI

Article

The Impact of Anatomical Characteristics on the Structural Integrity of Wood

Lukas Emmerich *, Georg Wülfing and Christian Brischke

Wood Biology and Wood Products, University of Goettingen, Buesgenweg 4, D-37077 Goettingen, Germany; georg.wuelfing@stud.uni-goettingen.de (G.W.); christian.brischke@uni-goettingen.de (C.B.)
* Correspondence: lukas.emmerich@uni-goettingen.de

Received: 8 February 2019; Accepted: 21 February 2019; Published: 24 February 2019

Abstract: The structural integrity of wood is closely related to its brittleness and thus to its suitability for numerous applications where dynamic loads, wear and abrasion occur. The structural integrity of wood is only vaguely correlated with its density, but affected by different chemical, physico-structural and anatomical characteristics, which are difficult to encompass as a whole. This study aimed to analyze the results from High-Energy Multiple Impact (HEMI) tests of a wide range of softwood and hardwood species with an average oven-dry wood density in a range between 0.25 and 0.99 g/cm^3 and multifaceted anatomical features. Therefore, small clear specimens from a total of 40 different soft- and hardwood species were crushed in a heavy vibratory ball mill. The obtained particles were fractionated and used to calculate the 'Resistance to Impact Milling (RIM)' as a measure of the wood structural integrity. The differences in structural integrity and thus in brittleness were predominantly affected by anatomical characteristics. The size, density and distribution of vessels as well as the ray density of wood were found to have a significant impact on the structural integrity of hardwoods. The structural integrity of softwood was rather affected by the number of growth ring borders and the occurrence of resin canals. The density affected the Resistance to Impact Milling (RIM) of neither the softwoods nor the hardwoods.

Keywords: brittleness; density; dynamic strength; High-Energy Multiple Impact (HEMI)–test; Resistance to Impact Milling (RIM)

1. Introduction

Most elasto-mechanical and rheological properties of wood are closely related to wood density and are therefore rather easily predictable. However, the anatomical features of wood, which can be wood species-specific, further affect especially dynamic strength properties such as the impact bending strength and shock resistance [1–3]. For instance, the large earlywood pores in ring-porous hardwoods such as English oak (*Quercus robur* L.), Sweet chestnut (*Castanea sativa* L.), Black locust (*Robinia pseudoacacia* L.) or Wych elm (*Ulmus glabra* Huds.) can serve as predetermined breaking points. Further deviations from an ideal homogeneous xylem structure such as large rays in European beech (*Fagus sylvatica* L.) or Alder (here: false rays, *Alnus* spp.), distinct parenchyma bands in Bongossi (*Lophira alata* Banks ex C. F. Gaertn.) or agglomerates of resin canals in Red Meranti (*Shorea* spp.), also have the potential to either strengthen or reduce the structural integrity of wood.

Similarly, wood cell wall modification affects different mechanical properties including the wood hardness and abrasion resistance, but also its brittleness and consequently its structural integrity. This has been shown previously with the help of High-Energy Multiple Impact (HEMI)-tests, where small wood specimens are subjected to thousands of dynamic impacts by steel balls in the bowl of a heavy vibratory mill. The fragments obtained are analyzed afterwards [4]. For instance, the weakening of cell walls by heat during thermal modification processes, especially in the middle lamella region,

leads to a steady decrease in the structural integrity of wood with increasing treatment intensity. The HEMI-test has further been used to detect fungal decay by soft rot, brown rot and white rot fungi (even in very early stages), the effect of gamma radiation, wood densification, wood preservative impregnation, wax and oil treatments, and different chemical wood modification processes [5].

It has previously been shown that the Resistance to Impact Milling (RIM), which serves as a measure of wood's structural integrity is very insensitive to varying densities, natural ageing, and the occurrence of larger cracks [5]. Furthermore, the RIM varies only little within one wood species, as shown for Scots pine sapwood (*Pinus sylvestris* L.) samples from trees in six Northern European countries [6]. However, the results from previous studies indicated that the structural integrity determined in HEMI-tests is not well correlated with wood density, since further variables such as wood species-specific anatomical characteristics of the xylem tissue interfere with the effect of density [7].

Objective

The aim of this study was to analyze the results from HEMI-tests of a wide range of softwood and hardwood species with an average oven-dry wood density in a range between 0.25 and 0.99 g/cm^3 and with multifaceted anatomical features.

2. Materials and Methods

One hundred replicate specimens of 10 (ax.) × 5 × 20 mm^3 were prepared from a total of 40 different wood species and separated between sapwood and heartwood, as listed in Tables 1 and 2.

To determine the oven-dry density (ODD), n = 10 replicate specimens of 10 (ax.) × 5 × 20 mm^3 per wood species were oven dried at 103 °C until a constant mass, weighed to the nearest 0.0001 g; the dimensions were then measured to the nearest 0.001 mm. The oven dry density was calculated according to the following equation:

$$\rho_0 = \frac{m_0}{V_0} \; [\mathrm{g\ cm^{-3}}] \quad (1)$$

where:

ρ_0 is the oven-dry density, in g·cm^{-3};
m_0 is the oven-dry mass, in g;
V_0 is the oven-dry volume, in cm^3.

Table 1. The oven-dry density (ODD), Resistance to Impact Milling (RIM), degree of integrity (I), and fine percentage (F) of different softwood species. The standard deviation (SD) is in parentheses.

Name [1]	Botanical Name	ODD [g cm^{-3}]		RIM [%]		I [%]		F [%]	
Scots pine sw	*Pinus sylvestris*	0.41	(0.02)	88.2	(0.9)	67.4	(1.1)	13.5	(1.1)
Scots pine hw		0.58	(0.04)	84.5	(0.8)	41.9	(3.1)	1.3	(0.4)
Radiata pine sw	*Pinus radiata*	0.43	(0.02)	88.8	(0.5)	55.4	(2.1)	0.0	(0.0)
Carribean pine hw	*Pinus carribaea*	0.39	(0.04)	87.3	(0.4)	52.4	(1.8)	1.1	(0.3)
European Larch sw	*Larix decidua*	0.56	(0.02)	85.2	(0.4)	44.5	(2.2)	1.2	(0.3)
European Larch hw		0.51	(0.02)	80.8	(1.5)	35.5	(4.8)	4.1	(0.4)
Douglas fir sw	*Pseudotsuga menziesii*	0.63	(0.02)	86.3	(0.4)	45.6	(1.8)	0.2	(0.2)
Douglas fir hw		0.51	(0.02)	82.2	(0.5)	34.8	(1.3)	1.9	(0.3)
Norway spruce	*Picea abies*	0.43	(0.03)	82.9	(1.7)	35.9	(6.1)	1.5	(0.4)
Coastal fir	*Abies grandis*	0.40	(0.06)	80.6	(0.5)	26.5	(1.3)	1.4	(0.4)
Western hemlock	*Tsuga heterophylla*	0.42	(0.03)	83.8	(0.7)	40.0	(2.1)	1.6	(0.3)
Yew	*Taxus baccata*	0.60	(0.03)	84.5	(0.9)	43.9	(3.2)	1.9	(0.3)

[1] sw = sapwood, hw = heartwood; heartwood if not otherwise indicated.

Table 2. The oven-dry density (ODD), Resistance to Impact Milling (RIM), degree of integrity (I), and fine percentage (F) of different hardwood species. The standard deviation (SD) is in parentheses.

Name [1]	Botanical Name	ODD [g cm^{-3}]		RIM [%]		I [%]		F [%]	
English oak sw	*Quercus robur*	0.49	(0.02)	83.3	(0.5)	44.2	(1.7)	3.7	(0.4)
English oak hw		0.59	(0.01)	87.3	(1.2)	59.0	(4.3)	3.3	(0.4)
Black locust	*Robinia pseudoacacia*	0.68	(0.05)	83.5	(1.2)	41.0	(3.9)	2.3	(0.2)
Sweet chestnut	*Castanea sativa*	0.50	(0.03)	78.1	(2.3)	36.0	(4.2)	7.9	(1.8)
Ash	*Fraxinus excelsior*	0.62	(0.02)	83.1	(0.8)	40.4	(2.6)	2.7	(0.3)
Locust	*Gleditsia sp.*	0.66	(0.02)	86.7	(1.1)	52.6	(3.4)	1.9	(0.4)
Common walnut	*Juglans regia*	0.63	(0.02)	85.2	(0.5)	49.8	(2.1)	2.9	(0.3)
Wild cherry	*Prunus avium*	0.55	(0.01)	86.7	(0.7)	53.0	(2.2)	2.0	(0.3)
Black cherry	*Prunus serotina*	0.64	(0.04)	87.7	(0.6)	54.9	(2.1)	1.4	(0.2)
Beech	*Fagus sylvatica*	0.66	(0.02)	88.0	(0.4)	55.9	(2.2)	1.4	(0.3)
Maple	*Acer sp.*	0.61	(0.01)	89.1	(0.6)	58.0	(2.3)	0.5	(0.1)
Lime	*Tilia sp.*	0.44	(0.01)	90.1	(0.8)	61.1	(2.6)	0.2	(0.3)
Birch	*Betula pendula*	0.57	(0.02)	87.9	(0.4)	54.2	(1.6)	0.8	(0.1)
Hazel	*Corylus avellana*	0.68	(0.02)	86.9	(1.0)	52.8	(3.9)	1.8	(0.2)
Boxwood	*Buxus sempervirens*	0.96	(0.01)	90.3	(0.9)	64.1	(3.7)	0.9	(0.0)
Poplar	*Populus nigra*	0.39	(0.02)	86.3	(0.3)	50.5	(0.9)	1.8	(0.3)
Alder	*Alnus glutinosa*	0.48	(0.01)	86.9	(0.9)	54.6	(3.3)	2.3	(0.5)
Kiri	*Paulownia tomentosa*	0.25	(0.02)	80.9	(1.5)	40.0	(4.0)	5.5	(0.9)
Shining gum	*Eucalyptus nitens*	0.74	(0.11)	83.2	(1.5)	46.7	(4.5)	4.6	(0.9)
Teak	*Tectona grandis*	0.63	(0.09)	84.1	(0.7)	48.0	(2.1)	3.9	(0.8)
Ipe	*Handroanthus sp.*	0.93	(0.02)	86.0	(0.5)	51.8	(1.2)	2.6	(0.7)
Merbau	*Intsia spp.*	0.74	(0.03)	68.1	(2.4)	27.9	(1.8)	18.6	(2.7)
Bangkirai	*Shorea laevis*	0.79	(0.05)	87.7	(0.7)	54.9	(1.9)	1.4	(0.4)
Balau	*Shorea spp.*	0.92	(0.03)	84.3	(1.1)	51.7	(2.8)	4.8	(1.0)
Bongossi	*Lophira alata*	0.97	(0.03)	85.9	(1.0)	51.9	(2.7)	2.8	(0.7)
Amaranth	*Peltogyne sp.*	0.88	(0.01)	88.6	(0.7)	57.9	(2.7)	1.1	(0.0)
Basralocus	*Dicorynia sp.*	0.81	(0.02)	84.8	(0.6)	50.9	(1.9)	4.0	(0.4)
Garapa	*Apuleia sp.*	0.76	(0.04)	86.7	(1.1)	53.0	(3.3)	2.1	(0.5)
Limba	*Terminalia superba*	0.50	(0.03)	83.2	(1.2)	45.1	(2.7)	4.1	(0.9)
Kambala	*Milicia sp.*	0.62	(0.03)	79.7	(0.7)	45.2	(2.7)	8.8	(0.4)
Massaranduba	*Manilkara bidentata*	0.99	(0.04)	85.9	(0.6)	53.2	(2.5)	3.2	(0.2)
Greenheart	*Chlorocardium rodiei*	0.96	(0.02)	85.9	(1.5)	49.9	(5.3)	2.1	(0.8)

[1] sw = sapwood, hw = heartwood.

Afterwards, selected density specimens were cut with a traversing microtome and used for digital reflected-light microscopy with a Keyence Digital microscope VHX 5000 (Keyence Corporation, Osaka, Japan). Cross section photographs were taken at a magnification of 30×, and the diameter of the earlywood vessels, the vessel density, and the wood ray density were determined at a magnification of 200× for both the soft- and hardwoods. For the tropical species, the listed anatomical features were determined at a magnification of 100×. Therefore, $n = 10$ replicate measurements were conducted per wood species to determine the ray density and vessel density. The earlywood vessel diameter was determined on $n = 30$ vessels.

Five times 20 specimens of 10 (ax.) × 5 × 20 mm^3 were submitted to High-Energy Multiple Impact (HEMI)–tests. The development and optimization of the HEMI-test have been described by [4] and [8]. In the present study, the following procedure was applied: 20 oven-dried specimens were placed in the bowl (140 mm in diameter) of a heavy-impact ball mill (Herzog HSM 100-H; Herzog Maschinenfabrik, Osnabrück, Germany), together with one steel ball of 35 mm diameter for crushing the specimens. Three balls of 12 mm diameter and three of 6 mm diameter were added to avoid small fragments from hiding in the angles of the bowl, thus ensuring impact with smaller wood fragments. The bowl was shaken for 60 s at a rotary frequency of 23.3 s^{-1} and a stroke of 12 mm. The fragments of the 20 specimens were fractionated on a slit sieve according to [9], with a slit width of 1 mm, using an

orbital shaker at an amplitude of 25 mm and a rotary frequency of 200 min^{-1} for 2 min. The following values were calculated:

$$I = \frac{m_{20}}{m_{all}} \times 100\ [\%] \quad (2)$$

where:

I is the degree of integrity, in %;
m_{20} is the oven-dry mass of the 20 biggest fragments, in g;
m_{all} is the oven-dry mass of all the fragments, in g.

$$F = \frac{m_{fragments<1mm}}{m_{all}} \times 100\ [\%] \quad (3)$$

where:

F is the fine percentage, in %;
$m_{fragments<1mm}$ is the oven-dry mass of fragments smaller than 1 mm, in g;
m_{all} is the oven-dry mass of all the fragments, in g.

$$RIM = \frac{(I - 3 \times F) + 300}{400}\ [\%] \quad (4)$$

where:

RIM is the Resistance to Impact Milling, in %;
I is the degree of integrity, in %;
F is the fine percentage, in %.

3. Results and Discussion

3.1. Structural Integrity

The Resistance to Impact Milling (RIM) varied between 68.1% (Merbau) and 90.3% (Boxwood). In contrast, the degree of integrity (I) varied significantly more, i.e., between 26.5% (Coastal fir) and 67.4% (Scots pine sapwood), as did the fine percentage (F): i.e., between 0.0% (Radiata pine) and 18.6% (Merbau). The data for the RIM, I, and F are summarized in Table 1 for the tested softwood species and in Table 2 for the hardwood species. Besides differences between the wood species, the three indicators showed differences in the variation within one species, here expressed as the standard deviation (SD). The highest variation was obtained for F, followed by I and RIM. This supports previous findings pointing out the benefit of using the combined measure RIM, which is of higher sensitivity to differences in the structural integrity paired with less scattering of data compared to I and F [4,7]. In total, the SD of the RIM was between 0.3% (Poplar) and 2.4% (Merbau), corresponding to coefficients of variation (COV) between 0.4% and 3.5%, which is very low compared to mechanical properties such as the bending or impact bending strength (e.g., [7]).

3.2. Impact of Oven-Dry Density on Structural Integrity

A clear relationship between the ODD and structural integrity did not become evident, as shown for all the examined wood species and separately for the softwoods, ring- and semi-ring-porous hardwoods and diffuse-porous hardwoods in Figure 1. The RIM seemed to be at least superposed by further parameters such as structural features and anatomical characteristics. This coincides with the data for the Ash, Scots pine and Beech previously reported by [8], who showed that the density and RIM were not even correlated within one wood species. More recently, [7] reported that the density and RIM were also poorly correlated when considering ten different wood species representing a range of ODD between 0.37 and 0.77 g/cm^3. However, according to [7] the RIM was fairly well correlated with the impact bending strength (IBS, $R^2 = 0.67$) and modulus of rupture (MOR, $R^2 = 0.56$), as determined

on axially matched specimens, which indicates that these strength properties are also at least partly affected by similar anatomical characteristics as the RIM is.

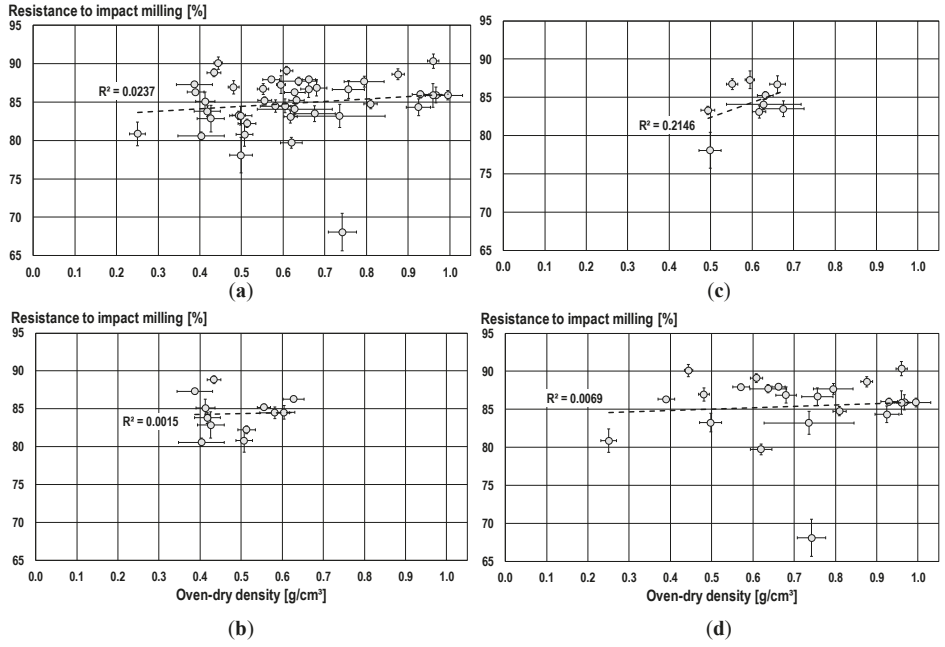

Figure 1. The relationship between the average oven-dry density and Resistance to Impact Milling (RIM): (**a**) all wood species (y = 3.1629x + 82.887); (**b**) softwoods (y = 1.1035x + 83.791); (**c**) ring- and semi-ring-porous hardwoods (y = 19.634x + 72.545); and (**d**) diffuse-porous hardwoods (y = 1.8475x + 84.086).

3.3. Impact of Anatomical Characteristics on Structural Integrity

The tested softwood species had a rather homogeneous and uniform anatomical appearance compared to the different hardwood species. However, even within this group the RIM varied between 80.6% and 88.8%. As summarized in Table 3, the softwood species differed also in the average tracheid diameter and in wood ray density. Nevertheless, the fracture patterns observed during the HEMI-tests were rather uniform, and fractures occurred predominantly along the growth ring borders in a tangential direction and along the wood rays and resin canals in a radial direction. The wood species showing an abrupt transition between the earlywood and latewood, such as the Larch and Scots pines, did not show a lower structural integrity compared to the species with a more gradual transition, such as the Norway spruce and Douglas fir, as one might expect due to a more sudden change of density within the tracheid tissue of one annual ring. Consequently, no fractures were observed along the transition line between the earlywood and latewood. In contrast to other softwood species, the Carribean and Radiata pines showed fractures in a tangential direction not only at the growth ring borders, but also where the resin canals ran in an axial direction.

As exemplarily shown for the heartwood of the Scots pine and Douglas fir in Figure 2, the major weak points, where fractures predominantly occurred, were the following: (a) the growth ring borders, where the less dense earlywood follows the dense latewood, and (b) the wood rays, which (1) consist of parenchyma cells, and (2) are running orthogonal to the main cell orientation in the tracheid tissue.

Table 3. The anatomical characteristics (tracheid diameter, ray density) and description of fractures during the HEMI-tests of different softwood species (standard deviation in parentheses).

Wood Species	Tracheid Ø [µm]		Wood Ray Density [mm^{-1}]		Fracture Behaviour tang.	rad.	Remarks
Scots pine sw	29	(6)	4.6	(1.2)	GR	RC	wider rings compared to hw
Scots pine hw	25	(5)	3.7	(1.5)	GR	RC	-
Radiata pine sw	22	(4)	4.4	(1.3)	GR	R, RC	-
Carribean pine hw	28	(4)	5.2	(1.2)	GR	R, RC	-
European larch sw	35	(7)	5.9	(1.7)	GR	R	wider rings compared to hw
European larch hw	35	(6)	4.4	(1.1)	GR	R	-
Douglas fir sw	25	(6)	4.3	(1.2)	GR	R, RC	-
Douglas fir hw	23	(5)	3.9	(1.2)	GR	R	-
Norway spruce	25	(5)	4.5	(1.0)	GR	R	-
Coastal fir	28	(5)	5.7	(1.3)	GR	R	-
Western hemlock	25	(5)	5.0	(1.3)	GR	R	-
Yew	10	(3)	7.1	(1.4)	(GR)	(R)	Irregular fracture pattern

GR = along growth rings, R = along rays; RC = along resin canals; tang. = tangential growth direction; rad. = radial growth direction.

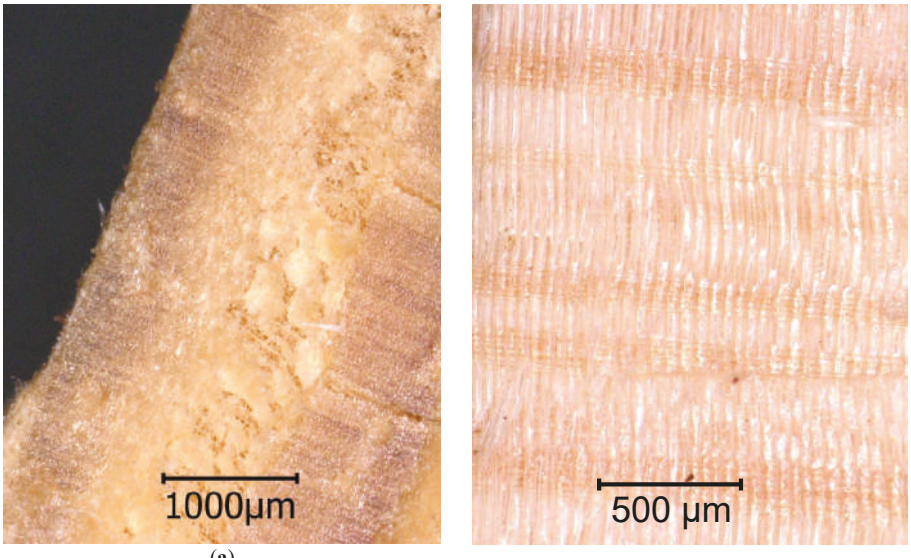

(**a**) (**b**)

Figure 2. The fracture pattern in the softwoods: (**a**) Cross section of the Scots pine heartwood, fracture along a growth ring border; (**b**) The radial fracture section of the Douglas fir heartwood, fracture along the rays.

The fractures in the ring-porous hardwood species often followed the wide-luminous earlywood vessels, such as in the English oak, Sweet chestnut, Ash, Locust, and Black locust (Table 4). The specimens consequently broke apart in a tangential direction. In addition, the fractures occurred along the latewood vessel fields where high portions of paratracheal parenchyma were present (Figure 3). The ring-porous hardwoods with broad wood rays, such as the English oak, also showed fractures running parallel to the latter. Finally, the average diameters of the earlywood vessels were not correlated with the structural integrity, although, in the earlywood of all the ring-porous hardwoods, the fractures occurred preferentially in a tangential direction following the vessel rings.

Table 4. The anatomical characteristics (earlywood vessel diameter, vessel density, ray density) and description of fractures during the HEMI-tests of different hardwood species (standard deviation in parentheses).

Wood Species	Earlywood Vessel Ø [µm]		Vessel Density [mm^{-2}]		Wood Ray Density [mm^{-1}]		Fracture Behaviour [1]	
							tang.	rad.
English oak sw [2]	247	(51)	7.7	(1.6)	8.4	(2.0)	EW	P
English oak hw	202	(49)	10.1	(2.0)	10.7	(1.8)	EW	P
Black locust	190	(40)	11.5	(1.0)	6.9	(1.1)	EW	R *
Sweet chestnut	209	(30)	7.7	(1.5)	11.8	(1.5)	EW	V-V
Ash [3]	169	(21)	13.8	(1.7)	6.6	(0.8)	EW	n.a.
Locust	165	(25)	16.1	(2.0)	4.4	(1.2)	EW	R, P *
Common walnut	134	(32)	7.7	(2.0)	5.7	(1.3)	V-V	V-V
Wild cherry	33	(8)	171.6	(31.3)	6.1	(1.4)	GR	R
Black cherry [4]	33	(9)	67.9	(22.9)	5.6	(1.3)	n.a.	R
European beech	40	(8)	131.9	(15.4)	3.0	(1.3)	GR *	n.a.
Maple [5]	46	(7)	54.5	(3.4)	7.9	(1.7)	GR	R *
Lime [6]	39	(9)	104.7	(14.0)	4.8	(1.1)	n.a.	n.a.
Birch	54	(13)	45.2	(8.5)	8.3	(2.4)	n.a.	R
Hazel	28	(6)	98.9	(20.2)	11.6	(2.5)	GR	n.a.
Boxwood [6]	10	(4)	213.9	(14.0)	11.0	(2.5)	n.a.	R *
Poplar [7]	58	(13)	33.7	(6.4)	11.0	(1.5)	n.a.	R
Alder	41	(10)	108.0	(16.7)	11.7	(2.0)	GR *	R
Kiri	164	(55)	5.2	(2.0)	2.4	(0.8)	V-V	V-V, R *
Shining gum [2]	144	(25)	7.6	(3.2)	11.3	(1.1)	V-V	V-V
Teak [8]	184	(57)	6.3	(1.7)	4.1	(0.7)	V-V	R *
Ipé [2]	103	(9)	23.2	(2.7)	7.8	(0.9)	P *	V-V
Merbau	250	(40)	4.0	(1.4)	4.2	(0.9)	V-V, P *	V-V, P *
Bangkirai	207	(32)	7.3	(1.7)	3.7	(1.3)	P	V-V, R *
Balau	137	(13)	11.9	(2.9)	9.1	(1.2)	P	V-V, R *
Bongossi	232	(41)	2.9	(1.1)	9.9	(1.2)	P	V-V, P *
Amaranth	109	(16)	4.4	(1.7)	6.9	(1.7)	P, V *	R
Basralocus [2]	190	(33)	2.8	(1.0)	7.9	(1.0)	P *	V-V
Garapa	121	(19)	15.2	(3.0)	8.3	(1.3)	P	V-V
Limba	139	(28)	4.4	(1.7)	10.2	(1.0)	n.a.	R
Kambala	193	(41)	2.8	(0.8)	4.4	(1.0)	(P)	R
Massaranduba	113	(18)	13.1	(3.3)	10.5	(1.5)	(P)	R
Greenheart [2]	90	(16)	14.0	(2.0)	7.5	(0.9)	n.a.	V-V

[1] n.a. = not available (no clear pattern evident), GR = along growth rings, R = along rays, RC = along resin canals, EW = along earlywood vessels, P = in parenchyma tissue, V-V = vessel to vessel, V = at vessels, * = characteristic plays minor role; remarks related to fracture patterns: [2] radial, parallel to rays; [3] no clear radial pattern; [4] very often parallel to rays; [5] parallel to growth rings; [6] irregular fracture pattern; [7] samples often compressed; [8] often at growth ring border.

This stands to some extent in contrast to findings by [2], who studied the perpendicular-to-grain properties of eight North-American hardwood species and found that the earlywood vessel area fraction negatively influenced the radial maximum stress and strain, whereas the ray width and area fraction were positively related to the maximum radial properties. The rays also affected the transverse stiffness significantly.

Studies conducted by [10] showed that wood rays have a positive effect on the tensile strength of English oak and European ash wood. However, as shown for the fragments obtained in the HEMI-tests, the latewood vessel fields turned out to be weak spots when it comes to dynamic loads in different anatomical directions. Therefore, the potentially positive effect of the wood rays on the structural integrity might be superposed by other anatomical features.

Finally, the RIM of the heartwood of the English oak (87.3%) was significantly higher than that of its sapwood (83.3%), which is to some extent surprising since sapwood is often considered to be less brittle than heartwood [11]. While the fine percentage (F) of both English oak materials was almost equal, the degree of integrity (I) of the heartwood was remarkably higher than that of the

sapwood, which might be related to the potential 'gluing' effects of the tylosis which were present in the earlywood vessels in the heartwood (Figure 3b), but were absent in the sapwood. Whether and to what extent the formation of tylosis has a positive effect on structural integrity would need to be further investigated using different generally tylosis-forming wood species.

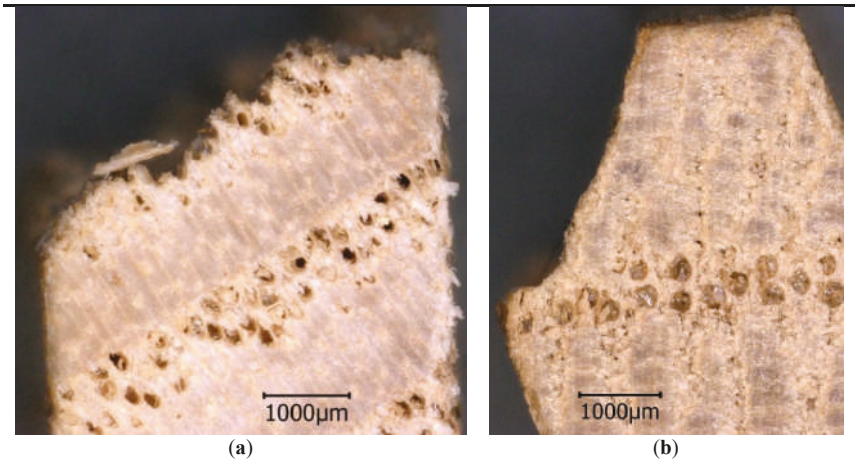

(**a**) (**b**)

Figure 3. The fracture pattern in the ring-porous hardwoods: (**a**) Cross section of the Ash, fracture within a ring of the earlywood vessels; (**b**) Cross section of the English oak heartwood, fracture along the field of the latewood pores and the adjacent parenchyma cells.

By far, the Sweet chestnut showed the lowest RIM among the ring-porous hardwoods, which might be related to its high wood ray density (Table 4), but no clear correlation between the ray density and structural integrity became evident (Figure 4). Furthermore, the radial fractures in the Sweet chestnut were also running from one vessel to the next. More likely, the higher percentage of vessels and axial parenchyma leads to a higher number of weak points within the xylem of the Sweet chestnut compared to the other ring-porous species within this study.

The group of semi-ring-porous hardwood species, which was represented by the Teak, Wild cherry and Walnut in this study, takes an intermediate position between the ring- and the diffuse-porous species. This also became evident when analyzing the fracture patterns obtained through the HEMI-test. As shown in Figure 5a for the Wild cherry, the fractures occurred along the growth ring borders but did not run through the earlywood vessel rings.

In the diffuse-porous hardwoods, the RIM varied most, i.e., between 80.9% (Kiri) and 90.3% (Boxwood), respectively. Although these two species also represent the extremes in ODD, the latter was not correlated with the structural integrity, as shown in Figure 1. Nevertheless, in contrast to the ring-porous hardwood species, the average earlywood vessel diameter of the diffuse-porous hardwood species was correlated with the RIM (R^2 = 0.4704), as shown in Figure 6. [12] studied angiosperm wood species and concluded that the tissue density outside the vessel lumens must predominantly influence wood density. Furthermore, they suggest that both the density and the vessel lumen fraction affect the mechanical strength properties.

It became also obvious that in different wood species such as the Kiri, Walnut, Shining gum and further tropical species, the fractures occurred between the vessels, both in the radial and tangential directions (Table 4). Consequently, the vessels turned out to be general weak points in the fiber tissue of the hardwoods, where the weakness increases with an increasing vessel diameter. Figure 7a shows, as an example for the Bongossi, that the vessels served as a starting point for the fractures independently from its anatomical orientation. Tropical species with comparatively small vessels such as the Amaranth, Bangkirai, Garapa, and Ipé showed a rather high RIM. On the extreme end of

the scale, the Merbau showed the lowest RIM and also the largest vessel diameters of all the species. Furthermore, distinct parenchyma bands and wood rays appeared to be weak (and therefore starting points for fractures) in tropical species as well, as also shown in Figure 7. The fractures cutting the wood rays appeared only where the rays were deflected by the vessels from their straight radial orientation.

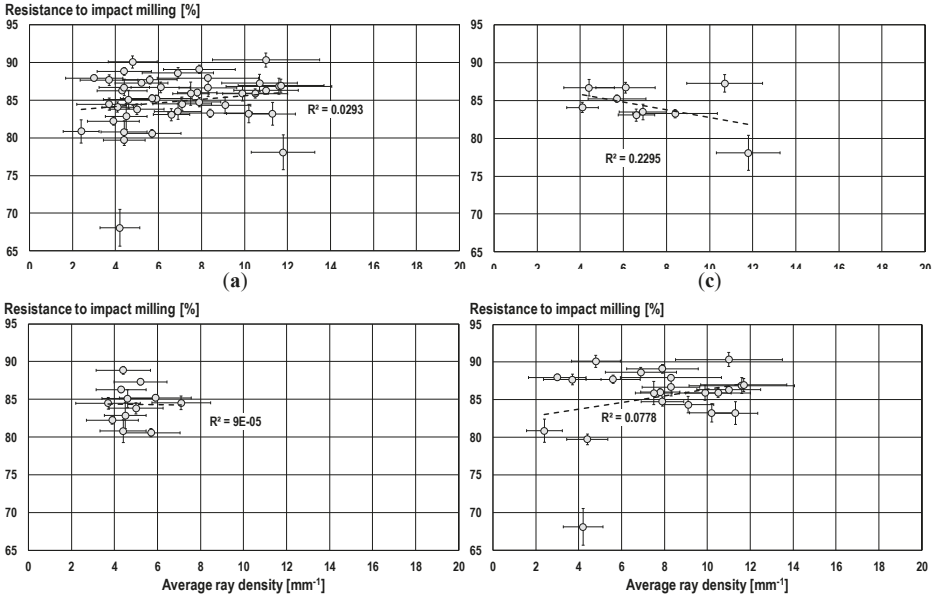

Figure 4. The relationship between the average ray density and the Resistance to Impact Milling (RIM): (**a**) all wood species (y = 0.2354x + 83.247); (**b**) softwoods (y = −0.0252x + 84.454); (**c**) ring- and semi-ring-porous hardwoods (y = −0.5083x + 87.875); (**d**) and diffuse-porous hardwoods (y = 0.4365x + 81.997).

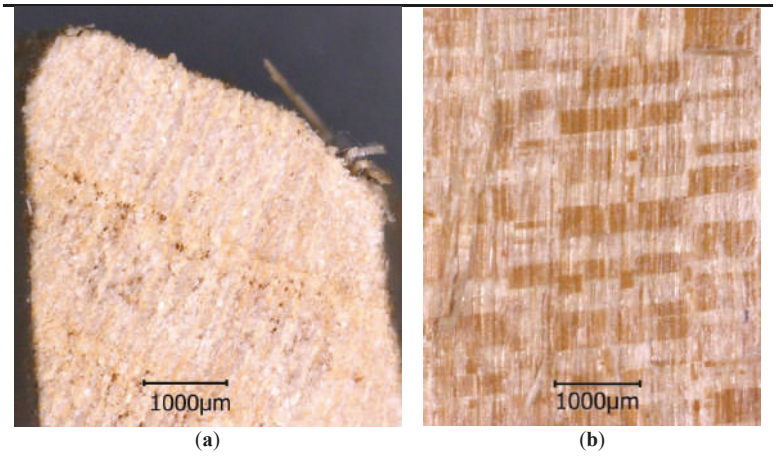

Figure 5. The fracture pattern in semi-ring-porous and diffuse-porous hardwoods: (**a**) the cross section of the Wild cherry, the fracture along a growth ring border; (**b**) the radial fracture section of the Alder, the fracture along the rays.

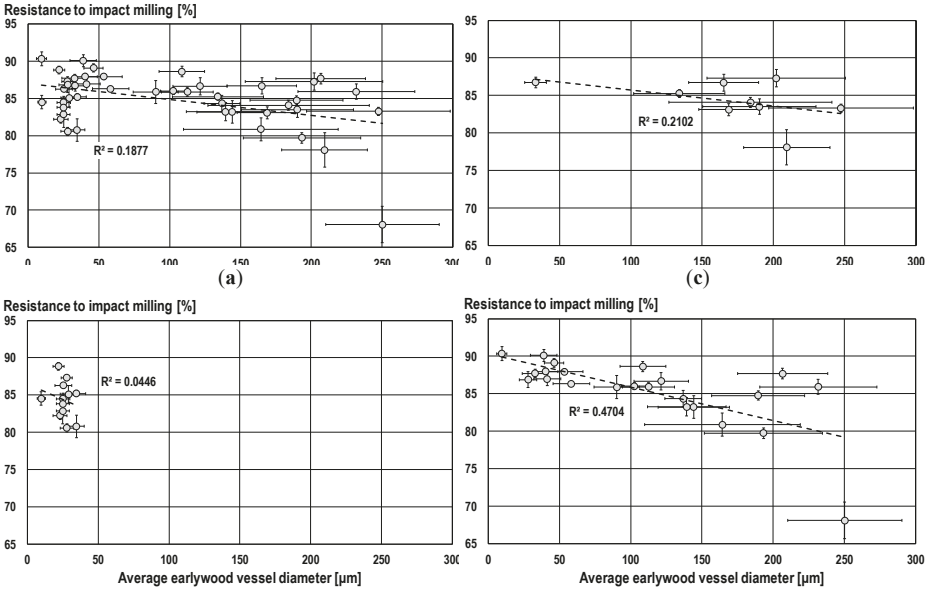

Figure 6. The relationship between the average earlywood vessel diameters and the resistance to impact milling (RIM): (**a**) all wood species (y = −0.0213x + 86.982); (**b**) softwoods (y = −0.0814x + 86.425); (**c**) ring- and semi-ring-porous hardwoods (y = −0.0213x + 87.857); and (**d**) diffuse-porous hardwoods (y = −0.0445x + 90.309).

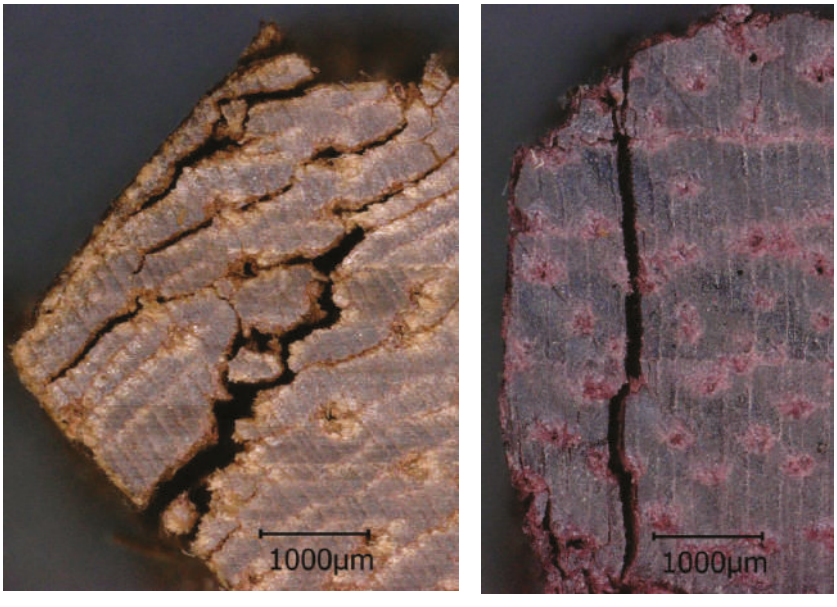

Figure 7. The fracture pattern in the diffuse-porous hardwoods: (**a**) the cross section of the Bongossi, the tangential fractures; (**b**) the cross section of the Amaranth—the radial fractures along the rays.

4. Conclusions

In this study, we showed that the differences in the structural integrity of wood and thus in the brittleness are predominantly affected by anatomical characteristics. The size, density and distribution of the vessels as well as the ray density of the wood were found to have a significant impact on the structural integrity of the hardwoods. The structural integrity of the softwoods was, on the other hand, affected by the number of growth ring borders and the occurrence of resin canals. The density affected the Resistance to Impact Milling (RIM) of neither the softwoods nor the hardwoods.

Consequently, for applications where the brittleness of wood is more relevant than its elasto-mechanical properties, which are generally strongly correlated with wood density, other anatomical characteristics need to be considered for assessing wood quality. In particular, where dynamic loads impact on wooden components, the brittleness of wood becomes a critical issue. Dynamic loads paired with long-term wear and abrasion can be expected, for instance, on outdoor flooring. Furthermore, during wood processing, machining and handling during industrial processes, numerous dynamic impacts occur and affect the structural integrity of wood.

Wood quality is consequently strongly purpose-specific and cannot be simply derived from wood density data. Anatomical features showed a high potential to serve as better indicators for the structural integrity of wood. Additional influences such as the occurrence of reaction wood, alternating rotational growth and other types of fiber deviations likely affect the structural integrity of wood to a similarly extent. In summary, the findings from this study confirmed the need for test methods other than standard strength tests. As long as the common knowledge about wood anatomy and its effects on mechanical wood properties is incomplete, methods are needed that are sensitive, reliable, and accurate enough to characterize the structures of wood in a comprehensive manner. As shown with the HEMI-method applied in this study, indicators can be delivered for instance of the structural integrity of wood. However, further tests are needed, paired with more detailed analyses of the anatomical and chemical constitution of the wood samples being tested, to achieve a fully satisfactory insight on the relationship between wood anatomy and its structural integrity.

Author Contributions: Mainly responsible for the conceptualization, methodology used for these investigations and also the data evaluation, data validation and formal analysis was L.E. together with C.B. Investigations and data curation were conducted by G.W. together with L.E. The original draft of this article was prepared by L.E. together with C.B. who was involved in the review and editing process of this article. L.E. and G.W. did care for the visualization, supervised by C.B. who had the project's administration.

Funding: This research received no external funding.

Acknowledgments: The authors gratefully acknowledge Florian Zeller (GD Holz, Germany), Uwe Herrmann (Vandecasteele Houtimport, Belgium), Miha Humar (University Ljubljana, Slovenia) and Martin Rosengren (Rönnerum, Sweden) for providing wood samples.

Conflicts of Interest: The authors declare no conflict of interest.

References

1. Ghelmeziu, N. Untersuchungen über die Schlagfestigkeit von Bauhölzern. *Holz Roh. Werkst.* **1938**, *1*, 585–601. [CrossRef]
2. Beery, W.H.; Ifju, G.; McLain, T.E. Quantitative wood anatomy–Relating anatomy to transverse tensile strength. *Wood Fiber Sci.* **1983**, *15*, 395–407.
3. Alteyrac, J.; Cloutier, A.; Ung, C.H.; Zhang, S.Y. Mechanical properties in relation to selected wood characteristics of black spruce. *Wood Fiber Sci.* **2007**, *38*, 229–237.
4. Rapp, A.O.; Brischke, C.; Welzbacher, C.R. Interrelationship between the severity of heat treatments and sieve fractions after impact ball milling: A mechanical test for quality control of thermally modified wood. *Holzforschung* **2006**, *60*, 64–70. [CrossRef]
5. Brischke, C. Agents affecting the structural integrity of wood. In Proceedings of the 10th Meeting of the Northern European Network on Wood Science and Engineering, Edinburgh, UK, 13−14 October 2014; pp. 43–48.

6. Zimmer, K.; Brischke, C. Within-species variation of structural integrity—A test on 204 Scots pine trees from Northern Europe. In Proceedings of the 12th Meeting of the Northern European Network on Wood Science and Engineering, Riga, Latvia, 12−13 September 2016.
7. Brischke, C. Interrelationship between static and dynamic strength properties of wood and its structural integrity. *Drvna Ind.* **2017**, *68*, 53–60. [CrossRef]
8. Brischke, C.; Rapp, A.O.; Welzbacher, C.R. High-energy multiple impact (HEMI)-test—Part1: A new tool for quality control of thermally modified timber. In Proceedings of the The International Research Group on Wood Preservation, Tromsø, Norway, 18–22 June 2006; IRG Document No: IRG/WP/06-20346.
9. ISO 5223. *Test Sieves for Cereals*; ISO (International Organization for Standardization): Geneva, Switzerland, 1996.
10. Reiterer, A.; Burgert, I.; Sinn, G.; Tschegg, S. The radial reinforcement of the wood structure and its implication on mechanical and fracture mechanical properties-a comparison between two tree species. *J. Mater. Sci.* **2002**, *37*, 935–940. [CrossRef]
11. Bamber, R.K. Sapwood and heartwood. In *Forestry Commission of New South Wales*; Wood Technology and Forest Research Division: Beecroft, Australia, 1987; Volume 2, pp. 1–7.
12. Zanne, A.E.; Westoby, M.; Falster, D.S.; Ackerly, D.D.; Loarie, S.R.; Arnold, S.E.J.; Coomes, D.A. Angiosperm wood structure: Global patterns in vessel anatomy and their relation to wood density and potential conductivity. *Am. J. Bot.* **2010**, *97*, 207–215. [CrossRef] [PubMed]

© 2019 by the authors. Licensee MDPI, Basel, Switzerland. This article is an open access article distributed under the terms and conditions of the Creative Commons Attribution (CC BY) license (http://creativecommons.org/licenses/by/4.0/).